Cranfield UNIVERSITY

School of Aerospace, Transport and Manufacturing

Francesco Silva

MECHANICAL PROPERTIES AND IMPACT ENERGY ABSORPTION OF HYBRID THERMOPLASTIC NANOCOMPOSITE STRUCTURES

PhD THESIS

Supervisors: Dr James Brighton and Dr Hrushikesh Abhyankar

- January 2016 –

This thesis is submitted in partial fulfilment of the requirements for the degree of Doctor of Philosophy

ABSTRACT

This thesis focuses on the mechanical properties and the impact energy absorption capabilities of injection moulded hybrid three-phase polymer composites. Its main aim is to investigate the effect of different micro and nano-sized filers on the mechanical properties; such as stiffness, strength, ductility, impact resistance and energy absorption capability; of short-fibre reinforced thermoplastic composites. Extensive experimental and numerical investigations were core to the research.

Six different, three-phase composites, were manufactured by the integration of two types of nano-reinforcements (either nano-silica or nano-clay), or micro-glass-spheres, into two types of short glass-fibre reinforced thermoplastic matrices (either Polypropylene (PP) or Polyamide (PA6)). The materials were characterized using Transmission Electron Microscopy (TEM), Wide Angle X-Ray Diffraction (WAXD) and optical microscopy. The effect of matrix and reinforcement material on the mechanical properties and the energy absorption capabilities of polymer composites were studied in detail. The results are compared with the properties of standard two-phase glass-fibre reinforced polymer composites. Initial experiments focused on quasi-static uniaxial tensile and compression tests, as well as quasi-static crash tests of the conical structures. Subsequently, dynamic drop weight impact crash tests of the conical structures were conducted to investigate the influence of the nano-reinforcement on the energy absorption capabilities of the polymer composites. To study propagation of the dynamic cracks and the energy absorbing mechanism, the impact event was recorded using a high-speed camera. The fracture surface was investigated with scanning electron microscopy (SEM). Furthermore, improved simulation tools were developed to accurately and effectively model nanocomposite structures subjected to dynamic loads. A constitutive model with orthotropic yield, strain rate sensitivity and strain

energy density based failure criterion, was developed and implemented into Ls-Dyna Finite Element (FE) code.

The results show that by changing the filler and the matrix material, it is possible to control the mechanical properties and the energy absorption capability of the glass-fibre reinforced polymer nanocomposites. An increase in the mechanical properties (stiffness, strength or ductility) of PA6 composites was observed. Furthermore, nano-silica and glass-spheres reinforcements were found to improve the energy absorption capabilities of PA6 composites by changing the mode of failure, whereas nano-clay reinforcement caused a decrease in that capability. Little or negative influence of the nano-fillers was observed, when combined with PP based composites.

The experimental findings were used to generate, calibrate and validate the user defined material model. The structural FE modelling proved that the model was capable of accurately and effectively representing the nanocomposite structures subjected to static and dynamic loads. Furthermore, it provided a valuable input for better understanding of the structural failure mechanism, observed in the three-phase nanocomposite structures.

ACKNOWLEDGEMENTS

I would like to thank Dr James Njuguna for giving me the opportunity to undertake this research and for all help and advice he gave me throughout this work. Further, I would like to thank Dr Rishi Abhyankar and Dr James Brighton for their advice and guidance required to complete this thesis.

I would like to acknowledge the European Commission for funding this study under the Project Reference No. 228536 - 2, and further all the project partners that were involved in this project. I would also like to acknowledge Rolls-Royce plc for sponsoring the final year of this study.

Further, I would like to thank Dr Kim Blackburn for his help with data acquisition for the impact tests and Dr Clive Temple for all the advice on English grammar and writing.

Thanks to all my colleges in Cranfield University who have helped me during my PhD. In particular: Sophia Sachse, Zakaria Mouti and Elias Nassiopoulos.

Finally, I would like to thank my family for all their support and encouragement.

ABBREVIATIONS

PP	-	Polypropylene
PA	-	Polyamide
SEM	-	Scanning Electron Microscopy
TEM	-	Transmission Electron Microscopy
FEM	-	Finite Elements Method
WAXD	-	Wide Angle X-Ray Diffraction
GF	-	Glass Fibres
GS	-	Glass Spheres
SiO_2	-	Silica Nano Particles
MMT	-	Montmorillonite
SEA	-	Specific Energy Absorption
RVE	-	Representative Volume Element
DAQ	-	Data Acquisition
UMAT	-	User Defined Material Model
UTS	-	Ultimate Tensile Strength
$CS_{6\%}$	-	Compressive strength at 6% strain

NOTATION

t	-	Time
T	-	Temperature
V	-	Velocity
M	-	Mass
E	-	Young's Modulus
G	-	Shear Modulus
C	-	Elastic Tensor
v	-	Poisson's Ratio
σ	-	Stress
$\overline{\sigma}$	-	Equivalent stress
τ	-	Shear Stress
ε	-	Strain
ε^p	-	Plastic Strain
$\dot{\varepsilon}$	-	Strain Rate
$\dot{\lambda}$	-	Plastic Multiplier
φ		Yield function
H	-	Hardening function
f	-	Failure Function
U	-	Strain Energy Density
$\bar{x}$	-	Average data
$\hat{\sigma}$	-	Standard deviation

TABLE OF CONTENTS

LIST OF FIGURES

LIST OF TABLES

1. Introduction

1.1 Background and motivation

The increasing need for high performance structures, in the automotive and the aerospace sectors, demands a continuous development of new engineering materials. Unique mechanical properties, together with low specific weight, can be achieved by a combination of different constituents into one macroscopic composite material. Coupling high strength reinforcement with a supporting matrix creates a novel material with the improved characteristics, which could never be obtained using either of the constituents separately [1]. These types of materials are particularly desirable in structures where high strength to weight ratio is of great importance. They also offer several advantages over conventional metallic materials; such as high stiffness and strength, superior fatigue properties and good corrosion resistance.

Thermoplastic polymers, such as polypropylene (PP) and polyamide (PA), are widely used in the automotive industry due to their good mechanical properties, simple manufacturing techniques and low cost. However, their application as structural materials is limited because of the insufficient stiffness and strength limits. That is why incorporation of fibre reinforcements has become a widely used technique to improve the mechanical properties such as strength and stiffness, but often, at the cost of reduced ductility and toughness.

Due to their numerous advantages, injection moulded short-fibre reinforced thermoplastic composites are currently the most prevalent composite materials in the automotive industry [2]. Structures made of these materials have already found several applications in elements such as: car and rail body panels, bumper fascia and beam, radiator grills, instrument panels, engine components and fuel lines. However, apart from the normal operating loads, many of these components are subjected to foreign object damage (FOD), or their function should provide good energy absorption capability (e.g. body

panels, bumpers, external engine components). This is why it is one of the major challenges for the automotive industry, to improve the ductility and toughness of fibre reinforced polymer composites, as these properties drive the ability of the structure to resist impact loads and absorb the impact energy.

Over the last decade intensive research in the field of composite materials proved that the addition of nano-sized fillers, rather than micro-sized fillers, can significantly enhance mechanical properties of the polymeric materials [3]. This is why the nanocomposites have become more and more attractive materials for the automotive sector. A desired improvement in the mechanical properties can be achieved by changing different parameters of the nano-filler; such as size, shape, material and volume fraction. Furthermore, by combining more than two constituents, it is possible to construct high performance hybrid nanocomposites. Appropriate combination of these constituents can provide significant increase in stiffness and strength of the composite material, without comprising its ductility and impact resistance. However, if inadequate mixture of the constituents is used, it could negatively affect the mechanical properties of the composite. Despite many challenges of the nanotechnology, the prospects of high performance composite materials, capable of sufficient resistance to impact loads, as well as the ability to effectively absorb the energy of the impact, drive the need for extensive research in this field.

In case of light weight structures, made of polymer composites, the most widely used nano-reinforcements are silica based particles, due to their good mechanical properties and high thermal stability. Currently, around 70 % of the nano-materials used in the automotive industry are silica based nano-clays [4]. Although there has been a significant amount of research carried out on the mechanical properties of polymers filled with nano-particles, there is limited research work published on the effect of nano fillers on the mechanical

properties of hybrid fibre reinforced nanocomposites. Furthermore, the understanding of the mechanical response and fracture mechanism of hybrid nanocomposite structures, subjected to dynamic loads, is equally limited.

The use of advanced composite materials also requires sophisticated numerical tools. These tools should provide an accurate and effective prediction of the structural response, for the components made of these materials. The existence of a Finite Element (FE) model for the hybrid nanocomposite material can lead to a significant improvement in the design process of a new product. Furthermore, a method capable of predicting the failure mechanism in the hybrid nanocomposite structure could provide a valuable input required to produce an optimized, high performance and low weight structure. A reliable modelling method can also reduce the amount of structural testing required, leading to a significant cost reduction. Although there are a number of numerical models for composite materials, implemented into commercial FEM software such as Ls-Dyna [5] (Mat: 22, 54, 55, 58, 59, 158 and 161), there is still a need for improvements, especially within the field of composite plasticity and failure. Furthermore, the existing models are generally built for specific applications, and therefore, may not be applicable if novel materials or different loading cases are investigated.

1.2 Aims and objectives

One of the main concerns when using the short-fibre reinforced thermoplastic composites, for structural automotive applications, is the insufficient ability of the structure to resist the impact loads and absorb the impact energy. Although different configurations of fibres and micro fillers can provide significant improvements in properties such as stiffness and strength, they usually lead to an important drop in ductility and toughness of the composite.

That is why the main aim of this thesis is to investigate the effect of different micro and nano-sized fillers on the mechanical properties - such as stiffness, strength, ductility, impact resistance and energy absorption capability - of hybrid short-fibre reinforced thermoplastic composites. Furthermore, the thesis aims to obtain a better understanding of the relation between the mechanical properties of the hybrid nanocomposite material and the fracture mechanism of the hybrid nanocomposite structure. The final aim is to develop reliable numerical tools, to effectively model hybrid nanocomposite structures subjected to crashing loads.

In order to realise these aims the following key objectives are established:

- Fabrication of hybrid three-phase polymer based (polyamide and polypropylene) glass-fibre reinforced composites, filled with micro (glass spheres) and nano (silica and MMT) particles.
- Study morphology of the manufactured composites.
- Derive the mechanical properties of the composites.
- Study fracture mechanism and energy absorption capabilities of the hybrid composite structures.
- Develop a material model to accurately capture all the mechanical properties of the hybrid composites.
- Utilize the developed model to gain better understanding of the crashing behaviour of the hybrid nanocomposite structures.
- Identify the influence of such parameters as matrix material, filler type, filler size and testing speed, on the fracture mechanism and energy absorption capabilities of the hybrid nanocomposites.

1.3 Methodology

In order to meet the aims and objectives of the thesis, the following methodology will be utilized (see Figure 1). First an extensive literature review will be carried out on which basis an appropriate fillers and polymer matrices will be selected. Subsequently, the composite materials will be prepared using different combinations of nano and micro fillers. A number of test samples and structures will be manufactured using novel hybrid three-phase composite materials (polymer/glass-fibres/nano-fillers. Some specimens will be used to study the morphology of the materials, i.e. crystalline structure of the composites, dispersion of the nano fillers and orientation of the fibres. The standard mechanical properties of the composites will be determined in a series of simple uniaxial tensile and compression tests. Furthermore, the fracture behaviour of the composite conical structures will be investigated in a series of static and dynamic crash tests. Using the information contained in the literature review and the results of specimen and structural testing, a novel numerical model for a composite material will be developed and implemented into Ls-Dyna software. The material model will be validated and calibrated using the results of the experiments. Both numerical and experimental results will be used to study in details the effect of the filler on the mechanical properties of the composites. The attention of this study will be directed towards the relation between micro and macro fracture process with crack propagation mechanism and their effects on energy absorption capability of the nanocomposite structures.

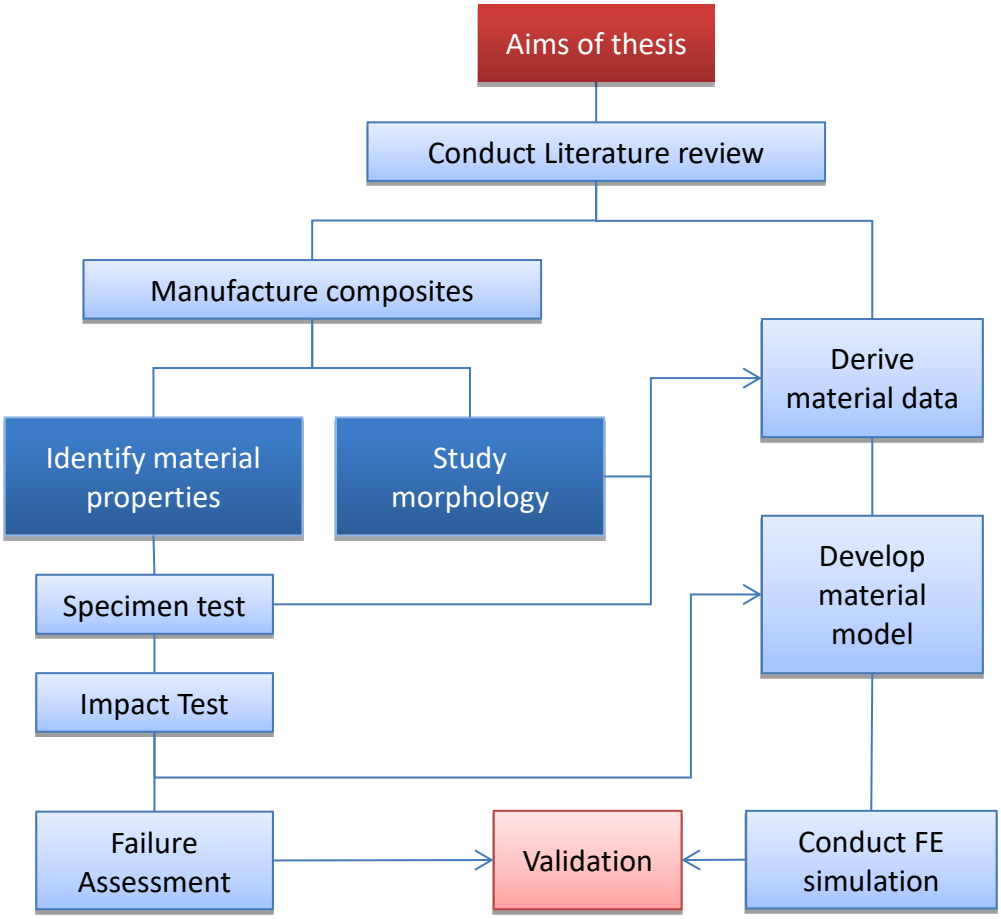

Figure 1: Methodology work flow chart

1.4 Structure of the thesis

Chapter 1: The first chapter introduces the reader to the subject of the thesis by presenting a background of the study as well as the main aims and objectives. The main focus is on the relation between the nano-filler and the mechanical properties of the fibre reinforced polymer composite.

Chapter 2: Literature survey on the effect of various nano-fillers on the mechanical properties of polymeric materials is shown in this chapter. Factors affecting the energy absorption capabilities of composite structures are described in detail. Furthermore, the main aspects of numerical methods for modelling composite structures are presented.

Chapter 3: This chapter presents the process for manufacturing the nanocomposite materials as well as the procedure for mechanical testing and material characterization. Subsequently, it presents the results of the material characterization carried out with Transmission Electron Microscopy (TEM), X-ray diffraction and optical microscopy. Finally, it presents and discusses the results of the mechanical testing, carried out using tensile and compressive, in static and dynamic conditions.

Chapter 4: This chapter shows the results from experimental investigation of the composite structures. This includes static and dynamic crash testing of conical structures made of eight different composite materials. It also presents the results of material failure investigation carried out using Scanning Electron Microscopy (SEM). The chapter concludes with a discussion on effect of different nano and micro fillers on the failure mechanism and energy absorption capability of studied composite materials.

Chapter 5: In this chapter a theoretical development of the numerical model for composite materials is presented. It details the rationale behind the selection of the material model formulation as well as procedure for numerical implementation into Ls-Dyna software, as user defined subroutine.

Chapter 6: This chapter focuses on the FE modelling of the composite structures carried out using the developed material model. It starts with the procedure for calibration of the model, using the experimental data. Subsequently, it details the results of the simulations and shows the correlation with the experimental

results. It also provides a further insight into failure mechanism of the composite conical structures.

Chapter 7: This chapter provides a general discussion about the mechanical properties and failure mechanism of the nanocomposite materials and structures, based on both experimental and numerical analysis.

Chapter 8: This chapter concludes the thesis work, summarizing the current understanding of the effect of different fillers on the mechanical properties and failure mechanism of fibre reinforced composites. It also identifies any further work required in the field of three-phase fibre reinforced composites, intended for structural applications, as well as requirements for improvements in the modelling methods.

2. Literature Survey

This chapter reviews the established knowledge regarding the mechanical properties of standard fibre-reinforced, as well as nano-reinforced, polymer composites and their application as structural materials. It also reviews the current state of the art of modelling techniques, that can be used to accurately represent advanced composite materials, subjected to static and dynamic loads.

2.1 Composite materials

Over the last four decades, polymers started to gradually replace conventional materials, such as metals, in various structural applications. This replacement processes happens mainly due to their numerous advantages, over the conventional materials, such as easy processing, productivity and low cost. However, to obtain comparable or improved mechanical properties in relation to metals, polymers are generally used in the form of composites.

Composites are materials which consist of two or more distinct constituents, which are separated with an interface region. The properties of a composite material are superior to those of constituent materials, and could never be obtained using either constituent separately [1]. Furthermore, combination of two distinct materials, provides the engineer with the potential to design structures with enhanced mechanical properties in specific directions. This makes the structures optimized for a particular loading path.

In the composite material, the stronger and harder phase is called the reinforcement. Its main function is to provide stiffness and strength to the composite. The reinforcement can be either fibrous or particulate. Typically, as a fibrous reinforcement, carbon, glass or aramid material are used [6]. Fibres can be either continuous or discontinuous (short), whereas particles can be

small or large. A general classification of the composites due to the reinforcement is illustrated in Figure 2. High performance structures are usually made of continuous fibres, which are mainly aligned in one direction. Such materials are characterized by high anisotropy. To overcome this issue, laminate structures have been developed. In these structures a number of plies are laid on each other, at different but specific directions, in order to resist multiaxial loading. However, the current manufacturing techniques for continuous fibre composites are complex, and therefore expensive. This is why their application is limited to industries where high performance and low weight are crucial and cannot be compromised by the cost. This includes the aerospace and motorsport industries [7].

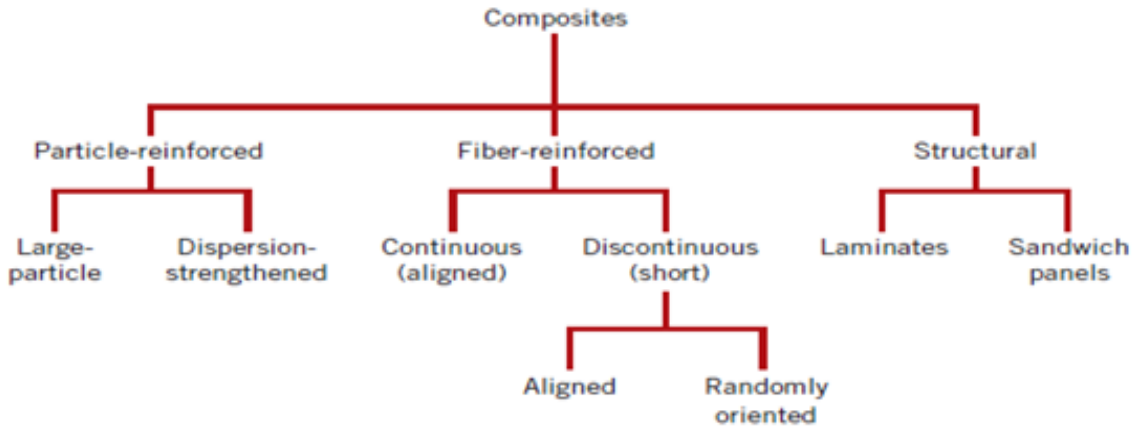

Figure 2: Classification of composites due to reinforcement

In order to reduce the manufacturing cost, discontinuous (short) fibre composites were developed. Their mechanical properties are inferior, in comparison to continuous fibres, but still can provide a sufficient reinforcing effect for various structural applications [8]. Other low cost composites are particulate reinforced composites. In their case the most prevalent reinforcements are glass, rubber, silica, metal or ceramic materials, in the form of particles or whiskers [9]. Particulate reinforced composites can be sub-divided into large particle composites (micro-sized) and dispersion

strengthened composites (nano-sized). Short-fibre and particulate reinforced composites are widely used in the automotive industry. To construct a composite, the fibres are embedded into a relatively less stiff and weaker phase, called the matrix. The main role of the matrix material is to transfer the loads and stabilize the fibres. The secondary function is to protect them from the external environment such as moisture, chemicals or mechanical damage [10]. The matrix material can be polymeric, metallic or ceramic.

Metal and ceramic matrix composites are mainly used for high temperature applications such as gas turbine manufacturing and the space industry. For low and medium temperature applications, mainly automotive or airframe manufacturing, polymer matrices are prevalent.

The most attractive polymers used as matrix materials are thermosets or thermoplastics. The main difference between the two polymers is in their respective molecular chains. Thermosets have cross-linked chains, which are characterized by strong chemical bonds. Thermoplastics have linear molecular chains with relatively weak forces of attraction. The main result of this difference is that the thermoplastics, once formed to the final solid shape, can be heated and re-melted back into a liquid form. By contrast, thermosets once formed and cooled to their final shape will suffer charring if reheated. Moreover, manufacturing of thermoset composites is complex due to the large number of components involved in the process such as base resin, curing agents, catalysts, flowing agents and hardeners. In terms of mechanical properties, thermosets are harder, stiffer and more brittle than thermoplastics. They are also able to sustain fibre loadings up to 80%, which results in remarkable enhancement in the mechanical properties of the composite [11]. That is why thermoset composites often find applications in high performance structures, such as primary airframe components. However, thermoplastics provide several advantages over thermosets. The main ones are associated with

their low manufacturing costs. Thermoplastics are flexible and easy to mould complex parts. Composites can be manufactured using simple methods such as extrusion ore injection moulding.

The last component of the composite material is the interface region. Its size is of tenths of a micron in cross-section, but despite the insignificant size its function is crucial for the performance of the composite. The interface region controls the fracture behaviour of the composite as well as its transverse, shear and flexural response [12; 13]. This is why if the bond is too weak, there is no load transfer between the matrix and the fibre, resulting in poor mechanical properties (stiffness and strength), but good energy absorption provided by the restricted crack growth. By contrast, if the bond is too strong, the composite is brittle, but at the same time it is strong end stiff. In order to achieve desired mechanical properties it is required to control the strength of the interface to provide a compromise between strength and toughness.

2.2 Short-fibres reinforced polymer composites

Due to the low manufacturing costs and relatively good mechanical properties, injection moulded composites made of thermoplastic matrix (mainly Polyamide (PA) and Polypropylene (PP)) and short glass fibres (GF), are currently the most prevalent materials used in the automotive industry [14].

Polyamide based composites have been successfully applied for automotive structures such as engine components (ex. oil pans, radiators and intercoolers), bumper beams, stiffeners and body panels. These applications require properties such as good structural strength and stiffness, as well as chemical and temperature resistance [2; 15; 16]. There are a number of different types of polyamides available to construct composite materials. However, the most widely used in the automotive industry are PA6 and PA66, due to their good resistance to wearing, good surface finish and superior heat ageing resistance

[17; 18]. PA6 is synthesised from one repeating monomer, which results in one carbon atom in the monomer unit. PA66 is synthesised from two different repeating monomers, which results in two carbon atoms in each monomer unit (see Figure 3). In general, the two polymers have similar mechanical properties. However, PA6 has better ductility and toughness, better long term heat resistance, better impact resistance in low temperatures, better surface quality, as well as lower cost. The main disadvantages of PA6 in relation to PA66 are lower modulus, lower wear resistance, lower short term heat resistance and higher moisture absorption [17].

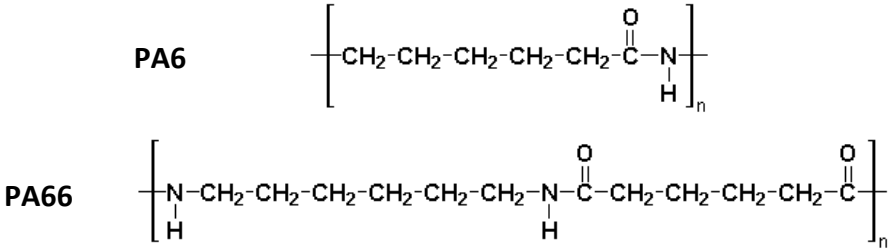

Figure 3: Monomers of PA6 and PA66

Polypropylene based composites have found several automotive applications such as interiors (trim items, instrument panels), exteriors (bumper fascia, air inlet, wheel house liners), under the hood (fuse block cover, fan shroud, coolant reservoir). Polypropylene is produced by polymerizing propylene molecules (monomer units) into very long polymer molecule or chain (see Figure 4). Its mechanical properties such as stiffness strength and ductility are lower than those of polyamide. However, it is a very attractive material for the automotive industry due to its low cost, colourability, chemical resistance and UV stability. Composites made of polypropylene can meet several different requirements for automotive components such stiffness, impact and heat resistance, as well as appearance [19].

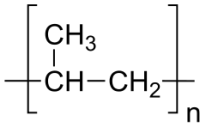

Figure 4: Monomer of PP

2.2.1 Mechanical properties

The key factors determining the mechanical properties of injection moulded short glass-fibre reinforced thermoplastic composites are: fibre content, length, diameter and orientation; as well as the interfacial strength and the matrix material.

The effect of fibre length on the mechanical properties of short-fibre reinforced polyamides was studied by Bernasconi et al. [20], as well as Hassan et al. [21]. In these studies it was proved, that the length of the fibres has a significant effect on the mechanical properties of the composites. The researchers observed that the composites with shorter glass-fibres have statistically more total fibre length, and therefore, more total surface area. This results in a much better interfacial bonding between the fibres and the matrix. However, the reduction in fibres' length causes a reduction in strength and modulus. By contrast, the ductility of the composites was found to increase with decreasing fibres' length. This effect was attributed to the ability of the matrix to deform. If the long fibres are present in the composite, the movement of the matrix is restricted. This restriction reduces with decreasing fibre length, allowing for larger deformations of the composite before it fails.

The other parameter influencing the mechanical properties of the polymer composites is diameter of the fibres. Sato et al. [22] found that the strength of glass-fibre reinforced polyamide is not significantly affected by the diameter of the fibres, in the 7-13 μm range. However, if the diameter is below 7 μm, the strength of the composite falls dramatically. The authors demonstrated that this effect is a result of the increased number of fibre ends. The fibre ends act as stress concentration regions, which are accelerating formation of the micro-cracks. The decrease in diameter of the fibres results in significant increase in the number of fibre ends present in the composite. As a result there are

numerous stress concentration points within the composite, which are responsible for the reduction in its strength. Other researchers such as Thomason [23] and Ramstein et al. [24] , showed that the un-notched impact strength is highly dependent on the fibre diameter, but there is no significant effect on the tensile modulus.

Furthermore, the mechanical properties of the composite can be significantly affected by the fibre content. Thomason [25-27] carried out an extensive research to understand the influence of the fibre content on the mechanical properties of PA66 glass-fibre reinforced composites. The author observed an almost linear relation between the weight fraction of the fibres, and tensile stiffness and strength. However, the author noticed a large reduction in composite ductility with increasing number of fibres. Thomason also observed that an increase in fibre content can have a beneficial effect on impact behaviour of PA66 composites above 10 wt%. Similar conclusions were drawn by Gullu et al. [28] who studied both polyamide and polypropylene reinforced with short glass-fibres.

The last parameter which significantly affects the mechanical properties of the composite is the matrix material. It is well known that transverse and flexural properties of long-fibre reinforced composites are dominated by the matrix properties. In the case of short-fibre composites, the matrix material can also have a significant effect on the longitudinal properties of the composite. This is due to the fact that the fibres are discontinuous, and therefore the longitudinal loads between the fibres are transferred by the matrix. Gullu et al. [28], studied the mechanical properties of short glass-fibre reinforced polypropylene and polyamide 6. They reported, that at the same weight fraction of the fibres (15 and 30 wt%), the tensile properties of the composites are highly dependent on the matrix material. Tensile properties such as modulus, strength and ductility

of the polyamide 6 based composites were found to be superior to those of the polypropylene based composites.

2.2.2 Impact and energy absorption

Despite many advantages, the composite materials can suffer from some serious drawbacks. The main one is their response to impact loads such as foreign object damage, handling damage or crash. There have been many studies performed to investigate the impact properties of fibre reinforced polymer composites [2; 29-37]. It has been shown that the key factors influencing the dynamic response and fracture mechanism of composite materials are similar to those controlling the static mechanical properties, such as stiffness and strength. These factors are interfacial adhesion, fibre length and diameter, weight fraction of the fibres, as well as properties of the matrix. As it was previously discussed, the key role in controlling the fracture mechanism of composite materials has the interface region and the matrix material. Blumentritt et al. [38] studied in detail the fracture mechanism of short-fibre reinforced composites. They observed that fibres are pulled out with little matrix residuals, if the fracture occurs at the interface. If the fracture occurs at the matrix, the fibres are also pulled out but with visible residual of the matrix material. However, if the strengths of the matrix and the interface region are high, the failure of the fibres is predominant. Based on this observation and measurements of the mechanical properties, the researchers concluded that the failure mode has a significant influence on the impact resistance and energy absorption capability of the composite material. The composites failing by fibre fracture are generally strong and stiff with low toughness, whereas if matrix or interface failure is predominant, the composite is weak but tough. This is mainly attributed to the fibre bridging effect which prevents development of the crack, if the fibres stay unbroken during the fracture process. Furthermore, they observed that ductile matrix composites are much tougher than brittle

matrix composites, as the crack propagation in a ductile matrix requires much more energy. Nevertheless, the short-fibre composites, with either ductile or brittle matrices, fail primarily by fibre pull- out. This happens due to the defects present in the material as well as stress concentration regions in the vicinity of fibres, which induce micro-cracking in the interface region. Due to the big difference in stiffness, between the fibres and the matrix, their interface is known to be the region of the highest stress concentration in the composite. Furthermore, many researchers demonstrated that short-fibres act as crack initiators, but on the other hand work as crack propagation blockers [38; 39]. The stress concentration regions near the fibres accelerate the crack initiation but the propagating crack must often travel around the fibres which results in elevated energy dissipation capability of the composite.

The positive effect of fibre pull-out failure mode was also reported by Hassan et al. [21]. They observed that composites with longer fibres tend to fail in a more brittle manner, by fibre breakage, in relation to shorter fibres composites which fail in a more ductile manner by fibre pull-out.

Since the impact resistance and energy absorption capabilities of the composite materials are highly dependent on the properties of the matrix, the rubber toughening of the matrix material became a widely used technique in the industry. Incorporation of the rubber phase can prevent brittle failure of the composite, producing tough and impact resistant material with good strength and stiffness [40-42]. However, it has been reported that rubber toughening reduces the strength and stiffness of the composite [43], therefore an optimal balance must be established not to degrade the material performance. Mouti et.al [2] observed that rubber toughening of short glass-fibre reinforced polyamide 66 increased the ductility of the material by 26%, but at the cost of reduced stiffness by 16% and strength by 25%.

2.3 Energy Absorption of Composite Structures

Modern vehicle structures must be able to withstand severe impact loads, at the same time providing safety of the occupants. This is why structural materials used for crashworthy applications must be characterized by the energy absorption capability. In order to ensure survivability of the accident, the structure has to dissipate energy in a controlled manner. This is limited by two factors: induced decelerations and maintaining a survival space for occupants during a crash [44].

Energy absorbed throughout a collision is defined by the area under the load-displacement curve as shown in Figure 5 [45].

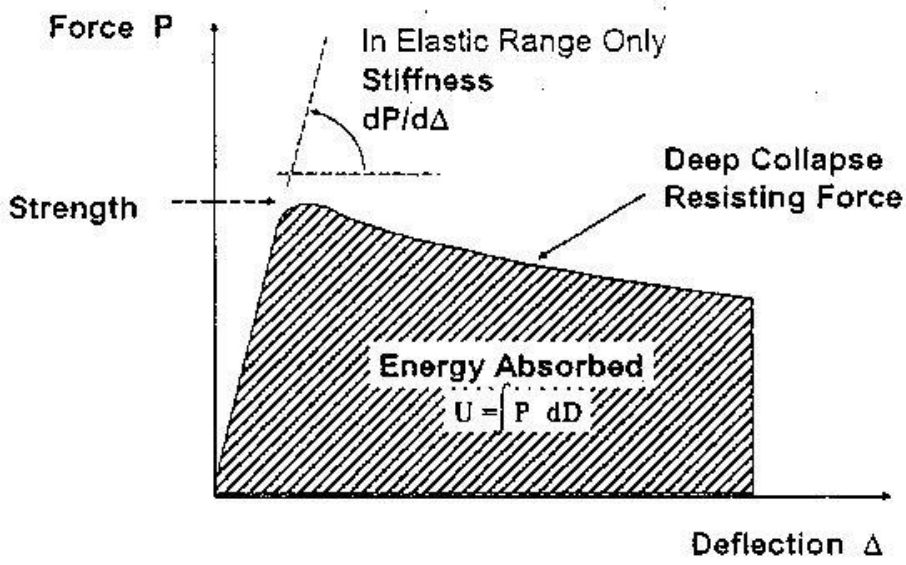

Figure 5: General load-displacement curve [45]

Analysing the above graph, it can be seen that the energy absorbed can be controlled by the value of the force and the amount of deformation. As mentioned before the maximum peak load is limited by the occupants' tolerance and the maximum deflection is limited by the geometry of the structure. In an idealized energy absorbing system induced load should be constant and just below the human tolerance limit. In reality the design of a

crashworthiness structure is always a compromise. As an example three different structural responses are compared in Figure 6. In the scenario with very stiff structure induced peak loads can highly exceed the allowable limit. In such a case occupants will suffer high decelerations while deformations of the structure are small. In case of the weak structure, induced peak loads are significantly reduced, but large deformations can affect the occupants causing serious injuries or even death. The third scenario is a compromise with the moderate value of the force and acceptable deflections not affecting occupants' space. In this scenario energy absorbed by the structure is maximized but within the limits of allowable load and deformation.

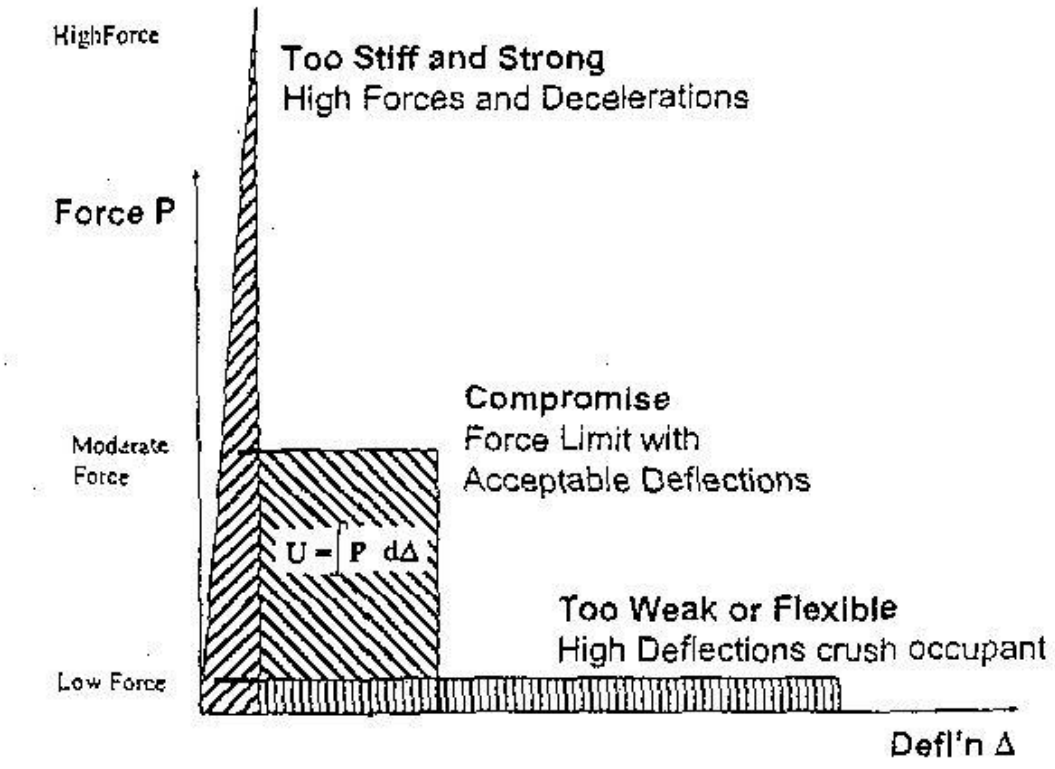

Figure 6: Various structural responses [45]

Traditionally metallic materials have been applied for the crashworthy structures due to their ability to sustain plastic deformations. By contrast, composite materials do not exhibit significant plastic deformations as they are

usually brittle. However, if they are properly designed they can absorb high amounts of impact energy by the progressive failure and delamination.

2.3.1 Crashworthy Criteria

The most useful parameter that allows meaningful comparison of the energy absorption capability of different materials and structures is Specific Energy Absorption (SEA). This parameter is defined as the amount of energy absorbed (area under the load-displacement curve) per unit mass of crashed material. This means that it takes into account the crashing length of the sample.

$$SEA = \frac{energy\_absorbed}{crashed\_mass} = \frac{\int F dx}{m_c}$$

Where: F – load, x displacement

2.3.2 Crash testing of composite structures

The most widely used method to evaluate the ability of a composite material to absorb the energy is axial collapse of a structural element. This technique has been applied by many researchers on various composite materials. The experiments presented in the literature vary in geometry and material of the specimen, as well as the parameters of the impact such as: velocity and energy. That is why, in order to directly compare energy absorption characteristics of the composite materials, it is necessary to operate with specific energy absorption (SEA) parameters, rather than total energy absorbed by the structure.

A summary of the results selected from the literature is presented in Table 1: Energy absorption of various composites . The most often used geometries of crash-samples are: cylinders, cones and squarer tubes. The materials which have been investigated the most extensively include: carbon, Kevlar and glass

as fibre materials; and epoxy, PEEK, polyester and vinylester as matrix materials.

Table 1: Energy absorption of various composites

Material	Type	Lay-up	Fibre content	Shape	SEA [kJ/kg]	Reference
Carbon/Epoxy	Laminate	0°/±15°	55 vol%	Square	75	[46]
	Laminate	0°/±45°	*	Square	46	[47]
Carbon/PEEK	Laminate	0°	61 wt%	Square	180	[48]
	Laminate	±30°	61 wt%	Square	127	[48]
Glass/epoxy	Laminate	0°/±15°	*	Square	30	[47]
	Laminate	0°/±45°	*	Square	31	[47]
Kevlar/epoxy	Laminate	0°/±15°	*	Square	9	[49]
	Laminate	0°/±45°	*	Square	21	[49]
Glass/vinyl-ester	Pultruded		68.4 wt%	Square	58	[50]
Glass/Polyester	Pultruded		61.8 wt%	Square	41	[50]
Glass/Polyester	Laminate	random	72 wt%	Cylinder	33,6	[44]
Glass/Polyester	Laminate	random	72 wt%	Cone 5°	33,1	[44]
Glass/Polyester	Laminate	random	72 wt%	Cone 10°	30,8	[44]
Glass/Polyester	Laminate	random	72 wt%	Cone 15°	20,9	[44]
Glass/Polyester	Laminate	random	72 wt%	square 5°	24,5	[44]
Glass/Polyester	Laminate	random	72 wt%	square 10°	23,2	[44]
Carbon/epoxy	Prepreg	±15°	*	Cylinder	94,3	[51]
Carbon/epoxy	Prepreg	±30°	*	Cylinder	68,9	[51]
Carbon/epoxy	Prepreg	±45°	*	Cylinder	68,1	[51]
Carbon/epoxy	Prepreg	±60°	*	Cylinder	61,9	[51]
Carbon/epoxy	Prepreg	±75°	*	Cylinder	54,5	[51]
Aluminium			N/A	Cylinder	78	[47]
Steel			N/A	Cylinder	33	[52]

* No information provided by the authors

The ability of a composite structure to absorb the energy is highly dependent on the mode of fracture. Materials which fail in a progressive manner, with extensive delamination and fragmentation, are able to absorb much higher energies than those materials which tend to fail in a brittle manner. Farley [46; 47; 49] found that thermoset composites reinforced with glass and carbon fibres fail progressively in fragmentation and splaying modes. On the other hand thermoset tubes reinforced with Kevlar failed in a progressive folding mode. Mamalis et al. [44] who studied polyester cones, cylinders and tubes, reinforced with random orientated glass-fibres, divided failure of the samples into four modes: progressive crashing with micro-fragmentation (Mode I), brittle fracture with catastrophic failure (Mode II and III, depending on the crack form), progressive folding and hinging, similar to the metallic tubes (Mode IV). The authors observed that fracture mode was significantly affected by geometry of the sample. Conical and square tubes with small semi-apical angles (5°-15°) tend to fail in a stable Mode I, whereas samples with large semi-apical angles (20°-30°) were found to fail in a brittle Mode II. They also found that wall thickness, related to number of composite layers, has a direct influence on the mode of failure. The collapse mode for large semi-apical angel samples has changed from stable to unstable, with increasing wall thickness. In the case of small angle samples, the collapse mode remained the same with increased thickness of the wall.

2.4 Nanocomposites

As discussed in the previous chapters, the use of short-fibre reinforced composites, in structural components, is often limited by their relatively low impact resistance and energy absorption capabilities [14]. In order to overcome these issues, nano-reinforcements have been introduced, due to their potential

to provide significant enhancements in the mechanical properties, without compromising its ductility and toughness.

Composite material is usually defined as a 'nano', if one of the constituents possess at least one dimension in the range of 1nm to 100nm [53]. The unique properties of the material reinforced with nano-particles come from the large number of interfacial effects, existing due to the high surface-area-to-volume ratio of the reinforcement. For the spherical nano-particles and nano-fibres this ratio is irreversibly proportional to their radius and its value can be even up to 1000 1/m.

There are several different nano-reinforcements widely used in the industry, which vary in the material and shape. This includes: nano-fibres, carbon nano-tubes, silver nano-particles, silica nano-particles and nano-clay plates. The most widely used nano-materials in polymer based composites are silica based, due to their good mechanical properties and high thermal stability. Currently, around 70 % of nano-materials used in the automotive industry are silica based nano-clays [4].

2.4.1 Nano-particle reinforced composites

In order to enhance physical and mechanical properties of the resin material, silica (SiO_2) nano-particles can be introduced [54]. Several researchers report significant improvements in properties such as: tensile strength, ductility, Young's modulus and impact strength; after reinforcing the material with nano-particles [55-59]. Jun Ma et al. [55] showed in their study that addition of 20wt% of silica nano-particles leads to the increase in Young's modulus by 40%, toughness from 0.73 to 1.68 $MPa/m^{1/2}$ and slight increase in the tensile strength.

An important issue in the manufacturing process of nanocomposites is appropriate dispersion of particles within a matrix. Existence of agglomeration regions, which can act as stress concentrators, may lead to an important drop in

composite performances [60-62]. Zheng and co-workers [63] compared the mechanical properties of nanocomposites with different quality of dispersion. They found that the material with uniformly distributed particles exhibits significant property improvements, while poorly distributed material indicates only a slight increase in the mechanical properties. Three different approaches have been studied by the authors in order to determine the most suitable manufacturing technique. The first one was to mix the un-pre-treated SiO_2 particles in the temperature of 120 ^{0} C, using an ultrasonic energy. In the second one, particles were pre-treated using a coupling agent and afterwards treated for twenty minutes with the ultrasonic waves. In the last approach the pre-treated particles were also dispersed using the ultrasonic waves, but with assistance of a high-speed homogenizer with a rotational velocity of 24,000 rpm. After studying the structure morphology, using transmission electron microscope (TEM), the authors found that particles' dispersion obtained using the second and the third approach is of a good quality. Dispersion achieved using the first approach was relatively poor with visible particles' agglomerations, and the mechanical properties of the composite indicated a low increase of up to 8%. Regarding the well-dispersed material, manufactured using the second and the third method, the increase in mechanical properties was up to 30% and 110% respectively.

2.4.2 Nano-plate reinforced composites

If only one dimension of the reinforcement is in nanometer size we can classify it as a nanoplate. The most widely utilized types of nanoplates are silicate clay minerals and graphite, which both exist in the form of layered materials. The main advantage of layered nano-materials is their potentially large aspect ratio and unique intercalation/exfoliation characteristics [64]. The best properties of clay nanocomposite can be achieved if layers are separated and well dispersed within the matrix [54].

Clay-polymer nanocomposites can be divided into four main categories, due to their morphology, as shown in Figure 7. In a conventional miscible state, enhancement of composite properties is of little meaning. Distance between clay plates is minimal and there is no intercalation of the polymer matrix into the gallery. In the case of intercalated state, the polymer matrix exists between the clay layers, leading to the enhancement of the polymer's properties [65]. If the nanoplates are fully separated and dispersed within the matrix, then the clay is in the exfoliated state. These type of composites exhibit much better properties in relation to the intercalated ones, due to the higher homogeneity of the phase [66]. Achievement of the full exfoliation is a challenging technical problem, because of the large longitudinal dimensions of the nanoplates and their strong tendency to agglomerate [67]. The most common state of nano-clays is partial intercalation and exfoliation. In this case the exfoliated and intercalated layers are distributed randomly within the matrix and a significant increase in modulus and strength is observed when compared with the raw matrix [68].

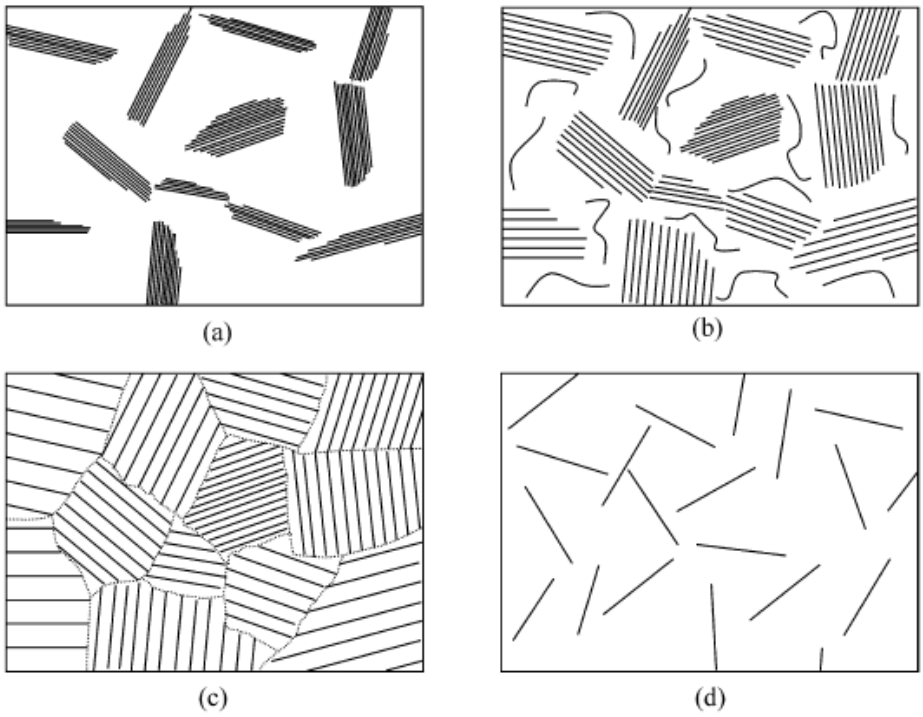

Figure 7: Morphology of nano-clay composites: (a) conventional miscible, (b) partially intercalated and exfoliated, (c) fully intercalated and dispersed and (d) fully exfoliated and dispersed [53]

The most commonly used clay material is Montmorillonite (MMT), due to its high surface area and surface reactivity [69]. MMT is a hydrous aluminium-silicate mineral in which aluminium octahedron is sandwiched between two tetrahedron silicon layers. The thickness of each layer is around 1nm, while the lateral dimensions vary from 30nm to more than several micro-meters. To improve mechanical properties of the MMT nanocomposite, a large surface contact area has to be created. In order to obtain a large aspect ratio in the range of 1000 the plates need to be uniformly-dispersed within the matrix, without breaking them into smaller pieces. In practice it is often difficult to achieve, because of the large shear stress induced during the mixing process, resulting in an aspect ratio of 30 to 300 [70].

In order to synthesize a clay nanocomposite it is important to modify the normally hydrophilic silicate surface to an organophilic one. This treatment

leads to the stronger interaction of the clay surface with the polymer matrix. Otherwise, physical mixture of the constituents may not create a nanocomposite [69].

There are four principle methods for preparing polymer-clay nanocomposites which are summarized below [71]. The first one is *in situ template synthesis*, where clay minerals are synthesized with a matrix using an aqueous solution, which contains building blocks of polymer and filler. A big challenge associated with this method is a tendency for the silicate layers to agglomerate. Furthermore, synthesis of the clay minerals requires high temperatures to decompose the polymers. This method was successfully applied by several researchers to synthesis double layered hydroxide-based nanocomposite [72; 73]. However, it is less suitable for layered silicates [74]. Another technique is *intercalation of polymer or prepolymer from solution*. In this method the layered silicate is exfoliated into single layers with the aid of a solvent in which the polymer is soluble. With this method it is possible to synthesize intercalated nanocomposites, based on polymers with low polarity. However, this technique is difficult to apply in industry due to the large amount of solvent required [75; 76].

The third technique is *in situ intercalative polymerization*, in which formation of the polymer can occur between the intercalated sheets. In this approach the layered silicates are swollen by the liquid monomer, while polymerization is initiated, either by heat or retardation, by the diffusion of the initiator, or by an organic initiator. At first this method was used for manufacturing of nylon-MMT nanocomposites, but later it was proved that it is well suited for thermoset clay nanocomposites [77].

The last method is known as a melt intercalation. In this approach the layered silicate is mixed with the polymer matrix in the molten state and no solvent is required [69]. The mixing process is realized mechanically using

conventional methods like extrusion or injection moulding [78]. The biggest advantage of this method is that it is suitable for preparation of polymers, which cannot be synthesized using absorption and in-situ techniques. That is why it is very popular in the manufacturing of thermoplastic nanocomposites [69].

2.5 Mechanical properties of nanocomposites

One of the main reasons for adding reinforcements into polymeric materials is to enhance their strength and stiffness properties. The most important parameter which affects these properties is load transfer between composite phases, realized via shear stress induced in the interface region. If high-modulus filler is added into low-modulus matrix, the stress in the composite is transferred into the stiffer phase, causing more loads to be carried by the filler. That is why efficiency of the stress transfer across composite phases depends on the quality of the interfacial region. This includes interfacial strength and stiffness [79]. If weak coupling exists between the phases, then the load transfer is poor and properties of the composite are dominated by the matrix. Enhancement of interfacial properties causes the load to be transferred more efficiently, leading to an increase in composite modulus and strength.

An important influence on the properties of the interfacial region is the aspect ratio of the reinforcement. The higher the aspect ratio of the reinforcement is, the bigger the load carrying area, and the higher the composite modulus and strength. This phenomenon explains unique properties of the materials reinforced with nano-fillers. Large numbers of small fillers in nanocomposite increases the available interfacial area, leading to the significant enhancement of the mechanical properties. The effectiveness of nano-fillers in reinforcing polymeric materials depends on several factors, which are defined and summarized below.

2.5.1 Filler size

It is well known that incorporation of rigid micro-fillers usually increases composite stiffness, but at the cost of reduced ductility. This is caused by the stress concentration regions that exist in close proximity of the reinforcement. In the case of nano-fillers, the stress concentrations are significantly reduced, therefore, composite ductility can be maintained at a constant level or even improved, in relation to the net polymer, as the filler may act as a crack propagation blocker.

The size effect of TiO_2 particles on mechanical properties of epoxy resin was investigated by Ng et al. [80]. The authors studied tensile properties of the epoxy material reinforced with nano (32nm) and micro (0.24μm) particles at constant 10% weight fraction. The obtained results show that incorporation of micro-particles increased modulus of the epoxy resin, but decreased its ductility. On the other hand, incorporation of nano-particles increased both the modulus and the ductility of the composite.

2.5.2 Volume fraction of fillers

Another important factor which can have a significant impact on stress-strain behaviour of nanocomposites is content of the filler. In contrast to micro-particles, which reduce composite strength at high filler content, the nano-particles offer an increase in both modulus and strength, with rising fraction of the filler. However, bad dispersion of particles or existence of agglomeration regions may cause stress concentrations, which initiate local cracks, resulting in reduced ductility of the composite. This phenomenon is especially augmented at high filler loadings (more than 5 vol%) where agglomerations are more likely to occur [81].

Zhang et al. [82] studied mechanical properties of epoxy resin with addition of 25nm silica nano-particles at various weight fraction, ranging from 0 to 22.7wt.%. Effects of their study indicate that increase in the filler content results

in enhancement of modulus, micro-hardness and fracture toughness, while flexural strength does not change with increasing particles content. The best value of impact resistance was found at nano-particles content of 3 vol%. The relative improvements in the mechanical properties are summarized in Figure 8.

Several other researchers report significant increase in Young's modulus with rising content of the filler, as it is shown in Table 2. However, there have been exceptions reported to this general trend. For example, Bharadwaj et al. [83] found that modulus of PE/Clay nanocomposite decreased with the increasing clay content. To explain this phenomenon, morphology of the sample was studied by the authors using X-ray diffraction and TEM. The main observation made was that the increasing clay concentration leads to the progressive decreases in the degree of cross-linking of the polyester resin, in the presence of clay. Furthermore, a large decrease in the mechanical properties of the 2.5 wt% sample, in relation to 10 wt% sample, was explained by the exfoliation occurring at a more global scale in the sample containing 2.5wt% of clay.

Table 2: Tensile modulus of various nanocomposites

Nanocomposite	Filler content		Modulus [GPa]	Ref.
PP/SiO2	0	[vol%]	0.94	[67]
	1.25		1.13	
	2.75		1.25	
PA6/MMT	0	[wt%]	1.11	[84]
	4.7		1.87	
	5.3		2.04	
PC/MWNT	0	[wt%]	2.00	[85]
	2		2.6	
	5		3.4	
PE/Clay	0	[Wt%]	0.95	[83]

1	0.75
2.5	0.2
5	0.31
10	0.29

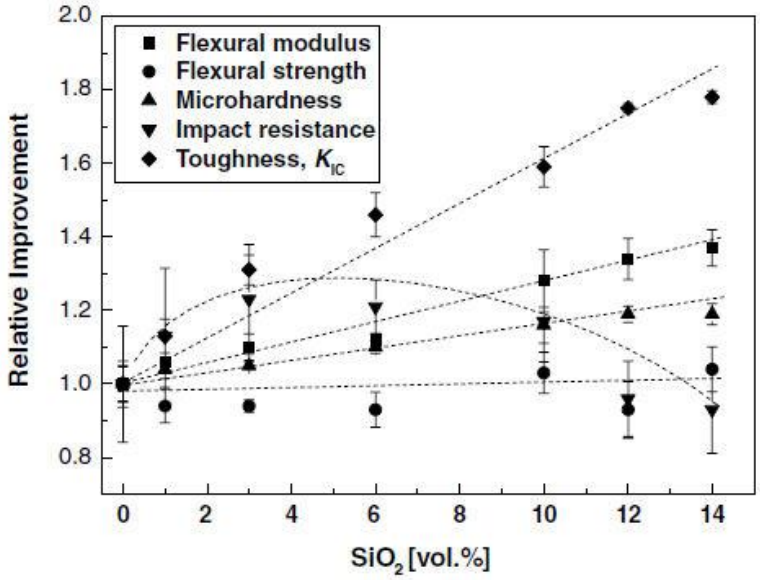

Figure 8: Improvements in mechanical properties due to the volume fraction of nanosilica fillers in epoxy matrix [82]

2.5.3 Filler shape

As discussed in the previous chapters, the biggest influence on the mechanical properties of nanocomposites was an aspect ratio of the filler, which is closely related to its shape. Figure 9 shows three typical geometries, which can be used as reinforcement in nanocomposites. Each of these possesses different surface-area-to-volume ratios, which can be expressed using the following equations [86]:

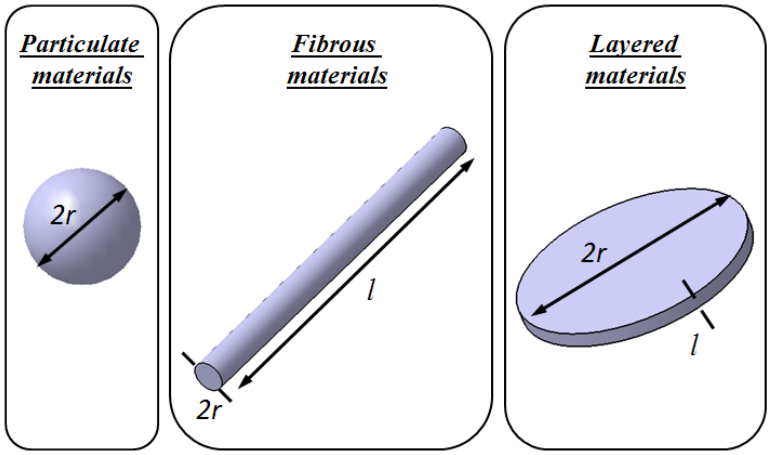

Figure 9: Various reinforcement geometries

- Particulate materials

$$\frac{A_s}{V_s} = \frac{4\pi r^2}{4/3\pi r^3} = \frac{3}{r} \tag{2.1}$$

- Fibrous materials

$$\frac{A_f}{V_f} = \frac{2\pi r^2 + 2\pi rl}{\pi r^2 l} = \frac{2}{r} + \frac{2}{l} \qquad l < r \tag{2.2}$$

- Layered materials

$$\frac{A_l}{V_l} = \frac{2\pi r^2 + 2\pi rl}{\pi r^2 l} = \frac{2}{r} + \frac{2}{l} \qquad r > l \tag{2.3}$$

If we compare surface-area-to-volume (SV) ratios of the particulate and cylindrical (fibrous and layered) materials we obtain the following relation:

$$\frac{SV_s}{SV_c} = \frac{3}{2(1+r/l)} \tag{2.4}$$

If filler is in the form of plate ($r>l$) or short rod ($l<2r$), then its SV ratio is bigger than that of a spherical particle. On the other hand, spherical particles have bigger SV ratio in relation to long fibres ($l>2r$). Influence of r/l ratio on SV ratio of the filler is shown in Figure 10.

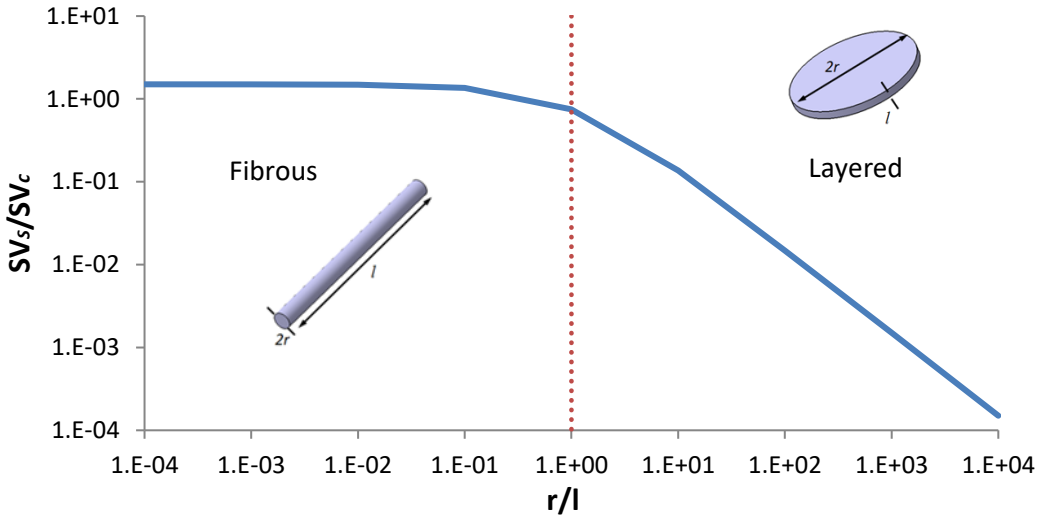

Figure 10: (SV_s) to (SV_c) ratio as a function of particle radius (r) to length (l) ratio

Based on these relations it can be concluded that the best surface properties can be achieved using plate geometries. However, the mechanical properties of nanocomposites depend on various factors such as: size, dispersion and volume fraction of the filler. This is why it is difficult to directly compare different shapes of the filler in an experiment. For example, cylindrical fillers are difficult to disperse in a homogeneous manner, at high volume fraction. Therefore, mechanical properties of the non-homogeneously dispersed filler of one shape are not directly comparable with properly dispersed filler of the other shape; even at the same volume fraction.

2.6 Energy Absorption of Nanocomposite materials

Polymer materials like PP and PA are widely used in the automotive industry because of their good mechanical performance, processing properties and low cost. On the other hand their application as structural materials is limited due to their relatively low impact resistance [87]. Incorporation of various nano-sized filers including: nano-particles (SiO_2, TiO_2, $CaSiO_3$, Al_2O_3), carbon nanotubes, and clay nano-plates can offer an appropriate solution to this problem [88; 89]. Many researchers report increase in both stiffness and impact toughness if the filer is in nano-metric size. Several important factors

influencing energy absorption capability of nanocomposites are summarized in the following chapters.

2.6.1 Particles stiffness

Bartczak et al. [90; 91] studied the influence of particles' stiffness on the mechanical properties of polymer matrix nanocomposites. Impact response of the high density polyethylene with addition of elastic rubber and rigid calcium carbonate $CaCO_3$ particles was investigated by means of notched Izod impact testing. Results of their experiments show that addition of 22 vol.% of elastic rubber causes an increase in notch toughness more than 16 times. However, a decrease by 50%-60% in the Young's modulus and yield stress by 40%-50%, was observed in relation to the net polymer. On the other hand incorporation of 25 vol.% of rigid $CaCO_3$ particles leads to an increase in notch toughness up to 15 times, as well as significant increase in Young's modulus and slight decrease in yield stress.

Mechanical properties of epoxy vinyl ester reinforced with core shell rubber (CSR) nanoparticles, which consist of a soft rubber core and a glassy shell, were investigated by Subramaniyan et al. [92]. The authors found that addition of CSR is able to improve the fracture toughness of net resin even more than MMT nano-clay with the same weight fraction. Furthermore, they proved that hybrid blends of CSR and nano-clays can provide good balance between toughness, strength and elastic modulus. In the other experiment, carried out by the same authors, nano-clay particles were added to the conventional polymer-glass fibre composite. It transpired that interlaminar fracture toughness decreased after the addition of nano-clay particles. The possible reason of this phenomenon was alignment of the particles along the fibres.

2.6.2 Particles geometry

Addition of Al_2O_3 nano-whiskers, glass-fibres and wallastonite into polymer matrix improves the fracture toughness significantly, while incorporation of the plate shaped particles of MMT, into the same matrix material, was found to decrease it [93]. A favourable effect on the impact toughness was also observed after the addition of amino-functionalized MWCNTs [94] or small amounts of SWCNTs [95]. Moreover, it was observed by Kireitseu [96] that the composite impact toughness and stiffness are highly dependent on the modulus of nano-tubes. Usage of silica (SiO_2) nanoparticles with polymer, can also lead to an increase in impact toughness of the composite material, if the particles are properly dispersed in the matrix and no agglomeration regions exist [60].

2.6.3 Volume fraction and inter-particle distance

Important Influence on the impact toughness of nanocomposites has inter-particle distance S, independently of the reinforcement geometry. Its value is closely related to the concentration φ and average size of the particles d (see Figure 11), which can be described using the equation 2.5, assuming ideal dispersion of the particles [82].

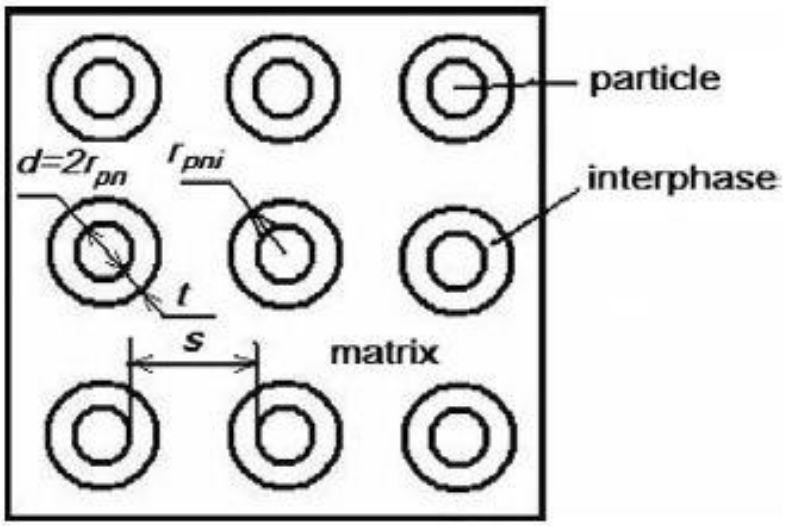

Figure 11: Inter-particle distance [88]

$$S = d \cdot \left[\left(\frac{\pi}{6\phi} \right)^{1/3} - 1 \right] \qquad (2.5)$$

Zhang et al. [82] found that if inter-particle distance is smaller than average particle size d, then composite toughness increases significantly as is the case presented in Figure 12. Similar conclusions were drawn by Wetzel et al. [97] who compared experimental fracture toughness with theoretical data presented in ref. [98]. This phenomenon can be explained by the fact that distance between particles is small enough to build around them, a three dimensional network of interphase region. If the inter-particles' distance is below the critical value then material behaviour is dominated by the properties of this region, and therefore it creates an energy-dissipating toughening mechanism [82].

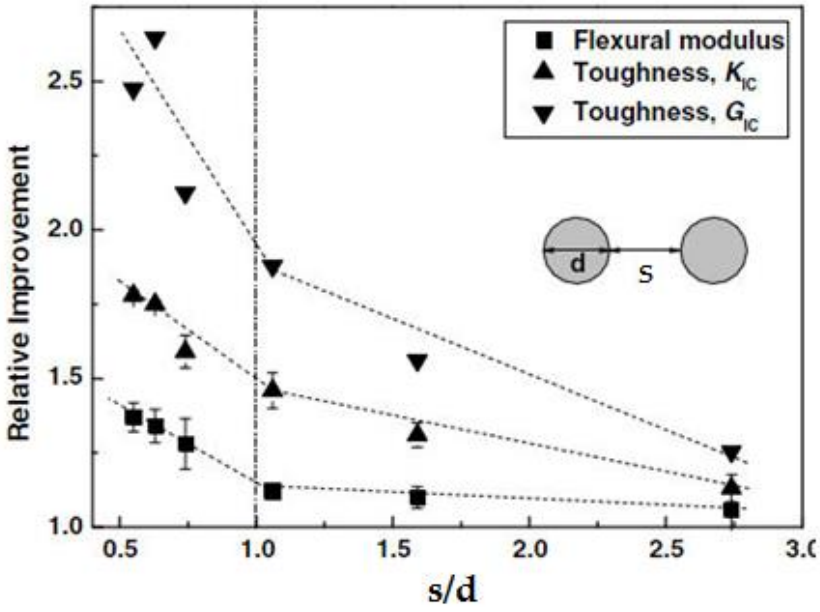

Figure 12: Improvements in mechanical properties due to the inter-particle distance [82]

2.6.4 Effects of particles size

Effect of the particles size on the mechanical properties of the polyurethane foams was studied by Javni et al. [99]. Incorporation of nano-sized filler was found to increase the compression strength of the foam, and to decrease its rebound resilience. On the other hand the addition of micro-sized fillers was found to lower the hardness and compression strength, at the same time leading to an increase in rebound resilience. This indicates that foams reinforced with nano-particles are able to absorb higher amounts of impact energy.

According to the analytical studies carried out by Chen et al. [100], energy dissipation due to the interfacial debonding is highly dependent on the size of particles. Figure 13 shows the effect of particles' size, varying from nanometer to micrometer, on the energy dissipation. The material ability to dissipate energy increases significantly with increasing size of the particles up to 140nm, whereas particles bigger than this indicate a gradual decrease in the material performance.

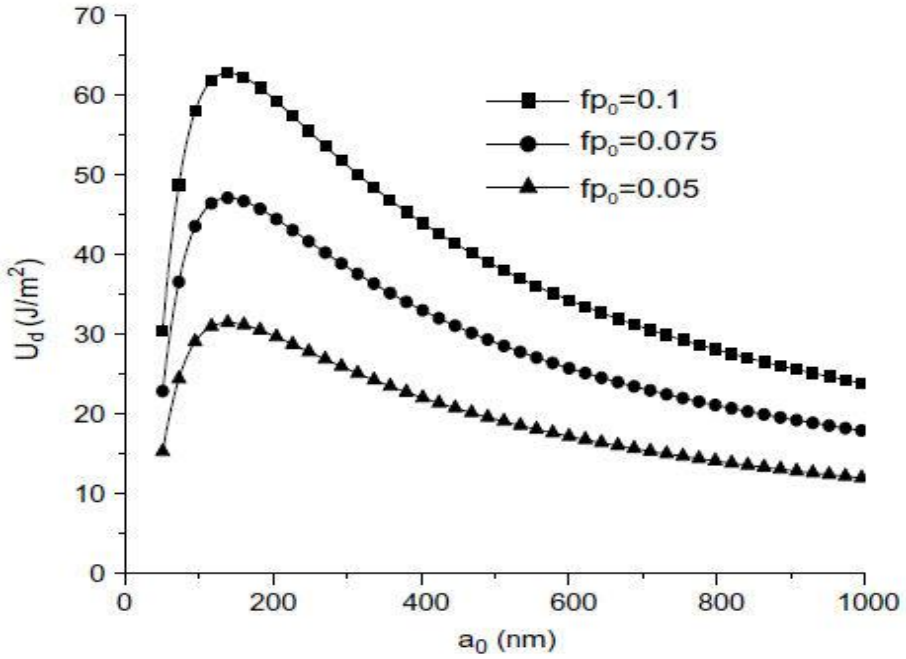

Figure 13: Energy dissipation against average radius of the filler (fp_0 – initial volume fraction of particles) [100]

Cho et al. [101] investigated the mechanical properties of polymer composites due to the size of the reinforcing particles. Results of their study show that size of particles has a small influence on interfacial fracture toughness of the nano-composite. Furthermore, a slight increase in Young's modulus was observed with reduced particles size for both micro and nano sized particles. The value of tensile strength was found to increase with reduction in size of micro particles, whereas reduction in size of nano particles was found to decrease the tensile strength of the material.

2.7 Hybrid nanocomposites

Another class of composite materials, which consist of more than one filler, is called hybrid nanocomposites. They are usually made from three separate phases; such as matrix, fibrous reinforcement and nano-fillers. The rationale behind use of hybrid nanocomposites is to balance the mechanical properties of the material, by an appropriate combination of the constituents. As discussed in Chapter 2.2, the introduction of short-fibres into polymeric matrix results in reduction in toughness. On the other hand, loading of more than 10wt% of nano-fillers lead to poor dispersion, and therefore, bad mechanical properties. That is why it is of interest to investigate whether a combination of all three constituents would provide desired properties. Although there has been an extensive research carried out on the properties of two-phase composites, only few preliminary studies have been undertaken so far to explore the benefits of using the hybrid nanocomposites [102].

Akkapeddi [103] showed that there is a clear tendency to increase the mechanical properties of polyamide 6, primarily filled with short glass-fibres, when MMT is added as secondary filler. The author reports that 3-4 wt% of the nano-filler can provide enhancement in stiffness which is equivalent to 10-15 wt% of glass-fibres. Similar increase in stiffness, after addition of nano-filler to

glass-fibre reinforced polyamide 6, were reported by Clifford et al. [104]. Furthermore, Daud et al. [105] proved that hybrid composites (PA 6 with woven glass fibres and layered silicates) offer 30% improvement in flexural and compressive strength in relation to standard two-phase composites. The results obtained by Wu et al. [106] showed that increase in stiffness and strength, of carbon-fibre or glass-fibre PA 6 composites filed with nano-clay, can be achieved without compromising their impact strength. Contrary, Yoo et al. [102] proved that tensile strength increases and ductility decreases with increasing content of organoclay in glass-fibre reinforced PA 6. Furthermore, Izod impact strength was shown to decrease with increasing content of the nano-clay.

2.8 Modelling of Nanocomposites

It is well known that interactions between nano-filler and matrix have significant impact on the energy absorption mechanism and the fracture behaviour of nanocomposites [61]. That is why modelling of these materials becomes a challenging task, due to the wide range of length scales that need to be considered in the analysis. Numerical methods for modelling of nanocomposites include: Molecular Dynamics (MD), continuum mechanics multiscale FE modelling, micromechanical FE and macroscopic FE modelling. MD methods consider interactions at atomistic scale and apply principles of quantum mechanics and molecular dynamics. These methods allow for determination of mechanical properties at nanoscale by solving the equations of motion of interacting atoms within interatomistic potentials [107]. MD simulations have been successfully applied to the investigation of crack propagation and fracture of individual single and multi-walled carbon nanotubes (CNT) [108-110], and predicting of the elastic properties in CNT reinforced composites [111; 112]. However, these techniques are computationally expensive, and therefore they are limited to studies of

individual particles and polymer chains [113]. A link to the modelling of larger structures is currently unavailable. For larger scale structures continuum mechanics and micromechanics based FE methods can be applied. A general description and the main challenges associated with these techniques are presented below.

2.8.1 Macroscopic modelling

Macroscopic modelling is a simplified approach where micro or nanoscopic interactions between matrix and reinforcement are neglected. Properties of the composite are homogenized before the analysis, producing anisotropic and homogenous continuum [114]. Effective properties based on an elasto-plastic stress-strain curve are obtained using mechanical testing. The most important parameters that need to be included in the composite material model are anisotropic yield and failure criterion as well as strain rate effects.

- **Yield and failure criteria**

A big challenge when composite materials are considered is modelling of yield and failure under the multiaxial loading. Most of the existing material models, implemented into commercial FE packages, were developed for metals, and therefore, they are based on von-Misses criterion. In this approach, only the deviatoric part of the stress tensor is taken in to account, when predicating the yield strength. In other words, yielding of the material is caused only by the distortional stress and it is not affected by the pressure. These assumptions are not necessarily correct for polymer composites. Contrary to metals, polymers' yielding and failure are dependent on hydrostatic pressure which is omitted in von Misses' theory. Several experiments confirmed that the hydrostatic part of the stress tensor increases polymers' yielding [115-121] and failure [122] stress. This effect is clearly visible as higher yield and failure stresses in simple compression than in simple tension.

In order to account for hydrostatic pressure effects several modifications of Tresca and von Misses criteria were proposed in the literature [119; 123; 124]. These formulations take into account both hydrostatic and deviatoric components of the stress tensor. The yield stress is then calculated as a linear or nonlinear function of the hydrostatic pressure. The simplest way to account for pressure effects is to expand the von Misses' criterion based on second invariant of stress tensor J_2 into a polynomial in first invariant of stress tensor J_1:

$$J_2 = k^2 + \alpha_1 J_1 \quad or \quad J_2 = k^2 + \alpha_1 J_1 + \alpha_2 J_1^2 \tag{2.6}$$

Caddell et al. [125] compared the yield stress predictions obtained using both linear and nonlinear pressure dependant models. In the case of polymers under the low pressure the linear representation is in a good agreement with experimental results, while the nonlinear characteristic is valid for the polymers under the high pressure.

In order to accurately describe yielding and failure of composite materials not only are the pressure effects important, but also the anisotropic behaviour of the material. A number of models have been proposed in the literature to describe yielding and failure of anisotropic materials. Furthermore, there have been many technical literature reviews carried out to study and compare applicability of these models [126-130]. Thus far the most widely used are the Hill [131], Tsai-Hill [132], Hoffman [133] and Tsai-Wu [134] criterions. These models were originally suggested as failure criteria of brittle materials but were later adopted as yield criteria for ductile materials [126].

The Hill criterion was developed for anisotropic metals as an extension of von Misses criterion to include anisotropy. It is represented by a quadratic function of the stress components with six independent material parameters, as shown in equation 2.7. Each parameter represents one of the three tensile strengths and three shear strengths. Hill criterion is pressure insensitive, therefore there is no

distinction between tensile and compressive strengths. It can be represented in the principal stress space by an elliptic paraboloid, symmetric in relation to the main axis.

$$F(\sigma_y - \sigma_z)^2 + G(\sigma_z - \sigma_x)^2 + H(\sigma_x - \sigma_y)^2 + 2L\tau_{yz}^2 + 2M\tau_{zx}^2 + 2N\tau_{xy}^2 = 1 \qquad (2.7)$$

Where: F, G, H, L, M and N are the coefficients related to uniaxial ultimate strengths.

Tsai adapted the Hill's model to orthotropic composites by finding a relation between the Hill's model parameters and strength parameters of the material. For a transversely isotropic composite it is expressed as follows:

$$\left(\frac{\sigma_x}{X}\right)^2 + \left(\frac{\sigma_y}{Y}\right)^2 + \left(\frac{\sigma_{xy}}{S}\right)^2 - \frac{\sigma_x \sigma_y}{X} = 1 \qquad (2.8)$$

Where: X, Y and S are the uniaxial ultimate strengths.

In order to take into account pressure sensitivity of anisotropic materials, Hoffman proposed an extension of Hill's theory, by introducing terms linear in the stress. In this criterion there are nine independent material parameters which correspond to three tensile, three compressive and three shear strengths. In this case the yield surface can be represented in the principal stress state as asymmetric elliptic paraboloid, stated as follows:

$$C_1(\sigma_y - \sigma_z)^2 + C_2(\sigma_z - \sigma_x)^2 + C_3(\sigma_x - \sigma_y)^2 + C_4\sigma_x + C_5\sigma_y + C_6\sigma_z + C_7\tau_{yz}^2 + C_8\tau_{zx}^2 + C_9\tau_{xy}^2 = 1 \qquad (2.9)$$

Where: C_i are the coefficients related to uniaxial ultimate strengths.

The model developed by Tsai-Wu is based on tensor polynomial theory proposed by Gol'denblat and Kopnov [135]. The main difference of the Tsai-Wu model in relation to Hoffman model is the existence of stress interaction terms. This is why to fully define the yield surface it is required to conduct not only

uniaxial tests, but also additional biaxial tests. For plane stress it can be expressed in the following form:

$$f_1\sigma_x + f_2\sigma_y + f_{11}\sigma_x^2 + f_{22}\sigma_y^2 + f_{66}\tau_{xy}^2 + 2f_{12}\sigma_x\sigma_y \quad (2.10)$$

Where: f_i are the coefficients related to uniaxial and biaxial ultimate strengths.

The validity of all the above models depends on the particular application and agreement with the experiments. Hill criterions are generally applicable for anisotropic materials which do not exhibit pressure sensitivity, such as metals. Hofmann and Tsai-Wu criterions are pressure dependant models and therefore are more appropriate for polymer based composites. The choice between Hoffman and Tsai-Wu, depends on the significance of the biaxial stress state. If biaxiality is of great significance, then the Tsai-Wu model is more adequate, as it allows for more accurate fit to the experimental data [136]. However, the biaxial testing necessary to calibrate the Tsai-Wu model are difficult and expensive to perform. As a consequence such tests are not always available.

Jones [137] analyzed applicability of all four theories for failure prediction in glass or boron fibre reinforced epoxy. He found that the best predictions can be achieved when using either Hoffman or Tsai-Wu models. The main prevalence of Tsai-Wu over Hoffman criterions is increased curve-fitting capability, due to the additional term in the equation. Similar conclusions were drawn by Narayanaswami et.al. [138], who studied the applicability of Hoffman and Tsai Wu criterions. Nevertheless, there have been many other strength criteria developed for anisotropic materials as reviewed by Sendeckyj et.al [128]. However, the authors conclude that those models are only appropriate for special applications, which they were developed for (e.g. plane stress or strain), and cannot be effectively applied for more general problems. They also indicate that Tsai-Wu criterion provides the most accurate strength predictions for a number of different composite materials.

An alternative approach to predict failure of composite materials is to use the strain tensor, rather than the strength tensor. Zhang et al. [139] proposed a strain based tensor polynomial failure criterion for anisotropic materials.

$$P_1\varepsilon_x + P_2\varepsilon_y + P_{11}\varepsilon_x^2 + P_{22}\varepsilon_y^2 + P_{66}\varepsilon_{xy}^2 + 2P_{12}\varepsilon_x\varepsilon_y \quad (2.11)$$

Where: P_i are the coefficients related to uniaxial and biaxial ultimate strains.

The authors indicate that due to the discontinuous stress distribution between reinforcement and matrix materials, the strength based criterion is not well suited for composite materials. By contrast the strain distribution between the constituents is much more uniform. This is why the strain based failure criterion is less sensitive to variations in experimental parameters. The model has been validated based on the experimental results of a graphite-epoxy composite under plane stress. The loadings and failure envelopes obtained using this criterion were shown to be less conservative in relation to max-strain, Tsai-Wu and max-stress criterions.

The more recent studies showed that the capability of stress or strain based models to accurately predict failure in anisotropic composites is limited. For materials exhibiting non-linear stress-strain response, the theory that includes both stress and strain in failure prediction could be much more accurate. Authors such as Sandhu [140; 141] and Zand [142] proposed a strain energy based failure criterion that takes into account the entire nonlinear stress-strain response of the material. The first attempt to develop an accurate strain energy based failure criterion was made by Sandhu [140; 141]. The author demonstrated that longitudinal,transverse and shear strain energies are all independent parameters. Based on this observation, he developed a model defined by the sum of appropriate exponents of strain energy components (longitudinal, transverse and shear). Wolfe et al. [143] refined the theory

proposed by Sandhu to include a variety of ply-unloading mechanisms. A comparison of the numerical predictions obtained by the author with the experimental observations of E-glass/MY750 composites, showed a good correlation. However, the areas which require further improvement were identified by the authors. This includes additional studies on the selection of the most appropriate load transfer mechanism from failed to unfailed lamina. This is why the model was further extended for the purpose of the World Wide Failure Exercise (WWFE) to accurately predict the response of composite materials under multiaxial in-plane and out of plane loads [142]. As a part of this exercise, Doudican et al. [144] compared the results obtained using the improved model with experimental results of four different composites. The model was found to be in very good agreement with the experimental data. The authors concluded that the model can be calibrated to predict the response of a composite material, regardless of its constituents or degree of homogenization. This is possible due to a generic nature of the material model parameters.

- **Strain rate effects**

While selecting the material model for polymer composites, it is also important to consider the strain rate effects. Most polymers exhibit significant rate dependency of modulus, yield and failure strengths. This brings additional complications to the modelling process, as not all material models are capable of representing these effects. Application of a rate independent model to a rate dependent material leads to an important error in the mechanical response predictions.

Rate dependent plasticity is commonly modelled by one of the two methods. The first method uses the rate-independent plasticity to calculate the response of a material, assuming rate dependant yield surface. In this approach the yield stress is a function of the strain-rate. This has been successfully applied to

model rate dependant anisotropic material by Drysdale [145]. The author developed constitutive equations appropriate to model rate-dependant anisotropic plasticity. This was realized by incorporation of the rate of deformation variable in the definition of the yield surface.

The most common approach to scale the yield stress, implemented into LS-Dyna, is the Cowper-Symonds equation. In this formulation the plasticity curve is scaled to other strain rates using the factor β defined as follows:

$$\beta = 1 + \left(\frac{\dot{\varepsilon}}{C} \right)^{\frac{1}{p}}$$

Where: $\dot{\varepsilon}$ - Strain rate p, C - material constants

The second method is based on the theory of viscoplasticity. In this formulation the strain rate is included in the stress integration algorithm (ex. backward Euler integration), i.e. the code uses the effective plastic strain rate in the corrector state of the integration scheme. There are two types of viscoplastic models: the overstress model and consistency model. The main feature of the overstress model is the rate-independent yield function, which can become larger than zero. This effect is known as overstress. The most commonly used overstress viscoplastic model was developed by Perzyna [146]. The alternative approach is to use the consistency viscoplastic model as presented by Wang [147]. In this model the viscous deformation is governed by time derivative of a rate-dependant yield surface. In other words, it is a combination of rate dependant plasticity with rate dependant yield function. Winnicki et al. [148] extended Wang's model to anisotropic materials, represented with the Hoffman yield criterion.

The main advantage of the rate independent plasticity, combined with rate dependant yield function, is reduced computation time. However, this is at the cost of reduced accuracy. For some materials not only is the yield strength

changing but also its brittleness. This is visible as a change in the shape of the stress strain curve. If only the yield strength is a function of the strain rate, the model may not be accurate, as illustrated in Figure 14.

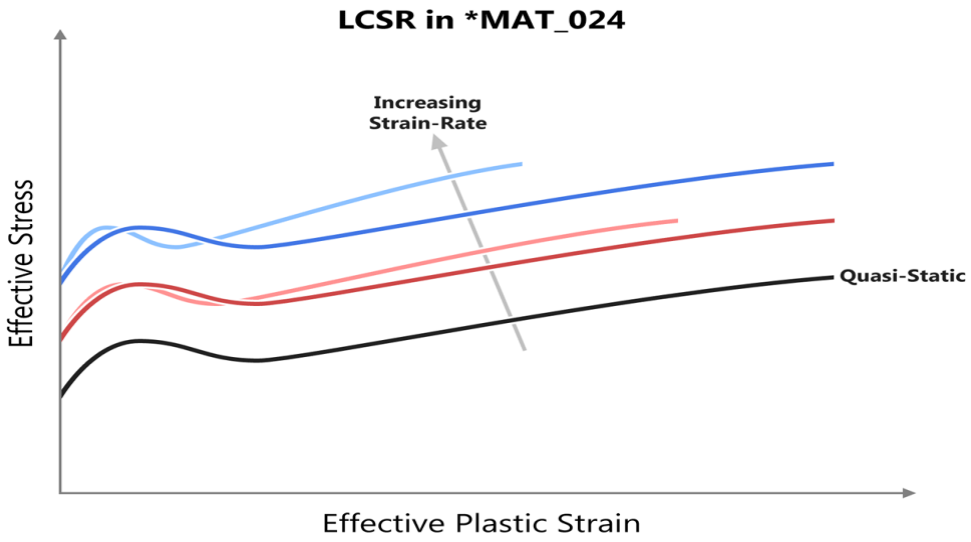

Figure 14: Brittleness effect on strain rate scaling [149]

The viscoplastic formulation can cope with this issue and provide more accurate results, especially when a wide range of strain rates is considered. However, this is associated with increased computation time and issues with model convergence. Several material models implemented in Ls-Dyna software (ex. Johnson-Cook), provide the option to use viscoplastic formulation in the stress integration algorithm. The choice is left for the user to decide, based on the requirements of the problem being analyzed.

Furthermore, polymeric materials often exhibit strain rate sensitivity of the elastic modulus, as illustrated in Figure 15 [150]. In order to cope with this issue several viscoelastic models have been proposed in the literature, such as: Maxwell model, Generalized Maxwell model and Kelvin-Voigt model. These models are particularly desirable when effects such as viscoelastic creep or stress relaxation are of great significance. If only rate dependency of stiffness is

considered, this can be modelled by simple linear or nonlinear scaling of the modulus.

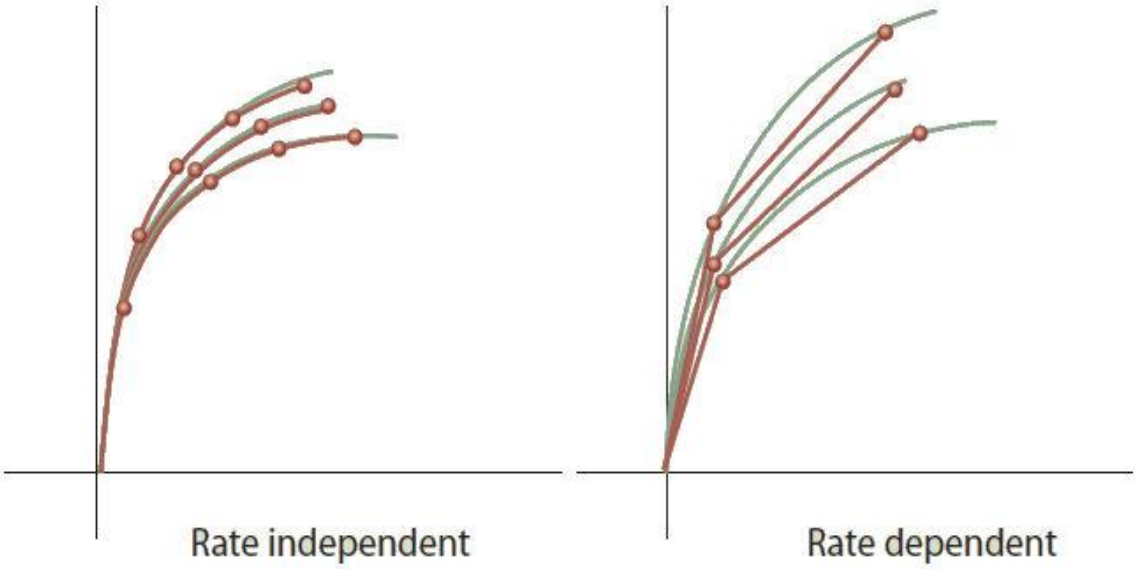

Figure 15: Strain rate effects [150]

2.8.2 Multi-scale modelling

In the multi-scale modelling each phase of the composite is considered separately. Loading and boundary conditions are applied both to the matrix and the reinforcement. The overall macroscopic properties of the material are then calculated as a function of the constituents, using a homogenization method. In contrast to the macroscopic approach, multi-scale modelling is able to provide detailed information about the interactions between the matrix and the reinforcement, leading to much more accurate results. Moreover, with this formulation, influence of the reinforcement content on the composite properties can be investigated without performing an expensive material testing, for each configuration. An important drawback of this method is much higher computation time in relation to the macroscopic approach, where the material properties are calculated 'off line' [151].

The main principle of the multi-scale modelling is the concept of Representative Volume Element (RVE). The RVE is defined as a volume 'V' of a heterogeneous material, which must be large enough to correctly reflect statistical fluctuations of the composite properties. It must ensure an accurate prediction of the effective properties like Young's modulus, Poisson's ratio and plasticity [152]. Furthermore, it must contain all the data which can influence a composite behaviour e.g. volume fraction, size and distribution of the filler.

To calculate the effective properties of the material various micromechanical models can be applied. The most widely used are Mori-Tanaka [153] and Halpin-Tsai [154; 155], based on Eshelby's equation [156; 157]. A description of these models can be found in reference [158].

Micromechanical models have been applied in several studies to predict elastic properties of nanocomposites [53; 159-163] as well as damage and failure [100; 164-166]. Luo et al. [53] studied the enhancement of properties of the epoxy matrix reinforced with silicate clay particles. A three-phase model, including the epoxy matrix, the exfoliated clay nano-layers and the nano-layer clusters was developed to account for partial exfoliation of nano-layers. The Mori-Tanaka method was applied to predict elastic properties of the material. Various parameters including the exfoliation ratio, clay layer and cluster aspect ratios, intra-gallery modulus, matrix modulus and matrix Poisson's ratio were taken into account. The exfoliation ratio was investigated using TEM micrographs and the estimated value (10%) was included in the model. Predicted values of elastic properties were found to be in close agreement with the experimental results. This is why the influence of various parameters on mechanical properties of the composite was studied further, using the same method. The authors observed that the biggest influence on overall modulus was the exfoliated fraction of clay.

A constitutive relation based on the micromechanical approach was applied by Chen et al. [164], to study the evolution of micro-voids in particulate-reinforced viscoelastic composites. Growth of the voids was considered by means of Eshelby's equivalent inclusion method. The macroscopic constitutive relation of the composite was derived according to the Mori-Tanaka scheme. Particles/matrix debonding was observed at a high tri-axial stress state which led to nucleation and growth of the voids. Final results obtained by the authors indicate that the biggest influence on the effective mechanical properties of the composite have macroscopic strain rate, relaxation time of matrix, adhesive strength and particles-size dispersity.

Boutaleb et al. [165] extended the micromechanical model based on the Eshelby formulation to predict stiffness and yield stress of silica reinforced polymer nanocomposites. The presented model takes into account an interphase region around the nanoparticles and calculates its elastic modulus as gradual transition from nanoparticle to the matrix. The third phase centred around the particle is assumed to be inhomogeneous. Each phase is described by its own elastic stiffness tensor C. The dispersion of the filler and the interphase region in the matrix was assumed to be random. The yield function of the composite was calculated using the averaging procedure derived by Ju et al. [167]. The numerical results obtained by the authors were in good agreement with the experiment. It was observed that the interphase region had a dominating effect on the yield stress of the composite. For the small particle size the stiffness of the interphase was relatively strong. Increase in size of the particle led to a softening of the interphase region. This indicates that the process of debonding was dominating in this case.

Smith et al. [168] developed a multi-level FE model to predict mechanical behaviour of nonlinear heterogeneous systems (see Figure 16). The multi-level procedure decomposes displacement field into the macro and micro scale.

Response of the material, at the micro level, is calculated using RVE with the microscopic mesh. At the macro level the structure is assumed to be homogeneous and it is described using macroscopic mesh. Solution of the RVE gives averaged stress σ_{RVE} and stiffness S_{RVE} tensors which are assigned to each macroscopic integration point. Subsequently, macroscopic stress and stiffness tensors are computed and the displacement vector F_{macro} is returned to the microscopic level.

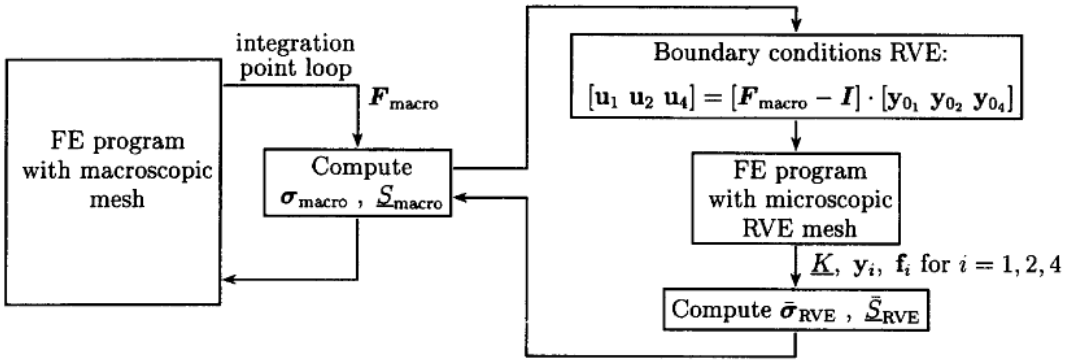

Figure 16: Computation procedure of multi-level FE model [168]

The procedure was evaluated by the comparison of the deformation of a perforated macroscopic sheet to the deformation of a homogenised sheet. A very good agreement was observed by the authors. The main drawback of the presented method is a large increase in computation time, which can be determined by the following multiplier: *number of RVE iterations* × *number of RVE integration points.* The author suggests that parallelization of the code and use of high-speed processors could reduce the impact of this problem.

2.8.3 Direct microscopic modelling

To predict the mechanical properties of composite materials a full three-dimensional RVE (see Figure 17) can be constructed using the FE method [169-173]. In this approach each phase of the composite is modelled explicitly. This includes size, shape and distribution of the filler. However, this method is

computationally expensive, when large and complicated structures are considered.

Chia [174] used the commercial FE package ABAQUS to study the interface effects on mechanical properties of MMT clay nanocomposites. The nano-fillers were assumed to be randomly orientated, randomly embedded, homogeneously dispersed and perfectly bonded in the matrix. The shape of the filler was approximated using circular discs to facilitate generation of the model.

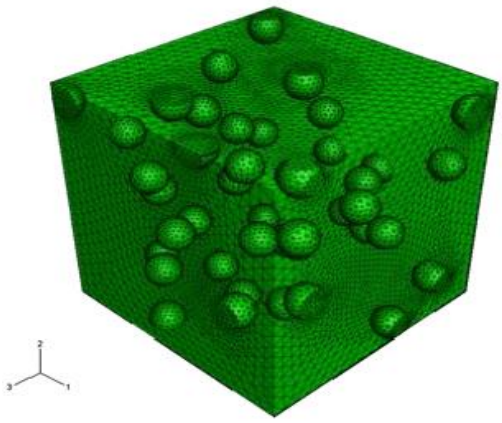

Figure 17: FE representation of the nanocomposite RVE [175]

Behaviour of the matrix was treated as isotropic-elastic-plastic and the effective clay layer as isotropic-elastic. The load applied to the RVE was varied from hydrostatic tension state to pure shear state. Failure of the clay gallery was described by traction-separation law. The author observed a formation of the local plastic zones around the clay particles, induced by the large mismatch in the modulus of the matrix and the reinforcement. With the increasing value of applied strain, intensive clay splitting was observed, leading to non-linear behaviour of the nanocomposite. The damage surface prediction presented in Figure 18, was found to be cohesive energy and pressure dependent as well as non-smooth.

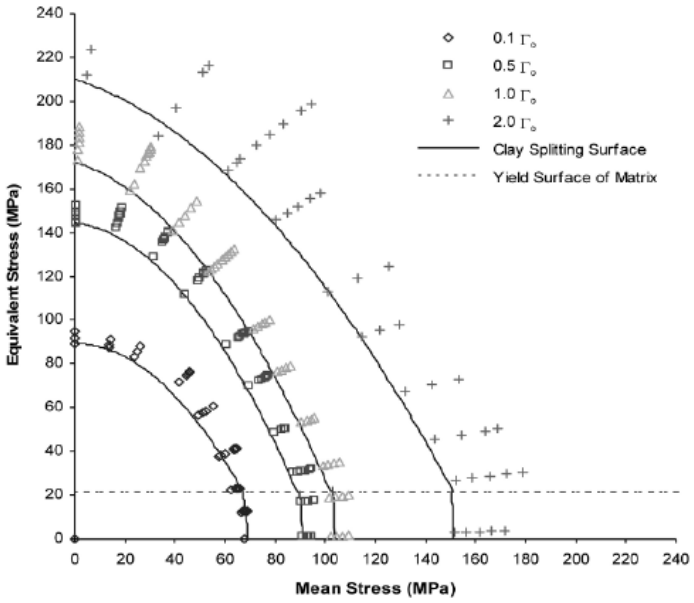

Figure 18: Damage surface of the nano-composite (Γ_0 – cohesive energy) [174]

In addition, an influence of the particles' sizes on the mechanical properties of polymer composites was investigated experimentally and numerically by Chao et al. [101]. The particles' sizes varied from micro (0.5mm) to nano (15nm) scale. An axisymmetric FE model was developed in order to better understand the size effects on the composite failure process. The particle/matrix debonding process was studied in terms of interfacial fracture toughness, fracture mode mixity and total strain energy release rate. The authors found that size of the particles does not have much influence on the interfacial fracture toughness. However, in the case of smaller particles the crack growth requires higher applied stress, due to the decrease of energy release rate with the decreasing particle size. The mode mixity was also found to be particle size independent and that the sliding mode becomes dominating with the crack growth. Moreover, it was observed that when the sliding mode prevails the fracture toughness increases exponentially.

2.9 Conclusion and recommendation

The literature review shows that short-fibre reinforced polymer composites are widely used in the automotive industry, due to their good mechanical properties and low cost. However, application of these materials in structural components is often limited by their brittleness and low impact resistance. It is possible to control the mechanical properties of short-fibre composites (stiffness and strength) by changing parameters such as fibre content, size, length, orientation and interfacial bonding. However, the increase in strength of the material is always associated with reduction in its toughness. To deal with this issue incorporation of rubber particles became a common technique used to improve toughness of polymer composites. The main drawback of this method is a reduction in strength of the composite. This is why the design of short-fibre reinforced composites is always a trade of between the strength and ductility of the material.

More recent studies show that incorporation of nano-fillers can provide significant enhancement of the mechanical properties; such as stiffness and strength without compromising its ductility. Furthermore, some studies proved that addition of nano-particles can lead to an increase in the ductility of a composite material.

Numerous studies have been carried out to investigate the mechanical properties of various nano-filled composite materials. Several factors, influencing the reinforcing capabilities of the nano-materials, were highlighted in the reviewed literature. This includes key parameters such as: shape and size of nano-fillers, matrix and filler material, interfacial strength and interphase characteristics, as well as volume fraction and quality of dispersion within a matrix. Mechanical properties and energy absorption characteristics of

nanocomposites were mainly characterized by means of tensile, flexural or Izod impact testing.

Although the mechanical properties of two-phase composites were extensively studied in the literature, only few preliminary studies were carried out on hybrid three-phase short-fibre reinforced thermoplastic composites. These results indicate positive effect of the nano-filler on the properties such as stiffness and strength. The effect of the third phase on ductility and impact strength of thermoplastic composites is still not fully understood.

Axial crashing is the most prevailing method used to measure the energy absorption capability of conventional composites. These types of experiments provide valuable information on the relation between micro and macro fracture process. They can also help to establish a correlation between the mechanical properties of a material and the fracture mechanism of a structure. Based on these experiments, it was determined that the ability of a composite structure to absorb the energy is highly dependent on the mode of fracture. It was also established that materials which fail in a progressive manner, with extensive delamination and fragmentation, tend to absorb much higher energies than those which tend to fail in a brittle manner.

While the mechanical properties of nano-reinforced materials have been studied extensively in the past, there is lack of crash experiments conducted on nano-composite structures. This is why the relationship between mechanical properties and fracture mechanism of nanocomposite structures is not yet fully understood. This includes fracture modes and the ability of the structure to crash progressively.

Regarding the numerical analysis, an extensive research has been carried out on various modelling techniques for composite materials. Macroscopic modelling has been extensively and effectively used to model elaso-plastic behaviour of composites. Various yield and failure criteria have been developed

to accurately predict the response of anisotropic materials and structures. This approach offers good compromise between quality of results generated and the computation time, especially when large structures are considered. While elasto-plastic behaviour of polymer based composites can be predicted with very good accuracy, the modelling of structural failure still remains a challenge. Strain energy based failure criteria were recently improved and applied for this purpose, providing good correlation with experimental data. However, there is still a need for validation and improvement of existing material models, especially when a new class of materials is being analyzed.

An alternative approach, based on direct FE representation of a small RVE, which explicitly models interactions between constituents, has been proposed by several researchers. It is the most accurate method to study the interactions between composite phases and to predict the mechanical properties of nano-materials. However, this approach is computationally expensive, and therefore not practical when large structures are considered. At the moment it is limited to analysis of a single RVE, to gain better understanding of the interactions between constituents building a composite. This is why multiscale simulations, based on homogenization theories, were developed. These methods proved to be very effective in predicting the influence of nano-filler parameters (size, shape, dispersion) on the elasto-plastic mechanical properties of a composite. These methods proved to be effective in modelling the material response on a small-specimen scale, due to the reduced computation time in relation to direct microscopic analysis. However, in relation to macro-modelling, the multi-scale modelling method is associated with increased computation time. Therefore, its applicability for modelling of complexes failure mechanisms in large structural components is limited.

2.9.1 Gaps in knowledge

Based on the literature review the following gaps in knowledge were identified:

- Currently there is a lack of information in the literature on the effect of nano-fillers on the mechanical properties such as ductility and impact strength of hybrid glass-fibre reinforced thermoplastic composites.
- At present there is a lack of research on the effect of silica nano-particles (SiO_2), on the mechanical properties of hybrid glass-fibre reinforced thermoplastic composites.
- The link between mechanical properties and fracture mechanism of three-phase composite structures has not been investigated in the literature, and therefore is not well understood.
- The yield and failure criteria for composite materials, available in the literature, have not been applied and validated for three-phase nanocomposites. Therefore, modifications and validation are required before they can be used in FE modelling of three-phase nano composite structures.

3. Mechanical Properties and Characterization of the Nano-composite materials

As it was shown in the literature review section, injection moulded PA and PP based composites are extensively used in the automotive industry. This is mainly due to their good mechanical properties combined with low manufacturing cost. However, it has been shown, that application of these materials in structural components is often limited by their brittleness and low energy absorption capabilities. A brittle behaviour in a structural component

subjected to impact loads is not desirable. This is why there is a continuous need for further improvements.

The most recent studies show that addition of nano-sized fillers, rather than micro-sized fillers, can improve the mechanical properties of a composite, such as stiffness and strength, as well as its ductility. This is why a combination of glass-fibres and nano-fillers into one composite may be a solution to the brittleness issue. In order to confirm this hypothesis, this chapter studies the influence of various nano-particles on the mechanical properties of injection moulded short-fibre reinforced polymer composites.

The chapter starts with details of the materials used for the purpose of this work, as well as the selected manufacturing techniques. Subsequently, it shows procedures for mechanical testing and material characterization. It also presents the results of the material characterization, carried out with Transmission Electron Microscopy (TEM) and X-ray diffraction. Finally, it shows and discusses the results of the mechanical testing, carried out using tensile and compressive samples, at both static and dynamic loads.

3.1 Materials

Two types of matrices were utilised to prepare hybrid three-phase nanocomposites: polypropylene (PP) Moplen HP500J from Basell Polyolefins and polyamide 6 (PA-6) Tarnamid T-30 from Zakłady Azotowe w Tarnowie-Mościcach, Poland. As a nano-filler two different types of silica-particles (SiO_2) and montmorillonite (MMT) for both polar and apolar matrices were selected. This includes: organically modified MMT designed for nonpolar polyolefin matrices (Dellite 72T from Laviosa); organically modified MMT designed for

polar matrices (Dellite 43B from Laviosa); fumed silica with hydrophobic properties (surface modified with dichlorodimethyl silane (DCMS)) for nonpolar polyolefin matrices (AEROSIL 974 from Degussa) and fumed silica with hydrophilic properties for polar polymer (AEROSIL 200 from Degussa).

Four different glass-reinforced composite materials, supplied by MACOMASS Verkaufs AG Germany, were used to prepare nano and glass reinforced composite samples: glass-fibre reinforced polyamide (MM-PA I 1F30) and polypropylene (MM-PP BI 24), as well as glass-spheres reinforced polyamide (MM-PA I 1K30) and polypropylene (MM-PP HE25).

3.2 Samples' preparation

Preparation of the nano and glass reinforced polymer composites was conducted in three main steps: preparation of the nano-composite granulate, mixing and extrusion of the nano and glass reinforced composite granulate and injection moulding of the macro-sample. The flow chart showing the preparation process is presented in Figure 19.

3.2.1 Nanocomposites preparation

In order to warrant the highest homogeneity of the composition, nano-filler and polymeric matrix, all in solid (powder) form, were premixed before extrusion. This activity was performed by the use of a turbomixer with rotatory blades. The pre-mixing phase consisted of two steps, the first one at lower speed (1,500 rpm) and the second one at higher speed (3,000 rpm). This choice was made in order to ensure the maximum homogeneity of the premix and, on the other hand, to subject the polymer to a small temperature stress, to improve binding between polymeric matrices and added fillers. Subsequently, the premixed materials were fed into the twin-screw extruder at a constant predefined rate. Once properly fed into the extruder, the materials were processed according to the predefined temperature profile: the choice of a co-

rotation twin screw extruder, characterized by a high length/diameter ratio (52), warranted the best dispersion and highest homogenization within the composite material in the melt phase.

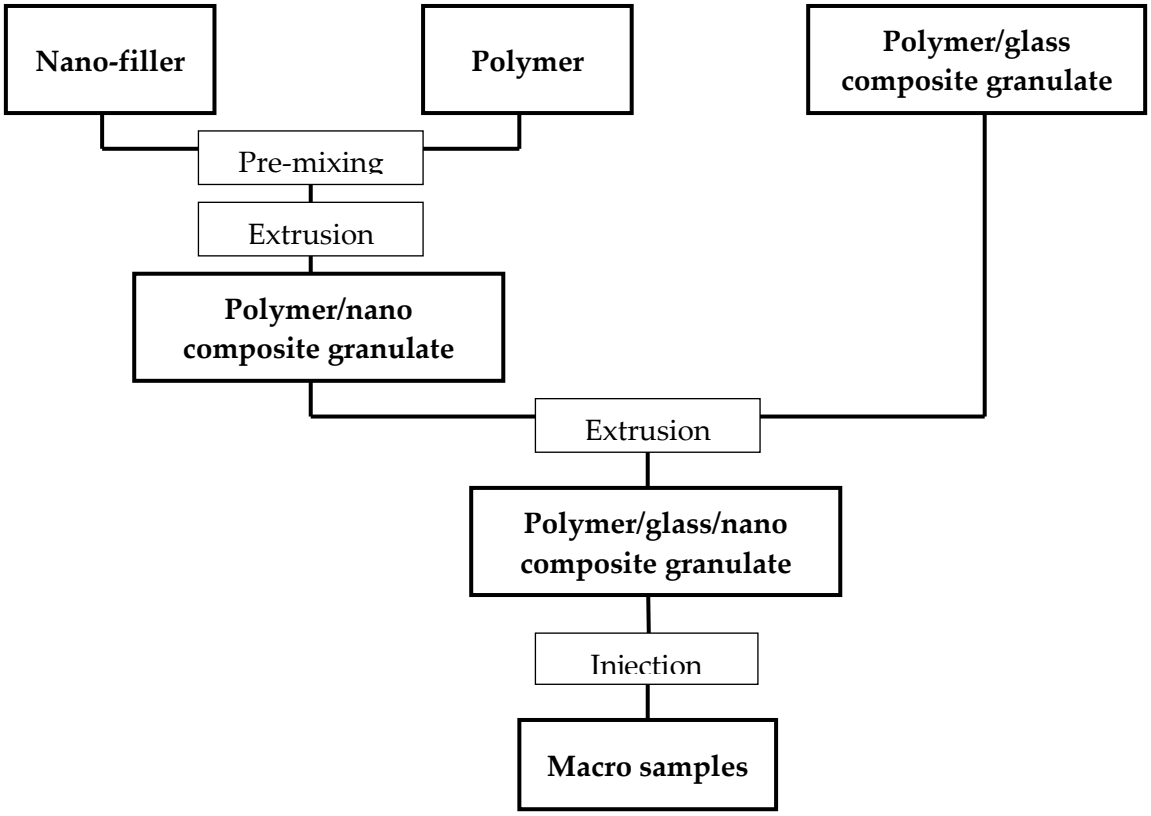

Figure 19: Samples preparation process

3.2.2 Macro-samples preparation

The manufacturing process of the hybrid nanocomposite specimens has been conducted in two steps. In the first one, granulates of the nano-particle reinforced polymers and glass-fibre reinforced polymers were mixed in the extruder. Nanocomposites based on polypropylene were obtained at temperatures: 180, 180, 185, 185, 190, 190, 190, 190, 195, 195, 200° C of 1^{th}-12^{th} barrel zones respectively, with melt pressure of 35-40 bar. The processing parameters for extrusion of PA6-based nanocomposites were as follows:

temperatures of barrel zones (1^{th} – 12^{th}) 240, 250, 250, 250, 260, 260, 260, 270, 270, 270, 280, 280º C and melt pressure 30-35 bar. The screw speed was set at 400 rpm for all prepared compositions. As a result eight different composite materials were prepared as shown in Table 3 and Table 4. In the second step, the specimens were produced using an injection moulding machine (Engel ES200/60 HL ST).

Table 3: **PP composites**

Name	PP/GF	PP/GF/GS	PP/GF/SiO2	PP/GF/MMT
Matrix	PP	PP	PP	PP
1^{st} filler [wt%]	GF [30%]	GF [30%]	GF [30%]	GF [30%]
2^{nd} filler [wt%]	-	GS [12%]	SiO_2 [2%]	MMT [2 %]

Table 4: **PA6 composites**

Name	PA/GF	PA/GF/GS	PA/GF/SiO2	PA/GF/MMT
Matrix	PA	PA	PA	PA
1^{st} filler [wt%]	GF [30%]	GF [30%]	GF [30%]	GF [30%]
2^{nd} filler [wt%]	-	GS [12%]	SiO_2 [2%]	MMT [2 %]

3.3 Experimental procedure

3.3.1 Tensile and compression tests

Quasi-static (0.01 [1/s]) and low strain rate (0.1 – 1 [1/s]) tensile tests were carried out on injection moulded tensile and compression bars, using Instron 5500R electro-mechanical tensile-compression machine, as shown in Figure 20a. Medium strain rate (10-100 [1/s]) tensile tests were carried out on a servo-hydraulic machine Mayes-Instron, as shown in Figure 20b. All experiments were conducted according to ISO-527 (tension - see Figure 22) and ISO-604

(compression – see Figure 23) standards. Five tests were carried out for each material to determine the scatter in the results. The load was measured using a 100kN load cell. In order to measure the displacement, two different methods were applied: mechanical extensometer and laser extensometer. Both measurements were taken at the same time in the quasi-static test, to ensure that they provide equivalent results. At test speeds other than quasi-static, only the laser extensometer was used. The mechanical extensometer was attached at the middle of the sample using rubber O-rings. In order to reflect the laser beam from the surface of the specimen, reflecting tapes were attached at the sides of the sample. Setup of the quasi-static tensile test is shown in Figure 21.

Figure 20: Testing equipment

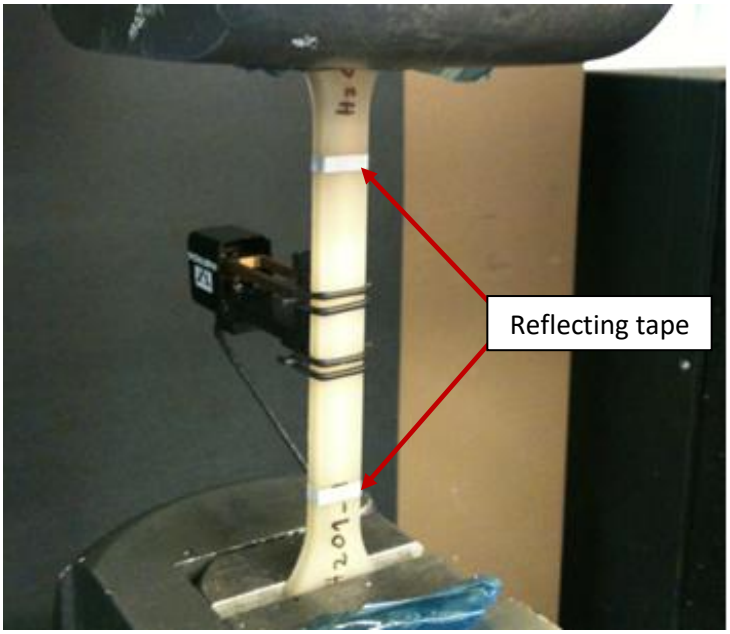

Figure 21: Tensile test- configuration with mechanical and laser extensometers

Table 5: Tensile specimen dimensions [mm]

l_2	Overall length	150
l_1	Length of narrow parallel-sided portion	60±0.5
r	Radius	60±0.5
l_2	Distance between broad parallel-sided portions	108±1.6
b_2	Width at ends	20±0.2
b_1	Width at narrow portion	10±0.2
h	Preferred thickness	4±0.2
L_0	Gauge length	50±0.5
L	Intial distance between grips	115±1

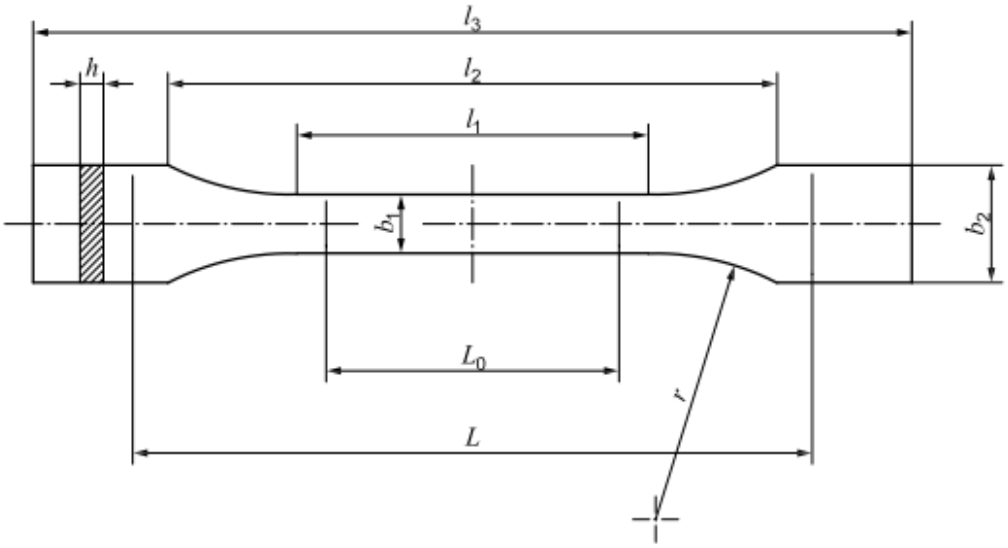

Figure 22: Tensile specimen

Table 6: Compression specimen dimension [mm]

l	Length	50
b	Width	10
h	Thickness	4

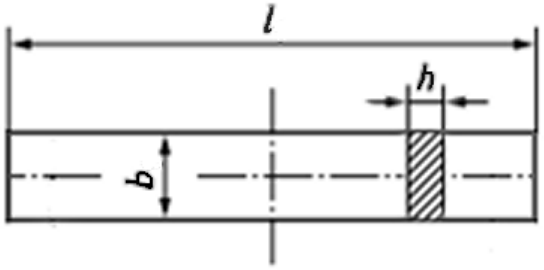

Figure 23: Compression specimen

3.3.2 Microscopic analysis

TEM Images of various nanocomposites were obtained at 120 kV, using a Philips CM20 scanning Transmission Electron Microscope. In order to prepare TEM samples, the composite granulates were compression moulded into thin films. Afterwards, the films were embedded into epoxy resin and cured over night at room temperature. Finally, ultra-thin sections were cut using ultra microtome and deposited on copper grids.

3.3.3 X-ray diffraction

X-ray diffraction experiments were carried out on a Philips X-Pert diffractometer, with a graphite monochromator placed in the front of the detector - λ_{Cu} = 1.5418 Å. The measurements used to determine the crystallographic structure of polymer composites were carried out in an angle range of 3-60º at 0,1º step. Material used for all structure analysis was in a shape of rectangle bars made by injection moulding.

3.4 Results

3.4.1 TEM

The representative TEM images of SiO_2 filled polymer composites are presented in Figure 24. A generally good state of dispersion was observed in both PP and PA matrices. There was a visible tendency of the particles to create small clusters within the polymer. Few of these clusters tended to create larger structures known as agglomerates. The size of the small clusters was in the range of 10 to 50 nm, whereas the size of the few agglomerates was in the range of 100 to 300 nm. Contrary to the PA composite, the agglomerates in the PP matrix were more likely to form chain-like branched structure.

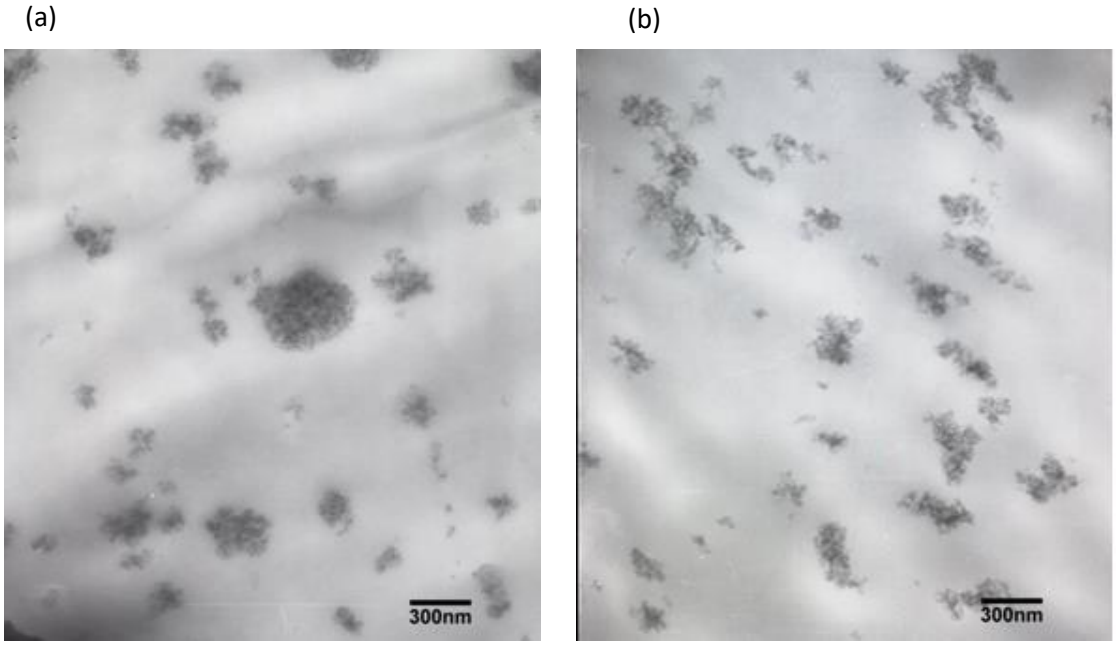

Figure 24: TEM images of SiO_2 reinforced (a) PA (b) PP

The morphology of MMT filled composites is shown in Figure 25. From the micrographs it could be observed, that in both matrices, MMT was partially intercalated and exfoliated. In other words, the polymer was present between the nano-plates which were randomly distributed. However, there were visible agglomerates within the polymer, which means that some of the nano-plates

were not fully separated from each other. Comparing the morphology of the PP and PA based composites it was observed that agglomeration regions were more significant in the case of the PA based composites. Moreover, the size of these agglomerates was observed to be bigger in relation to those existing in the PP matrix, and therefore, interlayer spacing between the plates was reduced as well. The aspect ratio of single nano-pates was in the range from 1:10 to 1:50, in both composites.

(a) (b)

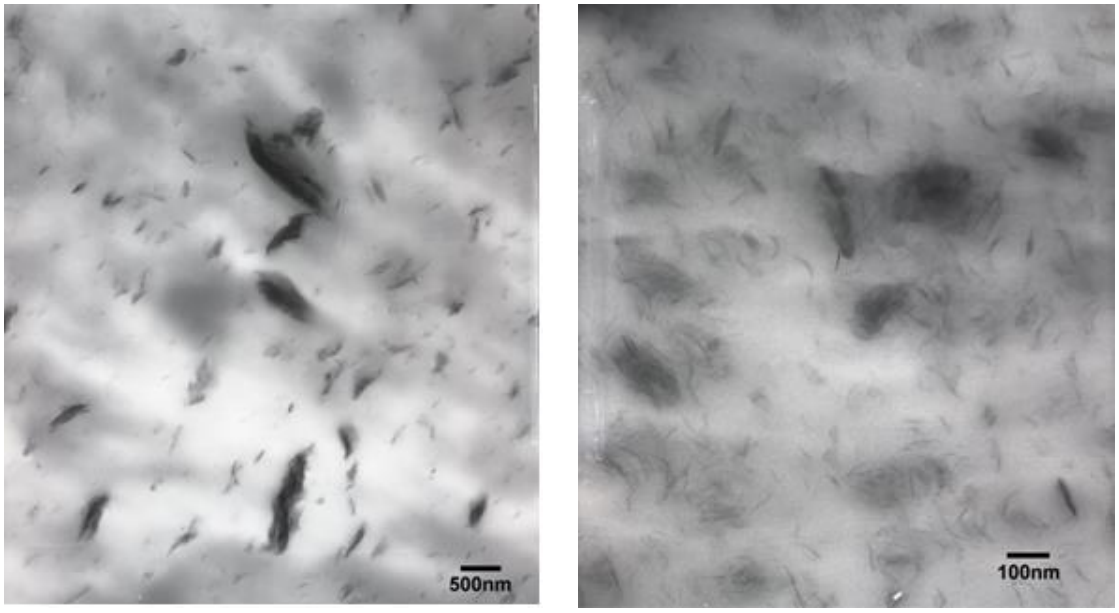

Figure 25: TEM images of MMT reinforced (a) PA (b) PP

3.4.2 WAXD diffractograms

Structure analysis of glass fibre reinforced panels fabricated from PP-based nanocomposites was carried out using the Wide Angle X-ray Diffraction (WAXD) method. Figure 26 - Figure 31 compare the diffractograms of the dust produced from glass fibre reinforced panels, composed of neat polymer with glass fibre and those containing both glass fibres and nano or micro fillers (MMT, SiO2 and GS), in a range of 2θ from 3 up to 60°. The diffraction peaks observed at the 4,2° and 6,3° for PP/GF/MMT sample can be correlated with the

presence of lamellar arrangement of MMT in produced powder. The crystal structure of PP was not significantly affected by the mechanical processing and resembled pattern of neat PP in a bulk form. Stronger peaks observed for dust of nanocomposite panels indicate more perfect and higher content of polypropylene crystal phase. There are no basic changes in the diffraction patterns of dusts prepared from glass fibre reinforced panels, independently on the matrix type. In other words dusts made of PA or PP panels and PA or PP based nanocomposite panels exhibited a similar pattern. The application of nanocomposite materials as a matrix for glass-fibre reinforced panels changed the susceptibility of the material to undergo structural changes under mechanical degradation. However, in the presence of nanoparticles, especially montmorillonite, the peak derived from the γ crystal phase of PA was strengthened indicating higher content of polymer crystal phase in dust made of nanocomposite panels. Such robust crystal morphology could originate from the processing conditions where polymer was subjected to high shearing and cooling rates which favored the formation of γ crystals.

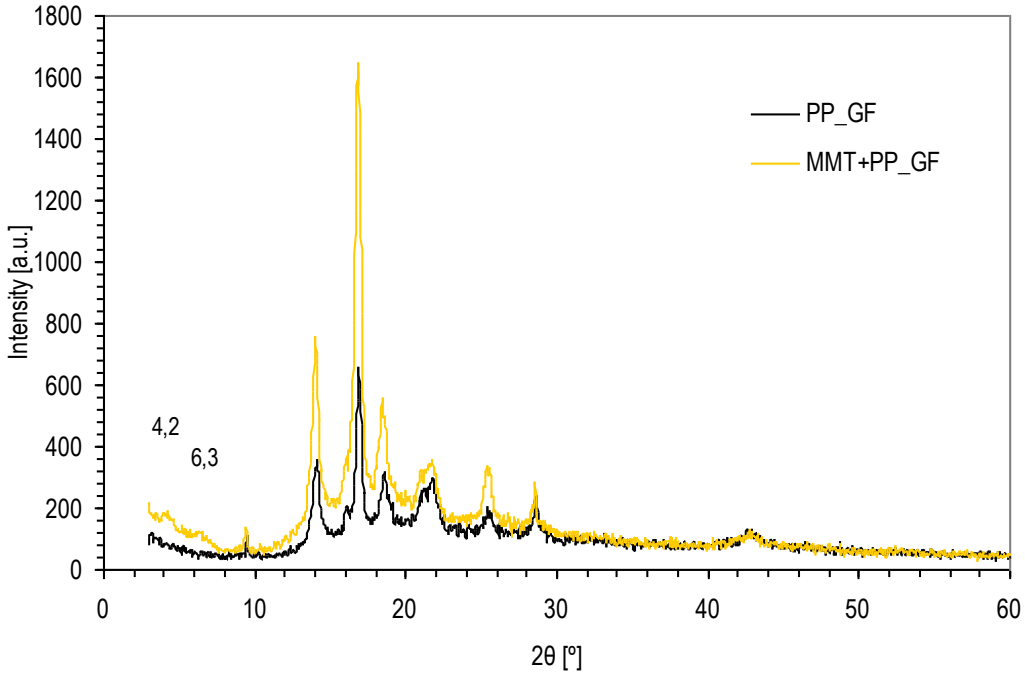

Figure 26: WAXD diffractograms of dust produced from PP and PP/MMT reinforced with glass fibres.

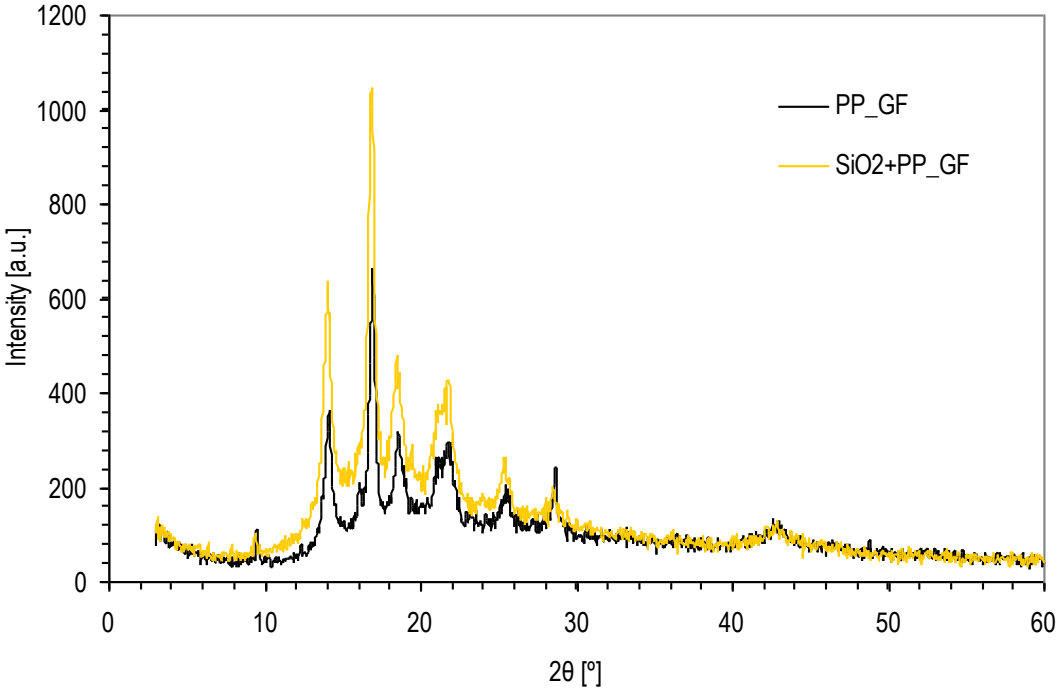

Figure 27: WAXD diffractograms of dust produced from PP and PP/SiO2 panels reinforced with glass fibres.

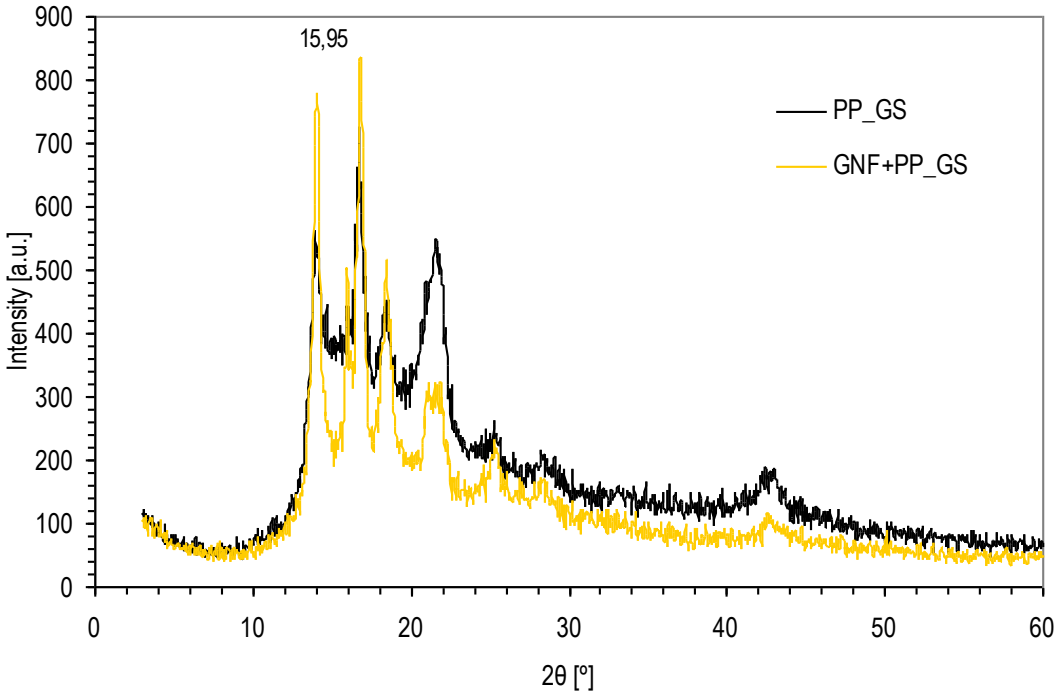

Figure 28: WAXD diffractograms of dust produced from PP and PP/GS panels reinforced with glass spheres

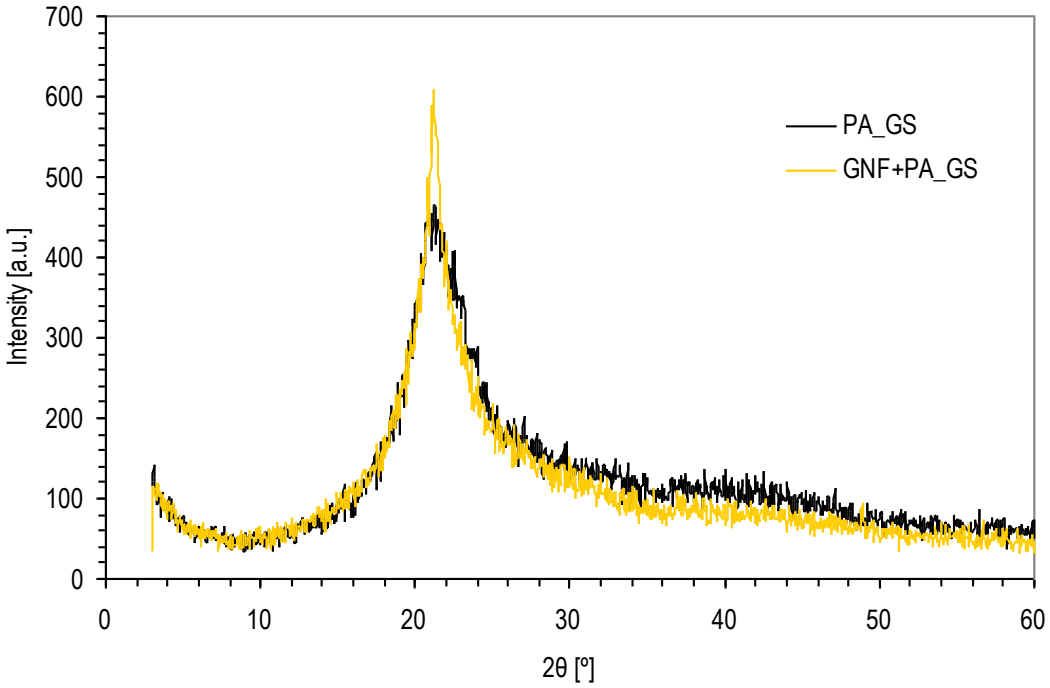

Figure 29: WAXD diffractograms of dust produced from PA and PA/GS panels reinforced with glass spheres.

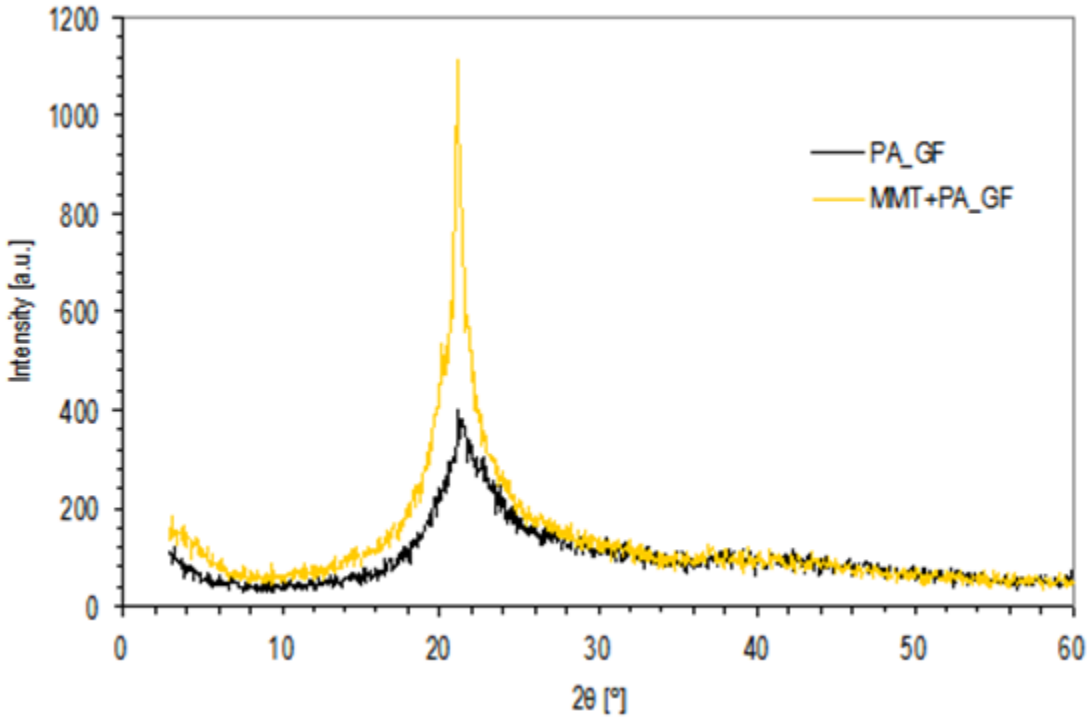

Figure 30: WAXD diffractograms of dust produced from PA and PA/MMT panels reinforced with glass fibre.

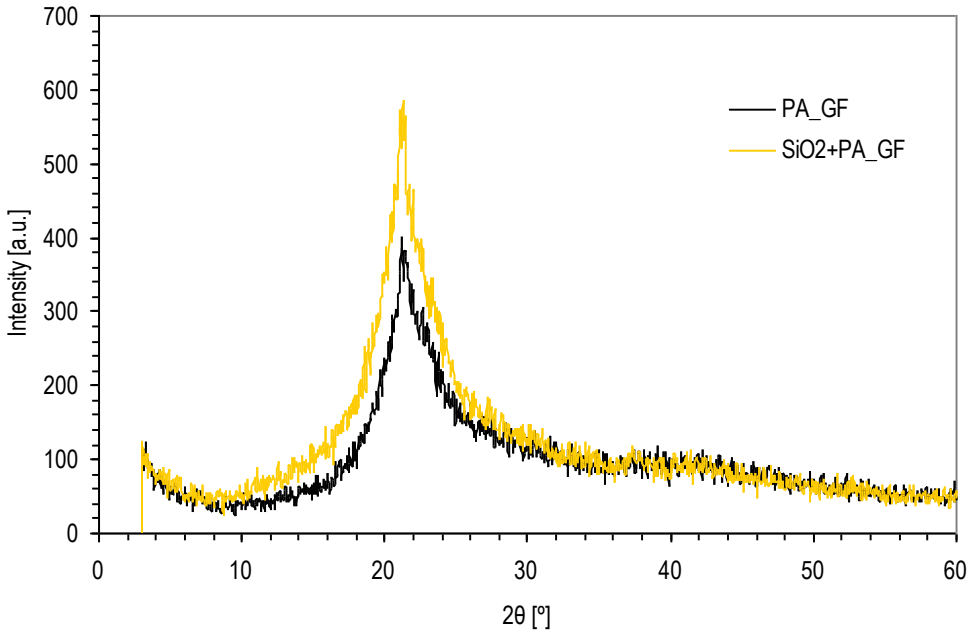

Figure 31: WAXD diffractograms of dust produced from PA and PA/SiO2 panels reinforced with glass fibre.

3.4.3 Optical microscope

The micro-structure of the composites, including size and distribution of glass-filers, was investigated with the optical microscope. Figure 32 shows the section taken in the cross flow direction. From this figure it can be seen that the fibres are in general uniformly distributed within the matrix. More detailed information about the orientation of the fibres can be extracted from the micrograph of the in-flow section, shown in Figure 33. It is clearly visible that the material indicates skin-core structure, which is typical for injection moulded short-fibre reinforced composites. This means that at the outer surfaces of the sample, fibres are mainly orientated in the inflow direction, whereas at the core, fibres tend to orientate in the cross-flow direction. In Figure 34, the size of the glass fibres and spheres has been measured. Both the fibres and the spheres diameter were around 14μm, whereas the length of the fibres was around 300 μm.

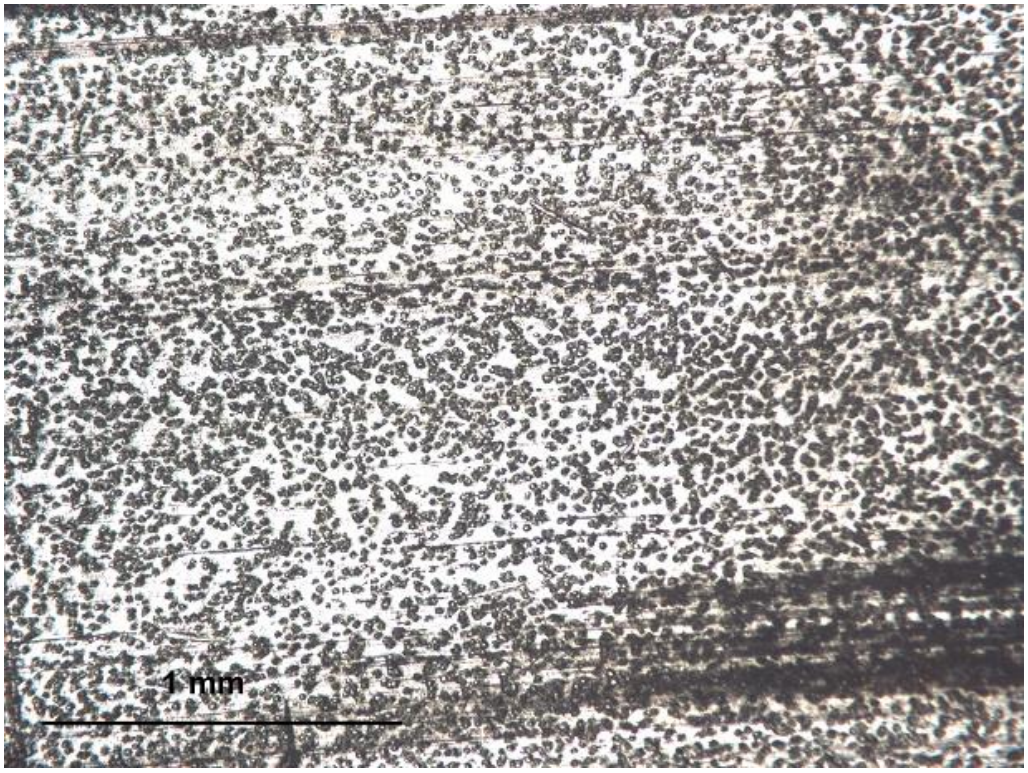

Figure 32: Cross-flow section

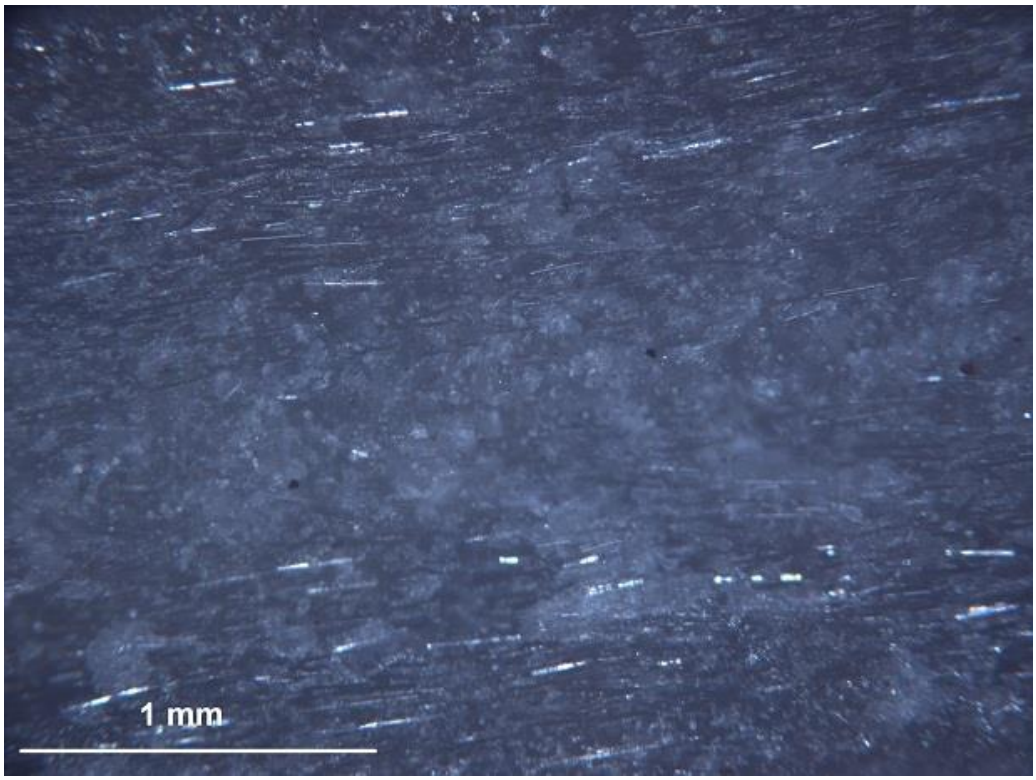

Figure 33: In-flow section

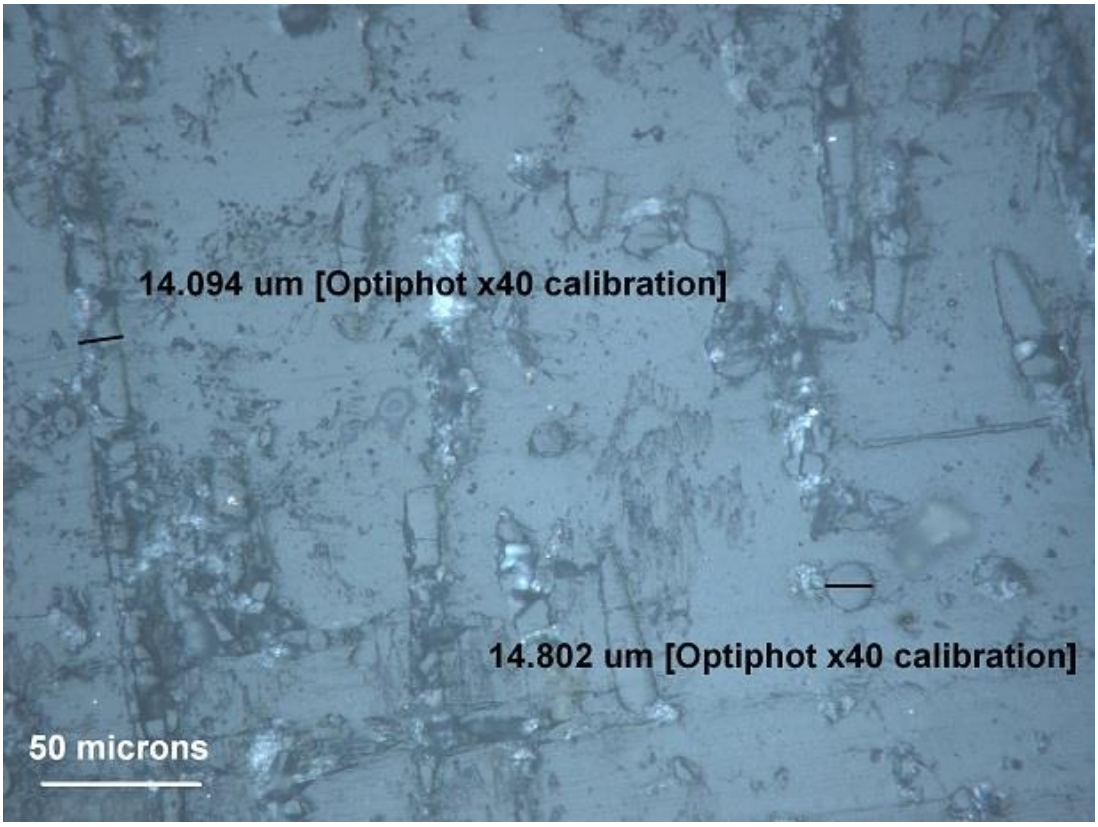

Figure 34: Size of the micro-fillers

3.4.4 Quasi-static mechanical tests

Tensile properties of eight different glass-fibre reinforced polymer composites, filled with nano and micro particles, were obtained at quasi-static conditions (0.01 [1/s]), as presented in Table 7 and Table 8. The tests were performed to gain a better understanding of the effect of various nano fillers on the mechanical behaviour of fibre reinforced composites. Furthermore, these tests were designed to collect relevant data required for FE simulations. The main results presented in this section are the average values ($\bar{x}$) derived from five repeated tests, conducted at each configuration of the specimen and loading condition. The scatter in the results is represented by the standard deviation ($\hat{\sigma}$). Figure 35 shows an example of the scatter observed in the tensile test. The specimens of all composites were tested in longitudinal tension. Moreover, the specimens of PA/GF and PA/GF/SiO_2 composites were tested in transverse direction, as well as in longitudinal compression.

The results obtained show that the mechanical properties of PP composites have a clear tendency to decrease after the addition of the secondary filler. Modulus, strength and elongation to break were decreased in almost all samples. The only improvement observed was in elongation to the break of PP/GF/SiO_2 composite. The biggest drop in all the properties was caused by the presence of GS micro-filler.

By contrast, the effect of secondary filler on the mechanical properties of PA composites was positive. The biggest enhancement in tensile modulus was observed in PA/GF/GS (27%) and PA/GF/MMT (20%), whereas in PA/GF/SiO_2 a decrease of 3.8% was observed. The tensile strength of MMT and GS filled composites increased by 3.2% and 4.5% respectively, whereas in PA/GF/SiO_2 composite the strength decreased by 8.2%. Elongation to break was found to increase in materials filled with SiO_2 (28%) and to decrease in PA/GF/MMT

(26%) and PA/GF/GS (60%) composites. Similar trends were observed in the specimens tested in transverse direction and compression.

It is important to note the orthotropic response of the composite materials. The specimens tested in transverse direction were less stiff and weaker, but conversely more ductile. Furthermore, the specimens tested in compression were stiffer, stronger and no failure was observed at strains up to 10%.

Table 7: Quasi-static mechanical properties – PP composites

Property	Material	Tensile Longitudinal		Tensile Transverse	
		$\bar{x}$	$\hat{\sigma}$	$\bar{x}$	$\hat{\sigma}$
Modulus [MPa]	PP/GF	6612	73.4	4312	51.74
	PP/GF/SiO2	5921	66.4	3961	46.69
	PP/GF/MMT	5955	65.5	-	-
	PP/GF/GS	5721	64.7		
UTS [MPa]	PP/GF	74.1	1.0	49.9	0.69
	PP/GF/SiO2	62.4	0.8	42	0.58
	PP/GF/MMT	61.7	0.8	-	-
	PP/GF/GS	47.4	0.6		
Failure Strain	PP/GF	0.028	0.0009	0.032	0.0010
	PP/GF/SiO2	0.029	0.0010	0.034	0.0011
	PP/GF/MMT	0.024	0.0008	-	-
	PP/GF/GS	0.013	0.0004		

Table 8: Quasi-static mechanical properties – PA composites

Property	Material	Tensile Longitudinal		Tensile Transverse		Compression Longitudinal	
		$\bar{x}$	$\hat{\sigma}$	$\bar{x}$	$\hat{\sigma}$	$\bar{x}$	$\hat{\sigma}$
Modulus [MPa]	PA/GF	6947	76.8	4300	51.60	7199	82.59
	PA/GF/SiO2	6677	74.5	4223	49.78	7081	80.49
	PA/GF/MMT	8686	95.1	-	-	-	-
	PA/GF/GS	9507	107.1				
UTS [MPa]	PA/GF	123.63	1.7	78	1.07	142	1.94
	PA/GF/SiO2	113.47	1.5	72.5	0.99	121.9	1.69
	PA/GF/MMT	127.83	1.7	-	-	-	-
	PA/GF/GS	129.38	1.8				
Failure Strain	PA/GF	0.05	0.0016	0.0594	0.0019	-	-
	PA/GF/SiO2	0.069	0.0023	0.081	0.0026		
	PA/GF/MMT	0.037	0.0012	-	-		
	PA/GF/GS	0.03	0.0010				

Figure 36 and Figure 37 show a comparison of the true tensile stress-strain curves of all studied materials. The composites indicate nonlinear elastic region with no distinct yield point which is typical for polymer based materials. The plastic region of PA composites is also nonlinear with a perfectly plastic characteristic, or even slight softening (PA/GF/MMT), observed beyond the UTS. In case of PP based composites, which are more brittle, the maximum stress corresponds to the point of failure. A clear difference between the PP and PA based composites is visible. The mechanical properties of PP based composites are inferior to those based on PA polymer. They are less stiff, weaker and more brittle.

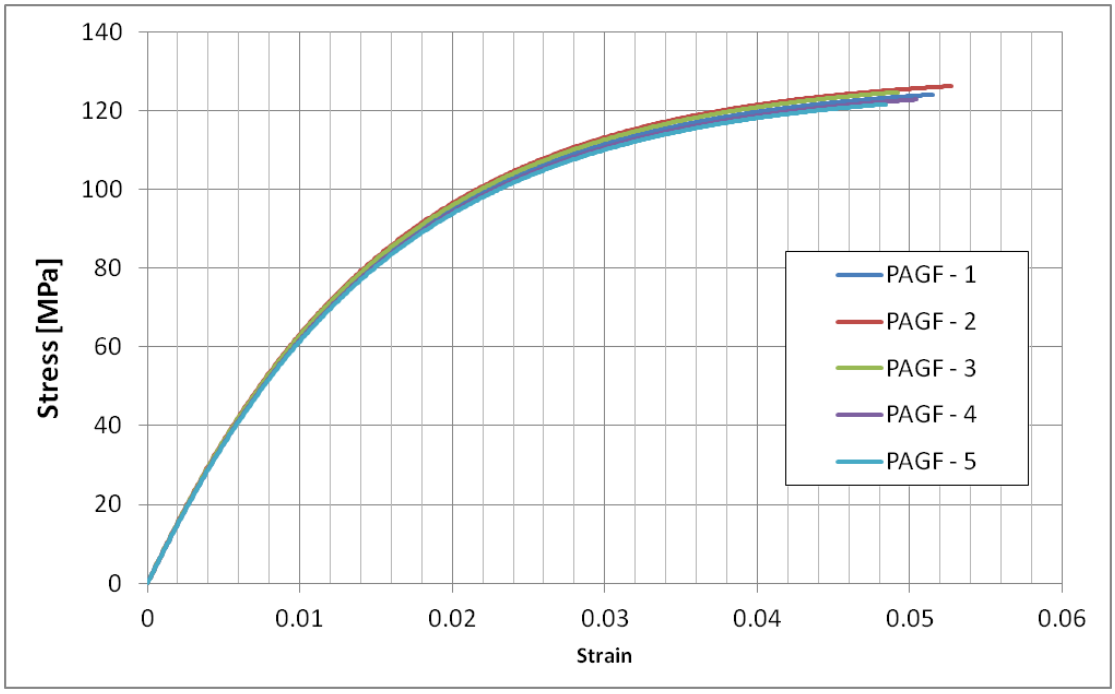

Figure 35: PAGF – tensile test scatter

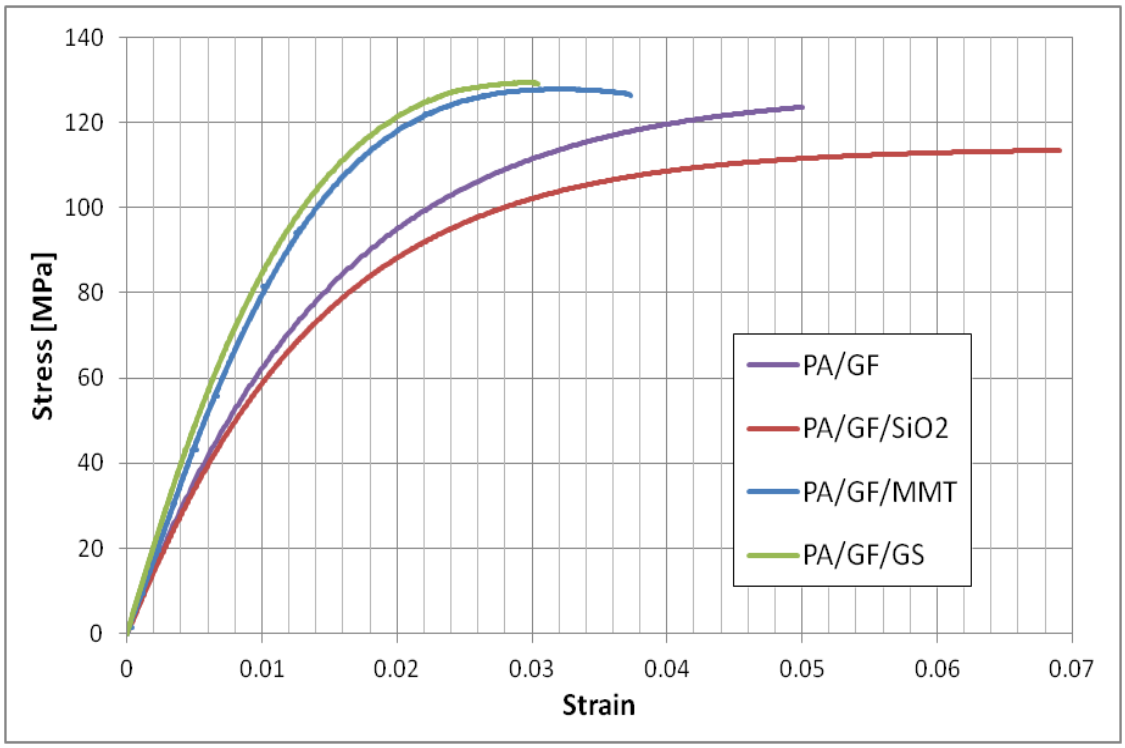

Figure 36: Stress-strain curves of PA composites

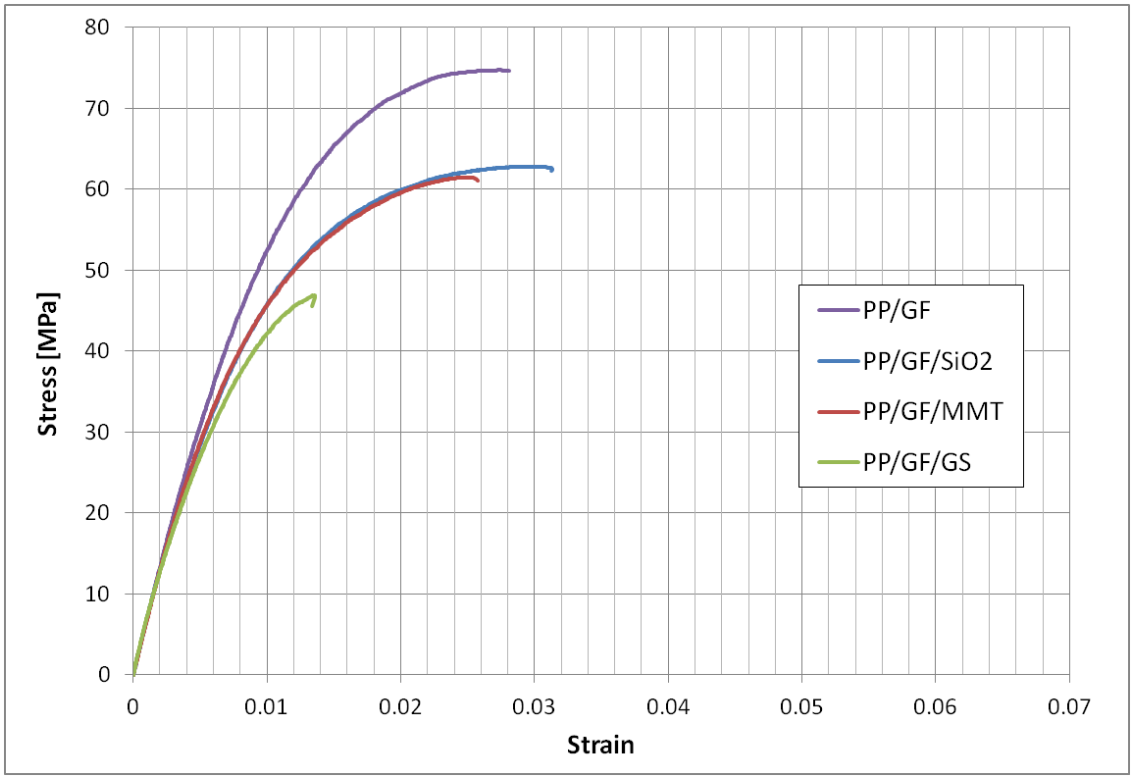

Figure 37: Stress-strain curves of PP composites

3.4.5 Dynamic mechanical tests

The mechanical properties of PA/GF and PA/GF/SiO_2 composites were investigated at five different strain rates, in both longitudinal and transverse directions, as shown in Table 9 and Table 10. The compressive properties were investigated at three different strain rates, as shown in Table 11. The stress-strain curves at those strain rates are presented in Figure 39 - Figure 44. It can be seen that at higher strain rates (10-100 [1/s]) the results were influenced by oscillations and the damping behaviour of the materials; a common issue at those strain rates. In order to provide more accurate data, the mathematical smoothing of the stress-strain curves was carried out.

It can be observed that both composites indicate significant strain rate sensitivity of all the mechanical properties, in both longitudinal and transverse directions, as well as in compression. At higher strain rates the materials become stiffer, stronger and more brittle. When increasing the strain rate from 0.01 to 100 [1/s], the tensile stiffness and strength of PA/GF composite, in longitudinal direction, increased by 42% and 37% respectively, whereas the ductility decreased by 34%. In the PA/GF/SiO_2 composite in the same range of strain rates, the stiffness and the strength also increased by 42% and 37% respectively, whereas the ductility decreasd by 27%.

Figure 38 shows the relationship between the mechanical properties (modulus and UTS) and the strain rate. It can be seen that in the range of 0.01 to 10 [1/s], the mechanical properties are a linear function of the strain rate, in a semi-logarithmic scale. Above the strain rate of 10 [1/s], a transition from medium to high strain rates occurs. In this region the material shows a sudden increase in strain rate sensitivity, i.e. a smaller change in strain rate will induce a larger change in the mechanical properties.

Table 9: Longitudinal mechanical properties at different strain rates

Property	Material		Strain Rate [1/s]				
			0.01	0.1	1	10	100
Modulus [MPa]	PA/GF	$\bar{x}$	6947	7711	8240	9002	11891
		$\hat{\sigma}$	77.9	86.4	92.4	109.0	143.9
	PA/GF/SiO_2	$\bar{x}$	6677	7412	8147	8882	10819
		$\hat{\sigma}$	75.5	83.9	92.2	107.5	131.0
UTS [MPa]	PA/GF	$\bar{x}$	123.63	139.94	154.27	167.43	195.11
		$\hat{\sigma}$	1.71	1.94	2.13	2.46	2.86
	PA/GF/SiO_2	$\bar{x}$	113.47	128.53	142.75	156.27	181.29
		$\hat{\sigma}$	1.57	1.78	1.98	2.29	2.66
Failure Strain	PA/GF	$\bar{x}$	0.05	0.049	0.046	0.039	0.033
		$\hat{\sigma}$	0.0017	0.0016	0.0015	0.0013	0.0011
	PA/GF/SiO_2	$\bar{x}$	0.069	0.066	0.061	0.059	0.05
		$\hat{\sigma}$	0.0023	0.0022	0.0020	0.0020	0.0017

Table 10: **Transverse mechanical properties at different strain rates**

Property	Material		Strain Rate [1/s]				
			0.01	0.1	1	10	100
Modulus [MPa]	PA/GF	$\bar{x}$	4300	4933	5233	5767	7200
		$\hat{\sigma}$	48.2	55.3	58.7	69.8	87.1
	PA/GF/SiO_2	$\bar{x}$	4223	4750	5208	52729	6979
		$\hat{\sigma}$	47.8	53.7	58.9	638.2	84.5
UTS [MPa]	PA/GF	$\bar{x}$	78	93.9	102.7	112	130
		$\hat{\sigma}$	1.08	1.30	1.42	1.64	1.91
	PA/GF/SiO_2	$\bar{x}$	72.5	81.8	88.1	96.9	114.3
		$\hat{\sigma}$	1.00	1.13	1.22	1.42	1.68
Failure Strain	PA/GF	$\bar{x}$	0.0594	0.0537	0.0512	0.0477	0.0425
		$\hat{\sigma}$	0.0020	0.0018	0.0017	0.0016	0.0014
	PA/GF/SiO_2	$\bar{x}$	0.081	0.078	0.075	0.069	0.06
		$\hat{\sigma}$	0.0027	0.0026	0.0025	0.0023	0.0020

Table 11: **Compressive mechanical properties at different strain rates**

Property	Material		Strain Rate [1/s]		
			0.01	0.1	1
Modulus [MPa]	PA/GF	$\bar{x}$	7417	8334	9183
		$\hat{\sigma}$	83.1	93.4	102.9
	PA/GF/SiO_2	$\bar{x}$	7081	7533	8233
		$\hat{\sigma}$	80.1	85.2	93.2
UTS [MPa]	PA/GF	$\bar{x}$	142	159.12	177.54
		$\hat{\sigma}$	1.96	2.20	2.46
	PA/GF/SiO_2	$\bar{x}$	122.43	142.02	156.22
		$\hat{\sigma}$	1.69	1.97	2.16

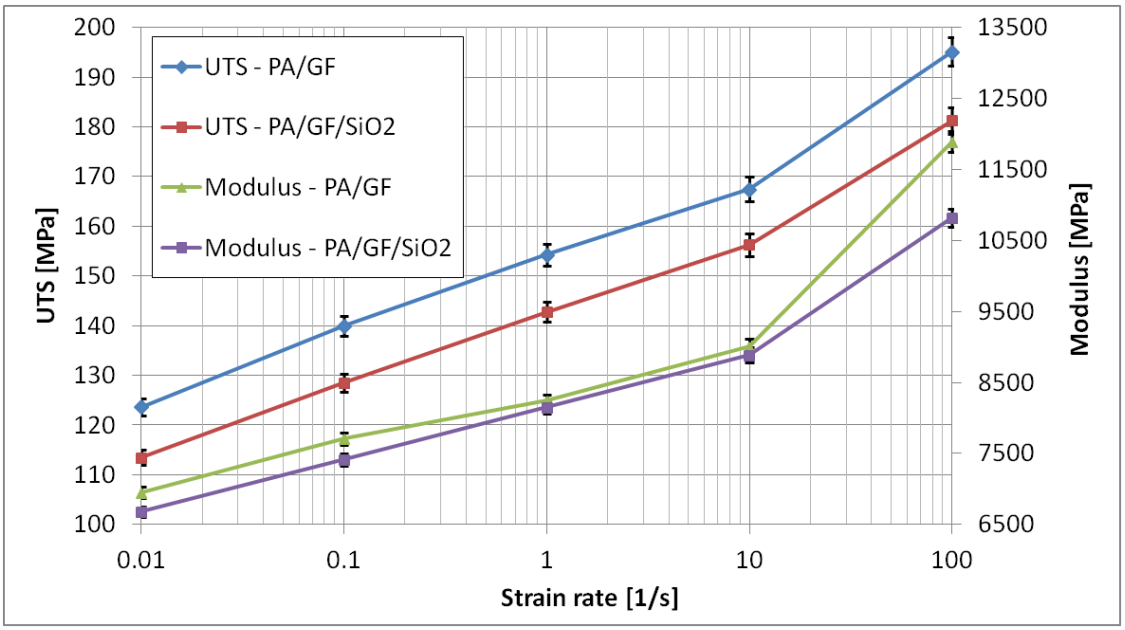

Figure 38: Strain rate behaviour of tensile modulus and strength

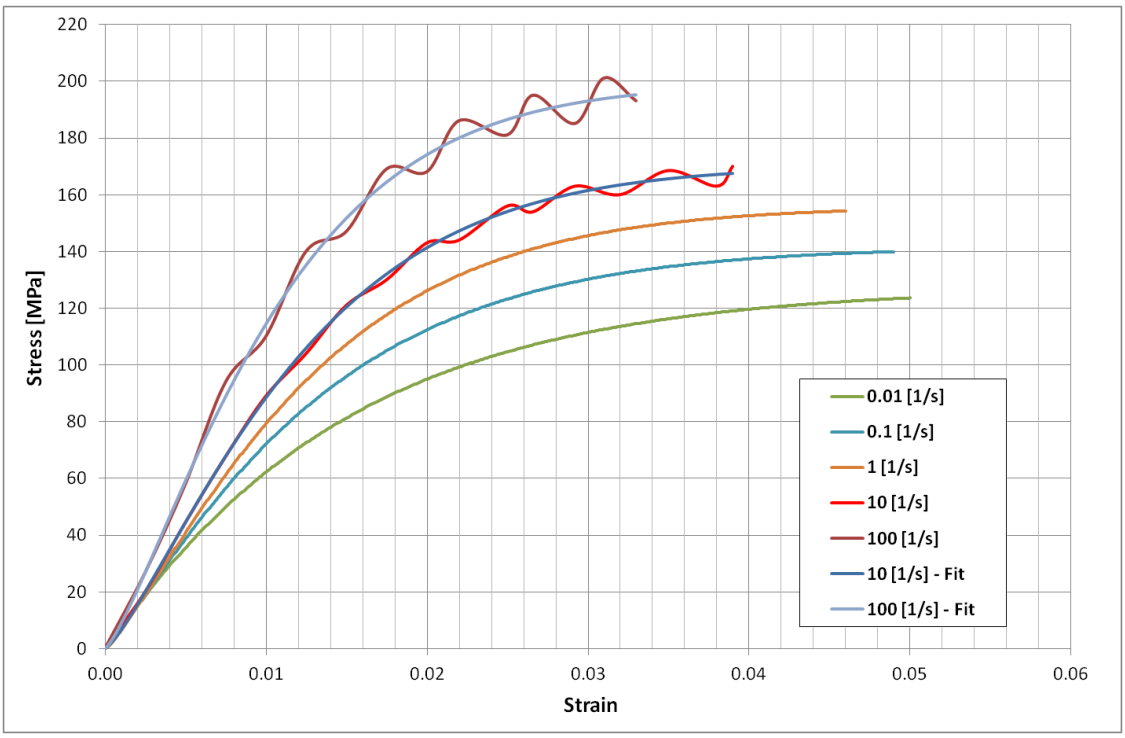

Figure 39: Longitudinal stress-strain curves of PA/GF at different strain rates

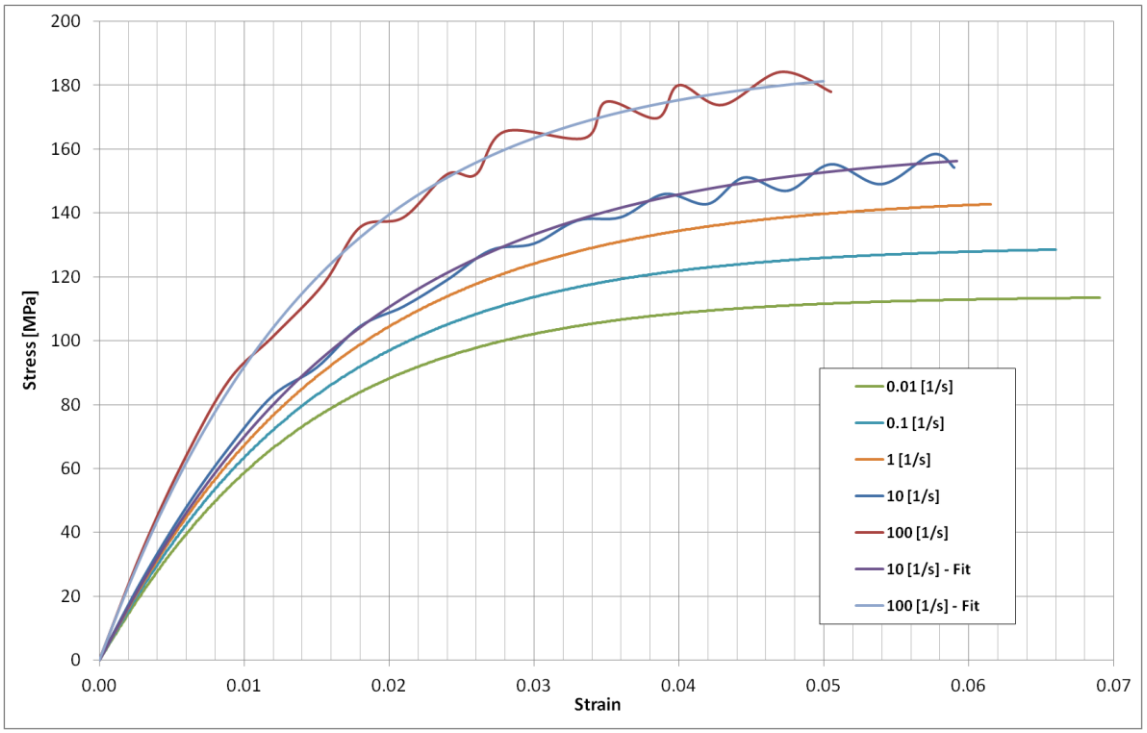

Figure 40: Longitudinal stress-strain curves of PA/GF/SiO_2 at different strain rates

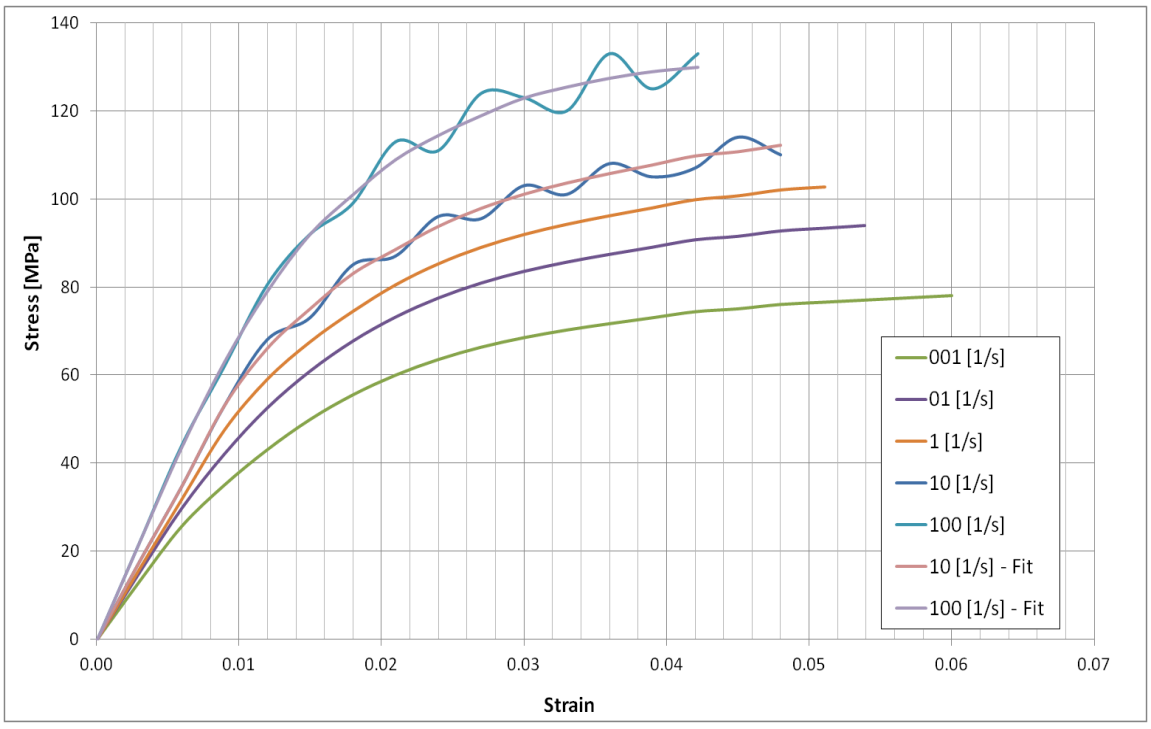

Figure 41: Transverse stress-strain curves of PA/GF at different strain rates

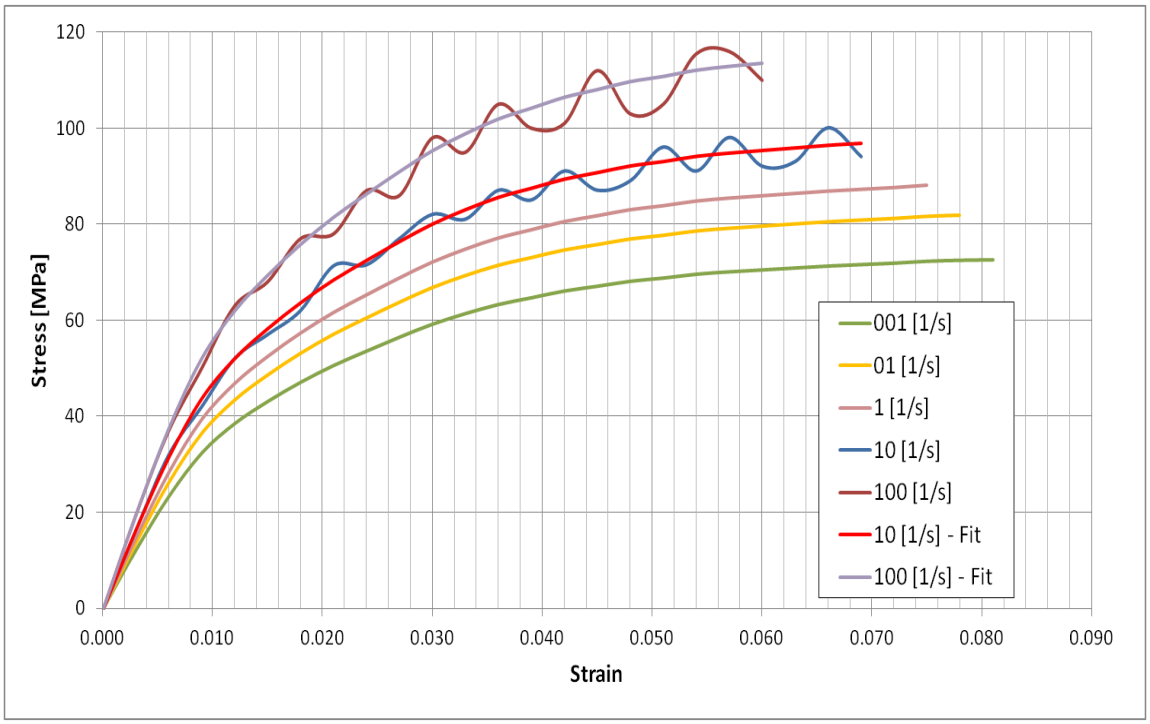

Figure 42: Transverse stress-strain curves of PA/GF/SiO_2 at different strain rates

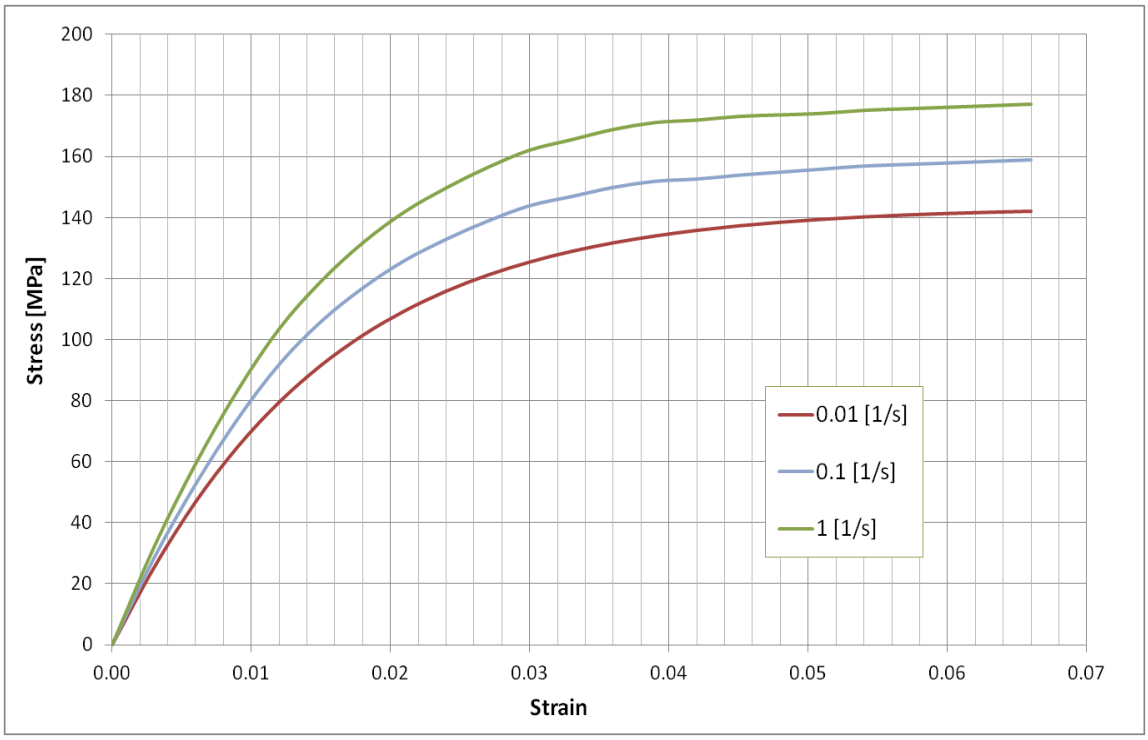

Figure 43: Compressive stress-strain curves of PA/GF at different strain rates

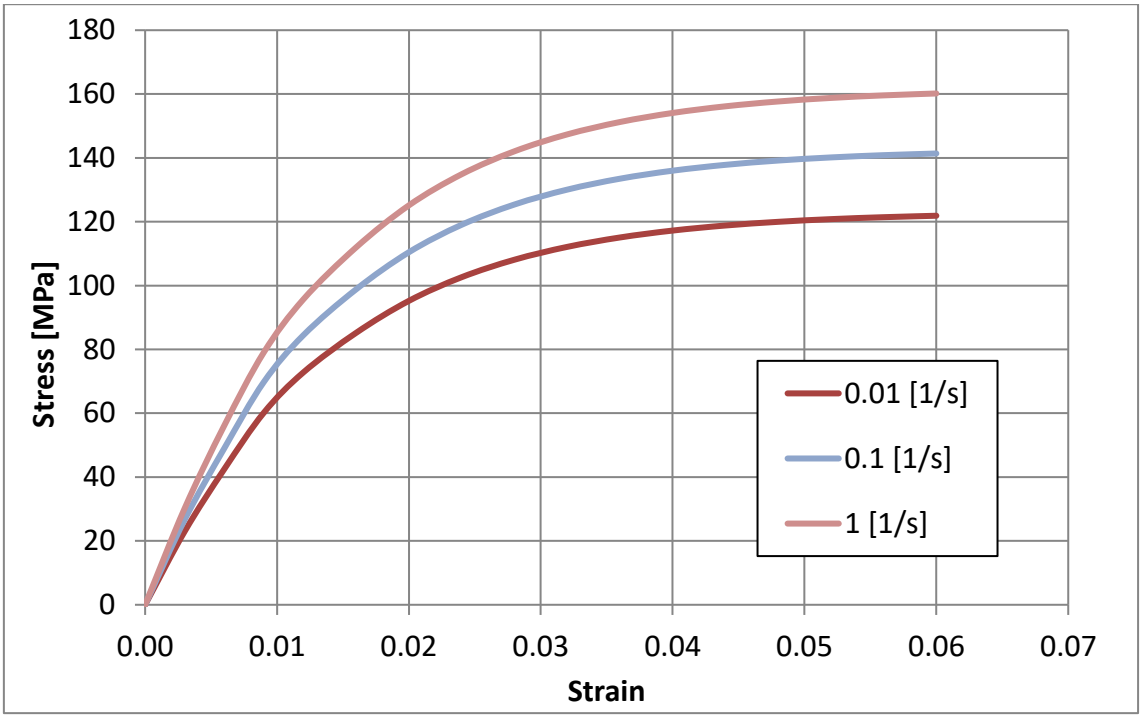

Figure 44: Compressive stress-strain curves of PA/GF/SiO_2 at different strain rates

3.4.6 Discussion

The negative effect of the secondary reinforcement on the mechanical properties of PP based composites may be attributed to the properties of the PP material itself. Good bonding between PP matrix and reinforcement is difficult to achieve without an appropriate coupling agent, which provides chemical coupling between non-polar polymer and polar reinforcement [176]. Another issue associated with PP based composites, is good dispersion of nano-reinforcement within a matrix. Usage of untreated nano-reinforcement, without a compatibilizer, in PP matrix can lead to a bad dispersion and existence of the agglomeration regions. This results in a lower ability of the material to achieve the strong interphase bonding [177]. As shown in section 3.4.1, there were some larger agglomerates present in the PP based composites. Thus a combination of dispersion issues and difficulties with achieving good bonding between PP matrix and the reinforcements caused the decrease in mechanical properties of the composites, after the addition of secondary fillers.

Regarding the PA based composites, there were also some agglomerates observed on TEM images. However, due to the good coupling capabilities of PA material, they did not deteriorate the mechanical properties of the composites. On the contrary, an improvement in the mechanical properties such as stiffness, strength or ductility was observed. However, it is important to note that each filler caused a change in a different property. This effect comes from the difference in the geometry, material and size of the fillers, and therefore their reinforcing mechanism.

In the composites filled with GS and MMT a significant increase in stiffness and small increase in strength were observed. This is a typical effect of a rigid reinforcement in a flexible matrix, which provides increase in stiffness but at the cost of reduced ductility. This phenomenon comes from the fact that the stress is transferred from the flexible matrix to the rigid reinforcement, leading to an increase in the stiffness. At the same time the ability of the material to sustain deformations is reduced, due to the stress concentrations existing around the reinforcement. Micro cracks can be initiated, and also accelerated, at the stress concentration regions. This effect causes failure of the material at a much lower strain in relation to the neat polymer. Partially intercalated and exfoliated MMT can generate such stress concentration regions causing reduction in the ductility of the material. The better the quality of the intercalation and exfoliation state, the lower the stress concentration regions, and therefore better mechanical properties of the composite. Similarly, GS fillers which are in micro size will introduce large stress concentration regions, further reducing the ability of the material to sustain plastic deformation.

An opposite behaviour was observed in the SiO_2 reinforced composite, which indicated a small increase in modulus, a small decrease in strength and a large increase in elongation. The reason for this behaviour comes from the nature of the nano-particles. Due to a small size of the particles the stress concentrations

around the interface region are insignificant. This is why the micro cracks, which origin from the stress concentration region, are difficult to initiate or accelerate. Furthermore, the particles act as crack blockers, leading to an increase in the ductility of the composite material.

3.5 Conclusions

Eight different glass-fibre reinforced polymer composites, filled with nano and micro particles were manufactured and tested. The morphology was studied using optical microscope, TEM and WAXD. The fibre distribution shows a skin-core effect, with fibres aligned in an inflow direction in outer surfaces, whereas fibres are aligned in a transverse direction in the centre of the specimen. A good state of dispersion was achieved in nano-filled materials, but with some visible agglomerates. The presence of nano-particles increased the crystalline phase of both PP and PA based composites.

The mechanical properties were tested in tension (longitudinal and transverse) and compression, at five different strain rates. Addition of the secondary filler into PP based composites had a negative effect on their mechanical properties. It is likely that this was caused by the presence of agglomeration regions in conjunction with bonding issues between the PP matrix and the fillers.

The effect of secondary fillers on the mechanical properties of PA based composites was positive. MMT and GS caused an increase in the stiffness and the strength. The SiO_2 filler increased the ductility of the composite, with little effect on its stiffness and strength. The increased ductility of the composite, without compromising its stiffness and strength, is a desirable property for energy absorbing structures. Therefore, the PA/GF/SiO_2 composite was selected for further assessment. Both PA/GF and PA/GF/SiO_2 composites were tested at five different strain rates in longitudinal and transverse tension. Additionally, compressive properties were derived at three different strain rates, for both

composites. The results show that addition of SiO_2 particles increases the ductility of the material in all the directions, as well as at both static and dynamic conditions. At the strain rate of 100 [1/s] the PA/GF/SiO_2 composite is 40% more ductile than the PA/GF composite. This proves that the common issue with brittleness of short-fibre reinforced composites can be diminished by incorporation of SiO_2 particles. This can increase the applicability of these composites for various structural applications, including crashworthiness.

4. Fracture Mechanism and Impact Energy Absorption of The Nanocomposite Structures

This chapter focuses on the testing of conical structures made of eight different composite materials. It aims to gain a better understanding of the fracture mechanism under static and dynamic loads. It also aims to find a correlation between the change in the mechanical properties and the effect of that change on the ability of the structure to crash progressively and absorb the energy of the impact.

The effect of various nano and micro sized fillers on the mechanical properties of fibre reinforced composites was studied in detail in Chapter 3. It was proved that the addition of various fillers can have an important effect on the mechanical properties of the composites. Each filler showed a different effect on the mechanical properties, due to the difference in the reinforcing mechanism, caused by the difference in shape, size and material of the fillers. However, as shown in the literature survey, the fracture mechanism of composite materials is a complex process. Unlike metals, composite materials fail and absorb the energy not only by plastic deformation, but also by the effects such as delamination or debonding of the fibres. That is why to gain better understanding of the failure mechanism in the nanocomosite structures, structural testing is required along the simple uniaxial specimen testing.

The most widely used method to evaluate the ability of a composite material to absorb the energy is axial collapse of a structural element. This technique has been applied by many researchers on various composite materials. The most often used shapes are cylindrical or square tubes, as well as cones. For the purpose of this work conical structures were selected. This choice was made as the conical shape triggers fracture, as well as progressive collapse of the

structure. This simplifies the structural testing process and makes the results more repeatable, and consequently comparable.

The chapter starts with details of the materials used for the purpose of this study, as well as the selected manufacturing techniques. Subsequently, it shows procedures for structural testing and characterization of the fracture surface. It demonstrates and discusses the results of the static and dynamic structural testing, carried out electro mechanical machine and high energy drop tower. It also presents the results of fracture surface characterization, carried out using Scanning Electron Microscopy (SEM).

4.1 Materials and manufacturing

Eight different composites were manufactured using the materials and procedures as described in section 3.1, and summarized in Table 3, Table 4 and Figure 19. The conical structures were manufactured using the injection moulding technique. The parameters used in the manufacturing process are described in detail in section 3.2.2. The outer dimensions of the conical specimen are shown in Figure 45 (a).

4.2 Experimental procedure

4.2.1 Quasi-static crash test

Quasi-static crash testing of the conical structures was carried out using an Instron 5500R electro-mechanical machine (see Figure 45 (b)). Two samples of each material were tested at a crosshead speed of 0.1mm/sec. The load was measured using a 100kN load cell and the displacement was measured using a built in crosshead displacement sensor. The samples were placed between the two mild steel plates, 10mm in thickness. The plates were not fixed to the sample in any way. During the test the data was collected at every second, corresponding to 0.1mm displacement.

In the Instron machine a measured data is automatically saved in the 'raw' data file. This can be imported to any data analysis software. Due to the large number of samples tested, Matlab script was created to facilitate the post-processing of the results. Subsequently, a quasi-static load-displacement curve was plotted, and the energy absorbed by the structure was calculated, using a numerical integration of the load-displacement curve. For this purpose a trapezium rule was applied, using function 'trapz' in Matlab.

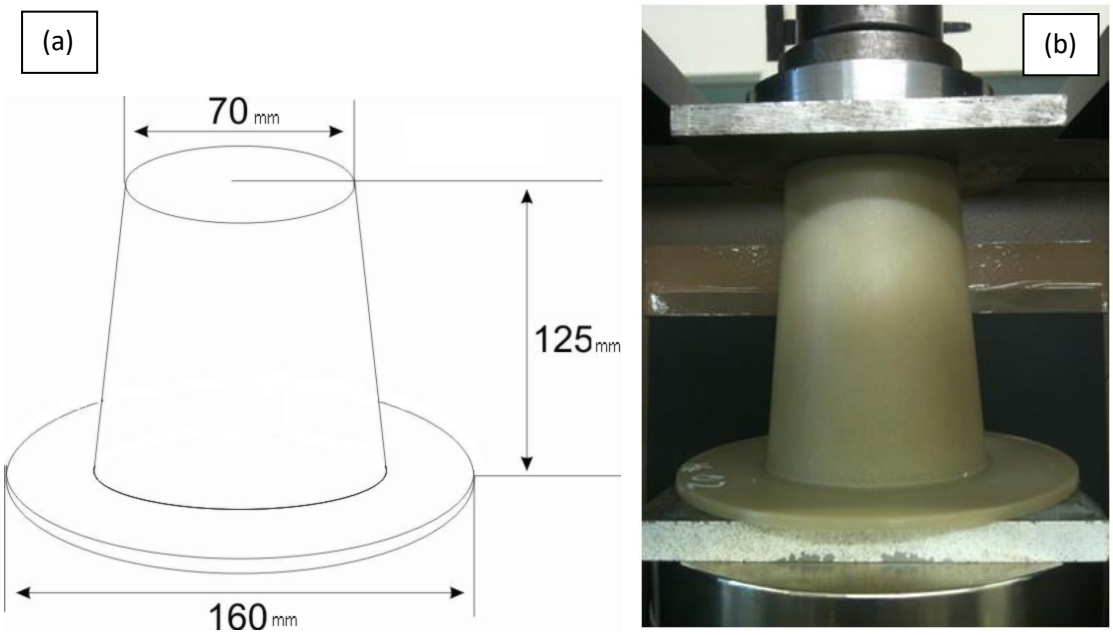

Figure 45: (a) Crash cone dimensions (b) Quasi-static crash test

4.2.2 Drop weight impact test

Impact tests of the crash cones were carried out on a High Energy Capacity Drop Tower Rig. This machine permits impact testing at up to 8m/s velocity and maximum falling weight of 300kg. However, this drop tower does not have a built in acquisition system for the measurement of load and displacement. As a consequence external devices were required.

The medium energy impact was carried out at the velocity V_1= 6.5 m/s and the impactor mass M_1= 142kg. The high energy impact was carried out at the velocity V_2= 8m/s and the impactor mass M_2= 188 kg. These give the overall impact energies of 3kJ and 6kJ. The load was measured using a 300kN load cell, placed underneath the sample. In order to measure shortening of the sample (beam displacement), the LVDT (Linear Variable Differential Transformer) displacement transducer was used, with precision of 0.01mm and maximum displacement speed of 10m/s. This device measures the displacement by the movement of the push rod, which controls transfer of the current between primary and secondary coils. Because the LVDT transducer uses a mechanical linkage, between the falling beam and the ground, it is necessary to provide a very precise and stable motion of the push rod. For this purpose a solid steel block was used, which was in contact with the rod during the whole impact event. In order to prevent bouncing of the displacing rod, the contact surface was covered with double-sided tape.

Both the load cell and displacement transducer were connected to the data acquisition system (DAQ), which converted analog input into a digital output signal. The signal from DAQ was converted and recorded as load and displacement every 0.05ms, using a DASYLab program created for the purpose of these experiments.

Furthermore, the impact event was recorded using a Phantom high speed camera with the frame rate of 1000 frames/sec, at 640x480 resolution. A camera trigger was constructed to ensure that video record starts just before the impact. For this purpose a Beam Brake Detector was used, which detects intersection of the infra-red light, and opens the circuit to trigger the camera. To prevent crashing of the load cell, safety wooden blocks were placed on both sides of the falling beam. The details of the experiment set up can be seen in Figure 46 and Figure 47. The design of the impactor is presented in Appendix D.

Figure 46: Drop tower setup

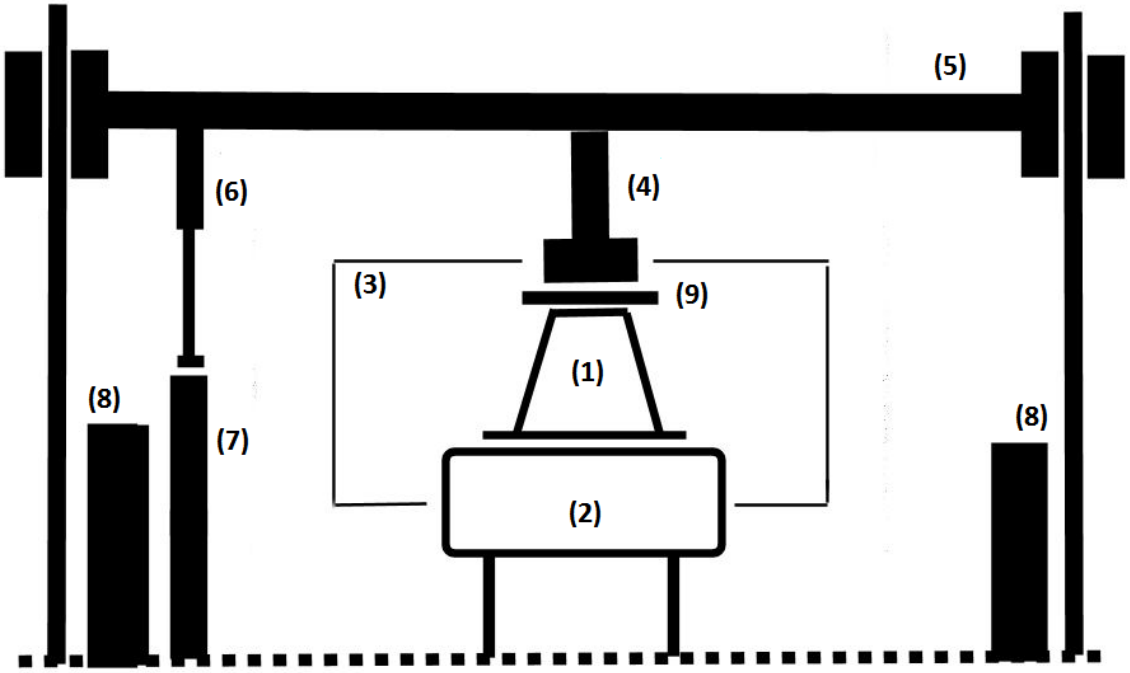

(1) - Crash Cone
(2) - Load cell
(3) - Crash chamber
(4) - Impactor
(5) - Falling beam
(6) - Displacement transducer
(7) –transducer support
(8) – Safety blocks
(9) – Steel plate

Figure 47: Schematic set up of the drop tower crash test

4.2.3 Microscopic analysis

The fracture surface of the conical samples was examined with a FEI XL30 field emission scanning electron microscope (SEM). The operating voltage was in the range of 10-20 kV and the specimens were gold sputtered to minimise charging of the sample. Furthermore, the chemical composition of the samples was investigated using an Energy-Dispersive X-ray Spectroscopy (EDX), integrated into SEM.

4.3 Results

4.3.1 Quasi-static crash test

Crashing behaviour and energy absorption characteristics of eight different composite materials were studied by means of a quasi-static crash test of the conical structures. Load displacement curves measured during the test are presented in Figure 48 and Figure 49. Pictures showing the condition of all the structures after the crash tests are presented in Figure 50 and Figure 51. Furthermore, to quantify the energy absorption capability of the structures, the key crashing parameters were extracted from the curves: total energy absorbed (E), specific energy absorption (SEA), mean crashing load, value of the initial load peak and failure mode.

The energy absorption characteristics of all the composites tested are listed in Table 12. It is important to note that the quasi-static tests were conducted as displacement controlled tests, with constant maximum displacement values in all experiments (90mm). This is why for this case the SEA parameter was a function of only the total energy absorbed by the structure, and not the crashing length (see Table 12).

Comparing the load-displacement curves, presented in Figure 48 - Figure 49, several important observations can be made. In all experiments the initial slope of the load curve is approximately linear. This is associated with the elastic deformation of the material. The first extremum, visible on the plots, indicates maximum load supported by the structure, which depends on the material's yield strength. Beyond this point, a sudden drop in load is observed due to the plastic deformation and formation of cracks. Subsequently, a progressive crashing occurs, which is visible as following sharp load-peaks. The magnitude of those load-peaks depends on the crashing characteristic of the material.

From Table 12 it can be seen that the energy absorption capability of PP based composites decreased after addition of the secondary fillers. This is consistent with the results obtained from uniaxial tensile tests. Including SEA, all the crashing parameters decreased by nearly 50%. Regarding the PA based composites, it can be seen that the change in the value of the initial peak, due to the reinforcement, is also consistent with the result of uniaxial tensile tests. The materials with increased strength (PA/GF/MMT and PA/GF/GS) induced higher initial load peaks, in relation to PA/GF composite, whereas weaker PA/GF/SiO_2 induced a lower initial load peak. However, all the other crashing parameters, such as mean crushing load and SEA, decreased after the addition of secondary fillers.

Table 12: Quasi-static crashing characteristics

Material	Crash length [mm]	Collapse mode	Initial peak [kN]	Mean crashing load [kN]	Energy absorbed [kJ]	SEA [kJ/kg]	Change in SEA [%]
PPGF	90	III	29.74	34.75	2.99	49.4	
PPGF/SiO_2	90	IV	26.59	17.86	1.48	24.4	-50.7
PPGF/MMT	90	IV	24.75	15.39	1.29	21.2	-57.0
PPGF/GS	90	IV	22.06	17.66	1.65	26.3	-46.9
PAGF	90	III	47.66	50.44	4.33	58.1	
PAGF/SiO_2	90	III	44.61	45.66	4.15	54.5	-6.1
PAGF/MMT	90	III	54.59	40.65	3.23	42.9	-26.2
PAGF/GS	90	III	55.10	45.74	4.11	51.7	-11.0

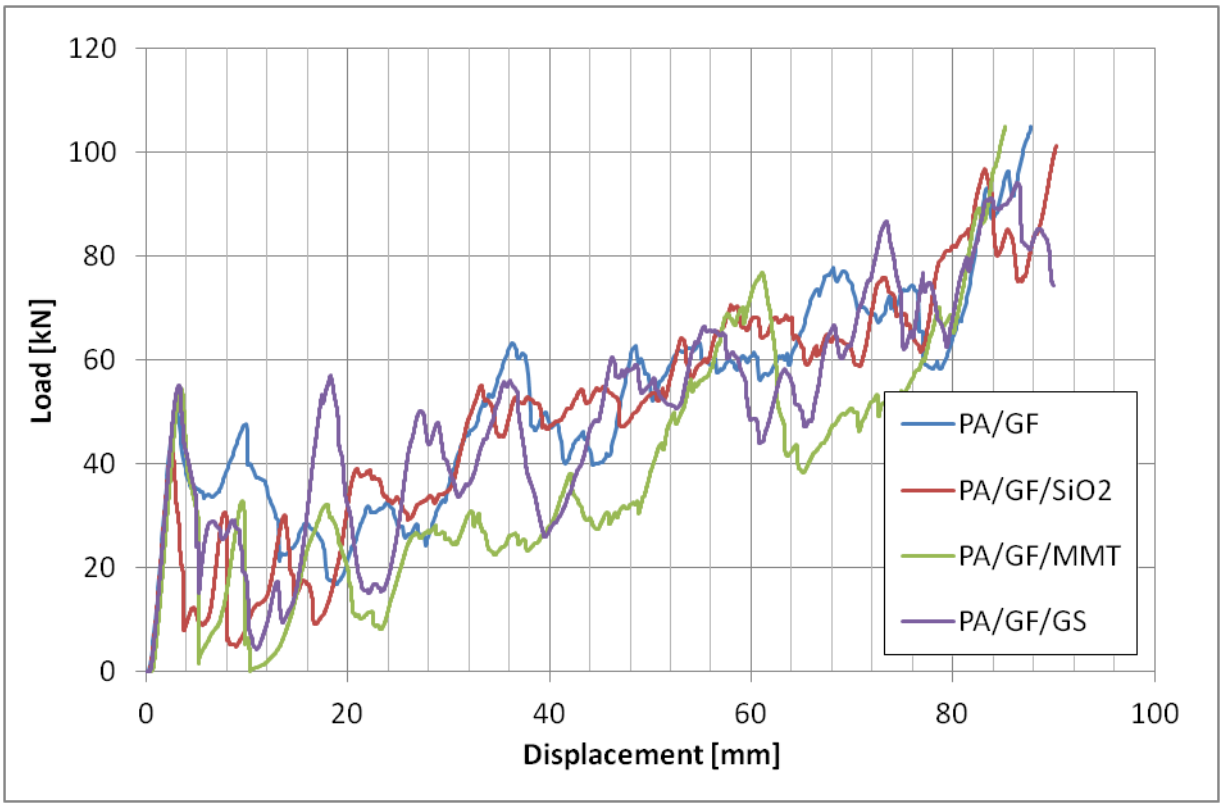

Figure 48 Static load-displacement curves - PA composites

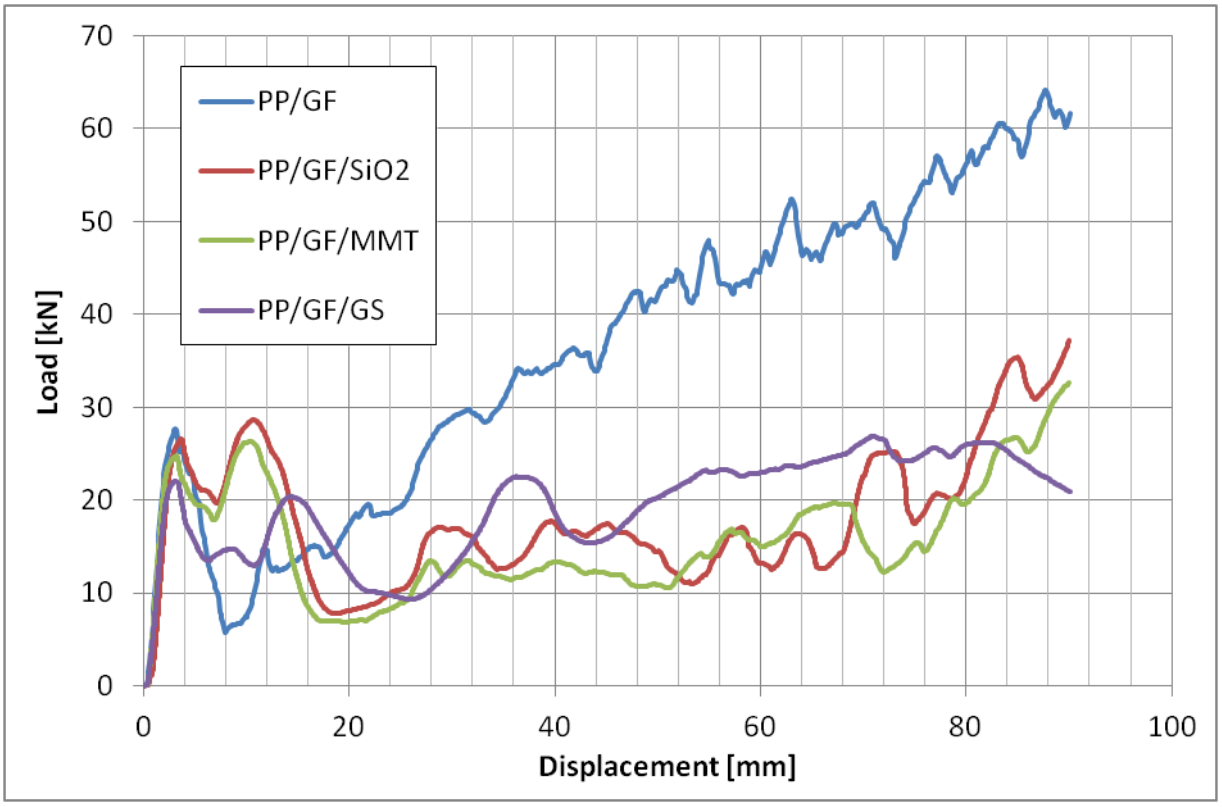

Figure 49: Static load-displacement curves - PP composite

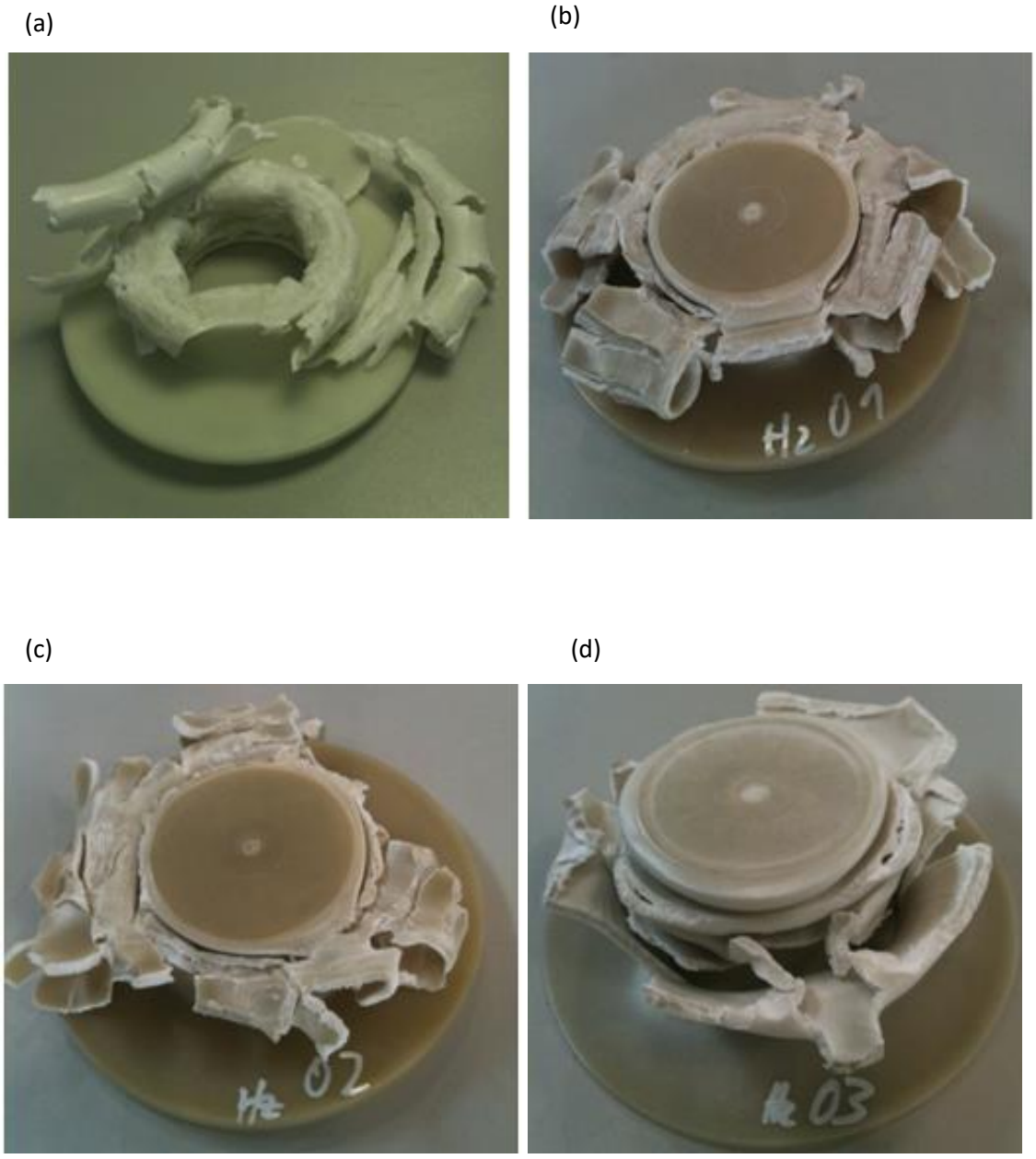

Figure 50: Static collapse mode of PP composites (a) PA/GF (b) PA/GF/SiO_2 (c) PA/GF/MMT (d) PA/GF/GS

(a) (b)

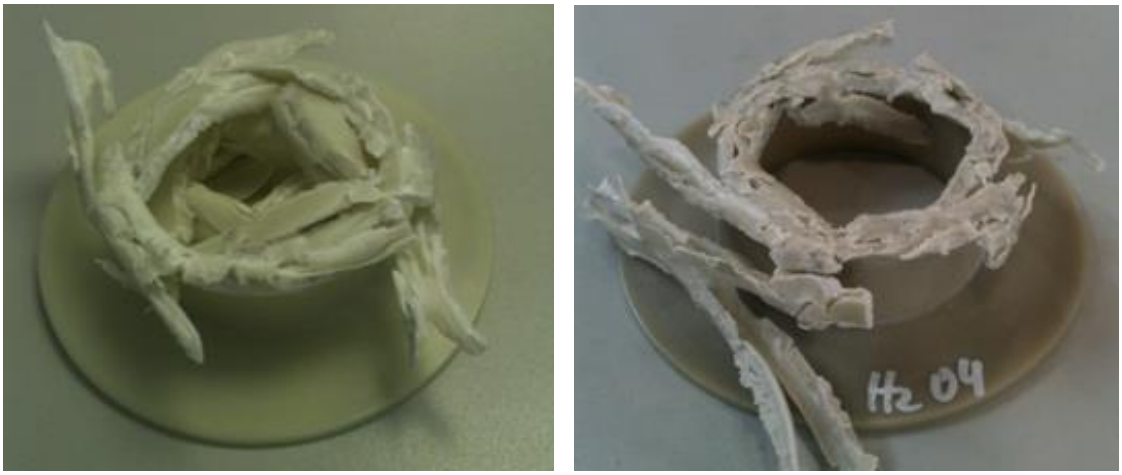

(c) (d)

Figure 51: Static collapse mode of PA composites a) PA/GF (b) PA/GF/SiO_2 (c) PA/GF/MMT (d) PA/GF/GS

4.3.2 Dynamic crash test

The energy absorption capability and crashing characteristics of the composite conical structures were investigated by means of a dynamic drop weight crash test. The structures were tested at two different impact energy levels: 3kJ and 6kJ. As the catastrophic failure was observed in the structures made from PA/GF and PA/GF/MMT composites at 3kJ impact energy, they were not tested at 6kJ to prevent damage of the data acquisition equipment. The dynamic load displacement curves measured during the tests are presented in Figure 52 to Figure 59. Pictures showing the condition of all the structures after the dynamic crash tests are presented in Figure 60 and Figure 61. It is important to note that drop weight impact tests are load controlled, with predefined impact energy. Hence, the SEA parameter is a function of both total energy absorbed and crashing length (see Table 13 and Table 14).

Table 13 and Table 14 show that that the energy absorption capability of the PP based composites decreased in the presence of the secondary fillers. The initial load peak and the mean crashing loads both decreased, whereas the crashing length increased after adding any of the fillers. Despite the decreased initial and mean crushing loads, the increase in crushing length caused that more (total) energy was absorbed by the composites with secondary fillers. However, the SEA parameter of these composites decreased, indicating that they were less effective in the impact energy absorption. This was a consequence of the negative balance between the total energy absorbed and the crushing length (i.e. the increase in the total energy absorption did not compensate the increase in crushing length). A small improvement in SEA was only observed in the PP/GF/SiO_2 composite, tested at 3kJ impact energy. This was due to a positive balance between the total energy absorbed by the structure and the crashing length (i.e. the increase in the total energy abortion compensated the increase in the crushing length).

Regarding the PA based composites, the effect of SiO_2 and GS fillers, on the energy absorption capability of the structures was positive (increase in SEA by 34.9% and 69.2% respectively), whereas the effect of MMT filler was negative (decrease in SEA by 7.6%). The net PA/GF composite failed in a brittle manner, characterized by low mean crashing loads, and large crashing length. This failure mode was less effective in the impact energy absorption, what was measured as a lower value of the SEA parameter in relation to the PP based composites.

The brittle behaviour of the PA based composite was diminished by the presence of SiO_2 particles. The initial peak load in PA/GF/SiO_2 was slightly reduced in relation to PA/GF composite. However, the mean crashing loads were significantly higher, leading to an increase in the total energy absorbed. Therefore, the increase in SEA parameter, due to SiO_2 filler, was caused by a combination of the reduction in the crashing length and the increase in the total energy absorbed by the structure.

In the case of PA/GF/GS composite, the value of the initial peak load, as well as the mean crashing loads, were significantly increased due to the high strength of the material. For the same reason, the material was able to effectively resist the crashing loads, leading to a significant decrease in the crashing length. This is why, despite the total energy absorbed by the stature decreasing after adding the GS fillers, the SEA parameter was significantly higher in relation to the neat PA/GF composite.

In the case of the MMT filled composite a combination of high strength and brittleness, induced a high initial load peak, but low mean crashing loads, similar to neat PA/GF composite. Furthermore, even higher brittleness led to a total failure of the structure, resulting in a significant increase in crashing length. A combination of large crashing length and unaffected total energy

absorbed resulted in a drop of SEA parameter, after adding the MMT filler to PA/GF composite.

It is also important to note that the SEA value was at a similar level in the composites tested at both low and high impact energies. A difference is only visible in the total energy absorbed, which is a natural effect of the different impact energies. This proves that the SEA parameter is able to effectively quantify the energy absorption capability of the structure, despite the difference in the initial loading conditions. However, a discrepancy was observed in the SEA values of PA/GF/SiO_2 composites tested at low and high energies. The explanation of this phenomenon can be found by analysing the fracture mechanism of this composite. The initial failure of the PA/GF/SiO_2 composite is caused by an extensive plastic deformation, which results in medium size debris detaching from the structure. This is visible on the graph as a flat low load period, right after the initial peak. Subsequently, a gradual increase in the load is observed, representing progressive crashing of the structure. This period corresponds to a stable fracture, resulting in small size debris detaching from the structure. The energy absorption effectiveness is much higher at this stage. Consequently the structure which remains longer in the stable fracture stage will have a higher SEA parameter. From the load displacement curves it can be seen that the ratio of the stable to unstable period is much higher in the structure tested at high impact energy.

Table 13: Dynamic crashing characteristics at 3kJ impact

Material	Crash length [mm]	Failure mode	Initial peak [kN]	Mean crashing load [kN]	Energy absorbed [kJ]	SEA [kJ/kg]	Change in SEA [%]
PPGF	29	I	115.3	83.45	2.25	145.11	-
PPGF/SiO_2	31	I	111.4	104.09	2.45	147.21	1.4
PPGF/MMT	36	I	102.5	80.36	2.54	129.94	-11.7
PPGF/GS	35	I	99.61	63.12	2.66	136.28	-6.5
PAGF	72	II	128.4	37.41	2.52	43.23	-
PAGF/SiO_2	55	III	123.7	56.27	2.76	66.434	34.9
PAGF/MMT	75	II	258.8	30	2.5	40.188	-7.6
PAGF/GS	22	III	269.6	104	2.02	140.38	69.2

Table 14: Dynamic crashing characteristics at 6kJ impact

Material	Crash length [mm]	Failure mode	Initial peak [kN]	Mean crashing load [kN]	Energy absorbed [kJ]	SEA [kJ/kg]	Change in SEA [%]
PPGF	61	I	99.81	102.75	5.87	156.4	
PPGF/SiO_2	51	I	104.1	91.43	4.51	146.39	-6.8
PPGF/MMT	58	I	101.8	89.87	5.21	145.8	-7.3
PPGF/GS	62	I	90.01	96.9	5.29	129.35	-20.9
PAGF	-	II	-	-	-	-	
PAGF/SiO_2	68	III	130.6	95.26	5.15	93.307	53.7
PAGF/MMT	-	II	-	-	-	-	
PAGF/GS	51	III	232.6	97.77	5.66	140.49	69.2

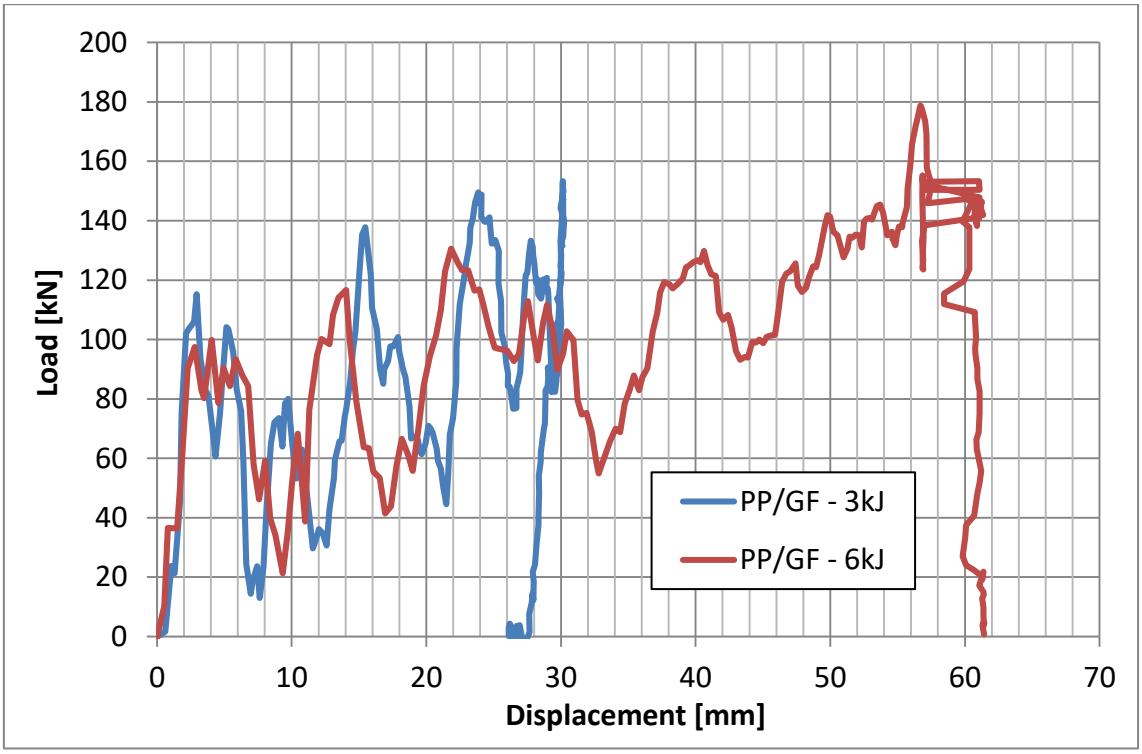

Figure 52: Dynamic load-displacement curves - PP/GF composite

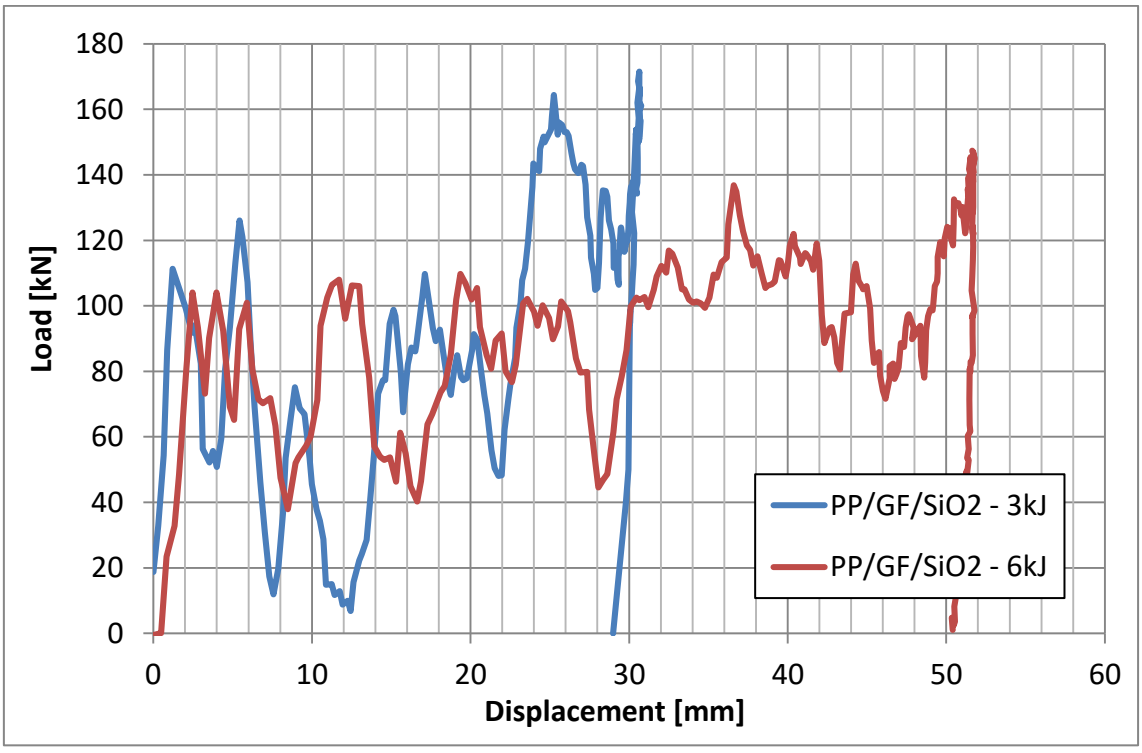

Figure 53: Dynamic load-displacement curves - PP/GF/SiO_2 composite

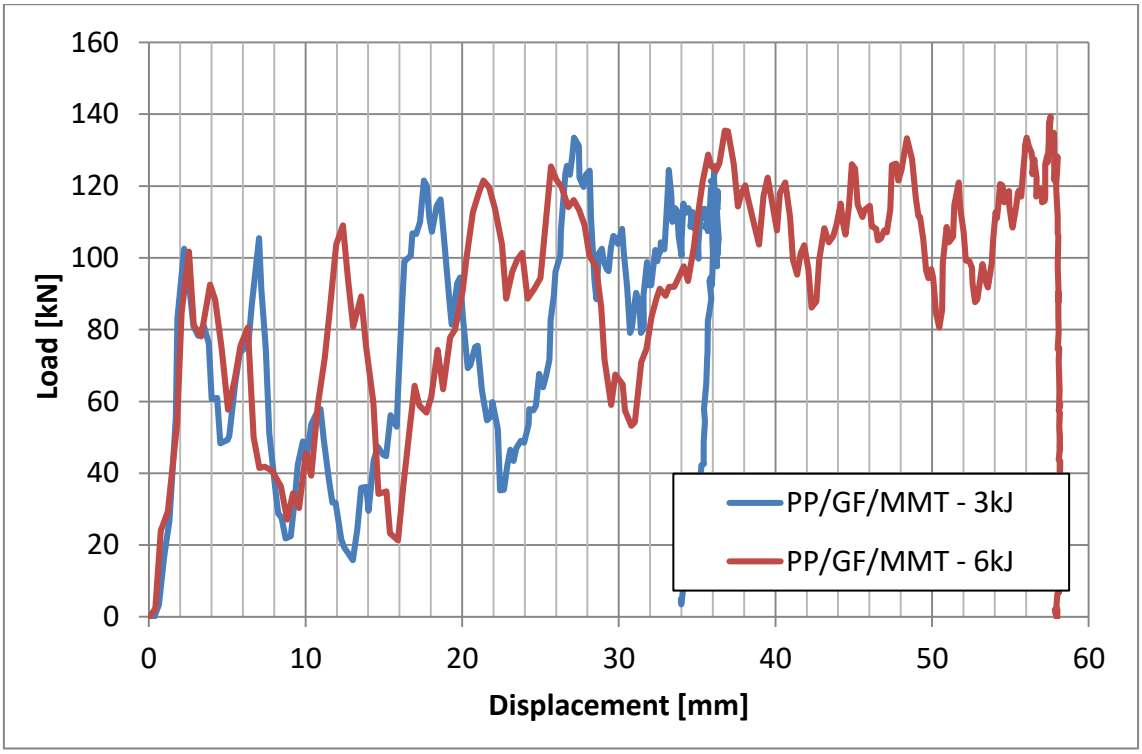

Figure 54: Dynamic load-displacement curves - PA/GF/MMT composite

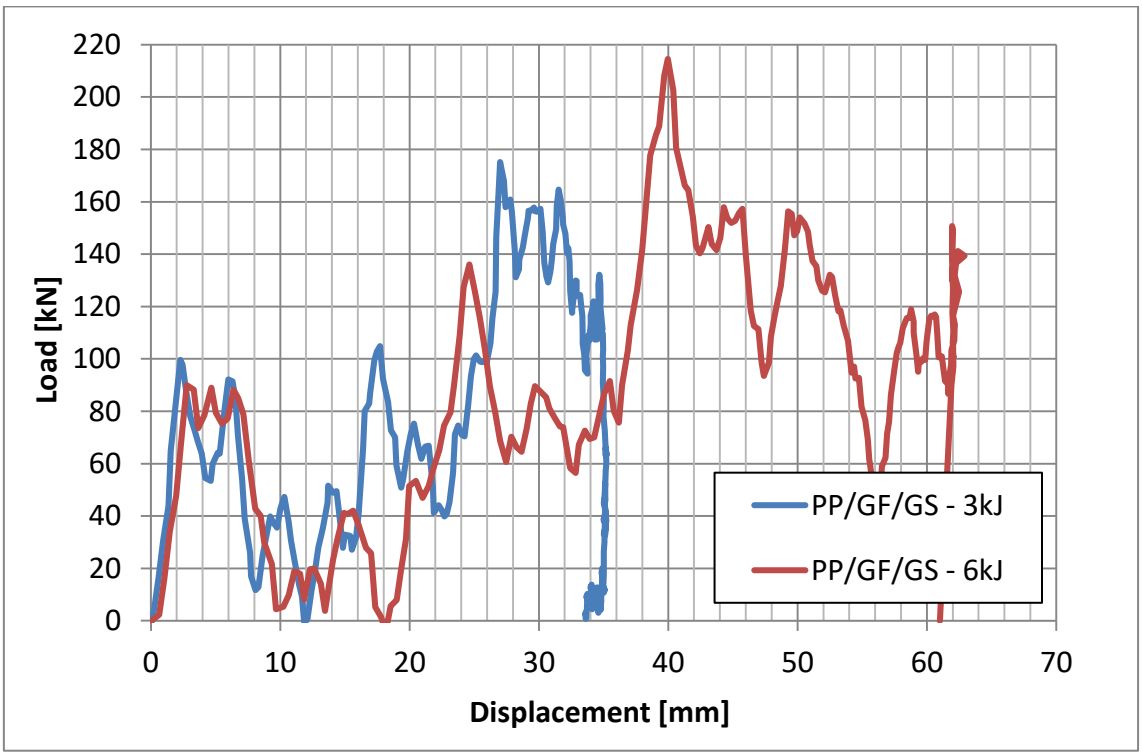

Figure 55: Dynamic load-displacement curves - PP/GF/GS composite

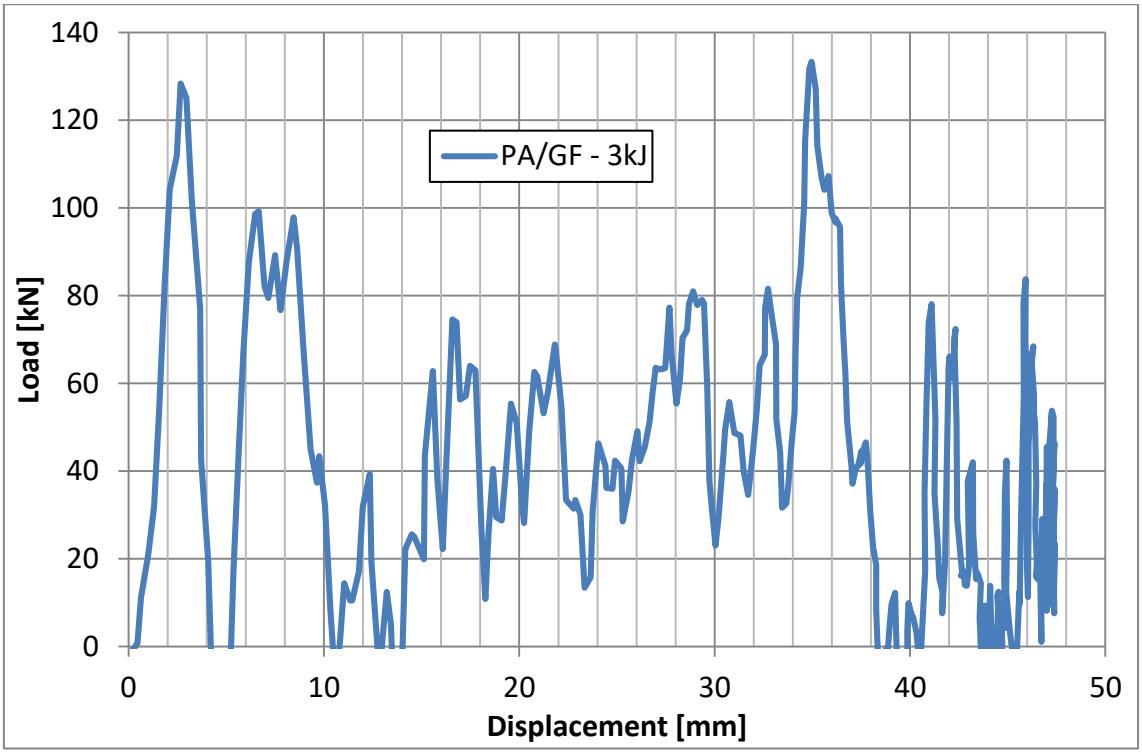

Figure 56: Dynamic load-displacement curves - PA/GF composite

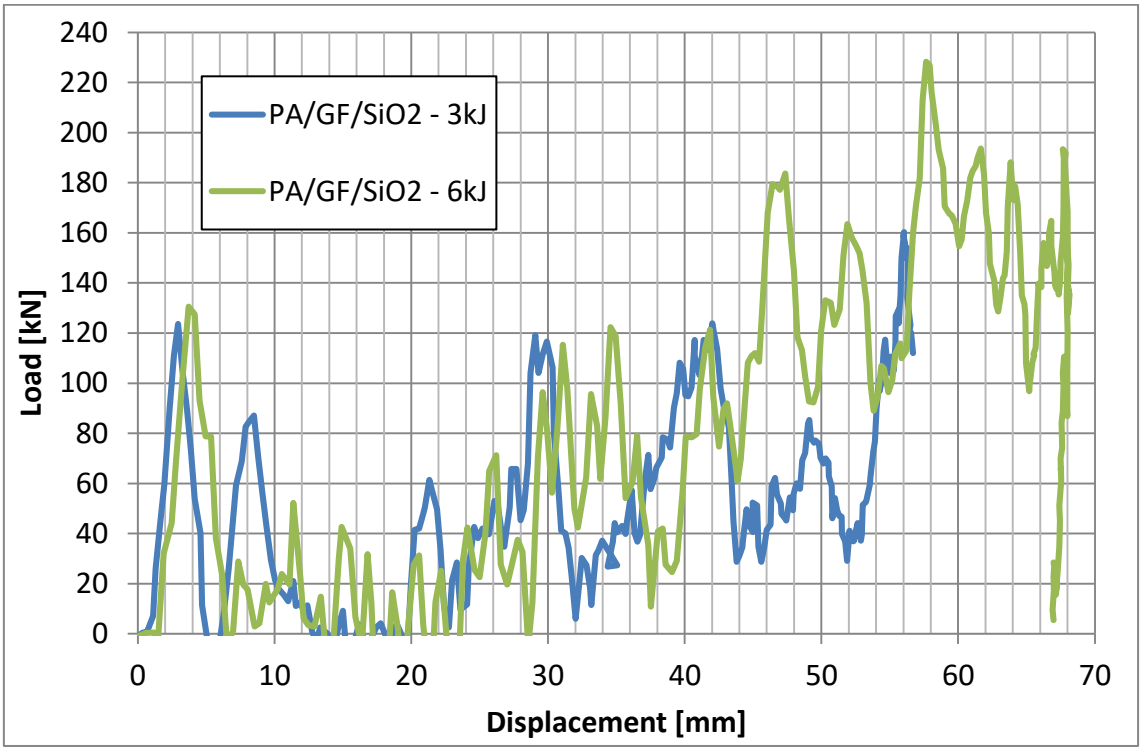

Figure 57: Dynamic load-displacement curves - PA/GF/SiO_2 composite

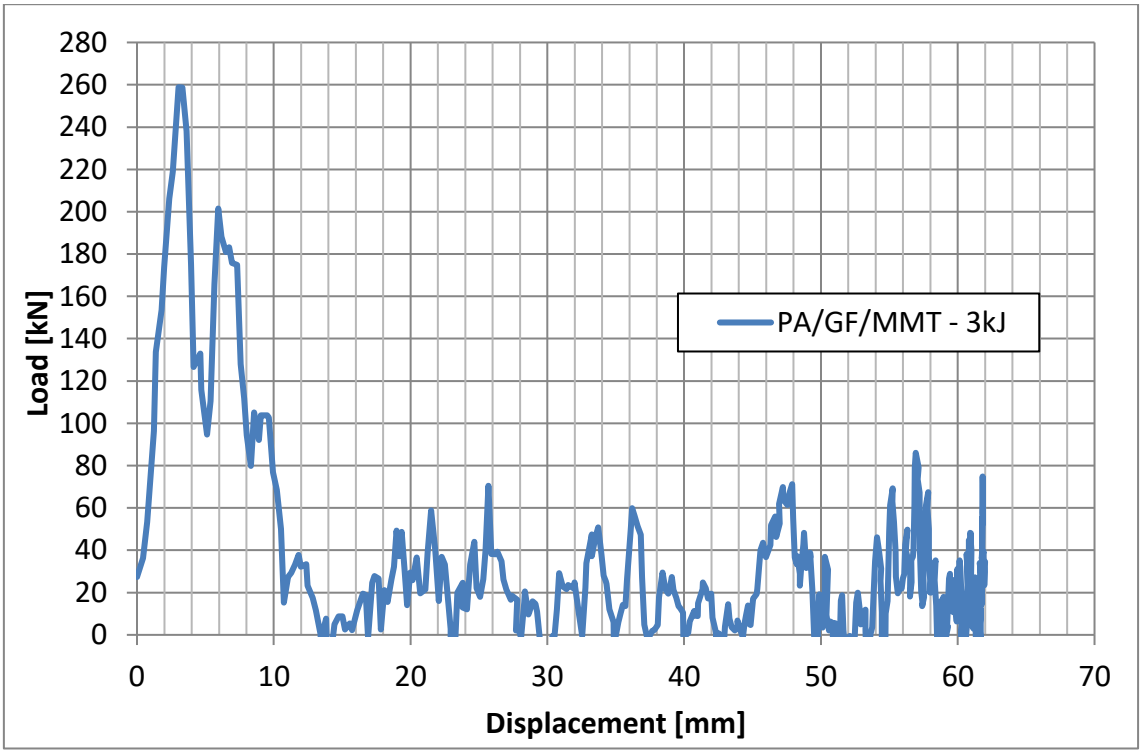

Figure 58: Dynamic load-displacement curves - PA/GF/MMT composite

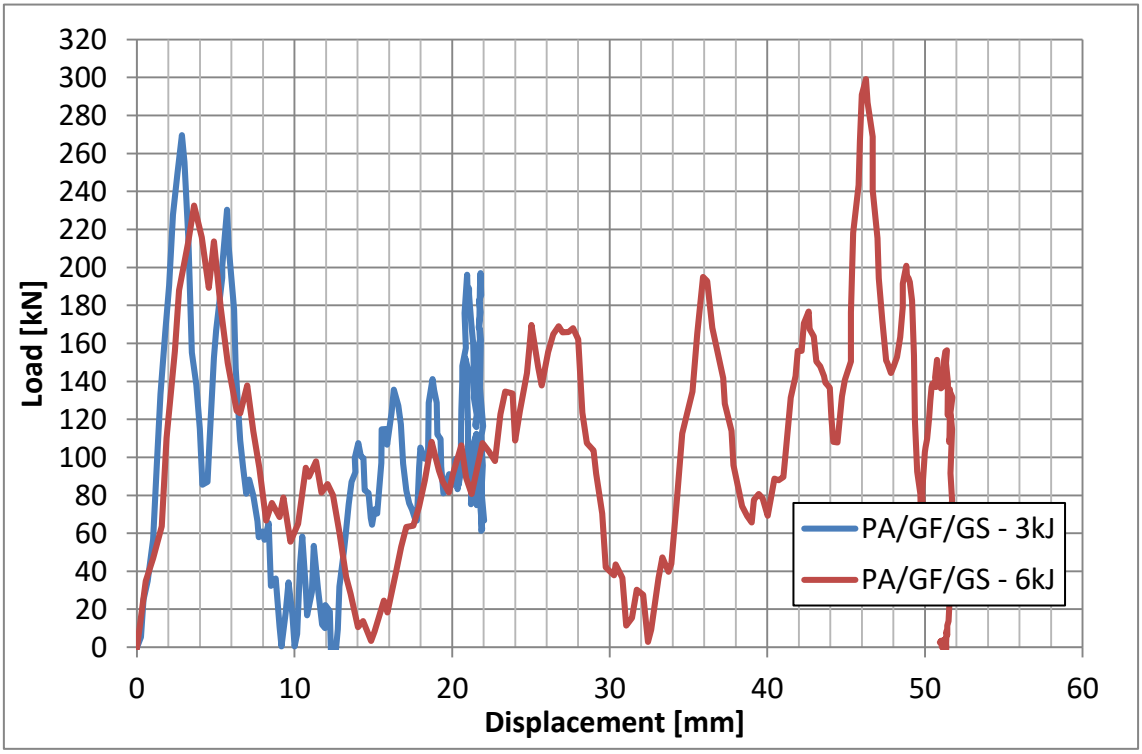

Figure 59: Dynamic load-displacement curves - PA/GF/GS composite

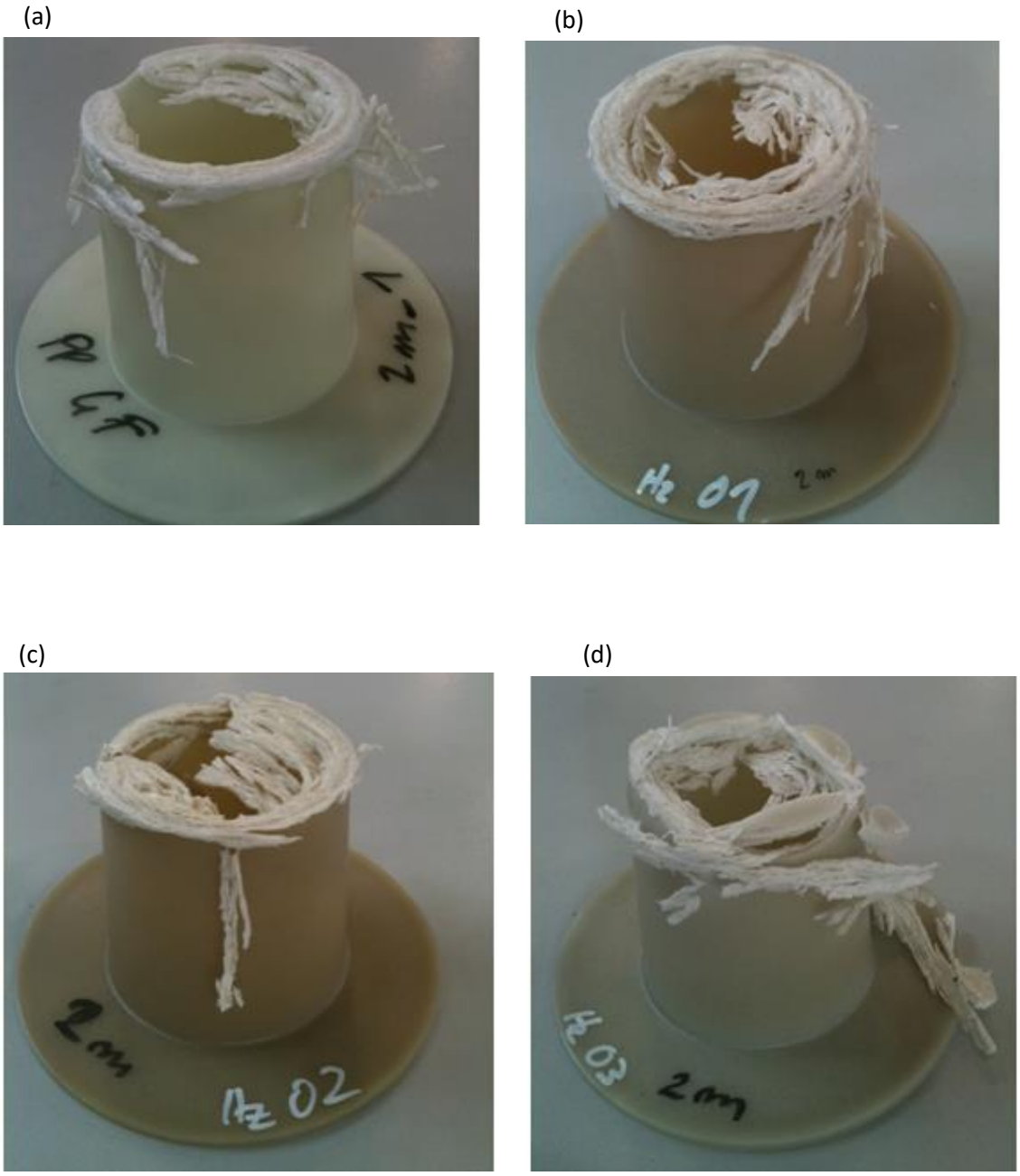

Figure 60: Dynamic collapse mode of PP composites at 3kJ (a) PP/GF (b) PP/GF/SiO_2 (c) PP/GF/MMT (d) PP/GF/GS

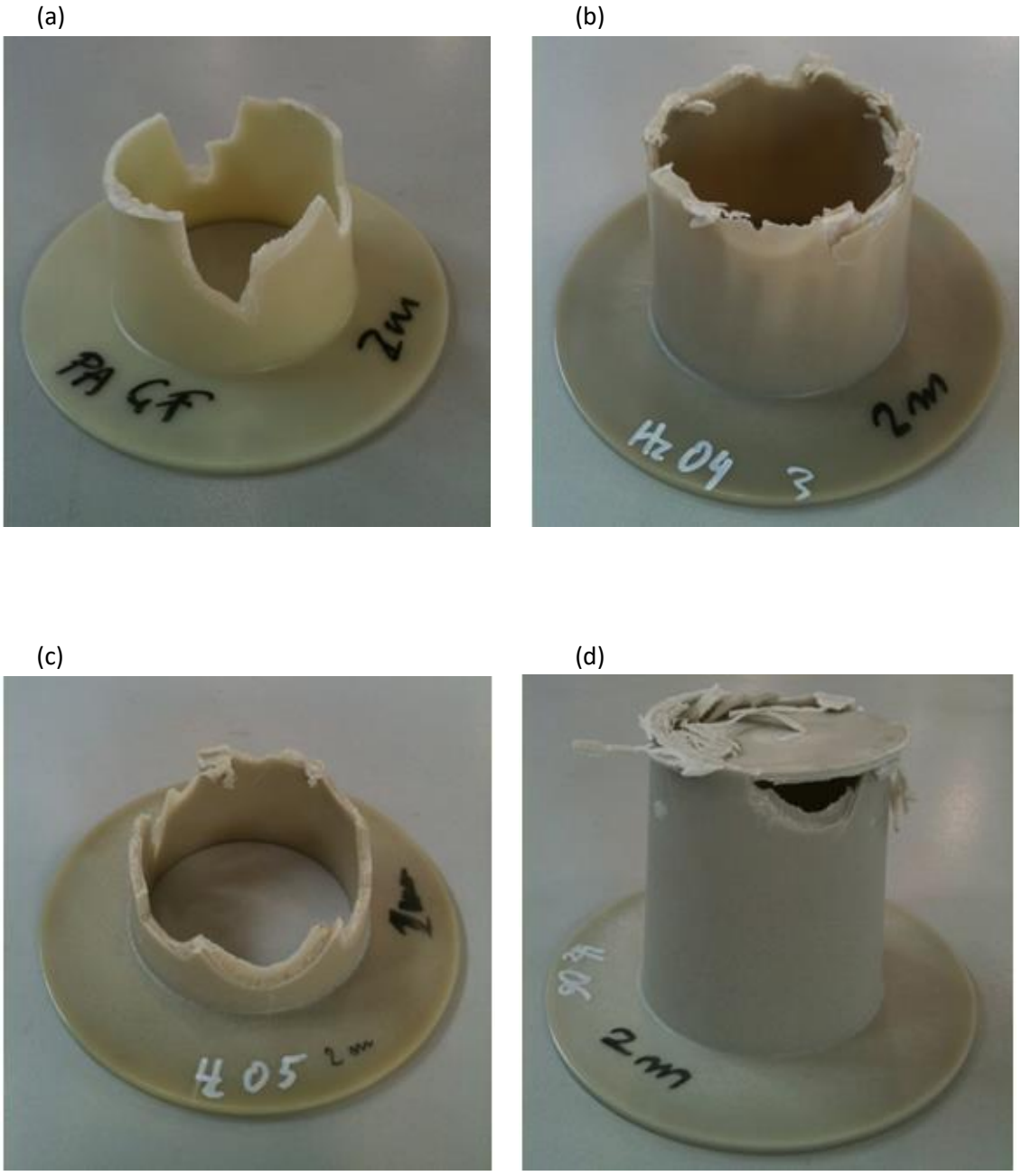

Figure 61: Dynamic collapse mode of PA composites at 3kJ (a) PA/GF (b) PA/GF/SiO_2 (c) PA/GF/MMT (d) PA/GF/GS

(a)

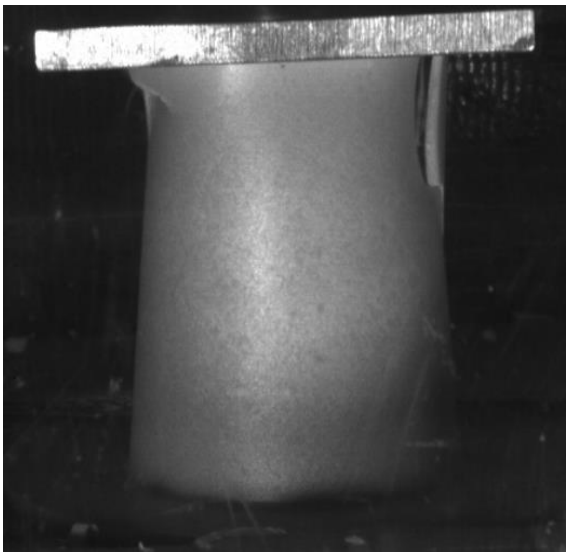

(b)

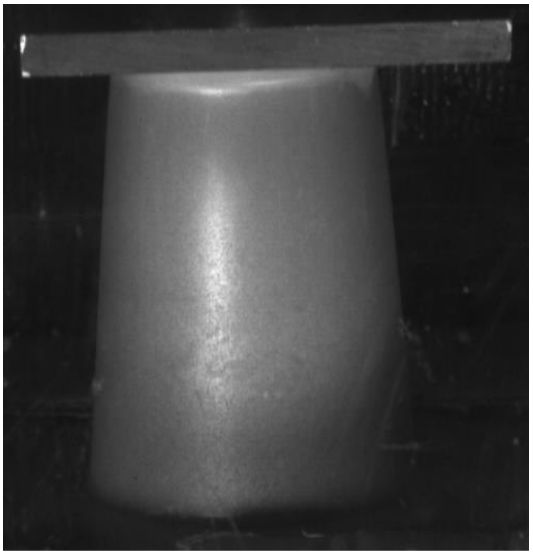

(c)

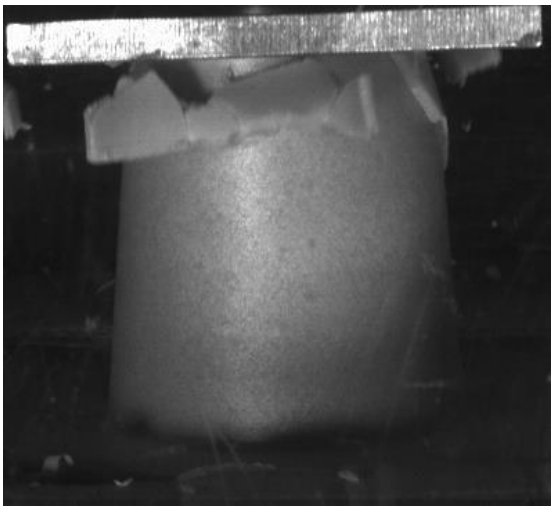

(d)

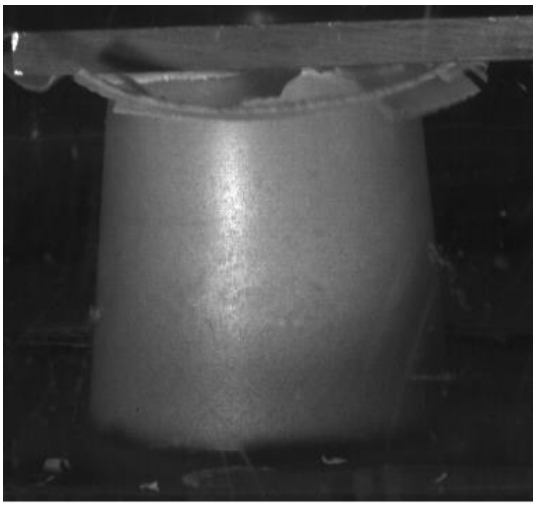

Figure 62: High speed camera records for 3kJ impact (a) PA/GF/MMT [t=2ms] (b) PP/GF/SiO_2 [t=2ms] (c) PA/GF/MMT [t=14ms] (d) PP/GF/MMT [t=14ms]

4.3.3 SEM and EDX analysis

The fracture surface of the conical samples tested under the dynamic load was examined using SEM. Figure 63 shows the micrographs of several PP-based composites. From these pictures it was possible to observe that the failure mode was a combination of matrix and fibre cracking, fibre pull-out and debonding. Very little plastic deformation of the matrix was visible, as there are no characteristic deformation paths and fibrous texture of the material. Conversely, a significant debonding and pull-out of the glass reinforcement was visible, with clean and smooth surface of the glass, what is a proof for poor interfacial adhesion. This observation indicates that the fracture at the interface was prevalent. Comparing the micrographs of nano-reinforced PP/GF and neat PP/GF composites, insignificant difference in the failure mode can be observed. This indicates a small influence of the secondary reinforcement on the mechanical behaviour of the PP composites.

The fracture surface of PA-based composites is presented in Figure 64. The difference in the failure mode in relation to PP-based composites is evident. The fracture is dominated by matrix and fibre cracking, with a distinct lack of fibres pull-out and debonding. The glass reinforcement is covered with polymer residuals, which is a sign of good interfacial adhesion. Moreover, there is a visible difference in the fracture mode between various PA composites. In neat PA/GF and PA/GF/SiO_2 composites the plastic deformation of the matrix is the most evident. An extensive plastic deformation is clearly visible in PA/GF/SiO_2 as non-smooth texture and characteristic deformation paths, indicating an increase in material's ductility. Contrary, in PA/GF/MMT and PA/GF/GS composites, the plastic deformation of the matrix is reduced, as a result of the transition to more brittle failure. This is visible as smooth texture and less evident deformation paths on the surface of the polymer.

Additional information about the composite materials was obtained with EDX analysis. Table 15 shows chemical elements found within the composites region. As the matrix in all samples is made from the polymer, mainly carbon elements were found. Traces of silicon elements where found in the matrices of some composites, indicating presence of silica based nano-material or glass within the polymer. Investigation of the glass reinforcements showed existence of elements such as: silica, oxygen, sodium and calcium. The EDX analysis did not explain the small particles visible on the fibres and polymer surface, despite the fact that silica elements were found, as these could be either separated nano particles or small pieces of the polymer mixed with the nano-material.

Table 15: Chemical Elements Content [%]

Material	Reinforcement						Matrix					
Ch. Element	C	O	Na	Al	Si	Ca	C	O	Na	Al	Si	Ca
PP/GF	0.0	43.3	0.0	7.1	25.6	15.3	89.9	0.0	0.0	0.0	0.0	0.0
PP/GF/SiO2	-	-	-	-	-	-	86.7	0.0	0.0	0.0	2.6	1.3
PP/GF/MMT	12.9	48.4	0.0	6.0	20.9	11.7	96.8	0.0	0.0	0.0	3.2	0.0
PP/GF/GS	13.3	44.3	7.4	0.0	25.8	4.2	100	0.0	0.0	0.0	0.0	0.0
PA/GF	0.0	33.3	0.0	7.5	26.5	19.3	100	0.0	0.0	0.0	0.0	0.0
PA/GF/SiO2	18.1	33.2	0.0	5.5	21.3	15.3	94.2	0.0	0.0	0.0	1.0	0.0
PA/GF/MMT	12.3	31.3	0.0	7.0	26.4	18.2	100	0.0	0.0	0.0	0.0	0.0
PA/GF/GS	0.0	57.9	0.0	0.0	42.0	0.0	100	0.0	0.0	0.0	0.0	0.0

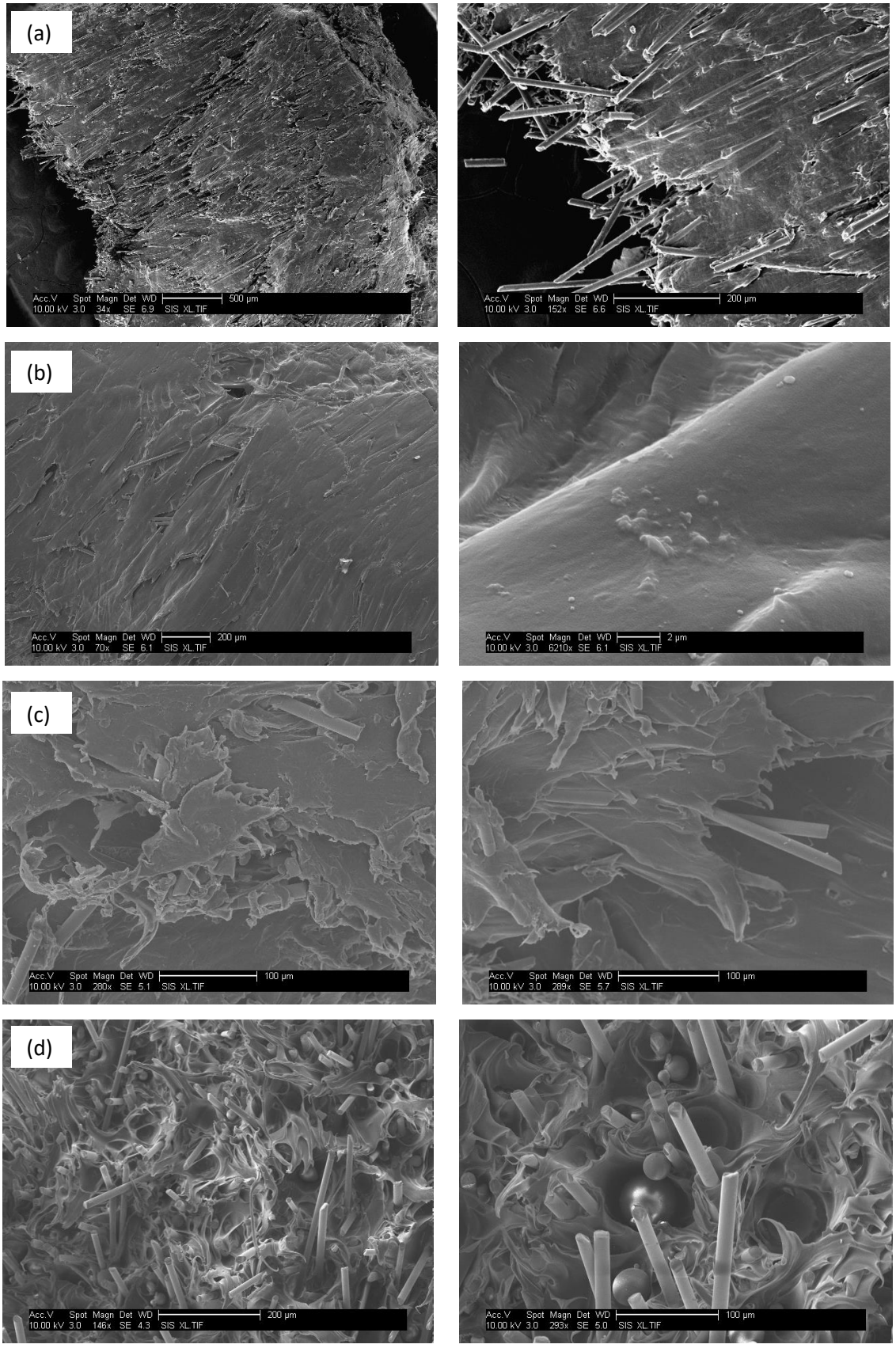

Figure 63: PP composites: (a) neat, (b) SiO_2, (C) MMT and (d) GS

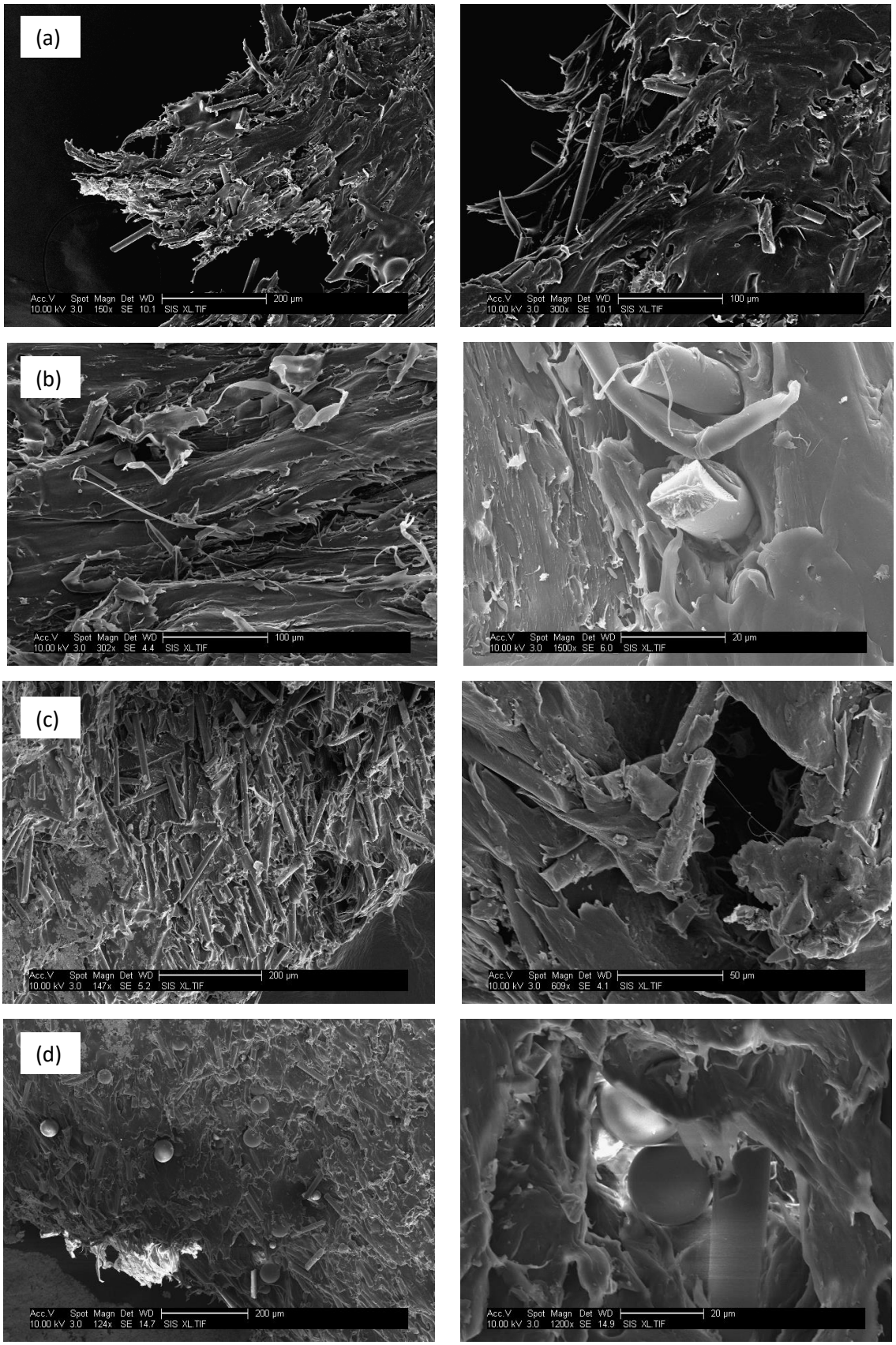

Figure 64: PA composites: (a) neat, (b) SiO_2, (C) MMT and (d) GS

4.4 Discussion

Quasi-static and dynamic crash testing of the conical structures was carried out to study the effect of secondary reinforcement on the energy absorption capabilities of polyamide and polypropylene based glass-fibre reinforced composites. Several static and dynamic load-displacement curves were recorded. Furthermore, failure of the structures was investigated with high speed camera and SEM. The most important observations from these experiments are discussed in detail in the following sections.

4.4.1 Failure modes

The mechanism of crack initiation and propagation was found to have a strong impact on the failure mode induced in the structure. The difference in the failure modes was identified by the visual comparison of the crashed samples (see Figure 60 and Figure 61), microscopic observation of the fracture surface (Figure 63 and Figure 64), as well as failure propagation visible on the high speed video records (example shown in Figure 62). As a result the following fracture modes were identified and classified:

Mode I - Progressive crashing with micro-fragmentation and delamination. This fracture mode corresponds to stable and progressive folding of the sample walls. The energy is dissipated throughout extensive delamination and debonding of the fibres. Local cracks initiate near the crashing zone. Furthermore, small fragments of the fractured material are being pushed both inside and outside from the cone wall. This mode was observed in all PP materials tested under dynamic load (see Figure 60), and results in very good energy absorption.

Mode II - Brittle fracture with large fragmentation. This fracture mode corresponds to unstable and catastrophic failure of the sample. Its characteristic part is the formation of large debris due to the propagation of axial cracks.

These cracks are initiated at the early stage of the impact event and cause a significant decrease in post-failure strength and stability of the structure. Mode II indicates low energy absorption capability. It was observed in PA/GF and PA/GF/MMT composites tested under the dynamic load (see Figure 61).

Mode III - Brittle fracture with progressive crashing and medium fragmentation. In this mode propagation of the axial cracks, initiated at the early stage of the impact event, stops quickly after the formation. Therefore, the size of the generated debris is significantly smaller than the debris size observed in Mode II. The propagation is inhibited by the ductility or strength of the material. Additionally, a delamination effect is observed, as a separation of the composite layers. This is why the structure does not suffer catastrophic failure, indicating relatively good energy absorption, compared to Mode II. This mode was observed in PA/GF/SiO_2 and PA/GF/GS composites tested under the dynamic load (see Figure 61), as well as in all PA based composites and PP/GF composite tested under the quasi-static load (see Figure 50 and Figure 51).

Mode IV - Progressive folding with mushrooming effect. In this fracture mode a combination of plastic deformation and progressive crashing is observed. At the early stage of the crash, the structure is subjected to the plastic deformation, which is visible as a mushrooming effect. After the formation of the second fold, axial cracks are initiated leading to a splitting of the shell wall. The cracks are initiated by the radial stress, generated due to the expansion of the wall. This mode is observed in all PP based materials, with the secondary reinforcement, tested under the quasi-static load (see Figure 50).

4.4.2 Energy absorption capability

Relating the energy absorption characteristic with the crashing characteristics, discussed in the previous section, it can be seen that the materials which fail in a progressive manner, with small local cracks induced

(modes I and III), are able to absorb much higher energies than those with large continuous cracks (modes II and IV). This is caused by the fracture mode having a direct influence on the crashing parameters such as crashing length, value of the peak loads and mean crashing load. The crashing length of the structure increases if large cracks and debris are initiated. For the same reason the post-failure strength of the material is also reduced, which is recorded as a decrease in the mean crashing load. As a result the specific energy absorption of the material, which depends on these two parameters, is reduced when failure modes II or IV are observed.

4.4.3 Effect of the strain rate

The effect of testing speed on the energy absorption capability of the polymer composites can be examined by the comparison of the results from static and dynamic crash tests, given in Table 12 to Table 14. An important difference in the energy absorption parameter can be observed between the composites tested under the static and dynamic load. In the static test the energy was the most effectively absorbed in PA composites, whereas in the dynamic test the effectiveness was significantly reduced. In addition, the weakening effect of secondary reinforcement in PP composite samples, tested under the quasi-static load is much more evident than in samples tested under the dynamic load. A similar trend was observed in PA composites, in which the addition of secondary reinforcement resulted in a reduction of the SEA parameter under the quasi-static load, whereas under the dynamic load the SEA parameter increased, due to the secondary reinforcement.

A reason for the large discrepancy in the energy absorbed by the structures under the static and dynamic load is due to the strain rate sensitivity of polymeric materials. At lower strain rates a polymer is usually more ductile, as the molecular chains can reorganize and align with the load applied at low

speed. However, if the load is applied at the high strain rate, the response of the material becomes much more brittle, as the molecular chains do not have enough time to reorganize.

In the carried out experiments, the transition from ductile to brittle behaviour was observed as a change in the energy absorption effectiveness. At low strain rates, weak and flexible PP composites were not able to resist the applied loads. This resulted in the formation of global cracks, initiated by the circumferential stress, which were easily growing with progressing compression (Mode IV). This effect resulted in a decrease in energy absorption capability. At high strain rates PP composites became stiffer and stronger but more brittle. Due to a good balance between the strength, stiffness and brittleness, the structural failure was more localized, as the global cracks induced by circumferential stress could not be so easily initiated (Mode I). This is why the failure was initiated by axial stress rather than circumferential. As a result the energy absorption capability of the PP composites was significantly increased at high strain rates. By contrast, in stiff and strong PA composites, increase in brittleness due to the high strain rate, caused the reduction of the strain limit, leading to the formation of severe cracks (Mode II). The cracks were formatted by an extensive plastic deformation, observed at an early stage of the impact event. With the reduced ductility, the cracks initiated by circumferential stress, could easily propagate into the structure. Consequently, the fracture mode of the material has changed (from Mode III to Mode II) causing a significant decrease in energy absorption capability at high strain rates.

4.4.4 Effect of the matrix material on energy absorption

Comparison of the SEA parameters of all studied materials is presented in Table 12 to Table 14. There is a significant difference, up to three times, in energy absorption capability between the composites made of PP and PA matrices. All PP composites were much more effective in the impact energy

absorption, in relation to PA composites. In order to explain this phenomenon deep studies of the fracture mechanism are required. As it was discussed in section 4.4.1, PP composites fail in a progressive and stable manner, whereas in PA composite the failure is more unstable. This is associated with the mechanical properties of the matrix and fibre-matrix interaction. PP is a material with relatively low strength, whereas PA is a high strength material. Furthermore, interfacial strength of PP based composites is much lower in relation to PA based ones. These differences can be observed at high speed video recordings and SEM micrographs. In PA composites the fracture surface is relatively smooth without delamination and visible fibres coming out from the matrix. Furthermore, the high strength and brittleness of the material causes the cracks and fragmentation, which are larger than in PP composites, reducing the energy absorption capabilities of the material. In the case of PP composites there is a significant delamination with visible fibres coming out from the matrix. The cracks and failure are localized in a close proximity to the impact point and they are not propagating along the structure. Delamination and debonding of the fibres increase the effectiveness of the energy absorption, while at the same time not causing the weakening of the non-crashed section of the structure.

4.4.5 Effect of the filler material on energy absorption

Comparison of the specific energy absorption parameter due to the filler's material is shown in Table 12 to Table 14. Both in the quasi-static and dynamic tests, the secondary reinforcement had a negative influence on the impact behaviour of all PP composites, reducing the value of the SEA parameter.

In PA composites, the SEA parameter increased in SiO_2 and GS reinforced composite, whereas it decreased in MMT reinforced ones. This variation in energy absorption capability is associated with the material stiffness, strength and ductility, which all affect its fracture mode. Neat PA/GF composite failed at

a relatively low load, in a brittle manner with large cracks propagating along the whole structure, induced by the circumferential loads (Mode IV). This resulted in the energy absorbed by the structure being relatively low.

Incorporation of SiO_2 particles has increased the ductility of the material, and therefore, it has changed the way in which it fractures. The brittleness of the material was significantly reduced which was observed as an increase in elongation to brake, determined in the tensile test. As a result the magnitude of circumferential stress and strain, induced in the structure, was insufficient to grow the cracks in the tougher material. This is why the non-crashed section of the structure did not lose structural integrity, resulting in a localized failure mode (Mode III).The opposite behaviour was observed in MMT reinforced composites. In this case the impact strength of the material was increased but at the cost of reduced ductility. This is why the nano-composite became even more brittle than the neat PAGF material. Hence, the circumferential stress and strain reached the maximum allowable limits and the crack propagated along the structure, leading to a complete failure of the sample. As a result the energy absorption capability of the material remained at a similar level, in spite of the increase in strength and stiffness.

The biggest increase in energy absorption capability was found in GS reinforced materials. However, the toughening mechanism was different from that observed in SiO_2 reinforced materials. In this case, both stiffness and impact strength were improved but with reduced ductility. As a result the crashing length of the cone was importantly reduced, due to the high resistance of the material. Hence, the stress and strain did not exceed the allowable limits and the cracks were not initiated in the non-crashed section of the structure.

4.5 Conclusions

Quasi-static and dynamic crashing behaviour of eight different polymer composites were studied in this chapter. It has been shown that the addition of the secondary reinforcement into glass-fibre reinforced polymer composites can have significant influence on the mechanical response of the material. The experiments demonstrate that by changing the matrix and the reinforcement material, it is possible to change the micro-mechanism of failure, and therefore control the energy absorption characteristics of the composite. Furthermore, it has been found that the fracture mechanism is highly dependent on the rate of applied loads.

The observed failure has been divided into four separate modes, due to the size of the cracks and debris initiated during a crash, as well as the corresponding energy absorption capability. The difference in the failure mode was observed after changing the matrix material, filler material or the testing speed.

The obtained results show that the energy absorption capability of PP based composites could not be improved by the addition of secondary fillers. This is a similar behaviour as observed in the uniaxial tensile test. However, in general the PP based composites were found to be more efficient in absorbing the energy of the impact. This is due to their ability to crash progressively, by local failure dominated by debonding and delamination.

Regarding the PA based composites, the effect of SiO_2 and GS fillers on the energy absorption capability was positive, whereas the effect of MMT was negative. The main reason for improved energy absorption capability is the reduced axial cracking of the structure induced by circumferential loads. The extensive cracking observed in the neat PA/GF composite was diminished by the two different mechanisms: firstly, improved ductility of the composite after

the addition of SiO_2 particles and secondly, improved stiffness and strength of the composite after the addition of GS particles. Both mechanisms reduced the cracking of the structure and made failure more localized near to the impact region. This prevented catastrophic failure of the structure, making it more stable and progressive.

The experiments undertaken improved the understanding of the fracture mechanism and correlation between the mechanical properties and mode of fracture of the composite. However, to gain full understanding of the fracture process it is required to conduct detailed FE modelling. It can provide better understanding of how the localized stress, global stress distribution and the stress multiaxiality affect the energy absorption capability of the structure.

5. Development of The Anisotropic Composite Material Model

The response of composite materials to the mechanical loading is a complicated phenomenon which requires advanced and sophisticated numerical models. The accuracy of the model depends on the level of complexity introduced into the constitutive relations, i.e. how precisely the model describes the behaviour of the material. However, the more complex the model is, the more computational power is required to generate the result. This is why an appropriate balance has to be established between the two requirements.

In order to understand the behaviour of hybrid three-phase nanocomposite materials at different loading conditions, a series of experiments was carried out, as described in Chapters 3 and 4. The results of these experiments can be used as an input for a definition of the requirements that the model needs to satisfy, in order to accurately and effectively predict the material response. Furthermore, an extensive literature review has been carried out and presented in Chapter 2, to verify the applicability of the existing theories to the modelling of nanocomposite structures. Based on the experimental results and the literature review, the areas for improvement in relation to the current theories were identified.

The review shown in Chapter 2 demonstrated that the most appropriate and effective method to model structures made of composites materials is macro-scale modelling. This is due to the good balance between the accuracy of the results and the complexity of the model, and therefore, computation time. Furthermore, there are several requirements that have to be satisfied by the model in order to accurately predict the behaviour of the composite, when subjected to elasto-plastic deformation and failure at different strain rates. The experiments indicated features of the numerical model that are crucial for an accurate representation.

The 3-phase composite materials were found to be highly anisotropic, with different yield and failure strength in tension and compression. Furthermore, the materials are subject to biaxial stresses (axial and circumferential), inducing both yielding and failure. Regarding the strain rate sensitivity, the materials were found to have rate sensitive elasticity, plasticity and failure.

There are several material models implemented in Ls-Dyna softw0are which have been used in the past to model polymers and composite materials. Table 16 [5] shows a summary of the standard Ls-Dyna models which could potentially be used for the purpose of modelling of nanocomposite structures.

Table 16: Ls-Dyna material models [5]

Ref. No.	Material Description	S_{rate}	Fail	Aniso	Tens
15	Johnson/Cook Plasticity Model	y	y		y
22	Composite Damage		y	y	y
24	Piecewise Linear Plasticity (Isotropic)	y	y		
54	Composite Damage with Chang Failure		y	y	y
55	Composite Damage with Tsai-Wu Failure		y	y	y
58	Laminated Composite Fabric		y	y	y
59	Composite Failure (Plasticity Based)		y	y	y
103	Anisotropic Viscoplastic	y	y	y	
158	Rate-Sensitive Composite Fabric	y	y	y	y
161	Composite MSC	y	y	y	y
162	Composite MSC	y	y	y	y

S_{rate} – Strain rate effects

Fail – Failure criteria

Aniso – Anisotropic/orthotropic

Tens – Tension handled differently than compression in some manner

It can be seen that only the last three models appear to fulfil all the defined minimum requirements. However, the model 158 is available only for the shell elements, which cannot be effectively used when variable wall thickness is considered. Thus, material models 161 and 162 are the most suitable models from the list in Table 16. However, these models are based on a damage mechanics approach, which has been developed to predict softening behaviour after damage initiation. In this formulation, after a period of elastic deformation, damage starts to form in the material causing a decrease in load carrying capability of the material. This is represented by the reduced stiffness matrix. Damage based models are well suited for modelling of unidirectional or woven laminates, where no significant plastic deformation is observed. The response of short-fibre composites is associated with extensive plastic deformation before the material fails. This is observed as a highly nonlinear stress-strain curve. This is why the most appropriate models for these composites should be based on plastic theory. However, none of the plasticity models currently available in Ls-Dyna can fulfil all the requirements to accurately represent 3-phase short-fibre reinforced polymer composite.

This is why the aim of this chapter was to develop a material model to fulfil all those requirements. The model was developed based on anisotropic plasticity with asymmetric yield surface and failure definition based on strain energy density. Furthermore, both elasto-plastic behaviour and failure are strain rate dependant.

The following sections present the theories which have been selected to model the mechanical response of 3-phase composites, as well as the development of new theories required to improve the current capabilities.

5.1 Theoretical Development

5.1.1 Anisotropic composite elasticity

A generalized Hooke's law, relating stresses to strains, for a three-dimensional elastic anisotropic solid can be expressed in the following form:

$$\sigma_i = C_{ij}\varepsilon_j \qquad i,j = 1,\dots,6 \tag{5.1}$$

where σ_i and ε_j are the stress and strain components and C_{ij} is the stiffness matrix. In the general form, the stiffness matrix consists of 36 components. However, due to symmetry, this number reduces to 21 independent components. Furthermore, if the composite material is orthotropic (has three orthogonal planes of material symmetry), this number further reduces to 9 independent components. Therefore, the stress strain relation can be expressed in the following form [10]:

$$\begin{bmatrix}\sigma_{11}\\ \sigma_{22}\\ \sigma_{33}\\ \sigma_{12}\\ \sigma_{23}\\ \sigma_{31}\end{bmatrix} = \begin{bmatrix} C_{11} & C_{12} & C_{13} & 0 & 0 & 0\\ C_{12} & C_{22} & C_{23} & 0 & 0 & 0\\ C_{13} & C_{23} & C_{33} & 0 & 0 & 0\\ 0 & 0 & 0 & C_{44} & 0 & 0\\ 0 & 0 & 0 & 0 & C_{55} & 0\\ 0 & 0 & 0 & 0 & 0 & C_{66}\end{bmatrix}\begin{bmatrix}\varepsilon_{11}\\ \varepsilon_{22}\\ \varepsilon_{33}\\ \varepsilon_{12}\\ \varepsilon_{23}\\ \varepsilon_{31}\end{bmatrix} \tag{5.2}$$

All nine independent components of the stiffness matrix can be expressed in terms of nine independent elastic engineering constants: E_1, E_2, E_3, G_{12}, G_{23}, G_{31}, v_{12}, v_{23}, v_{31}; which are: Young's modulus, shear modulus and poisons ratio respectively; in three different material directions. The components of the stiffness matrix can be calculated using the following expressions [10]:

$$C_{11} = \frac{E_1(1-v_{23}v_{32})}{\Delta} \qquad C_{12} = \frac{E_1(v_{21}+v_{31}v_{23})}{\Delta} \qquad C_{13} = \frac{E_1(v_{31}+v_{21}v_{32})}{\Delta}$$

$$C_{22} = \frac{E_2(1-v_{13}v_{31})}{\Delta} \qquad C_{23} = \frac{E_2(v_{32}+v_{12}v_{31})}{\Delta} \qquad C_{33} = \frac{E_3(1-v_{12}v_{21})}{\Delta} \tag{5.3}$$

$$C_{44} = G_{12} \qquad C_{55} = G_{23} \qquad C_{66} = G_{31}$$

$$\Delta = 1 - v_{12}v_{21} - v_{23}v_{32} - v_{31}v_{13} - 2v_{12}v_{23}v_{31} \tag{5.4}$$

As shown in Section 3.4.5, the composites indicate strain rate sensitivity of the elastic properties. Therefore, in this study, Young's modulus and shear modulus are expressed as functions of strain rate $E_i(\dot{\varepsilon})$, $G_i(\dot{\varepsilon})$, as discussed in Section 5.1.4.

5.1.2 Anisotropic composite plasticity

The most general form of the yield criterion is usually described in terms of stress invariants (I_1, J_2, J_3):

$$f(I_1, J_2, J_{3)} = 0 \tag{5.5}$$

Where I_1 is the first principal invariant of the Cauchy stress, which is directly related to the hydrostatic component of the stress tensor. In theory of plasticity it describes changes in pressure of a material. J_2 and J_3 are the second and third principal invariants of the deviatoric part of the Cauchy stress. J_2 invariant describes the distortional changes in the material, whereas J_3 invariant does not have a physical significance and is usually ignored. The most widely used yield criterion for isotropic materials was proposed by von Misses. It is based on the assumption that the hydrostatic part of the stress tensor does not influence yielding of the material. Therefore, plasticity is a function of only the deviatoric component of the stress tensor. The von Misses criterion is formulated as follows:

$$J_2 = k^2 \tag{5.6}$$

or in terms of Cauchy stress tensor:

$$(\sigma_y - \sigma_z)^2 + (\sigma_z - \sigma_x)^2 + (\sigma_x - \sigma_y)^2 + 6(\tau_{yz}^2 + \tau_{zx}^2 + \tau_{xy}^2) = 2\bar{\sigma}^2 \tag{5.7}$$

where the constant, k, is the yield stress determined in pure shear.

The von Misses yield criterion in stress space is a six-dimensional elliptical surface, which is symmetrical with respect to the space origin. The symmetry of the yield surface, in physical terms, represents an isotropic material, with

equal compressive and tensile yield strengths. However, in many engineering materials yield strength is not equal in each material direction. This is why, in order to account for anisotropy of metals subjected to large plastic strains, Hill [131] proposed an extension of the von Misses criterion. It uses a quadratic function of the stress components to describe pressure insensitive yielding and it has the following form:

$$F(\sigma_y - \sigma_z)^2 + G(\sigma_z - \sigma_x)^2 + H(\sigma_x - \sigma_y)^2 + 2L\tau_{yz}^2 + 2M\tau_{zx}^2 + 2N\tau_{xy}^2 = 1 \quad (5.8)$$

where F,G,...N are parameters describing the state of anisotropy.

Opposite to metals, polymeric composites usually exhibit high pressure dependency of yield. This is observed as higher yield strength in compression rather than in tension. In order to account for these effects, Hoffman [133] proposed a criterion, which is a pressure dependant yield model for anisotropic plastic deformation. It has been developed as an extension of the Hill criterion, by the introduction of the linear terms, describing differences between tensile and compressive strengths:

$$\begin{aligned} &C_1(\sigma_y - \sigma_z)^2 + C_2(\sigma_z - \sigma_x)^2 + C_3(\sigma_x - \sigma_y)^2 + C_4\sigma_x + C_5\sigma_y + C_6\sigma_z \\ &+C_7\tau_{yz}^2 + C_8\tau_{zx}^2 + C_9\tau_{xy}^2 = 1 \end{aligned} \quad (5.9)$$

where C_1...C_9 are nine material parameters describing the state of anisotropy, which can be determined from six uniaxial tension and compression tests and three shear tests. If the yield function $\phi(\sigma)$ is introduced, the Hoffman yield criterion will have the following form:

$$\begin{aligned} \varphi(\sigma) &= \alpha_{23}(\sigma_y - \sigma_z)^2 + \alpha_{31}(\sigma_z - \sigma_x)^2 + \alpha_{12}(\sigma_x - \sigma_y)^2 \\ &+\alpha_{11}\sigma_x + \alpha_{22}\sigma_y + \alpha_{33}\sigma_z + 3\alpha_{44}\tau_{yz}^2 + 3\alpha_{55}\tau_{zx}^2 + 3\alpha_{66}\tau_{xy}^2 - \overline{\sigma}^2 \end{aligned} \quad (5.10)$$

where $\overline{\sigma}$ is an yield strength. When the yield function is $\phi(\sigma) = 0$ then the material starts to yield. The material parameters α_{ij} can be calculated using the following expressions;

$$\alpha_{12} = \frac{\overline{\sigma}^{\,2}}{2}\left(\frac{1}{\bar{\sigma}_x^t\bar{\sigma}_x^c} + \frac{1}{\bar{\sigma}_y^t\bar{\sigma}_y^c} - \frac{1}{\bar{\sigma}_z^t\bar{\sigma}_z^c}\right)$$

$$\alpha_{23} = \frac{\overline{\sigma}^{\,2}}{2}\left(-\frac{1}{\bar{\sigma}_x^t\bar{\sigma}_x^c} + \frac{1}{\bar{\sigma}_y^t\bar{\sigma}_y^c} + \frac{1}{\bar{\sigma}_z^t\bar{\sigma}_z^c}\right)$$

$$\alpha_{31} = \frac{\overline{\sigma}^{\,2}}{2}\left(\frac{1}{\bar{\sigma}_x^t\bar{\sigma}_x^c} - \frac{1}{\bar{\sigma}_y^t\bar{\sigma}_y^c} + \frac{1}{\bar{\sigma}_z^t\bar{\sigma}_z^c}\right) \tag{5.11}$$

$$\alpha_{11} = \bar{\sigma}^2\frac{\bar{\sigma}_x^c - \bar{\sigma}_x^t}{\bar{\sigma}_x^t\bar{\sigma}_x^c} \qquad \alpha_{22} = \bar{\sigma}^2\frac{\bar{\sigma}_y^c - \bar{\sigma}_y^t}{\bar{\sigma}_y^t\bar{\sigma}_y^c} \qquad \alpha_{33} = \bar{\sigma}^2\frac{\bar{\sigma}_z^c - \bar{\sigma}_z^t}{\bar{\sigma}_z^t\bar{\sigma}_z^c}$$

$$\alpha_{44} = \frac{\overline{\sigma}^{\,2}}{3\bar{\sigma}_{yz}^2} \qquad \alpha_{55} = \frac{\overline{\sigma}^{\,2}}{3\bar{\sigma}_{xz}^2} \qquad \alpha_{66} = \frac{\overline{\sigma}^{\,2}}{3\bar{\sigma}_{xy}^2}$$

where $\bar{\sigma}_i^t$ and $\bar{\sigma}_i^c$ are the tensile and absolute compressive yield strengths in each direction of orthotropy, whereas $\bar{\sigma}_{ij}$ denote shear yield strengths.

It is important to note that the Hoffman yield criterion can be easily reduced to other more general yield functions. If the material is isotropic with equal tensile and compressive strengths ($\bar{\sigma} = \bar{\sigma}_x^t = \bar{\sigma}_x^c = \bar{\sigma}_y^t = \bar{\sigma}_y^c = \bar{\sigma}_z^t = \bar{\sigma}_z^c$), then the material parameters are: $\alpha_{12} = \alpha_{23} = \alpha_{31} = \frac{1}{2}$, $\alpha_{44} = \alpha_{55} = \alpha_{66} = 1$, $\alpha_{11} = \alpha_{22} = \alpha_{33} = 0$, and therefore, the Hoffman yield criterion reduces to the von Misses yield criterion (equation 5.7). If the material is anisotropic with equal tensile and compressive strengths ($\bar{\sigma}_x^t = \bar{\sigma}_x^c \neq \bar{\sigma}_y^t = \bar{\sigma}_y^c \neq \bar{\sigma}_z^t = \bar{\sigma}_z^c$) , then the material parameters are $\alpha_{12} \neq \alpha_{23} \neq \alpha_{31} \neq \alpha_{44} \neq \alpha_{55} \neq \alpha_{66}$, $\alpha_{11} = \alpha_{22} = \alpha_{33} = 0$, and therefore the Hoffman yield criterion reduces to the Hill yield criterion (equation 5.8).

As the Hoffman yield criterion captures all the features required to model 3-phase polymer composites, it has been selected for the purpose of this work.

The evolution of the yield surface described by Hoffman criterion is shown in Figure 65.

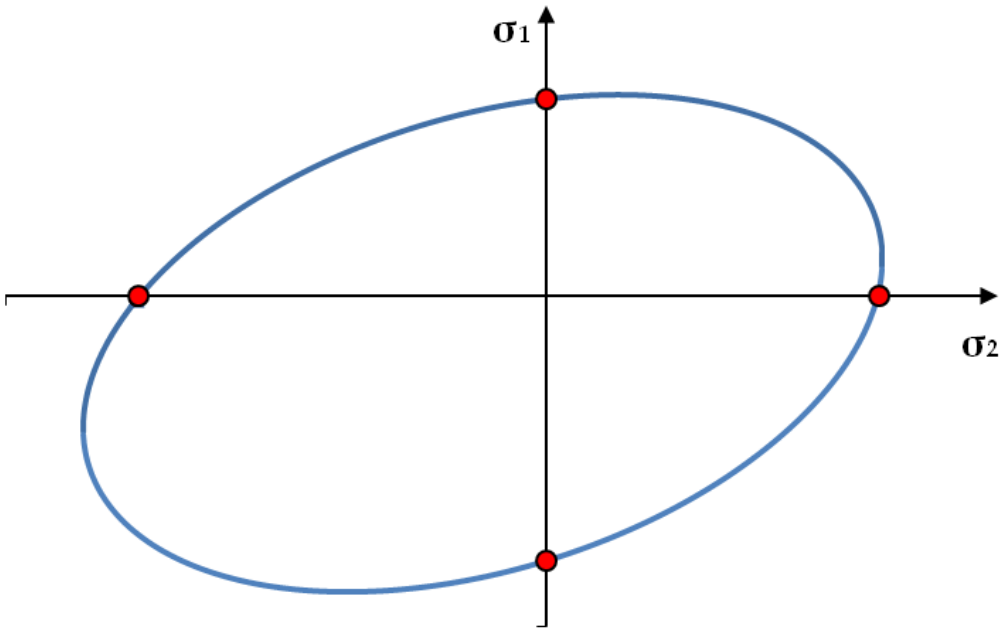

Figure 65: Hoffman's yield surface

5.1.3 Isotropic hardening model

Historically, yield strength of a material was also considered as a failure criterion, with the flow stress being a limiting value of allowable stress. However, in order to describe post yield behaviour of engineering materials, a hardening law is required. This law describes the evolution of yield surface when the material undergoes plastic deformation. In such cases the flow stress $\bar{\sigma}$ in equation 5.10 is no longer a constant, but it is a function of strain, strain rate and temperature. This is why a constitutive equation is needed, which properly describes a nonlinear, strain rate and temperature dependant, stress-strain relationship.

For the purpose of modelling a post yield behaviour of three-phase composite materials the following 2nd order exponential flow rule is proposed:

$$\bar{\sigma}(\bar{\varepsilon}^p, \dot{\varepsilon}) = a(\dot{\varepsilon}) \exp((\bar{\varepsilon}^p + \varepsilon_0)\, b(\dot{\varepsilon})\,) + c(\dot{\varepsilon}) \exp((\bar{\varepsilon}^p + \varepsilon_0)\, d(\dot{\varepsilon})\,) \quad (5.12)$$

where $b(\dot{\varepsilon})$ and $\mathrm{d}(\dot{\varepsilon})$ are strain hardening exponents; $a(\dot{\varepsilon})$ and $c(\dot{\varepsilon})$ are strength hardening coefficients. Both exponents and coefficients are functions of the strain rate $\dot{\varepsilon}$. $\bar{\varepsilon}^p$ is the effective plastic strain and ε_0 is the elastic strain to yield. The hardening parameters can be found by fitting a curve into the stress-strain curve at different strain rates. The use of second order exponential function provides an accurate fit to the highly nonlinear stress-strain curve.

5.1.4 Strain rate and temperature dependence

The importance of strain rate effect on the mechanical properties of the nanocomposites was shown in the series of experiments, as described in Section 3.4.5. It was observed that properties such as elastic modulus, yield strength, ductility and ultimate strength are highly dependent on the rate of applied loads. Hence, to accurately model a dynamic response of the composite structures, it is necessary to include strain rate sensitivity in the material model formulation. There are several different constitutive models that have been proposed in the literature to model strain rate effects. These models can be classified as either empirically or physically based, depending on their principal assumptions. Both types of the models have been described in detail in Section 2.8.1.

For the purpose of this work an empirical constitutive relation, based on a logarithmic function, has been proposed to model the strain rate sensitivity of different material constants. The following constants have been defined as functions of the strain rate:

- Elastic modulus:

$$E(\dot{\varepsilon}) = a_E \ln(\dot{\varepsilon}) + b_E \quad (5.13)$$

- Yield strength:

$$\bar{\sigma}(\bar{\varepsilon}^p, \dot{\varepsilon}) = K(\dot{\varepsilon}) \exp((\bar{\varepsilon}^p + \varepsilon_0)\, A(\dot{\varepsilon})\,) + M(\dot{\varepsilon}) \exp((\bar{\varepsilon}^p + \varepsilon_0)\, B(\dot{\varepsilon})\,) \tag{5.14}$$

Where hardening coefficients (K and M) and hardening exponents (A and B) are defined as functions of strain rate:

$$\begin{aligned} K(\dot{\varepsilon}) &= a_K \ln(\dot{\varepsilon}) + b_K \\ M(\dot{\varepsilon}) &= a_M \ln(\dot{\varepsilon}) + b_M \\ A(\dot{\varepsilon}) &= a_A \ln(\dot{\varepsilon}) + b_A \\ B(\dot{\varepsilon}) &= a_B \ln(\dot{\varepsilon}) + b_B \end{aligned} \tag{5.15}$$

- Strain energy density at failure:

$$U_f(\dot{\varepsilon}) = a_U \ln(\dot{\varepsilon}) + b_U \tag{5.16}$$

The parameters a and b are the rate sensitivity constants which can be determined, based on the experimental data developed at two different strain rates. In this formulation the material constants are linear functions of the natural logarithm of strain rate. This assumption is true for a small range of strain rates (from one to two orders of magnitude). However, as it has been shown through experiments (section 3.4.5) this is not true for a large range of strain rates (higher than two orders of magnitude). Hence, to obtain accurate predictions the parameters a and b need to be calculated separately for each pair of strain rates. A natural consequence of strain rate sensitivity defined in this manner is that the higher the resolution of the strain rates tested, the more accurate the predictions of the material constants achieved.

5.1.5 Failure criterion

Failure of the composite material occurs when both matrix and reinforcement are not able to sustain the applied loads. On the micro scale it is

caused by the matrix and fibre cracking, as well as debonding between the constituents. However, on the macro scale it can be considered as an excessive plastic deformation of the composite material, induced by the applied loads which reached a critical value. The strength limit is usually defined by an appropriate failure criterion which reduces the multi axial loading state into a simple form. Traditionally, material failure criteria for structural components were defined in either stress or strain space. However, neither of the two theories is able to accurately capture the effect of the entire nonlinear plastic stress-strain response of the material on its failure mechanism. This is why in case of highly nonlinear plasticity, the strain energy based criterion is much more relevant, as it takes take into account both stress and strain fields in the failure definition. The most general form of failure criteria for a composite exhibiting non-linear plasticity can be expressed in the following form:

$$f(\sigma, \varepsilon, K) = 1 \tag{5.17}$$

Where f is a scalar function stress (σ) and strain (ε), as well as material properties factor (K).

It has been proved by Sandhu [140] that for an orthotropic material the strain energies along its material axes in both tension and compression as well as shear, are all independent parameters. Based on this observation the author proposed a failure criterion, for a non-linear orthotropic composite material, which combines both stress and strain fields, using the strain energy density. The most general form of Sandhu's model can be written as follows:

$$\sum_{i=1,2,6} \frac{1}{K_i} \left[\int_{\varepsilon_i}^{\cdot} \sigma_i d\varepsilon_i \right]^{m_i} = 1 \tag{5.18}$$

Where σ_i and $\varepsilon_i$are the stress and strain components, m_i defines the shape of the failure surface in the strain energy density space and K_i is a material parameter determined in the uniaxial tests (tension, compression and shear). Sandhu's

model predicts the failure induced by a complex stress-strain state from a series of uniaxial tests. In other words, the Sandhu's failure surface must pass through two points, corresponding to the longitudinal and transverse strengths of a material. However, a failure criterion which also includes a biaxial stress-strain condition, such as the failure surface, and which must pass through three points instead of two, would be much more reliable. This is why an extension of Sandhu's theory is required, to include material parameter which is determined at a complex stress-strain condition, allowing more accurate multiaxial predictions to be made. Based on this requirement a new failure criterion is proposed in the following general form:

$$\sum \beta_i U_i^2 \; + \; \sum \beta_{ij} \, U_i U_j \; = \; 1 \tag{5.19}$$

Where $U_{i,j} = \int_{\varepsilon_{i,j}}^{\cdot} \sigma_{i,j} d\varepsilon_{i,j}$ are strain energy density components, β_i are material parameters determined in uniaxial stress-stain states and β_{ij} are material parameters determined in the multiaxial states-stain state. The subscripts *i* and *j* denote the material directions; their number can vary depending on the state of load. In the derivation of the strain energy based failure criterion the total strain energy density is divided into components with an actual physical interpretation. Subsequently, the components are integrated into one interactive multi-axial failure criterion which defines the failure surface.

If we consider a three dimensional stress-strain state, with three axial components and three shear components, then the strain energy density based failure criterion can be expressed in the following special form:

$$\beta_1 {U_1}^2 + \beta_2 {U_2}^2 + \beta_3 {U_3}^2 + \beta_4 U_4^2 + \beta_5 U_5^2 + \beta_6 U_6^2 \; + \tag{5.20}$$

$$\beta_{12} U_1 U_2 + \beta_{13} U_1 U_3 + \; \beta_{23} U_2 U_3 = 1$$

Where constants β_{1-3} can be determined in uniaxial tensile and compressive tests, in one longitudinal and two transverse directions; constants β_{4-6}can be determined in simple shear tests in three different material directions; β_{12} and β_{13} are coupling parameters, between longitudinal and transverse directions and β_{23} is a coupling parameter between the two transverse directions. The coupling parameters can be determined in a series of biaxial tests.

If the material directions correlate with principal directions (shear stresses are zero), then the failure surface in 2D strain energy density space is an ellipse which passes through three points. It is important to note that the failure surface defined in such form is symmetric (same strength in tension and compression). In order to capture different response of a material in tension and compression the biaxial factors (β_{ij}), must be evaluated separately in each loading case (in different strain energy density quadrants shown in Figure 66. Furthermore, the uniaxial parameters must be determined separately for either tensile or compressive loading case. An example shape of the failure surface defined by the equation 5.20, which passes through eight points determined in the experiment, is shown in Figure 66. The red dots on the plot represent material strengths determined in the uniaxial tests, whereas the green squares represent the strengths determined in the biaxial tests.

It can be seen that the shape of the failure surface consists of four independent ellipses. Each ellipse must pass through three experimental data points. The main advantage of the failure criterion defined in this is form, is that the shape of the failure surface in each quadrant is independent from the strengths in all the remaining quadrants. This allows a better fit into experimental data for a particular loading case.

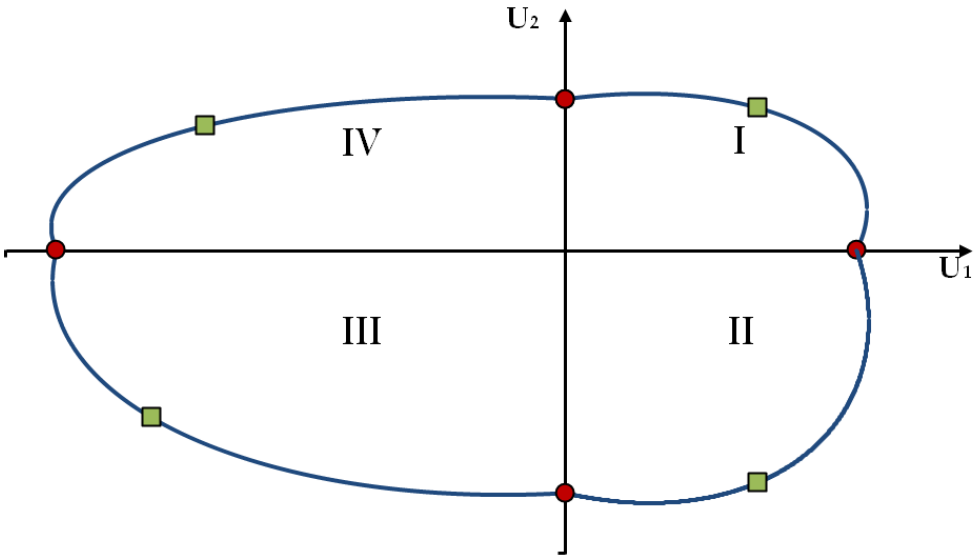

Figure 66: Failure surface in a strain energy density space

For a 2D stress-strain state the following four multiaxial loading conditions must be tested separately to determine all the material parameters:

$$\text{I - } \begin{cases} U_1 > 0 \\ U_2 > 0 \end{cases} \quad \text{II - } \begin{cases} U_1 > 0 \\ U_2 < 0 \end{cases} \quad \text{III - } \begin{cases} U_1 < 0 \\ U_2 < 0 \end{cases} \quad \text{IV - } \begin{cases} U_1 < 0 \\ U_2 > 0 \end{cases} \tag{5.21}$$

Where numbers I, II, III and IV correspond to strain energy density space quadrants, as shown in Figure 66.

If a 3D stress-strain state is considered then the failure surface is an ellipsoid, which can be divided into eight 3D quadrants, or twelve 2D quadrants corresponding to the strain energy density planes U_1-U_2, U_1-U_3 and U_2-U_3. Therefore, for a 3D stress-strain state the following twelve multiaxial loading conditions must be tested separately to determine six uniaxial and twelve multiaxial independent material parameters.

$$\text{I - } \begin{cases} U_1 > 0 \\ U_2 > 0 \\ U_3 = 0 \end{cases} \quad \text{II - } \begin{cases} U_1 > 0 \\ U_2 < 0 \\ U_3 = 0 \end{cases} \quad \text{III - } \begin{cases} U_1 < 0 \\ U_2 < 0 \\ U_3 = 0 \end{cases} \quad \text{IV - } \begin{cases} U_1 < 0 \\ U_2 > 0 \\ U_3 = 0 \end{cases}$$

$$\text{V - } \begin{cases} U_1 > 0 \\ U_2 = 0 \\ U_3 > 0 \end{cases} \quad \text{VI - } \begin{cases} U_1 > 0 \\ U_2 = 0 \\ U_3 < 0 \end{cases} \quad \text{VII - } \begin{cases} U_1 < 0 \\ U_2 = 0 \\ U_3 < 0 \end{cases} \quad \text{VIII - } \begin{cases} U_1 < 0 \\ U_2 = 0 \\ U_3 > 0 \end{cases} \tag{5.22}$$

$$\text{IX - } \begin{cases} U_1 = 0 \\ U_2 > 0 \\ U_3 > 0 \end{cases} \quad \text{X - } \begin{cases} U_1 = 0 \\ U_2 > 0 \\ U_3 < 0 \end{cases} \quad \text{XI - } \begin{cases} U_1 = 0 \\ U_2 < 0 \\ U_3 < 0 \end{cases} \quad \text{XII - } \begin{cases} U_1 = 0 \\ U_2 < 0 \\ U_3 > 0 \end{cases}$$

It can be seen that the shape of the 3D ellipsoid is controlled by the shape of the ellipses defined on the 2D strain energy density planes. In this formulation there is no triaxial coupling parameter, defining an additional point in a 3D space, which the failure surface needs to pass through. This assumption is acceptable for the purpose of this study as the triaxial stress-strain level is negligible in thin-walled structural components.

5.2 Numerical implementation

The anisotropic elastic-plastic material model with failure was implemented into Ls-Dyna software as a user defined subroutine (UMAT). The model combines the anisotropic elasticity with the Hoffman's plasticity model and anisotropic strain energy density based failure criterion. The model was implemented with a rate sensitive elasticity, plasticity and failure within the framework of the theory of rate-independent plasticity. This is one of two most commonly used methods for modelling of rate dependent phenomena, in which the parameters of the model, e.g. yield stress, are scaled based on the strain rate. The second common method is viscoplasticity in which the plastic deformation is assumed to be a viscous flow, driven by excess of the applied stress component over the current static yield stress. More details of the two models are discussed in section 2.8.1.

The Ls-Dyna software uses an explicit time integration algorithm to solve the fundamental conservation equations, based on continuum mechanics. At the

beginning of each time step the software provides increments of strain components, calculated at the previous time step. The function of the user defined subroutine is to calculate the stress components, using these inputs, and output the values together with any history variables defined within the subroutine. The stress state, at the end of the time step, is calculated by means of an integration of the rate constitutive equations, in an incremental procedure. The integration procedure used for the purpose of this work is based on the return mapping algorithm, as proposed by Simo et al. [178] and Ortiz et al. [179]. In this formulation the strain increment is at first assumed to be elastic. Subsequently, using a standard Hooke's law, an elastic stress state (trial stress) is calculated. The actual value of stress is then calculated using a return mapping algorithm (see Figure 67) together with all the other plastic variables. The numerical procedure for integrating the elasto-plastic constitutive equations, for rate independent plasticity with rate dependent flow rule, is explained next.

In the finite element method the stress is updated at the Gauss points with given incremental deformation [179]. The function of the material model is to update the known state variables ε_n, ε_n^p, σ_n (total strain, plastic strain and stress) from a converged state B_n to their corresponding values ε_{n+1}, ε_{n+1}^p, σ_{n+1} at updated state B_{n+1}. To calculate the incremental plastic strain the Prandtl - Reuss flow rule is utilized:

$$\dot{\varepsilon}^{\,p} = \dot{\lambda}\,\frac{\partial\bar{\sigma}(\sigma)}{\partial\sigma} \tag{5.23}$$

Where $\frac{\partial\bar{\sigma}(\sigma)}{\partial\sigma}$ is a vector normal to the yield surface and $\dot{\lambda}$ is a constant known as the 'plastic strain-rate multiplier'.

In order to update the stress state it is therefore required to find the unknown parameter $\dot{\lambda}$. It is important to note that in incremental theory the equivalent plastic strain increment is equal to plastic multiplier:

$$\Delta\bar{\varepsilon}^{p} = \frac{\sigma : \dot{\varepsilon}^{p}}{\bar{\sigma}(\sigma)} = \frac{\sigma : \dot{\lambda}\frac{\partial\bar{\sigma}(\sigma)}{\partial\sigma}}{\bar{\sigma}(\sigma)} = \frac{\dot{\lambda}\,\bar{\sigma}(\sigma)}{\bar{\sigma}(\sigma)} = \dot{\lambda} \tag{5.24}$$

Where $\bar{\sigma}(\sigma)$ is a first order homogeneous function:

$$\bar{\sigma}(\sigma) = \sigma\frac{\partial\bar{\sigma}(\sigma)}{\partial\sigma} \tag{5.25}$$

The main steps in the numerical procedure, to integrate the elasto-plastic constitutive equations, for rate independent plasticity with rate dependent flow rule are as follows:

At first a trial stress is calculated using the Hook's law:

$$\sigma_{n+1}^{(trial)} = \sigma_n + C : \dot{\varepsilon}_{n+1} \tag{5.26}$$

Using this trial stress components, the yield function and its derivative are calculated:

$$\bar{\sigma}_{n+1}^{(trial)} = \bar{\sigma}(\sigma_{n+1}^{(trial)}) \tag{5.27}$$

The size of the yield surface is calculated using the hardening flow rule:

$$H = K(\dot{\varepsilon})\exp((\bar{\varepsilon}^{p} + \varepsilon_0)\,A(\dot{\varepsilon})\,) + M(\dot{\varepsilon})\exp((\bar{\varepsilon}^{p} + \varepsilon_0)\,B(\dot{\varepsilon})\,) \tag{5.28}$$

Subsequently, a check for yielding is performed:

$$\phi_{n+1}^{(0)} = \bar{\sigma}_{n+1}^{(0)} - H^{(0)} \leq 0 \tag{5.29}$$

If the value of the yield function is lower than zero, then the material is elastic and trial stress state is set as a final value. If the yield function is larger than zero, then the material response is plastic, and the trial stress have to be iteratively returned to the yield surface by calculating the plastic multiplier $\dot{\lambda}$ using sub-steps i.

In order to obtain the stress in the next state (n+1) the sequential procedure is utilized:

$$\sigma_{n+1}^{(i+1)} = C : \left[\varepsilon_{n+1} - \varepsilon_{n+1}^{p}\right] \tag{5.30}$$

and since,

$$\varepsilon_{n+1}^{p} = \varepsilon_{n}^{p} + \Delta\varepsilon^{p} \tag{5.31}$$

Then

$$\sigma_{n+1}^{(i+1)} = C : \left[\varepsilon_{n+1} - \varepsilon_{n}^{p}\right] - C : \Delta\varepsilon^{p} \tag{5.32}$$

Combining equations 5.32 and 5.23 we obtain:

$$\sigma_{n+1}^{(i+1)} = \sigma_{n+1}^{(i)} - \dot{\lambda}\left[C : \frac{\partial \bar{\sigma}_{n+1}^{(i)}(\sigma)}{\partial \sigma}\right] \tag{5.33}$$

The only one unknown in the equation 5.33 is $\dot{\lambda}$. As suggested by Simo and Ortiz, the plastic multiplier can by derived by linearization of the yield function around the current values of the state variable, using Taylor's expansions:

$$0 = \phi^{(i)}\left(\bar{\sigma}_{n+1}^{(i)}, \bar{\varepsilon}_{n+1}^{p(i+1)}\right) + \frac{\partial \phi^{(i)}}{\partial \sigma}\left(\sigma_{n+1}^{(i+1)} - \sigma_{n+1}^{(i)}\right) + \frac{\partial \phi^{(i)}}{\partial \bar{\varepsilon}^{p}}\left(\bar{\varepsilon}_{n+1}^{p(i+1)} - \bar{\varepsilon}_{n+1}^{p(i)}\right) \tag{5.34}$$

From equation 5.33

$$\sigma_{n+1}^{(i+1)} - \sigma_{n+1}^{(i)} = -\dot{\lambda}\, C : \left[\frac{\partial \sigma_{n+1}^{(i)}(\sigma)}{\partial \sigma}\right] \tag{5.35}$$

and

$$\bar{\varepsilon}_{n+1}^{p(i+1)} - \bar{\varepsilon}_{n}^{p(i)} = \dot{\lambda} \tag{5.36}$$

Therefore equation 5.34 becomes

$$0 = \phi^{(i)}\left(\bar{\sigma}_{n+1}^{(i)}, \bar{\varepsilon}_{n+1}^{p(i+1)}\right) + \frac{\partial \phi^{(i)}}{\partial \sigma} : \left[-\dot{\lambda}\, C : \frac{\partial \sigma_{n+1}^{(i)}(\sigma)}{\partial \sigma}\right] + \dot{\lambda}\, \frac{\partial \phi^{(i)}}{\partial \bar{\varepsilon}^{p}} \tag{5.37}$$

After transformation, the plastic multiplier can be found from the following formula:

$$\dot{\lambda} = \frac{\phi^{(i)}}{\frac{\partial \sigma^{(i)}(\sigma)}{\partial \sigma} : C : \frac{\partial \sigma^{(i)}(\sigma)}{\partial \sigma} - \frac{\partial H^{(i)}}{\partial \varepsilon^{p}}} \tag{5.38}$$

The complete algorithm of the UMAT is shown in Figure 68.

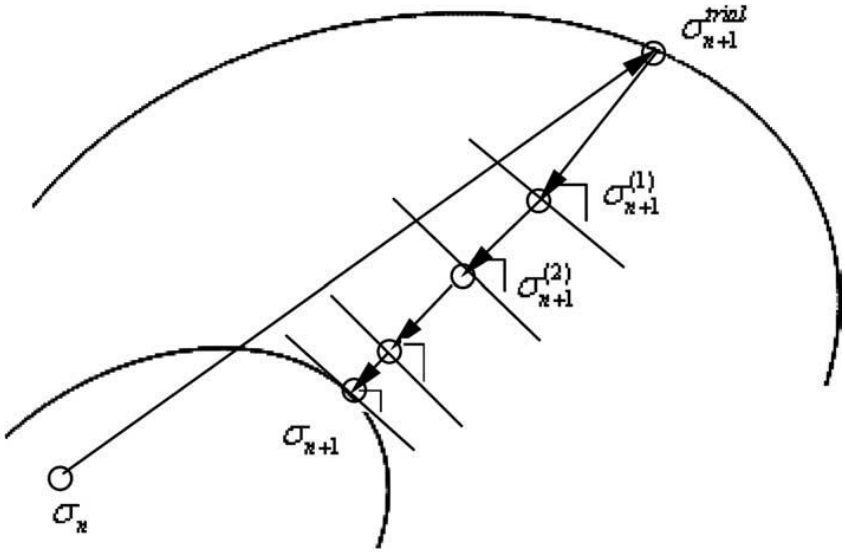

Figure 67: Return of trial stress to yield surface

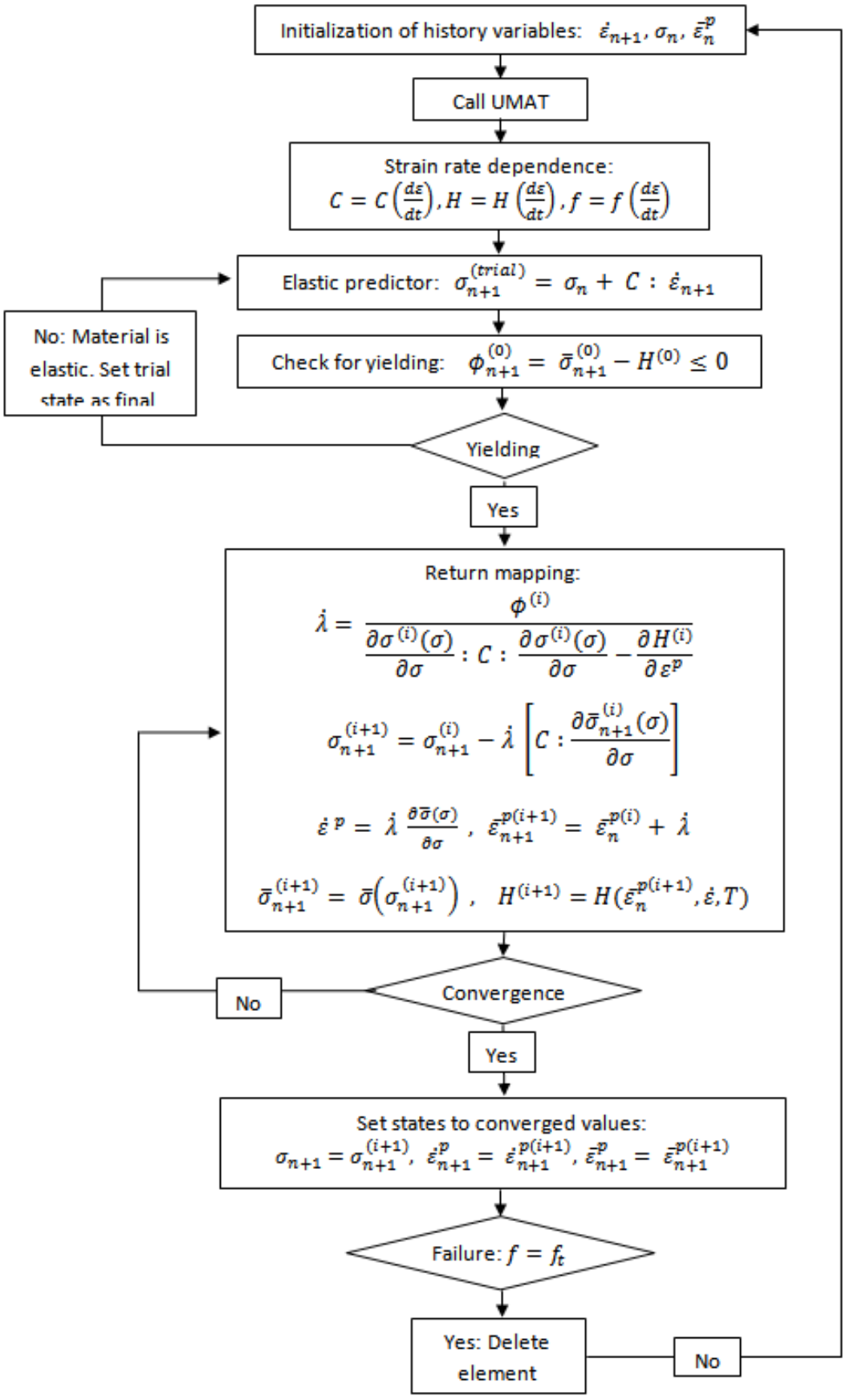

Figure 68: UMAT algorithm

5.3 Conclusions

The mechanical properties and energy absorption capabilities of the 3-phase polymer composite materials were determined in a series of experiments. The results show that the materials are anisotropic and, with highly nonlinear plasticity different in tension and compression, as well as rate sensitive modulus, yield and strength. None of the currently available material models in Ls-Dyna can accurately represent all these requirements. This is why a user defined material model has been developed and implemented into Ls-Dyna. The model incorporates anisotropic elasto-plasticity, with pressure sensitive yield function, based on Hoffman criterion. Furthermore, the hardening is represented by a 2^{nd} order exponential function, which allows an accurate fit into highly nonlinear plasticity data. The failure of the material has been represented by the strain energy density based criterion. With this approach both stress and strain is taken into account in the failure definition. This is a more realistic approach in relation to strength or stain based criteria, which allows better fit into experimental data, especially at multi-axial loading. The strain rate sensitivity has been implemented into definition of elasticity, plasticity and failure. The strain rate dependency of plastic deformation has been implemented within a framework of stain independent plasticity with strain rate dependant yield surface. The stress integration procedure selected for this model is based on a return mapping algorithm. The calibration of the model and the accuracy of its predictions are presented in the following chapter.

6. FE Modelling of the Nanocomposite Structures

The crashing behaviour of the conical structures, subjected to static and dynamic loads, has been investigated and discussed in Chapter 4. The video records of the crashing event provided valuable information on the structural failure mechanism. However, to obtain a full understanding of the fracture mechanism it is required to conduct a detailed FE simulation. This can provide information about the effect of the stress distribution, stress biaxiality and the mechanical properties of the structure, on its fracture response.

For this purpose, an orthotropic elasto-plastic strain rate sensitive material model with strain energy density based failure criterion was implemented into Ls-Dyna, as a user defined material model UMAT (See Chapter 5 and Appendix E). As this model has never been used to model 3-phase composite structures, it requires extensive calibration and validation, to ensure good quality results.

The best improvement in the energy absorption capability was observed in the PA based composite filled with SiO_2 particles. That is why the PA/GF/SiO_2 composite along with standard PA/GF composite were selected for the purpose of the FE modelling. This selection allows comparison of the materials characterized by significantly different failure mode.

The first section of this chapter describes the development of the FE models (geometry, mesh and boundary conditions) of tensile and compression samples, as well as conical structures. The procedure for calibration of the UMAT using the experimental data is presented in section 6.2. The results of the simulated specimen and structural testing are presented and compared to the experimental observations in section 6.3.

6.1 Development of the FE models

The geometry of the specimens and the conical structures was generated using CATIA v5 CAD software and saved as neutral IGES files. In order to generate the mesh and boundary conditions the IGES files were imported to the pre-processor software (HperMesh from Altair HyperWorks 11). The FE simulations were processed with LS-Dyna 971 R4.0 solver provided by Oasys.

The following unit system was used in all models: Length (mm), Time (s), Mass (Ton), Force (N), Energy (mJ) and Stress (MPa). This gives the secondary units as follows: Velocity (mm/s) and Mass Density (Ton/mm^3).

6.1.1 Modelling of the specimen testing

The FE model of the tensile and compression specimens was built using 8-node solid elements. In total, 3440 elements were generated for tensile specimen and 1000 for compression specimen, with four elements through thickness (see Figure 69 and Figure 70). To represent the clamping of the specimens in the grips, the displacements were fully fixed on one side of the specimen using *BOUNDARY_SPC control card. The traction was applied on the other side of the specimen using the control card *BOUNDARY_PRESCRIBED_ MOTION, with a predefined time-displacement curve.

In order to reduce the computation time, the quasi-static tests were carried out with strain rate sensitivity off, using explicit analysis. Furthermore, the testing speed was scaled up, whereas the termination time was scaled down, by a factor of 100. To compare the numerical results with the experimental stress-strain curve a database output was specified using option *DATBSE_SPCFORC, which returns values of boundary SPC reaction forces. This output corresponds to the force measured by the load cell in the actual tests. The reduced input files of tensile and compressive specimens are shown in Appendix A.

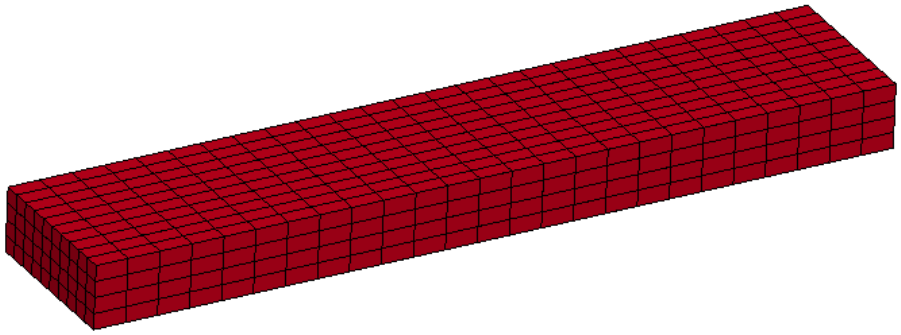

Figure 69: Compression sample FE model

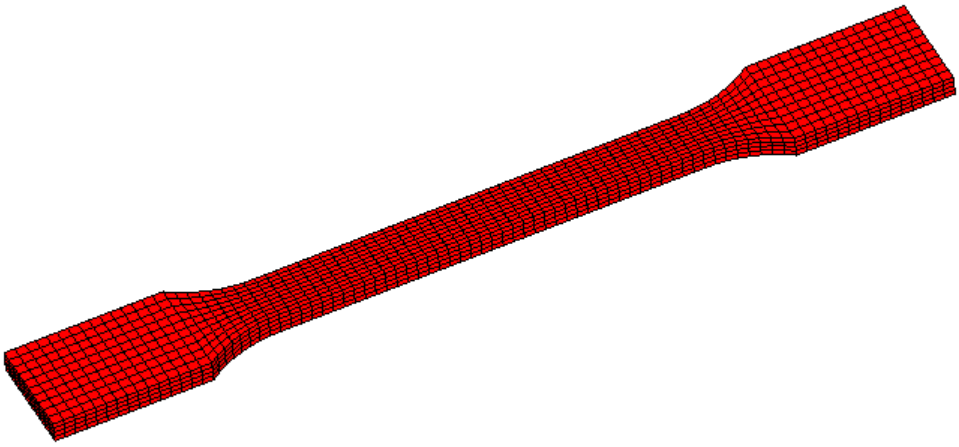

Figure 70: FE model of the tensile bar

6.1.2 Modelling of the quasi-static crash test

The FE model of the crash cone is presented in Figure 71. It consists of 19440 8-node solid elements, with four elements through thickness, required to correctly represent bending of the cone wall. The usage of 3D-elements was required due to the variable thickness of the wall along the cone height. In order to restrain movement of the structure, axial displacement was fixed at the bottom surface of the cone. The compression of the structure was realized by means of rigid wall, progressively moving with constant velocity of 0.1mm/s. A contact between the rigid wall and the cone structure was provided using control card Contact-Eroding-Single-Surface. This formulation was required to ensure that inner elements go into contact with the rigid wall after the erosion of the structure and deletion of the elements on the outer surface. Moreover, to

provide contact between the cone elements, an automatic contact control card was specified. A friction coefficient of 0.3 was used in all types of contact. The hourglassing control card with option one (viscous form) was applied. A default value of 0.1 for hourglass coefficient was used, as recommended in the Ls-Dyna manual [5].For the purpose of the model validation, the RWFORC option in Database control card was specified to plot the reaction forces, which correspond to the load required to compress the structure. The reduced input file of the crash cone FE model is presented in Appendix B.

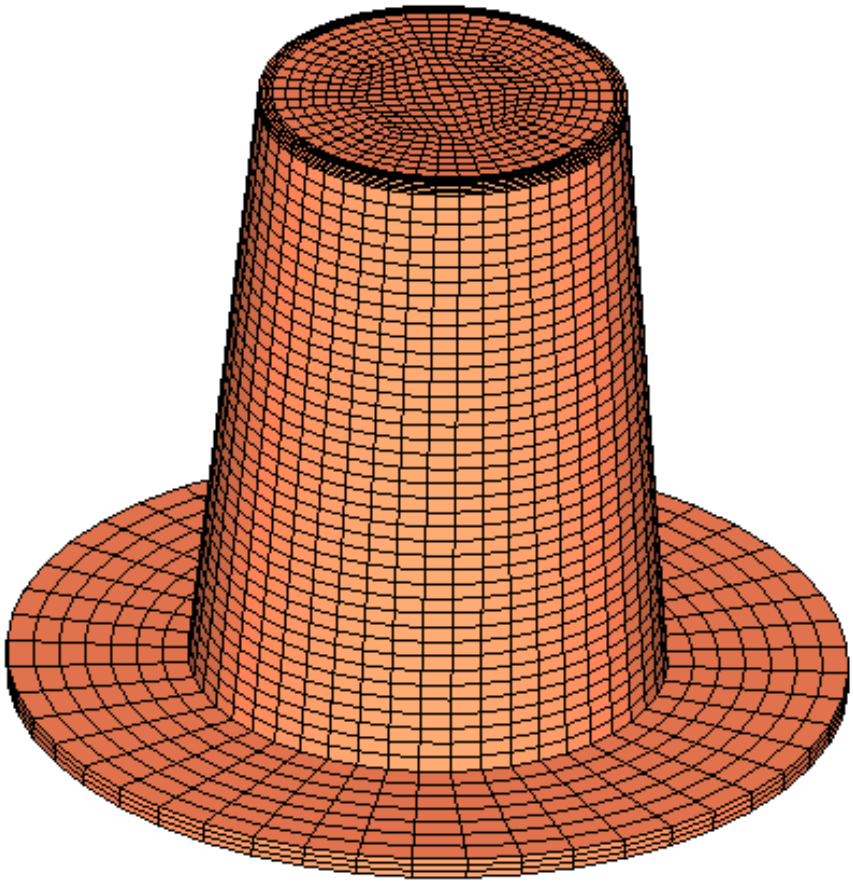

Figure 71: FE model of the quasi-static crash test

6.1.3 Modelling of the dynamic crash test

The FE model of the dynamic crash test is shown in Figure 72. The model consists of three separate components: crash cone, steel plate and impactor. This is an exact representation of the actual drop tower test. The total number of elements (solid 8-node) in the model is 14955. The material response of the cone was represented using the UMAT, whereas for the plate and the impactor the rigid material model was used. The crashing of the sample was realized by means of initial velocity of 6.5m/s applied to the impactor. The contact between the impactor and the plate was defined using a surface to surface contact card. The contact between the plate and the cone was defined using the contact eroding single surface control card. Furthermore, the self-contact between the wall was defined using an automatic contact control card. A friction coefficient of 0.3 was used in all types of contact. For the purpose of the model validation, the RWFORC option in Database control card was specified, to plot the reaction forces, which correspond to the load measured by the load cell. In the first trial run hourglassing was observed on the top surface of the cone (see Figure 73), therefore hourglassing control card with option four (stiffness form) was applied. The best value of the hourglass coefficient was found to be 0.03. It was checked, by the comparison of the stiffness and internal energy of the model, that it has very little influence on the final results and completely removes the hourglassing issue from the model. The reduced input file of the crash cone FE model is presented in Appendix C.

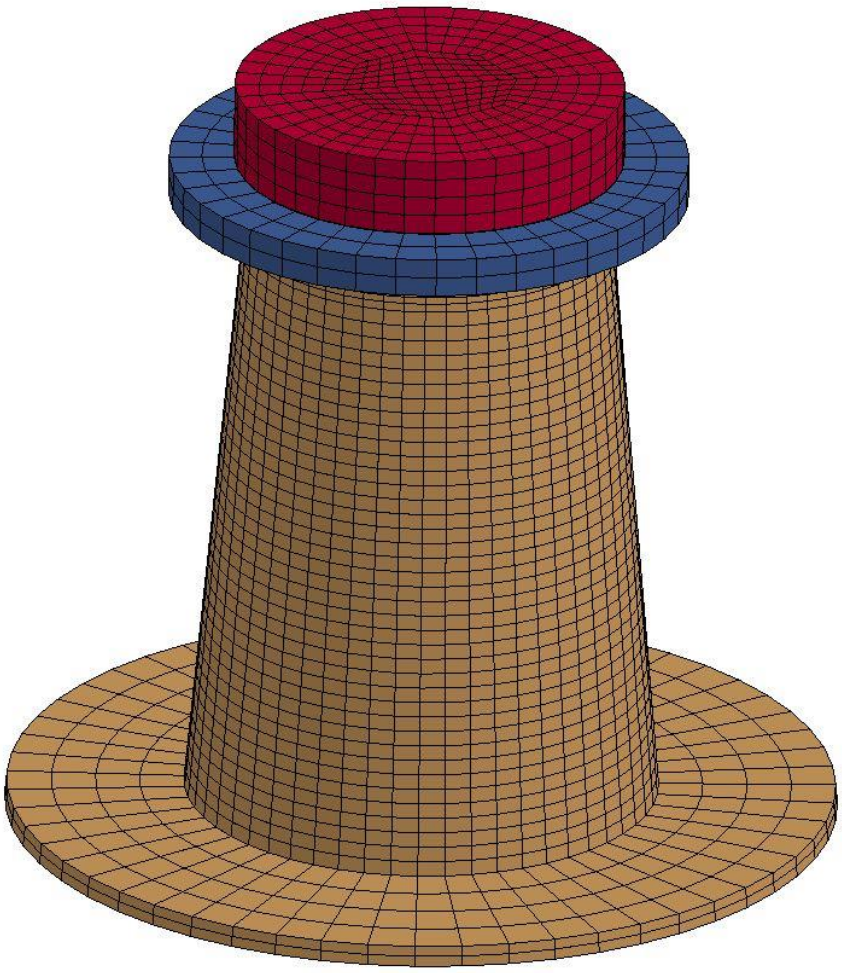

Figure 72: FE model of the dynamic crash test

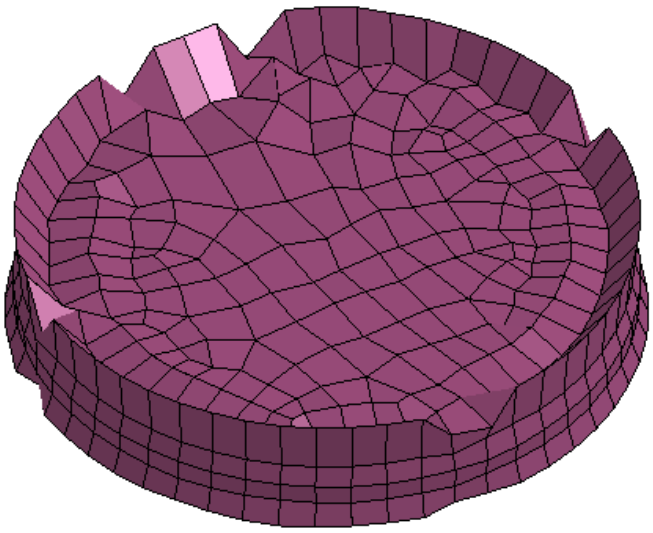

Figure 73: Hourglasing on the top surface

6.2 Material Model Calibration

This section details all the steps carried out to calibrate the UMAT for the purpose of modelling of the composites. The results of the experiments, presented in Chapter 3, were used to determine all the parameters of the model and verify that the selected formulation is appropriate for finite element simulation of 3-phase composite materials and structures.

6.2.1 Orthotropic elasticity

The formulation of the orthotropic elasticity is defined by the stiffness matrix as shown in Section 5.1.1. The stiffness matrix components can be calculated from the following set of equations:

$$C_{11} = \frac{E_1(1 - v_{23}v_{32})}{\Delta} \qquad C_{12} = \frac{E_1(v_{21} + v_{31}v_{23})}{\Delta} \qquad C_{13} = \frac{E_1(v_{31} + v_{21}v_{32})}{\Delta}$$

$$C_{22} = \frac{E_2(1-v_{13}v_{31})}{\Delta} \qquad C_{23} = \frac{E_2(v_{32}+v_{12}v_{31})}{\Delta} \qquad C_{33} = \frac{E_3(1-v_{12}v_{21})}{\Delta} \tag{6.1}$$

$$C_{44} = G_{12} \qquad C_{55} = G_{23} \qquad C_{66} = G_{31}$$

$$\Delta = 1 - v_{12}v_{21} - v_{23}v_{32} - v_{31}v_{13} - 2v_{12}v_{23}v_{31}$$

where E_1, E_2, E_3, are elastic modulus in three material directions; G_{12}, G_{23}, G_{31} are the shear modulus and v_{12}, v_{23}, v_{31} are the Poisson's ratios. The values of the material constants have been determined in the series of tensile tests (see Chapter 3.4), carried out in two different directions (0°- longitudinal and 90° - transverse) and at five different strain rates (0.01, 0.1, 1, 10 and 100 [1/s]). The material is assumed to be transversely orthotropic; therefore, values of the two transverse elastic modulus (E_2 and E_3) and shear modulus (G_{12} and G_{31}) are equal. The elastic properties of PA/GF and PA/GF/SiO_2 materials were derived using a linear fit of the average experimental data, as illustrated in Figure 74 - Figure 77 . This was done in both longitudinal and transverse directions, as well as at all the studied strain rates. The values of the fitted elastic constants, used

in the model, are summarized in Table 17. As the shear tests were not carried out, due to the insignificant shear stresses observed in the conical crash tests, the values of the shear modulus were taken from the literature. This was calculated by finding a ratio between tensile and shear modulus, reported in the literature, of the following composite: BASF Capron® 8233G 33% Glass-Filled Nylon 6 [180]. Each tensile modulus E_1 was divided by the ratio (2.7) to find the value of the shear modulus G. The values of the Poisson's ratio were assumed to be equivalent with the above BASF material.

Table 17: Elastic UMAT parameters

Material	Property	Strain rate [1/s]				
		0.01	0.1	1	10	100
PA/GF	E_1 [MPa]	7167	7833	8667	9667	12167
	E_2 [MPa]	4333	5000	5333	5833	7333
	G_{12} [MPa]	2654	2901	3210	3580	4506
	G_{23} [MPa]	2654	2901	3210	3580	4506
	v_{12}	0.35				
	v_{23}	0.35				
PA/GF/SiO_2	E_1 [MPa]	6800	7600	8333	9167	11167
	E_2 [MPa]	4223	4750	5208	5729	6979
	G_{12} [MPa]	2519	2815	3086	3395	4136
	G_{23} [MPa]	2519	2815	3086	3395	4136
	v_{12}	0.35				
	v_{23}	0.35				

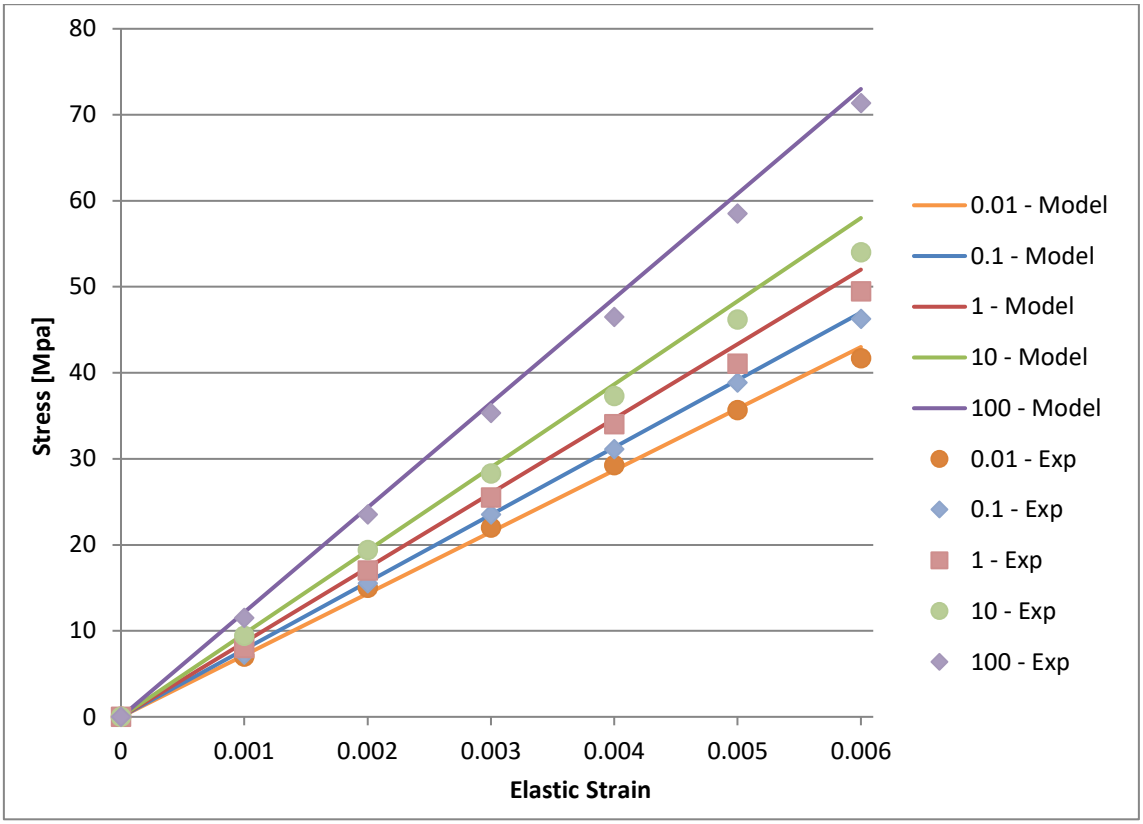

Figure 74: Fitting into elastic properties of PA/GF in longitudinal direction

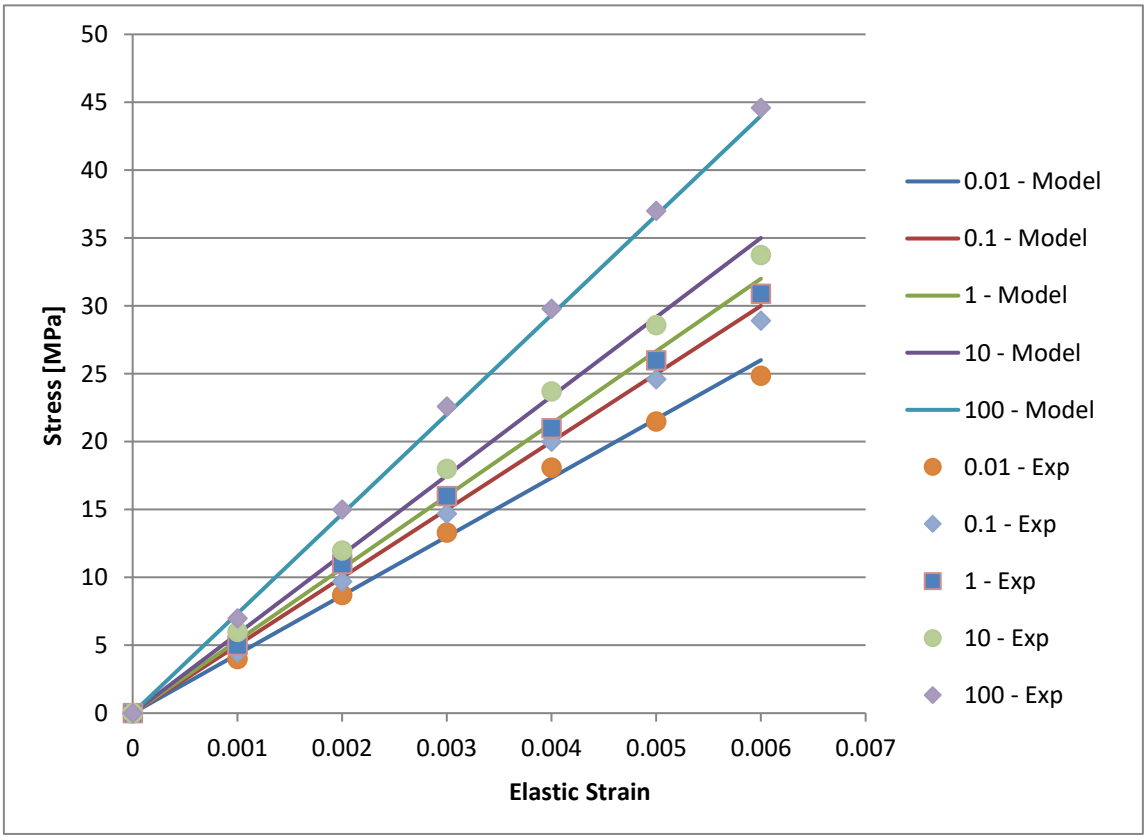

Figure 75: Fitting into elastic properties of PA/GF in transverse direction

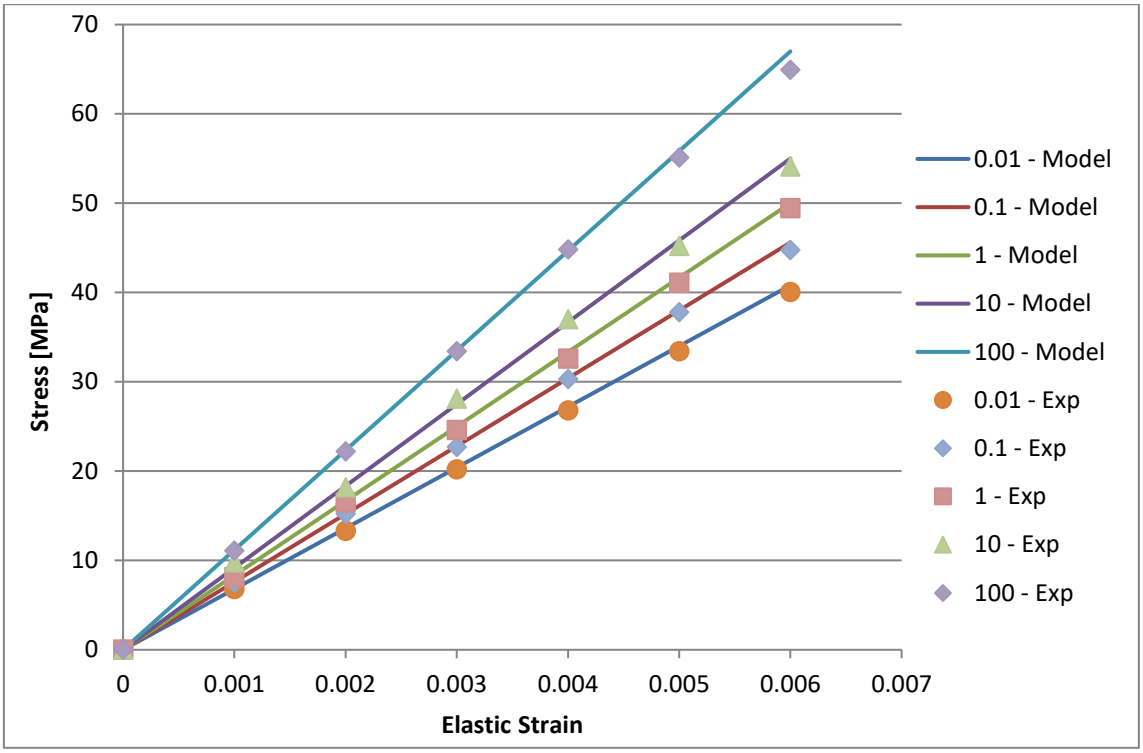

Figure 76: Fitting into elastic properties of PA/GF/SiO_2 in longitudinal direction

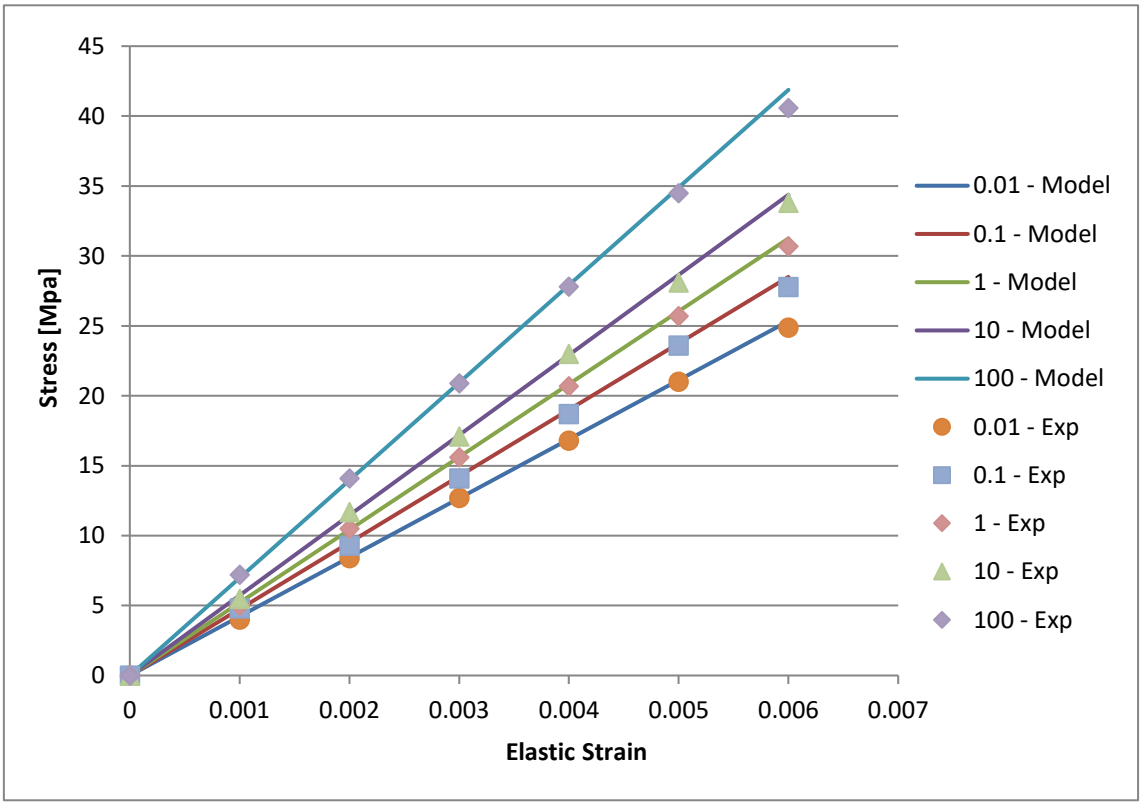

Figure 77: Fitting into elastic properties of PA/GF/SiO_2 in transverse direction

6.2.2 Hardening function

The isotropic strain hardening model is defined by the nonlinear 2nd order exponential function (see chapter 5.1.3). To fully define the model it is required to determine four hardening parameters (a, b, c and d). For this purpose the experimental tensile plastic stress-strain curves were fitted using 2nd order exponential function, available in the Matlab curve fitting tool (cftool). The fitting was carried out only for the average longitudinal tensile test data, at each strain rate. The plastic response of the material in transverse direction and compression is defined using an orthotropic yield function (parameters fitting shown in Chapter 6.2.3). The results of the fitting for PA/GF and PA/GF/SiO_2 materials are visualised in Figure 78 and Figure 79. The values of the hardening model parameters are summarized in Table 18 and Table 19.

Table 18: Hardening coefficients PA/GF

Strain rate [1/s]	Hardening coefficients			
	a [MPa]	b	c [MPa]	d
0.01	112.7	0.0240	-116.2	-1.31
0.1	135.0	0.0100	-126.7	-1.39
1	152.0	0.0055	-150.0	-1.47
10	166.0	0.0050	-169.0	-1.60
100	195.0	0.0050	-209.0	-1.82

Table 19: Hardening coefficients PA/GF/SiO_2

Strain rate [1/s]	Hardening Coefficients			
	a [MPa]	b	c [MPa]	d
0.01	105.0	0.0060	-91.0	-1.15
0.10	114.5	0.0110	-97.0	-1.1
1	126.5	0.0125	-105.0	-1.05
10	137.0	0.0150	-120.0	-1.15
100	167.0	0.0070	-148.0	-1.05

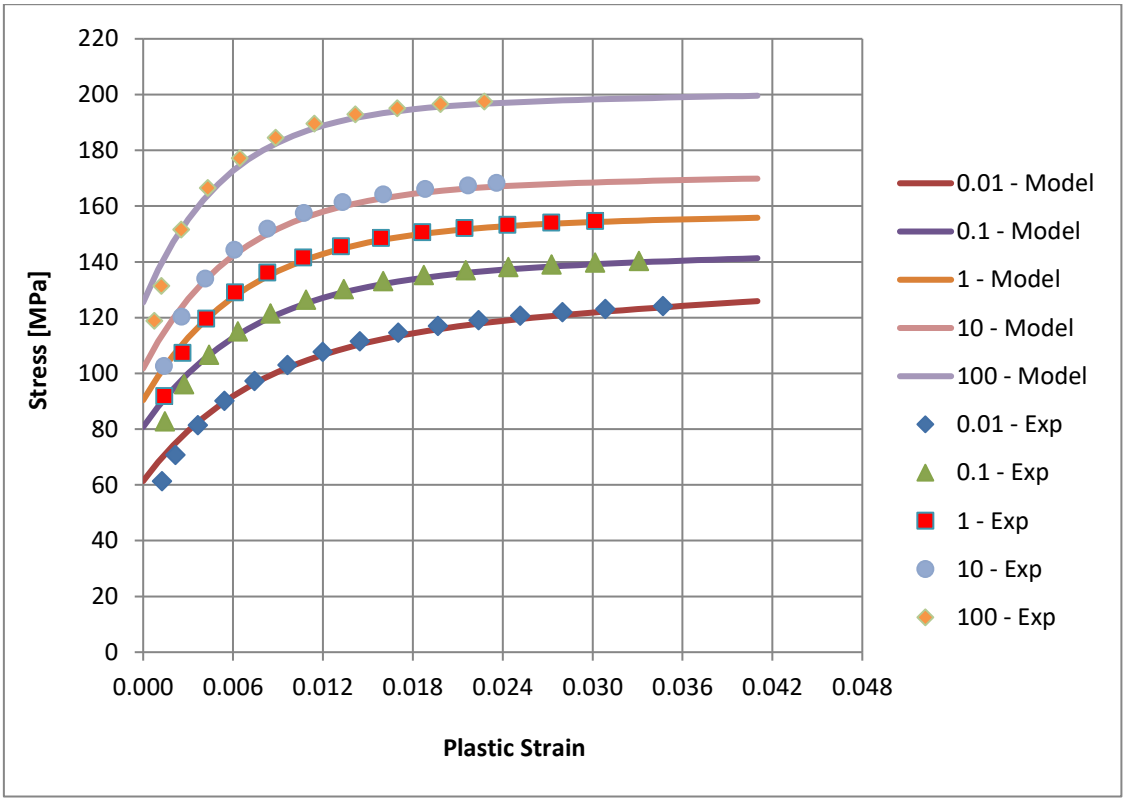

Figure 78: Hardening function fitted into plastic properties of PA/GF

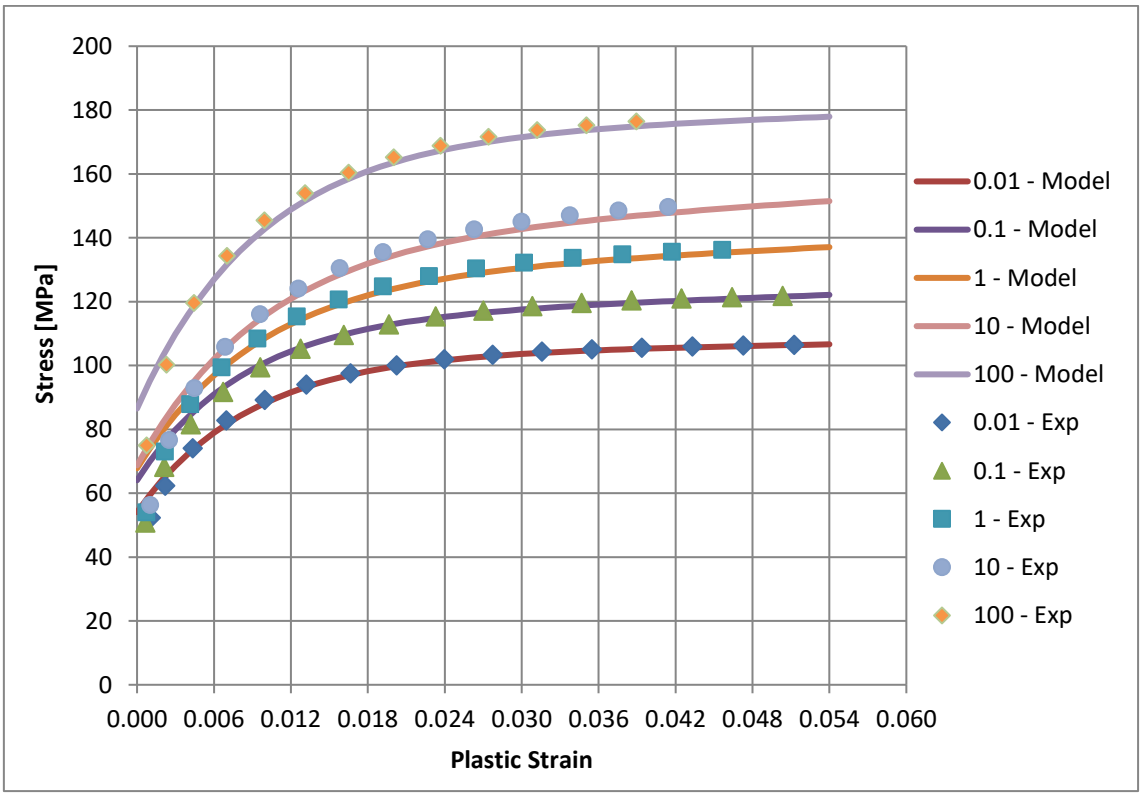

Figure 79: Hardening function fitted into plastic properties of PA/GF/SiO_2

6.2.3 Orthotropic yield function

The yield function is described using orthotropic and pressure sensitive Hoffman yield criterion, as defined in Chapter 5.1.2 The parameters of the yield function can be determined using the following set of equations:

$$\alpha_{12} = \frac{\overline{\sigma}^{\,2}}{2}\left(\frac{1}{\bar{\sigma}_x^t\bar{\sigma}_x^c} + \frac{1}{\bar{\sigma}_y^t\bar{\sigma}_y^c} - \frac{1}{\bar{\sigma}_z^t\bar{\sigma}_z^c}\right)$$

$$\alpha_{23} = \frac{\overline{\sigma}^{\,2}}{2}\left(-\frac{1}{\bar{\sigma}_x^t\bar{\sigma}_x^c} + \frac{1}{\bar{\sigma}_y^t\bar{\sigma}_y^c} + \frac{1}{\bar{\sigma}_z^t\bar{\sigma}_z^c}\right)$$

$$\alpha_{31} = \frac{\overline{\sigma}^{\,2}}{2}\left(\frac{1}{\bar{\sigma}_x^t\bar{\sigma}_x^c} - \frac{1}{\bar{\sigma}_y^t\bar{\sigma}_y^c} + \frac{1}{\bar{\sigma}_z^t\bar{\sigma}_z^c}\right) \tag{6.2}$$

$$\alpha_{11} = \bar{\sigma}^2\frac{\bar{\sigma}_x^c - \bar{\sigma}_x^t}{\bar{\sigma}_x^t\bar{\sigma}_x^c} \qquad \alpha_{22} = \bar{\sigma}^2\frac{\bar{\sigma}_y^c - \bar{\sigma}_y^t}{\bar{\sigma}_y^t\bar{\sigma}_y^c} \qquad \alpha_{33} = \bar{\sigma}^2\frac{\bar{\sigma}_z^c - \bar{\sigma}_z^t}{\bar{\sigma}_z^t\bar{\sigma}_z^c}$$

$$\alpha_{44} = \frac{\overline{\sigma}^{\,2}}{3\bar{\sigma}_{yz}^2} \qquad \alpha_{55} = \frac{\overline{\sigma}^{\,2}}{3\bar{\sigma}_{xz}^2} \qquad \alpha_{66} = \frac{\overline{\sigma}^{\,2}}{3\bar{\sigma}_{xy}^2}$$

where $\bar{\sigma}_i^t$ and $\bar{\sigma}_i^c$ are the yield strengths determined in tensile and compressive tests, and in each direction of orthotropy, whereas $\bar{\sigma}_{ij}$ denote shear yield strengths. The above equations were implemented in the material model; therefore, the user needs to specify only the values of the yield strengths, determined from the experimental data. The yield strengths were extracted from the tensile and compressive stress-strain curves at the total strain of 0.6%. The value of 0.6% strain was found to provide an optimal fit to the experimental data. The main challenge in the yield function fitting was to accurately represent the transition from linear to nonlinear response of the material. In reality, polymers indicate a nonlinear elastic region which exists between linear elasticity and nonlinear plasticity [181]. In the material model used in this study the nonlinear elastic region is omitted, in order to simplify the model formulation, and therefore to save computation time. This approach will induce a small error in stress prediction, in the transition region, which has very little influence on the final result of the strain and failure predictions. This

will be shown in more detail in the results section (Chapter 6.3.1). The values of the yield strengths determined from the experiments are summarized in Table 20. As the shear test was not carried out, the values of the shear yield strengths were derived based on the literature [180]. Using the yield function, the shear stress-strain curves were generated as shown in Figure 81 and Figure 82.

Table 20: Yield strengths [MPa]

Material	Direction	Strain rate [1/s]				
		0.01	0.1	1	10	100
PA/GF	σ_{yt1}	43.1	47.2	52.1	58.4	73.2
	σ_{yt2}	26.2	30.1	32.3	35.1	44.3
	σ_{yc1}	48.5	53.1	58.7	65.5	82.4
	σ_{xy}	20.5	22.5	24.8	27.8	34.9
PA/GF/SiO_2	σ_{yt1}	40.8	45.6	50	55	67
	σ_{yt2}	25.3	28.5	31.3	34.4	41.9
	σ_{yc1}	46.1	51.5	56.5	62.1	75.6
	σ_{xy}	19.4	21.7	23.8	26.2	31.9

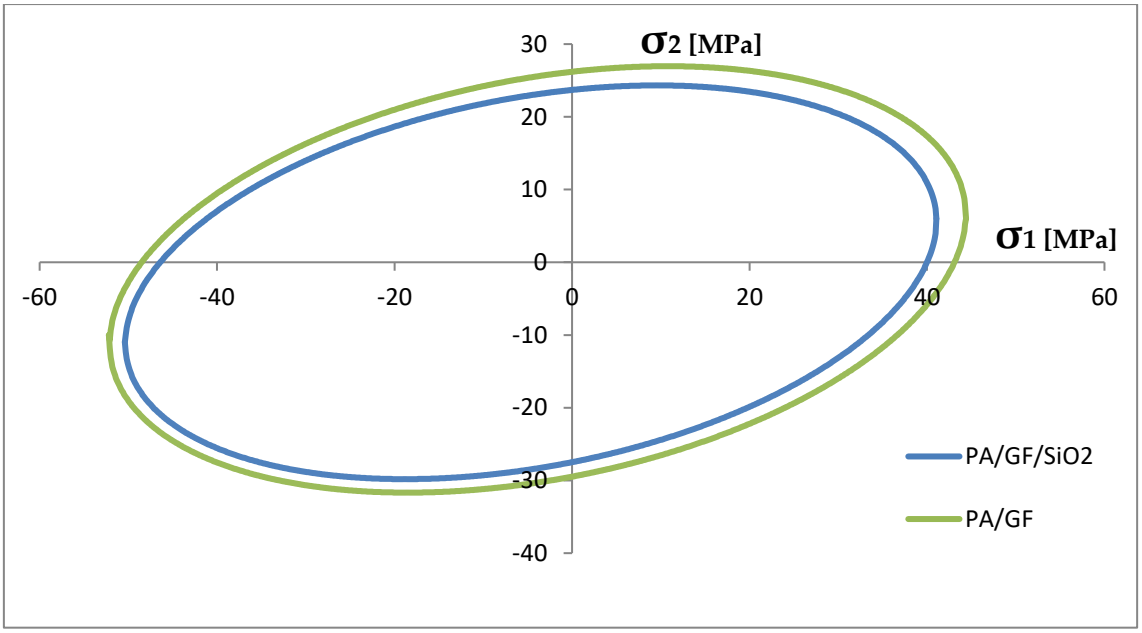

Figure 80: Yield surfaces

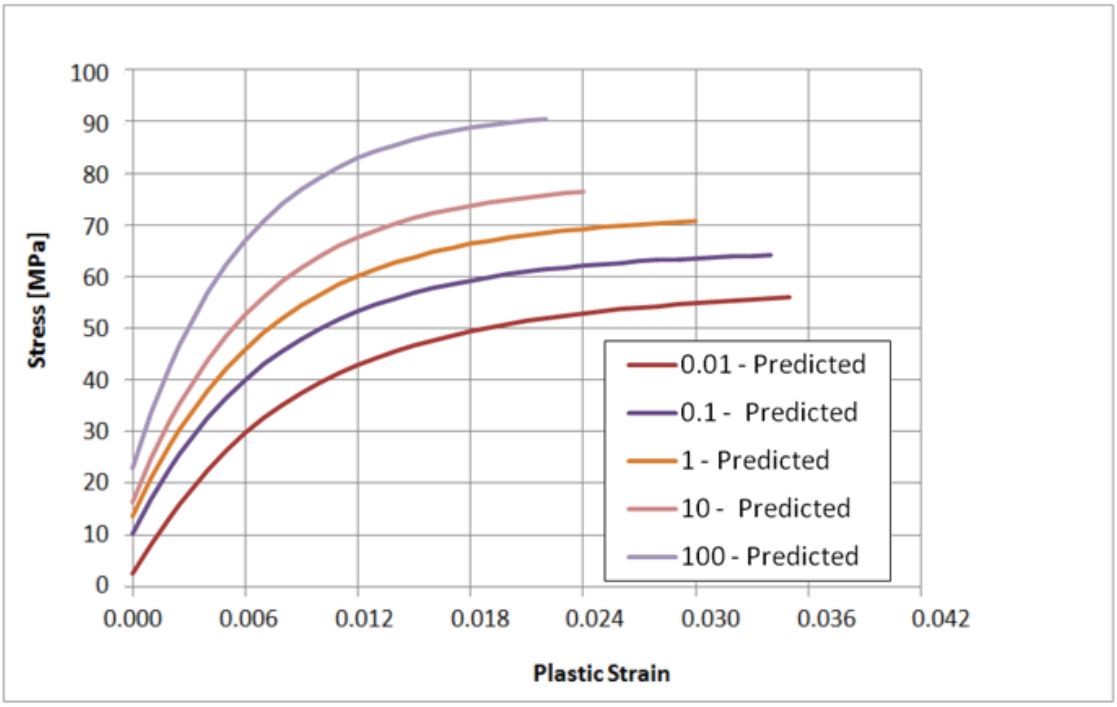

Figure 81: Predicted plastic shear stress-strain curves PA/GF

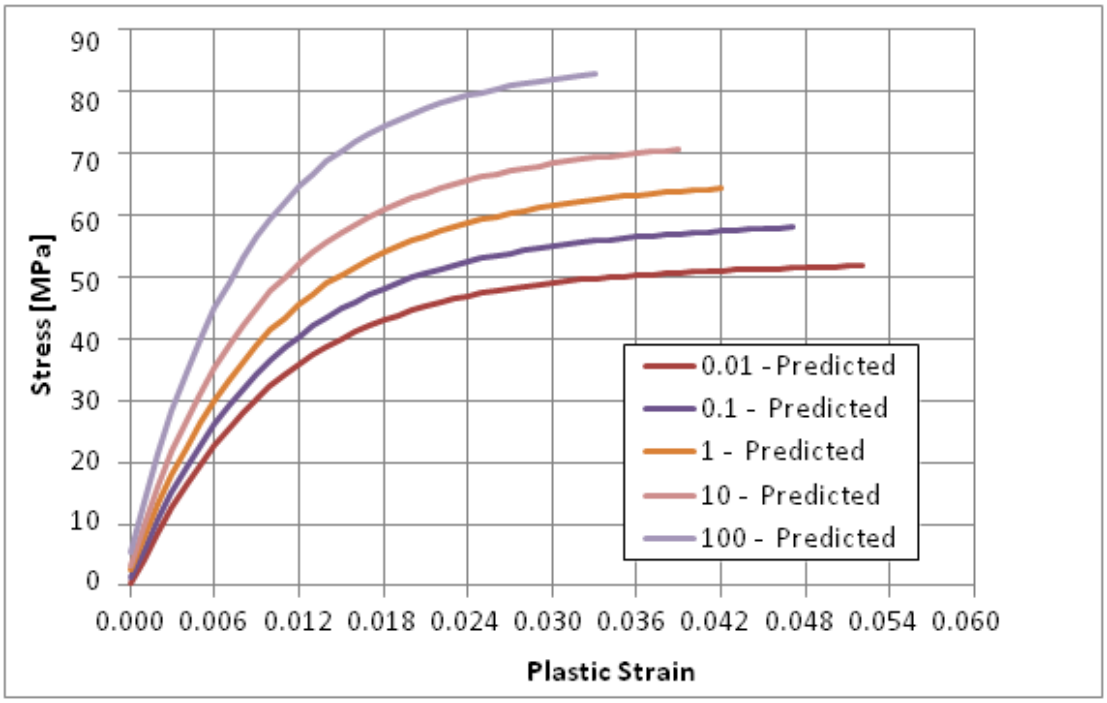

Figure 82: Predicted plastic shear stress-strain curves for PA/GF/SiO2

6.2.4 Orthotropic failure function

The definition of the failure is based on the strain energy density, represented by the orthotropic and pressure sensitive function, as described in Chapter 5.1.5. The parameters of the yield function can be determined using the following set of equations:

$$\begin{gathered}
\beta_{12}^{I} = \overline{SE}^{\,2}\left(\frac{1}{SE_x^{t\,2}}\right) \quad \beta_{23}^{I} = \overline{SE}^{\,2}\left(\frac{1}{SE_y^{t\,2}}\right) \quad \beta_{31}^{I} = \overline{SE}^{\,2}\left(\frac{1}{SE_z^{t\,2}}\right) \\
\beta_{12}^{II} = \overline{SE}^{\,2}\left(\frac{1}{SE_x^{t\,2}}\right) \quad \beta_{23}^{II} = \overline{SE}^{\,2}\left(\frac{1}{SE_y^{t\,2}}\right) \quad \beta_{31}^{II} = \overline{SE}^{\,2}\left(\frac{1}{SE_z^{c\,2}}\right) \\
\beta_{12}^{III} = \overline{SE}^{\,2}\left(\frac{1}{SE_x^{t\,2}}\right) \quad \beta_{23}^{III} = \overline{SE}^{\,2}\left(\frac{1}{SE_y^{c\,2}}\right) \quad \beta_{31}^{III} = \overline{SE}^{\,2}\left(\frac{1}{SE_z^{c\,2}}\right) \\
\beta_{12}^{IV} = \overline{SE}^{\,2}\left(\frac{1}{SE_x^{t\,2}}\right) \quad \beta_{23}^{IV} = \overline{SE}^{\,2}\left(\frac{1}{SE_y^{c\,2}}\right) \quad \beta_{31}^{IV} = \overline{SE}^{\,2}\left(\frac{1}{SE_z^{t\,2}}\right) \\
\beta_{12}^{V} = \overline{SE}^{\,2}\left(\frac{1}{SE_x^{c\,2}}\right) \quad \beta_{23}^{V} = \overline{SE}^{\,2}\left(\frac{1}{SE_y^{t\,2}}\right) \quad \beta_{31}^{V} = \overline{SE}^{\,2}\left(\frac{1}{SE_z^{t\,2}}\right) \\
\beta_{12}^{VI} = \overline{SE}^{\,2}\left(\frac{1}{SE_x^{c\,2}}\right) \quad \beta_{23}^{VI} = \overline{SE}^{\,2}\left(\frac{1}{SE_y^{t\,2}}\right) \quad \beta_{31}^{VI} = \overline{SE}^{\,2}\left(\frac{1}{SE_z^{c\,2}}\right) \\
\beta_{12}^{VII} = \overline{SE}^{\,2}\left(\frac{1}{SE_x^{c\,2}}\right) \quad \beta_{23}^{VII} = \overline{SE}^{\,2}\left(\frac{1}{SE_y^{c\,2}}\right) \quad \beta_{31}^{VII} = \overline{SE}^{\,2}\left(\frac{1}{SE_z^{c\,2}}\right) \\
\beta_{12}^{VIII} = \overline{SE}^{\,2}\left(\frac{1}{SE_x^{c\,2}}\right) \quad \beta_{23}^{VIII} = \overline{SE}^{\,2}\left(\frac{1}{SE_y^{c\,2}}\right) \quad \beta_{31}^{VIII} = \overline{SE}^{\,2}\left(\frac{1}{SE_z^{t\,2}}\right) \\
\beta_{44} = \frac{\overline{SE}^{\,2}}{3\overline{SE}_{yz}^{2}} \quad \beta_{55} = \frac{\overline{SE}^{\,2}}{3\overline{SE}_{xz}^{2}} \quad \beta_{66} = \frac{\overline{SE}^{\,2}}{3\overline{SE}_{xy}^{2}}
\end{gathered} \tag{6.3}$$

where $\overline{SE}_i^t$ and $\overline{SE}_i^c$ are the failure strain energy densities in tension and compression, determined in each direction of orthotropy, whereas $\overline{SE}_{ij}$ denotes failure strain energy densities in shear. The above equations were implemented into the material model; therefore, the user needs to specify only the values of the strain energy densities, determined from the experimental data. As the material is assumed to be transversely orthotropic the failure function parameters are equal in transverse directions 2 and 3. Furthermore, based on the experimental results, it was assumed that the failure in compression does

not occur, therefore a sufficiently large number was selected for this parameter. Due to all these assumptions the number of failure function parameters reduces from 10 to 7. The failure strain energy densities at uniaxial stress conditions (SE_{fti}) were determined by numerical integration of the experimental plastic stress-strain curves, as shown in Figure 78 and Figure 79. The strain energy densities corresponding to shear stresses and strains were derived based on the predicted curves as shown in Figure 81 and Figure 82. The numerical integration was carried out using trapezoid method implemented in the Matlab software (trapz). The biaxial failure parameters were determined using the results of the quasi-static crash test, by manual optimization. The values of the failure function parameters, determined from the experiments, are summarized in Table 21. The failure surfaces are shown in Figure 83.

Table 21: Strain energy densities at failure [mJ/mm^3]

Material	Direction	Strain rate [1/s]				
		0.01	0.1	1	10	100
PA/GF	SE_{ft1}	3.9	3.88	3.73	3.62	3.56
	SE_{ft2}	2.88	2.87	2.86	2.85	2.84
	SE_{fxy}	1.51	1.50	1.45	1.40	1.38
	SE_{fc1}	30				
	Bi_1	-1.2	-0.2	-0.2	-0.2	-0.2
	Bi_2	0.1	0.1	0.1	0.1	0.1
	Bi_3	-0.01	-1	-1	-1	-1
	Bi_4	0.2	3	3	3	3
PA/GF/SiO_2	SE_{f1}	4.99	4.98	4.98	4.97	4.97
	SE_{f2}	4.22	4.21	4.21	4.2	4.2
	SE_{fxy}	2.19	2.18	2.18	2.18	2.18
	SE_{fc1}	30				
	Bi_1	-0.2	-0.2	-0.2	-0.2	-0.2
	Bi_2	0.1	0.1	0.1	0.1	0.1
	Bi_3	-1	-1	-1	-1	-1
	Bi_4	3	3	3	3	3

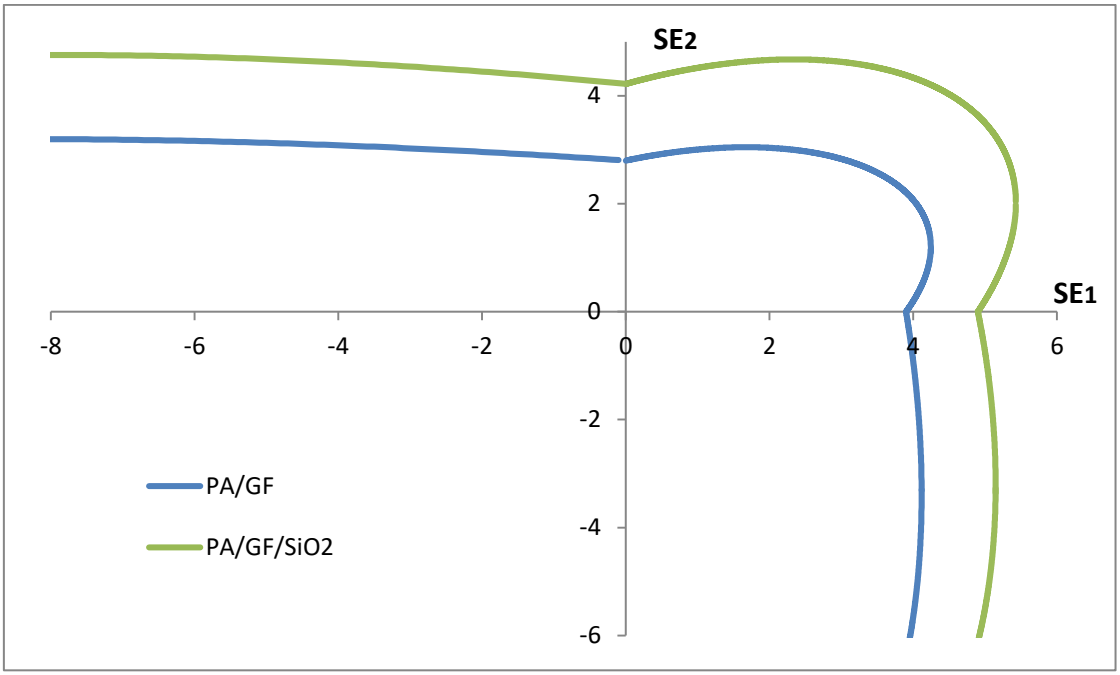

Figure 83: Failure surfaces

6.3 Results

The following sections contain the results of the FE analysis of the specimen (tensile and compression) and structural testing (static and dynamic crash test). The analysis was carried out using the UMAT implemented in Ls-Dyna software (see chapter 5) and calibrated against the experimental data (see section 6.2). The numerical results were compared against the experiments which were discussed in more detail in Chapters 3 and 4.

6.3.1 Tensile test

Comparison between the data obtained in the experiments (data points) and the numerical simulations (continuous lines) is shown in Figure 84 to Figure 87. The simulations were carried out for PA/GF and PA/GF/SiO_2 materials, in both longitudinal and transverse directions. It can be seen from the results of the longitudinal tensile test that the UMAT is able to predict both elastic and plastic deformation of the sample with good accuracy. A slightly nonlinear elastic region was approximated as linear, up to the value of the yield stress. This

approximation induces a small error in stress predictions, within the elasto-plastic transition region. The error was found to be below 2% of the actual stress value in all simulations, and has a negligible effect on the final results of the analysis. Beyond this point the material behaviour is precisely predicted by the hardening curve, fitted to the experimental results. It can also be seen that the selected strain rate sensitivity formulation provides an excellent match with the experimental data. Not only is the yielding accurately predicted, but also the whole nonlinear region is precisely matched at each strain rate. This result proves a big advantage of scaling all the hardening parameters with the strain rate, rather than just the yield strength, which does not allow the shape of the curve to be changed at higher strain rates.

From the results of the simulations carried out in the transverse direction, it can be seen that the orthotropic formulation of the model provides good representation of the composite material response. Both elastic and plastic behaviour were predicted with a good accuracy. However, as the plastic response of the material, in the direction different from longitudinal tension, is defined only by the yield function, the model cannot be exactly fitted to the experimental data for those conditions. Despite this limitation the UMAT accurately predicted the plastic behaviour of the sample at different strain rates, just by scaling the stress-strain curve with the yield strength, as can be seen in Figure 85 and Figure 87. In this case, deviations from the experimental data are higher, but do not exceed 3% of the actual stress, at any stage of the test.

Regarding the prediction of the material failure, it can be seen that the modelled samples failed at almost exactly the same conditions as in the experiment, regardless of the strain rate or loading direction. Comparison of all the key results from the simulations and the experiments is shown in Table 22 - Table 25.

Table 22: PA/GF longitudinal – numerical vs. experimental results

Strain Rate [1/s]		0.01	0.1	1	10	100
Modulus [MPa]	Model	7167.0	7833.0	8667.0	9667.0	12167.0
	Exp.	7066.7	7707.2	8533.3	9571.4	12033.3
	Error [%]	1.4	1.6	1.5	1.0	1.1
Yield [MPa]	Model	43.1	47.2	52.1	58.4	73.2
	Exp.	42.4	46.3	51.1	57.4	71.7
	Error [%]	1.6	2.0	1.9	1.7	2.0
UTS [MPa]	Model	122.9	138.8	153.2	166.4	195.5
	Exp.	123.9	139.8	154.1	168.3	196.6
	Error [%]	0.8	0.7	0.5	1.2	0.6
Failure Strain	Model	0.0523	0.0480	0.0452	0.0415	0.0363
	Exp.	0.0520	0.0486	0.0451	0.0410	0.0361
	Error [%]	0.6	1.2	0.2	1.3	0.6

Table 23: PA/GF transverse – numerical vs. Experimental results

Strain Rate [1/s]		0.01	0.1	1	10	100
Modulus [MPa]	Model	4333	5000	5333	5833	7333
	Exp.	4300	4933	5233	5767	7200
	Error [%]	0.8	1.3	1.9	1.1	1.8
Yield [MPa]	Model	26.2	30.1	32.3	35.1	44.3
	Exp.	25.6	29.6	31.7	34.6	43.5
	Error [%]	2.3	1.7	1.9	1.4	1.8
UTS [MPa]	Model	80.4	92.8	102.6	111.6	131.4
	Exp.	78.0	93.9	102.7	112	130.0
	Error [%]	3.0	1.3	0.1	0.5	1.1
Failure Strain	Model	0.0594	0.0537	0.0512	0.0477	0.0425
	Exp.	0.0600	0.0539	0.0511	0.0480	0.0422
	Error [%]	0.9	0.4	0.3	0.7	0.7

Table 24: PA/GF/SiO_2 longitudinal – numerical vs. experimental results

Strain Rate [1/s]		0.01	0.1	1	10	100
Modulus [MPa]	Model	6800	7600	8333	9167	11167
	Exp	6683	7450	8233	9017	10817
	Error [%]	1.7	2.0	1.2	1.6	3.1
Yield [MPa]	Model	40.8	45.6	50	55	67
	Exp	40.1	44.7	49.4	54.1	64.9
	Error [%]	1.7	2.0	1.2	1.6	3.1
UTS [MPa]	Model	113.1	128.9	143.7	155.9	180.9
	Exp	113.5	128.5	142.8	156.1	181.7
	Error [%]	0.4	-0.3	-0.7	0.1	0.4
Failure Strain	Model	0.0696	0.0665	0.0630	0.0601	0.0514
	Exp	0.0691	0.0662	0.0627	0.0600	0.0511
	Error [%]	0.7	0.4	0.5	0.1	0.5

Table 25: PA/GF/SiO_2 transverse – numerical vs. experimental results

Strain Rate [1/s]		0.01	0.1	1	10	100
Modulus [MPa]	Model	4223	4750	5208	5729	6979
	Exp	4147	4632	5117	5637	6762
	Error [%]	1.8	2.5	1.8	1.6	3.1
Yield [MPa]	Model	25.3	28.5	31.3	34.4	41.9
	Exp	24.9	27.8	30.7	33.8	40.6
	Error [%]	1.8	2.5	1.8	1.6	3.1
UTS [MPa]	Model	74.9	84.5	94.1	102.4	121.6
	Exp	76.1	85.9	92.5	101.7	119.8
	Error [%]	1.7	1.6	-1.7	-0.7	-1.4
Failure Strain	Model	0.0806	0.0788	0.0749	0.0693	0.0631
	Exp	0.0810	0.0780	0.0750	0.0690	0.0630
	Error [%]	-0.5	1.0	-0.1	0.5	0.2

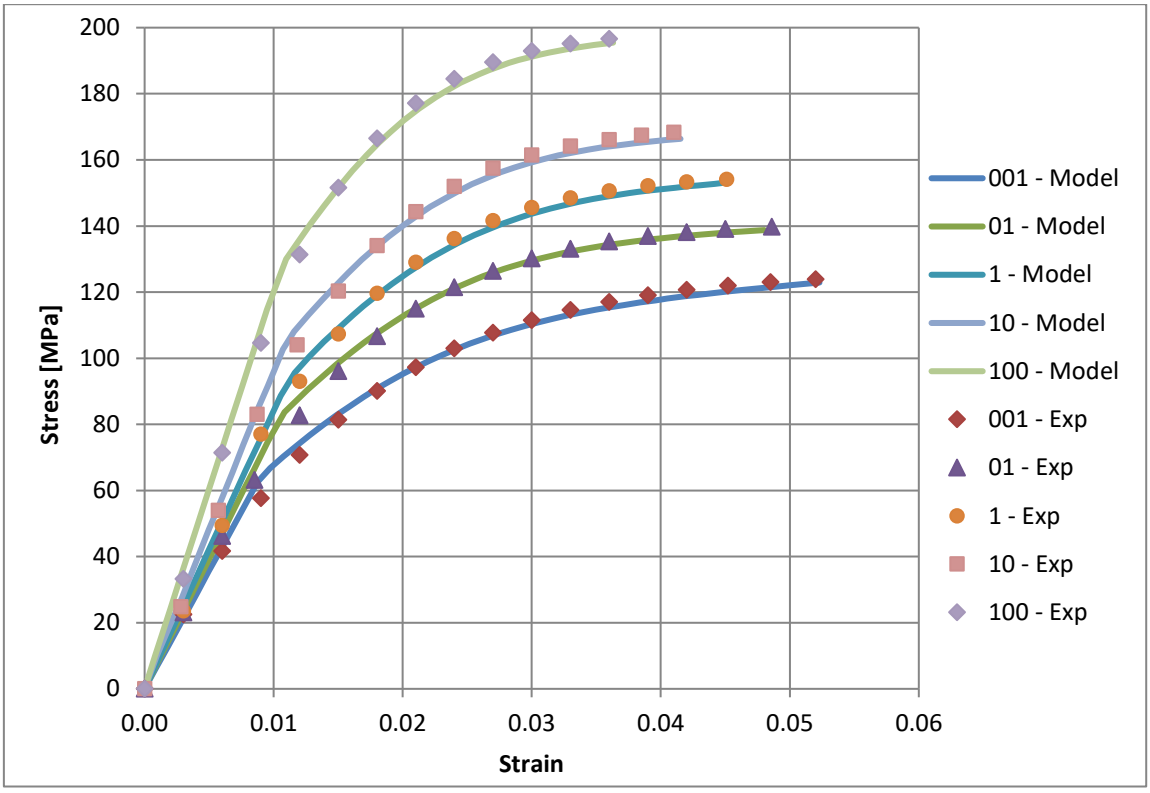

Figure 84: Predicted and experimental stress-strain curves PA/GF – longitudinal direction

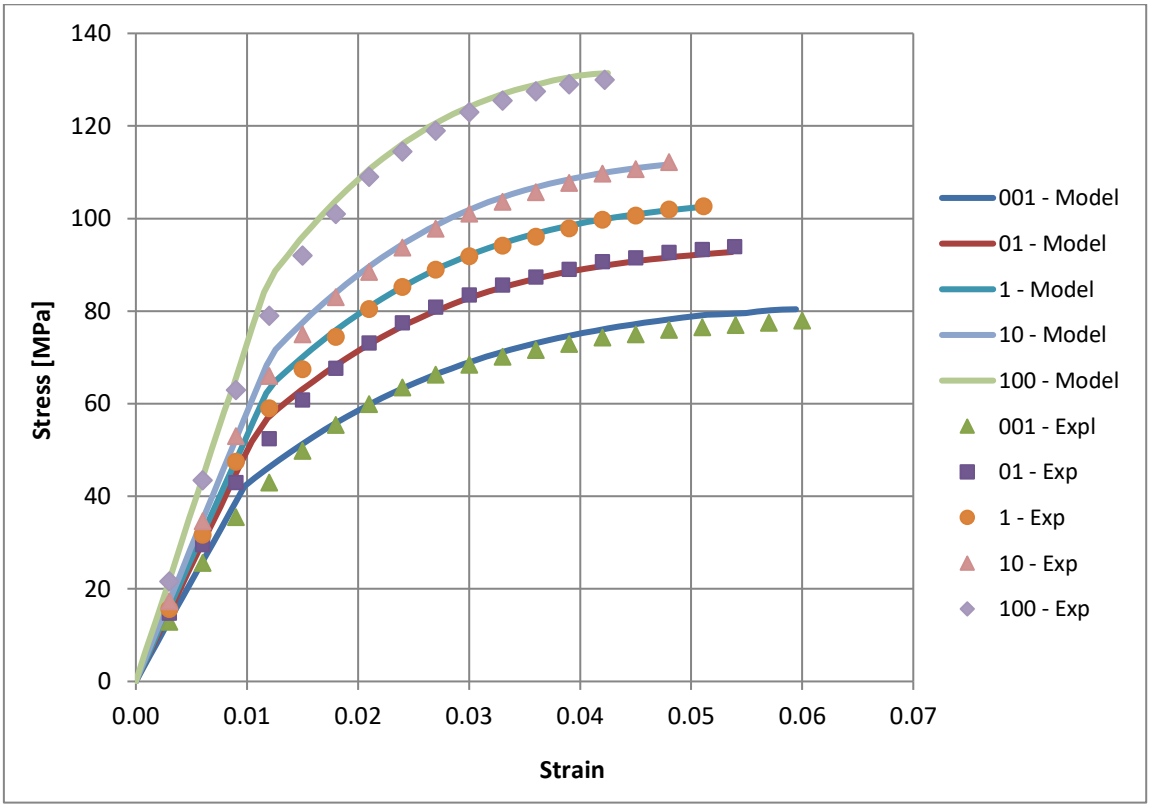

Figure 85: Predicted and experimental stress-strain curves PA/GF – transverse direction

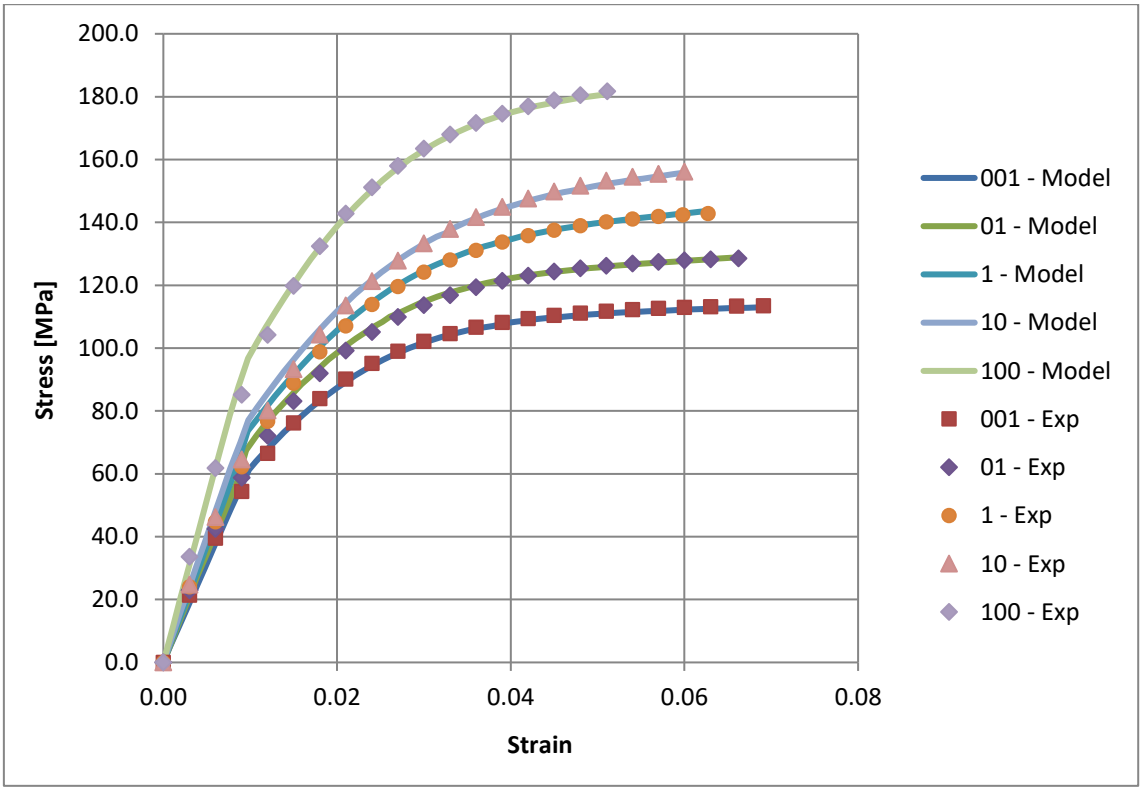

Figure 86: Predicted and experimental stress-strain curves PA/GF/SiO_2 – longitudinal direction

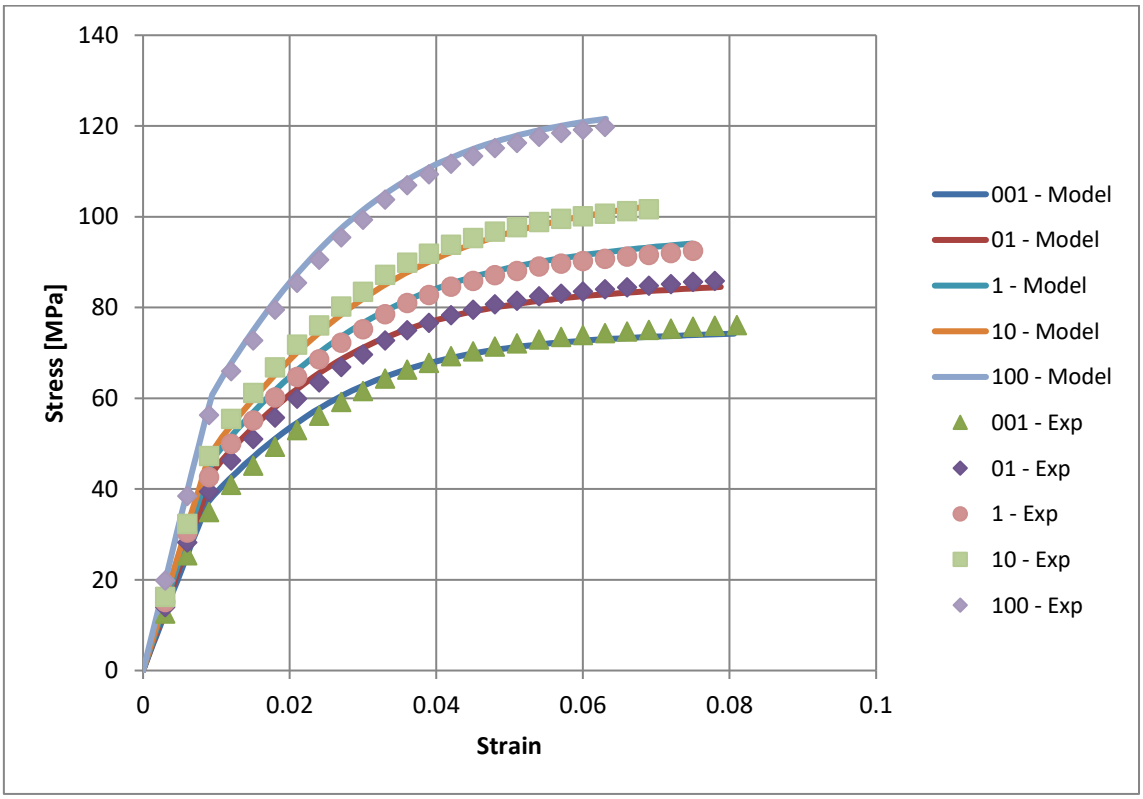

Figure 87: Predicted and experimental stress-strain curves PA/GF/SiO_2 – transverse direction

6.3.2 Compression test

Comparison of the compressive stress-stress curves obtained in the experiments (data points) and the numerical simulations (continuous lines), is shown in Figure 88 and Figure 89. Comparison of all the key results from the simulations and the experiments is shown in Table 26 and Table 27.

The simulations were carried out for PA/GF and PA/GF/SiO_2 materials at five different strain rates. The experiments were carried out at only three different stain rates as shown in section 3.4.4.

It can be seen that the UMAT is able to predict both elastic and plastic deformation, of the compression sample, with a good accuracy. However, the deviations from the experimental data are more elevated, in relation to the longitudinal tensile test, as the plastic response in compression is governed only by the yield function. This means that the hardening coefficients cannot be fitted directly to the compressive stress-strain curves. Despite this limitation the UMAT accurately predicted the plastic behaviour of the sample at different strain rates, just by scaling the stress-strain curve with the yield strength.

Table 26: PA/GF compression – numerical vs. experimental results

Strain Rate [1/s]		0.01	0.1	1	10	100
Modulus [MPa]	Model	7740	8569	9201	10473	13152
	Exp	7417	8344	9183	-	-
	Error [%]	4.17	2.63	0.19	-	-
Yield [MPa]	Model	48.45	53.64	57.60	65.56	82.33
	Exp	46.43	52.23	57.49	-	-
	Error [%]	4.17	2.63	0.19	-	-
$CS_{6\%}$ [MPa]	Model	143.22	156.82	171.56	184.48	213.93
	Exp	142.00	159.00	177.00	-	-
	Error [%]	0.85	-1.39	-3.17	-	-

Table 27: PA/GF/SiO_2 compression – numerical vs. experimental results

Strain Rate [1/s]		0.01	0.1	1	10	100
Modulus [MPa]	Model	7089	8217	9190	9825	12004
	Exp	7081	8167	9083	-	-
	Error [%]	0.11	0.62	1.16	-	-
Yield [MPa]	Model	45.88	51.27	58.45	61.82	75.21
	Exp	44.61	51.45	57.23	-	-
	Error [%]	2.77	-0.36	2.10	-	-
$CS_{6\%}$ [MPa]	Model	123.38	137.80	153.18	167.71	194.89
	Exp	121.87	141.37	155.51	-	-
	Error [%]	1.22	-2.59	-1.52	-	-

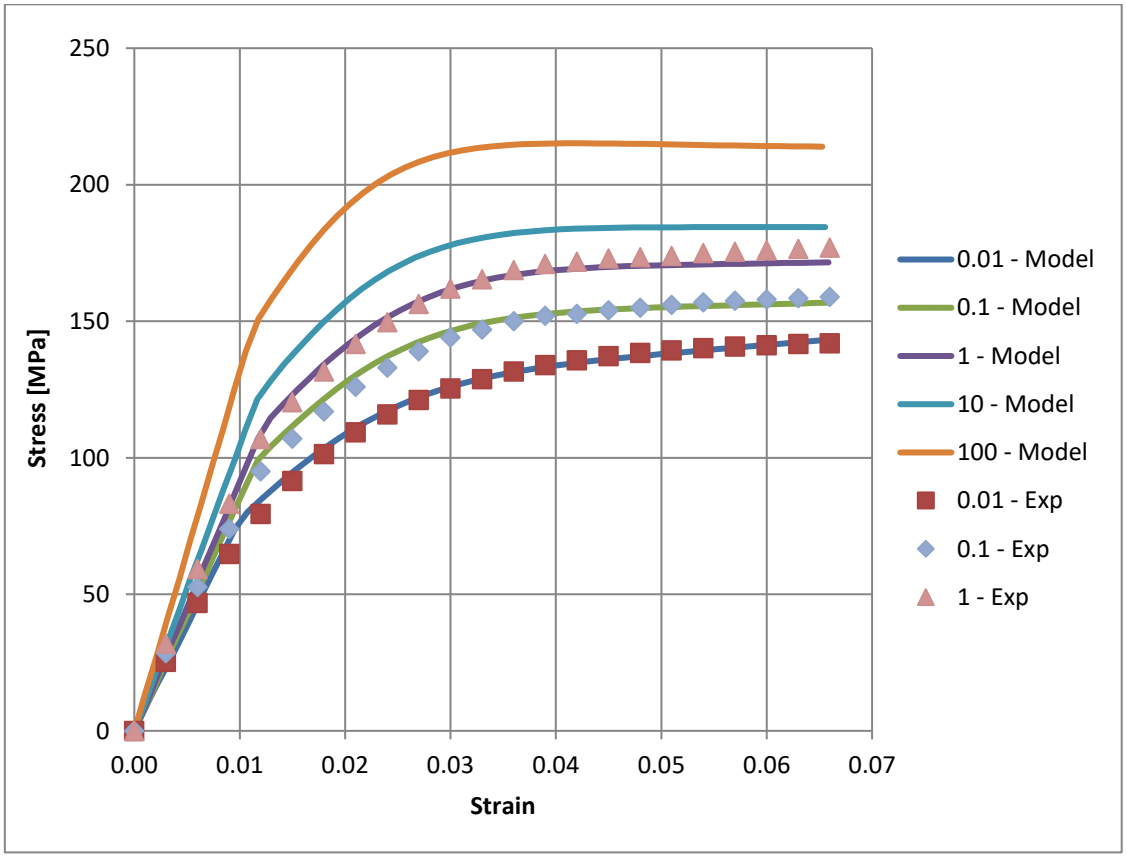

Figure 88: Predicted and experimental stress-strain curves PA/GF - compression

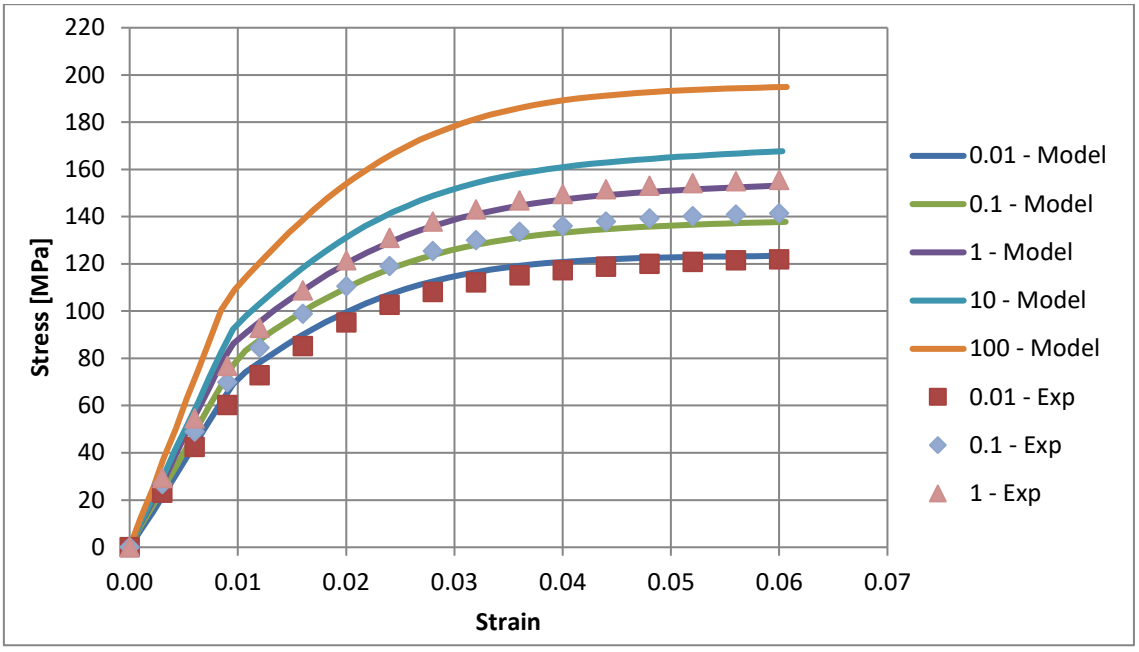

Figure 89: Predicted and experimental stress-strain curves PA/GF/SiO_2 – compression

6.3.3 Quasi-static crash test

Main results concerning the energy absorption capabilities of the composite structures are listed in Table 28. A visual comparison of the modelled and actual crashing tests are presented in Figure 90 - Figure 99. A comparison of the load-displacement curves, from the numerical simulations and the experiments, is presented in Figure 100 and Figure 101.

Analyzing the obtained data it can be seen, that the models represented the crashing behaviour of the conical structures with good accuracy. Table 28 shows that the impact energy absorption, predicted by the model, is lower by around 11% in relation to the experimental result, for both composites. This is due to the lower crashing loads predicted in the simulation, in relation to those measured in the experiment. However, despite this limitation, the model correctly captured the difference between the energy absorbed by the PA/GF and PA/GF/SiO_2 composites. The higher energy absorption of PA/GF composite is caused by the higher crashing loads measured during the tests. The main reason for that is higher stiffness and strength of the PA/GF composite in

relation to PA/GF/SiO_2. As the differences in the material properties were taken into account in the modelling process, accurate predictions were obtained using the FE models.

Table 28: Quasi-static crashing characteristics

Material	Crash length [mm]	Collapse mode	Initial peak [kN]	Mean crashing load [kN]	Energy absorbed [kJ]	Energy prediction error [%]
PA/GF_FE	90	III	53.3	43.1	3.8	11
PA/GF_Ex	90	III	49.9	50.4	4.3	
PA/GF/SiO2_FE	90	III	49.9	40.4	3.6	12
PA/GF/SiO2_Ex	90	III	44.6	45.66	4.1	

Figure 90 to Figure 99 show that the model predicted the failure mode of the structures, made of PA/GF and PA/GF/SiO_2 composites (mode III). At each stage of the crash test, the model effectively represented the structural response of the sample. This is visible as a combination of elasto-plastic deformation and progressive failure. The failed material falls out form the structures as both small and large fragments of broken material. The final shape of the crashed specimens (Figure 94 and Figure 99), is similar in both the experiment and the FE simulation. It consists of remaining unbroken fragment of the structure, surrounded by broken and squeezed pieces of the material, present both outside and inside the sample.

Figure 90: Modelled and experimental quasi-static crash test PA/GF – 10mm displacement

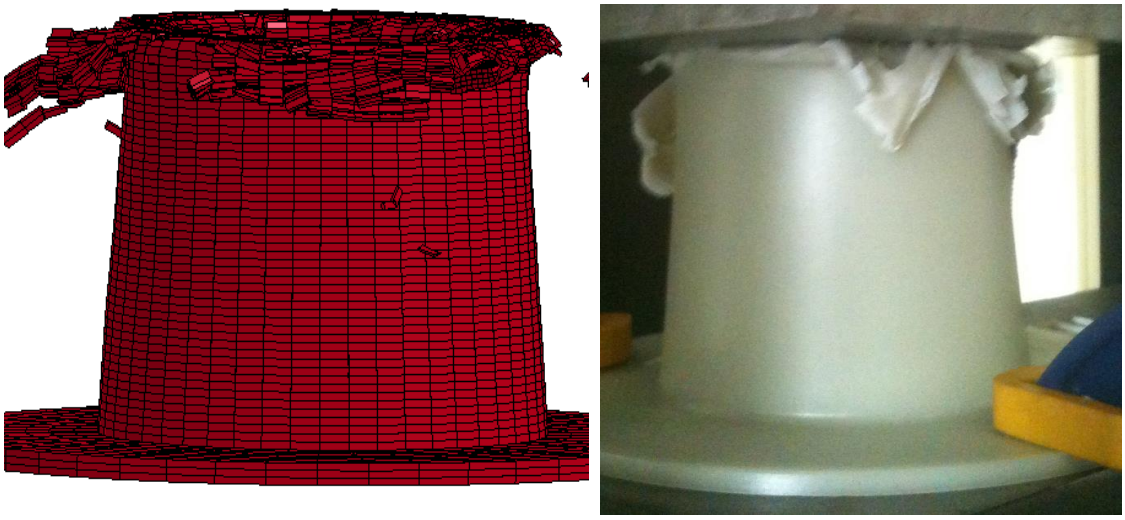

Figure 91: Modelled and experimental quasi-static crash test PA/GF – 45mm displacement

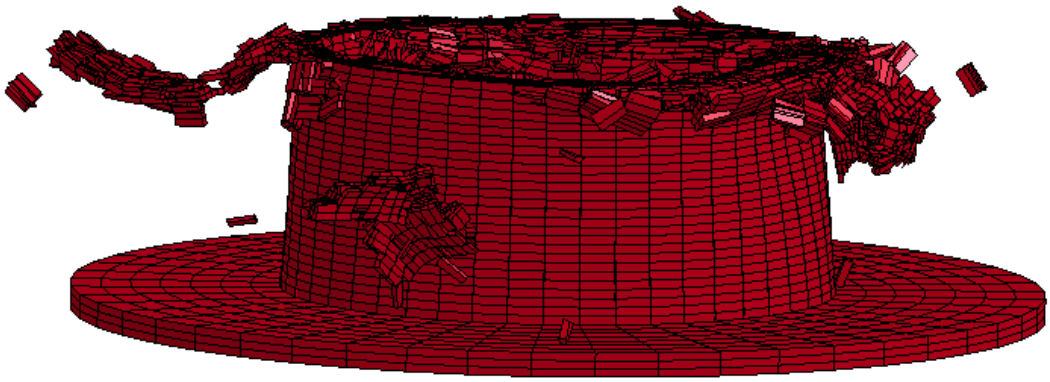

Figure 92: Modelled quasi-static crash test PA/GF – 90mm displacement

Figure 93: Experimental quasi-static crash test PA/GF – 90mm displacement

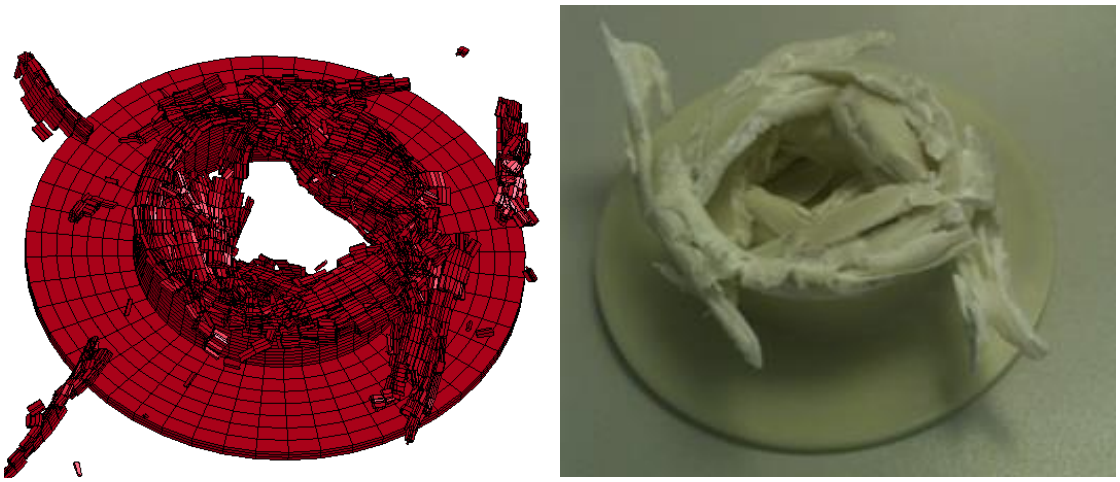

Figure 94: Experimental quasi-static crash test PA/GF – final shape

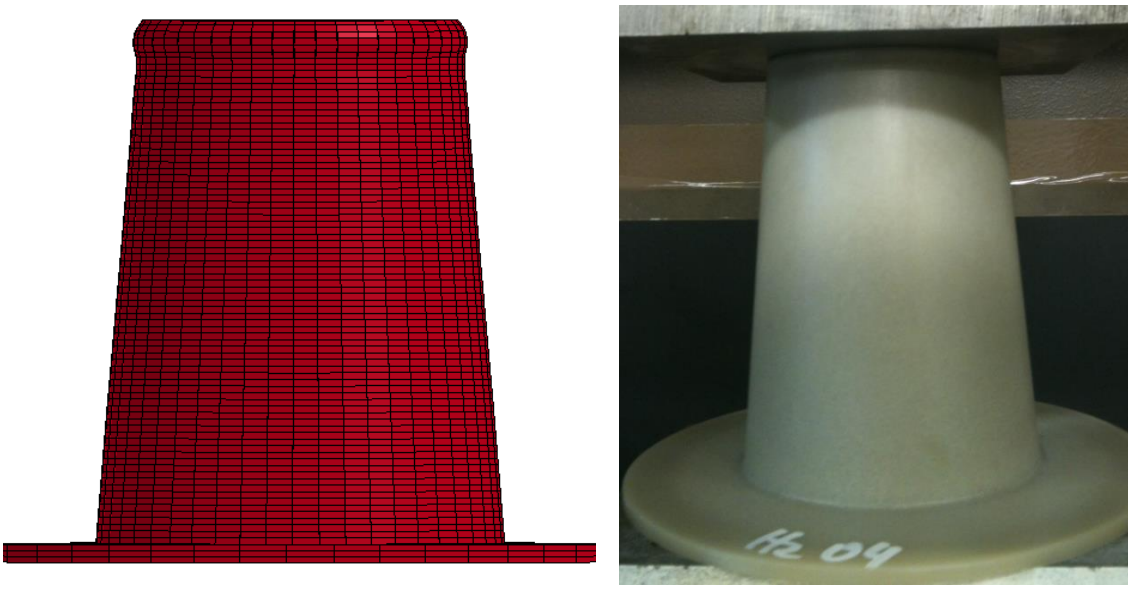

Figure 95: Modelled and experimental quasi-static crash test PA/GF/SiO_2 – 1.5 mm displacement

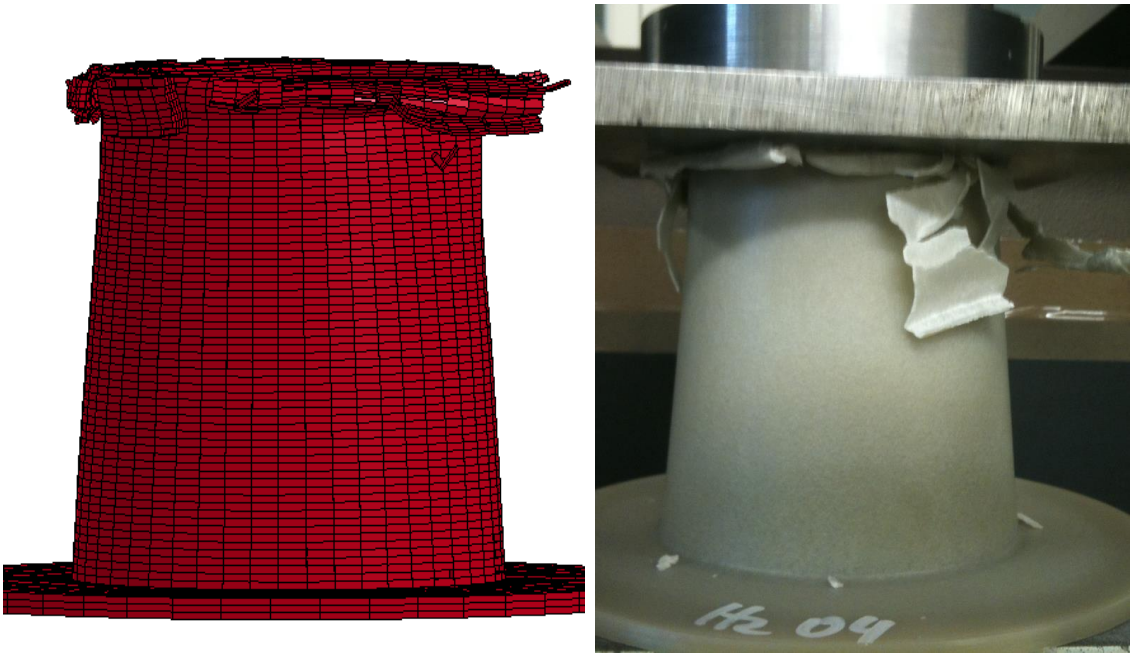

Figure 96: Modelled and experimental quasi-static crash test PA/GF/SiO_2 – 10mm displacement

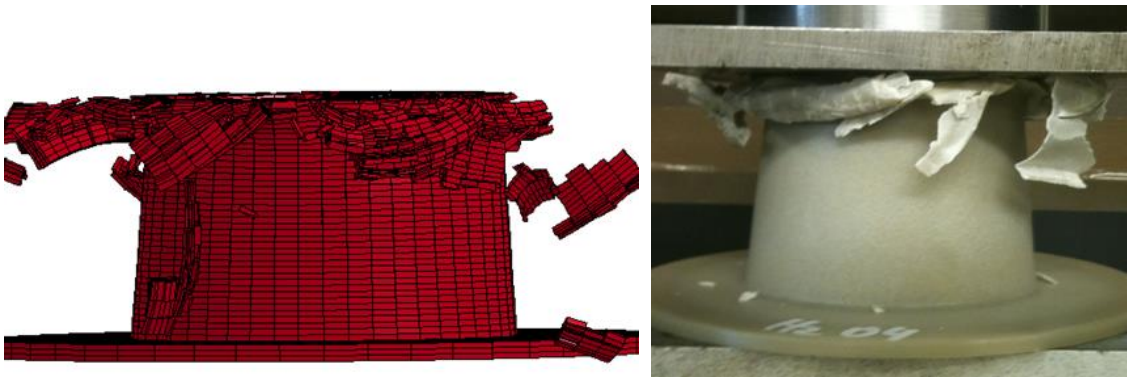

Figure 97: Modelled and experimental quasi-static crash test PA/GF/SiO_2 – 60mm displacement

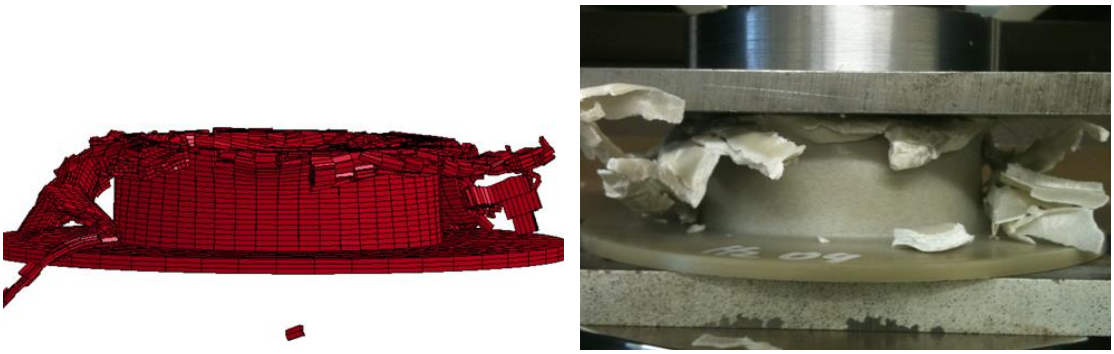

Figure 98: Modelled and experimental quasi-static crash test PA/GF/SiO_2 – 90mm displacement

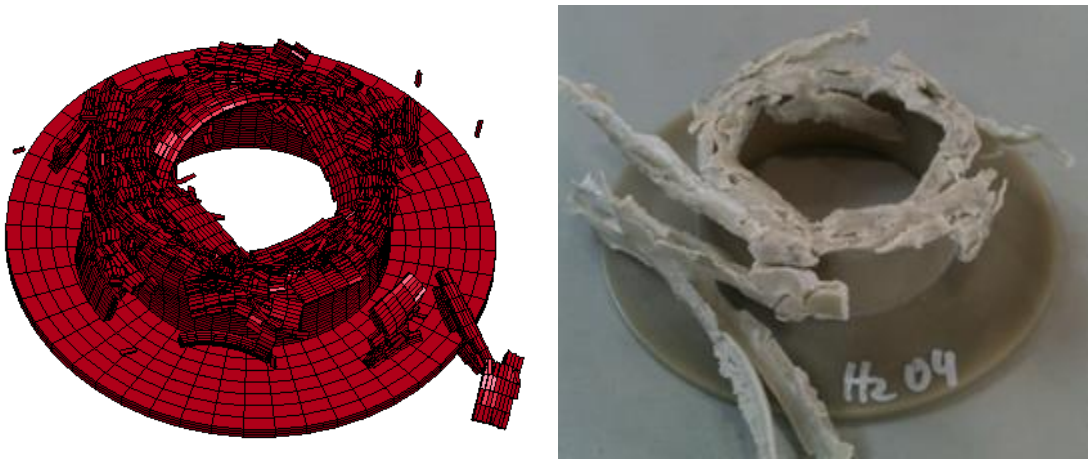

Figure 99: Experimental quasi-static crash test PA/GF/SiO_2 – final shape

Furthermore, it can be seen that the model also predicted the shape of the load displacement curve. Figure 100 and Figure 101 show that both the measured and predicted loads rise with displacement. This effect is induced by the increasing thickness of the cone wall. The load rises during the elasto-plastic deformation until the stresses reach the ultimate strength. Subsequently, the fracture starts to form in the structure, and is visible on the curve as reduction or stabilization of the load, depending on the stage of the crashing event. The two phenomena- elasto-plastic deformation and failure- occur alternately during the whole duration of the crash. This is visible on the load-displacement plot as an irregular shape of the curve.

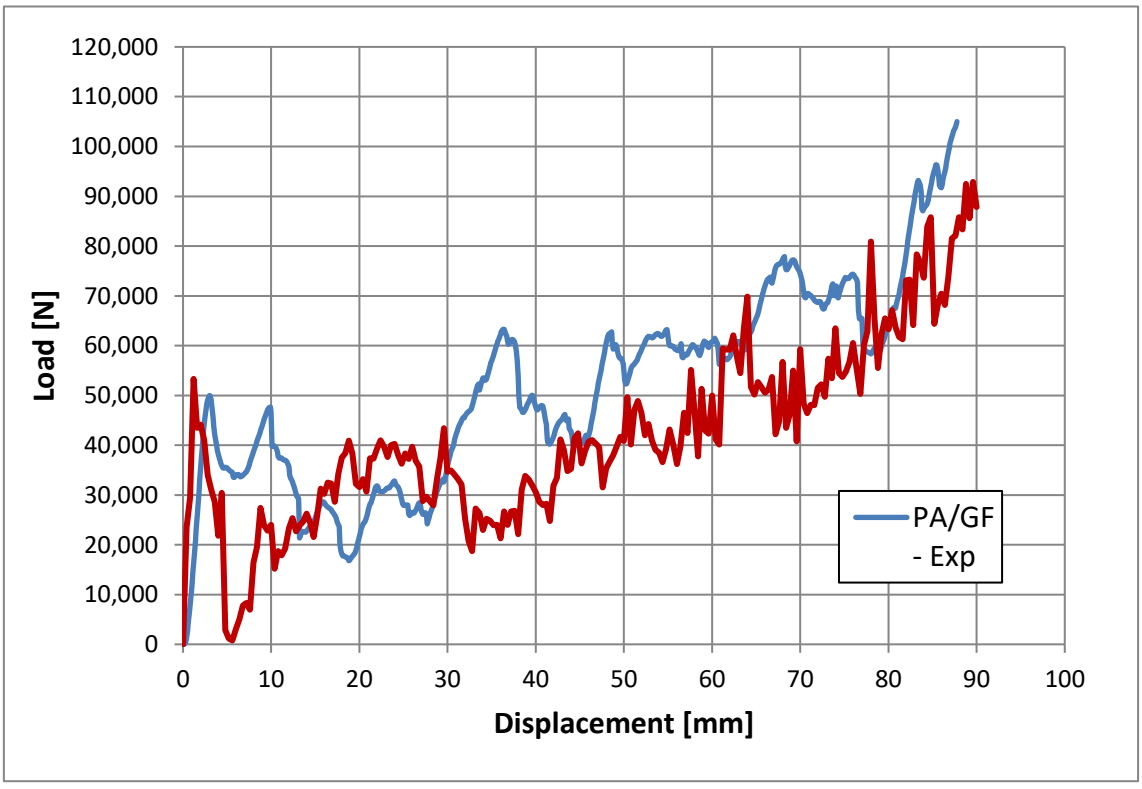

Figure 100: Quasi-static load-displacement curves PA/GF

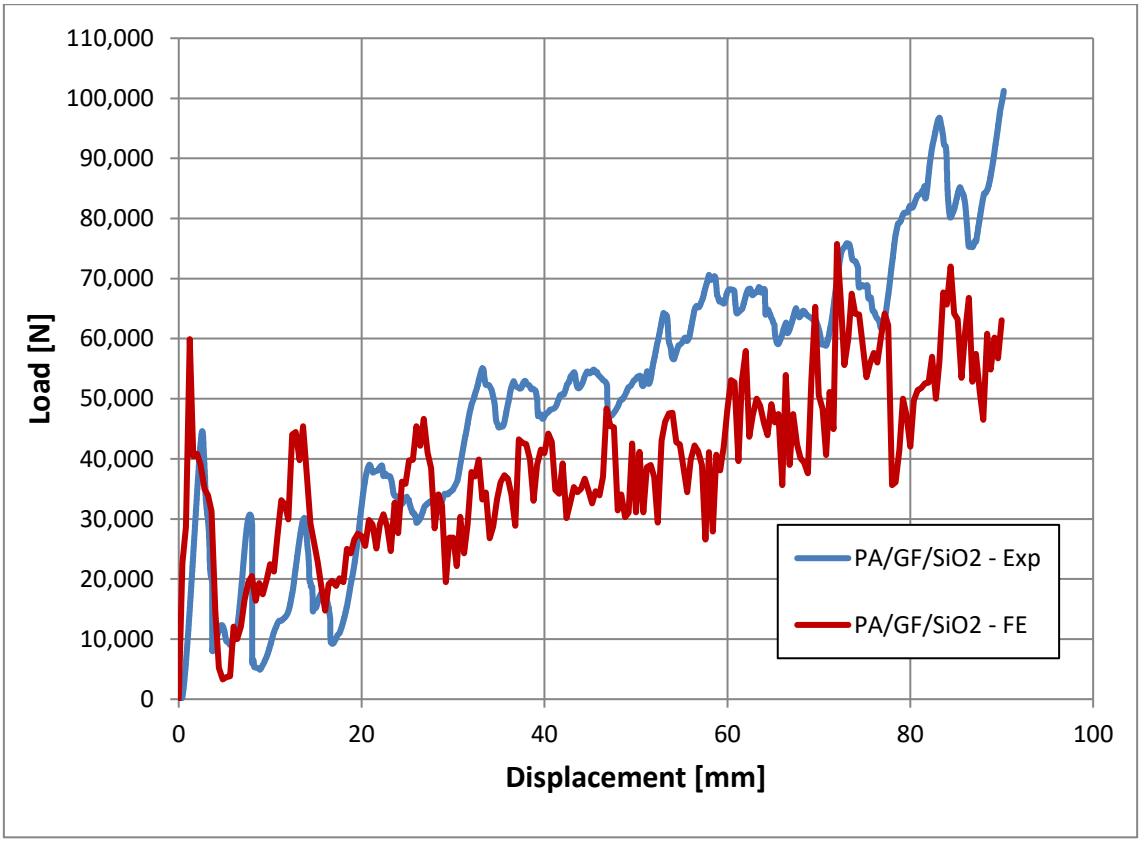

Figure 101: Quasi-static load-displacement curves PA/GF/SiO_2

It is important to note that the crashing event consists of two distinctive stages, defined by the location of the failure initiation point. This is either on the outer or inner surface of the cone wall. At an early stage of the crash, the elasto-plastic deformation is initiated by the axial compressive loads (see Figure 102 and Figure 105). When the structure loses its stability, a plastic axisymmetric bulge starts to form (see Figure 103 and Figure 106).

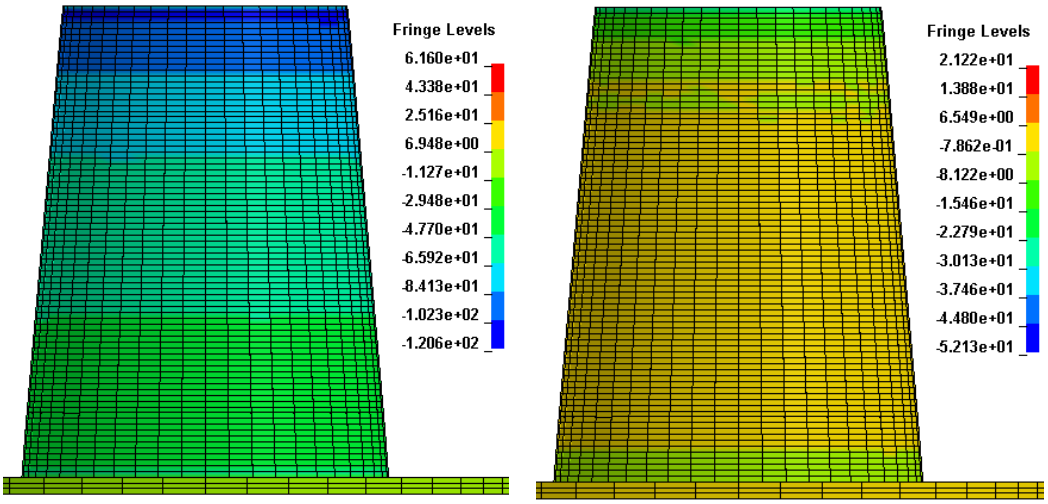

Figure 102: Axial (left) and circumferential (right) stress plots [MPa] PA/GF– 1mm displacement

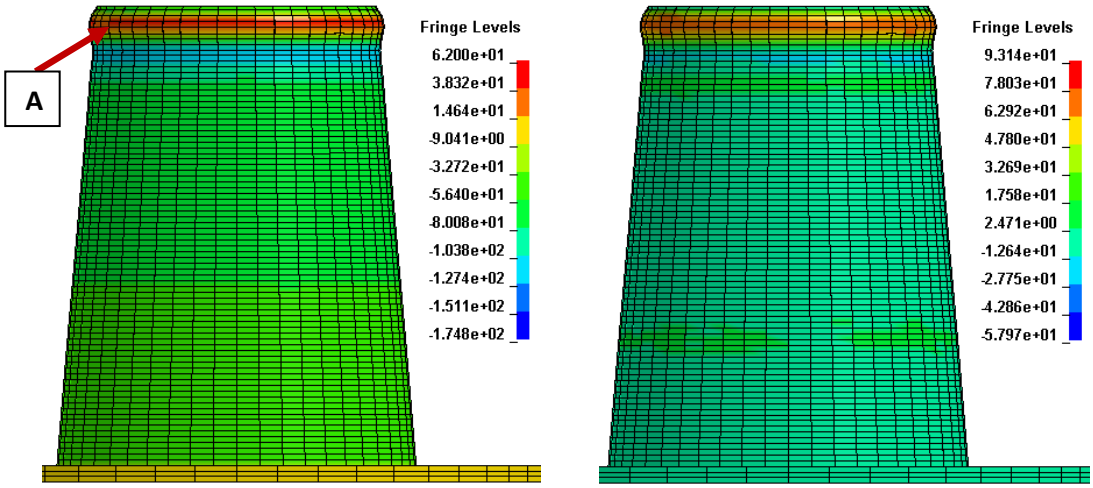

Figure 103: Axial (left) and circumferential (right) stress plots [MPa] PA/GF – 2mm displacement

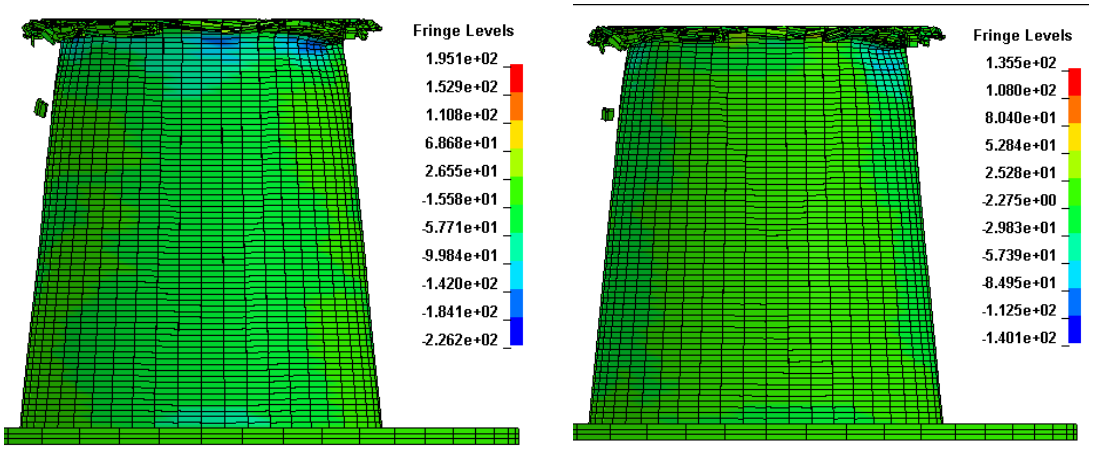

Figure 104: Axial (left) and circumferential (right) stress plots [MPa] PA/GF – 15mm displacement

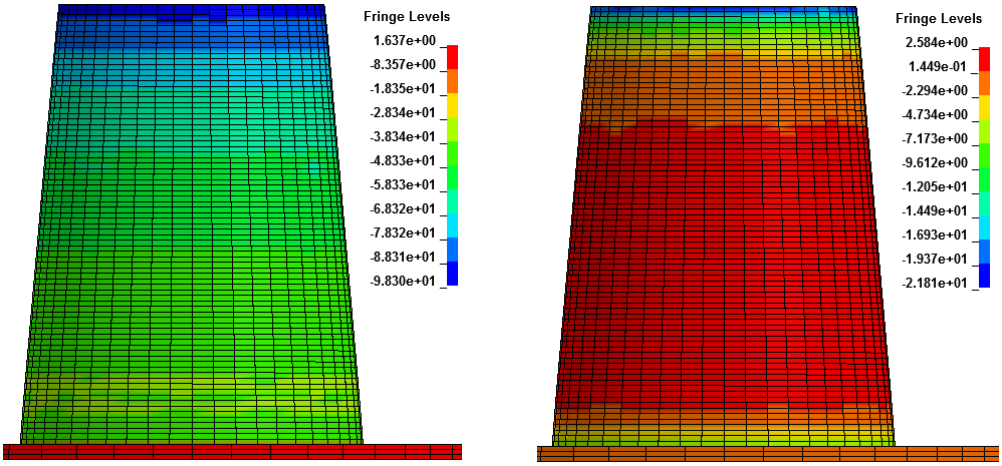

Figure 105: Axial (left) and circumferential (right) stress plots [MPa] PA/GF/SiO_2– 1mm displacement

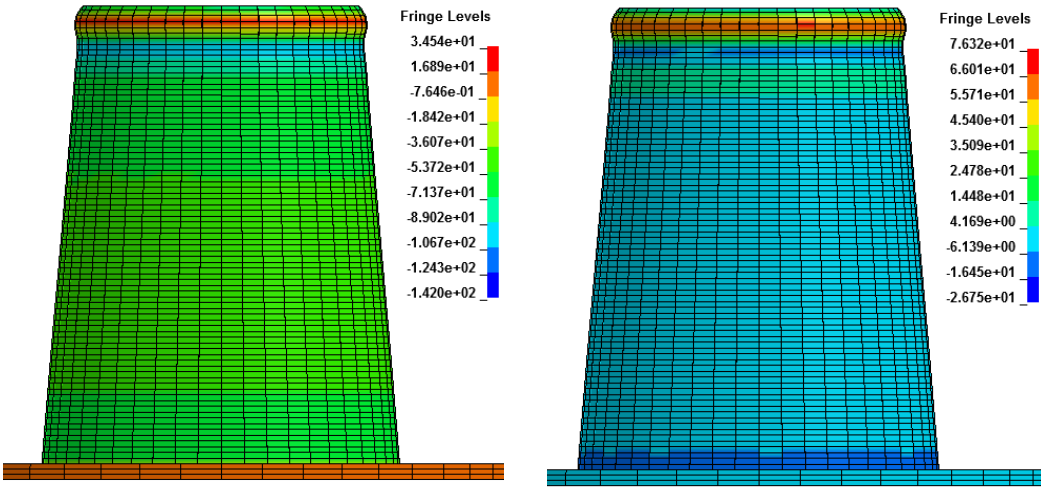

Figure 106: Axial (left) and circumferential (right) stress plots [MPa] PA/GF/SiO_2– 2mm displacement

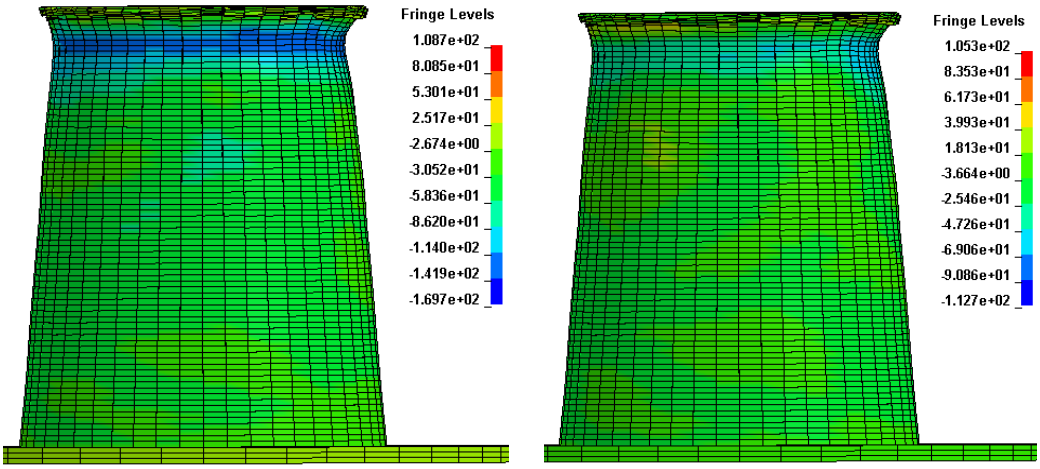

Figure 107: Axial (left) and circumferential (right) stress plots [MPa] PA/GF/SiO_2 – 15mm displacement

At this point the stress field changes from uniform uniaxial compressive to biaxial tensile, on the outer surface, and biaxial tensile-compressive on the inner surface of the wall. This can be clearly seen in Figure 108, when the axial compressive stress reaches its maximum, the plastic bulge is initiated. Subsequently, the axial compressive stress starts to drop and then switches to a positive value. At the same time the hoop stress starts to rise. When both axial and hoop stress reach their maximum, the failure of the structure starts to initiate on the outer surface of the wall. This is visible on the plot as a sudden drop in stresses. This proves that the failure of the structure is a result of the biaxial stress condition.

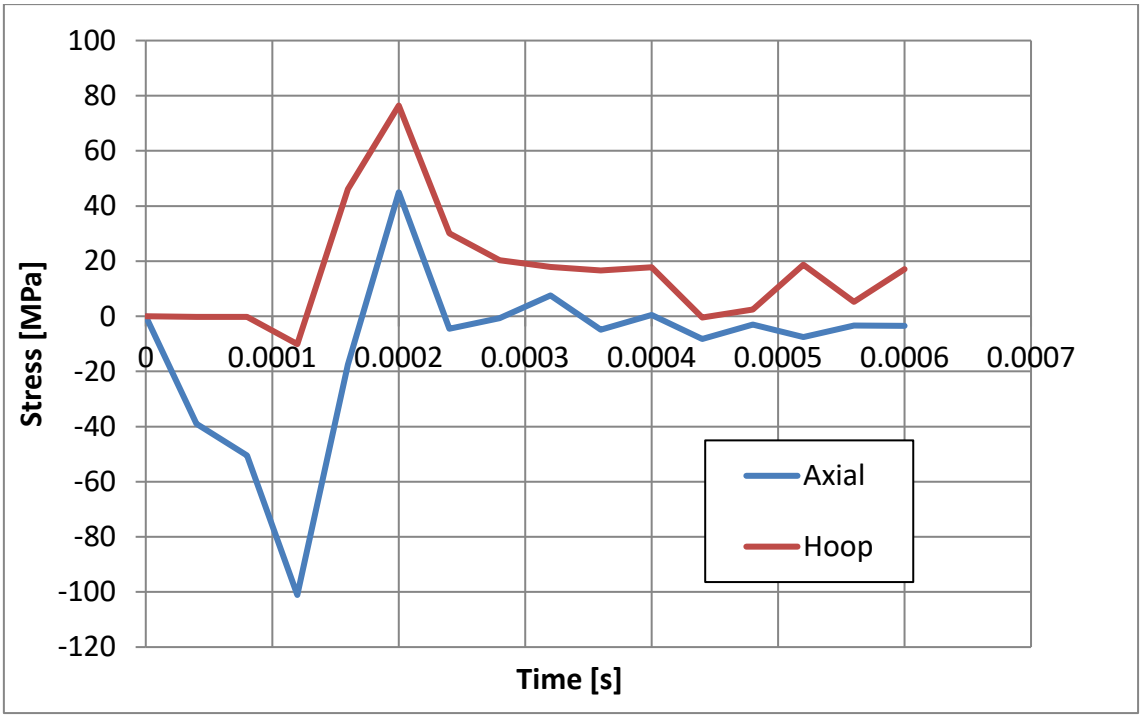

Figure 108: Axial and circumferential stress plots at the outer surface (point A in Figure 103)

In the next stage of the structural collapse the crashed material is being pushed inside the sample. This is causing an expansion of the cone walls followed by their bending (see Figure 109 to Figure 111 and Figure 112 to Figure 114).

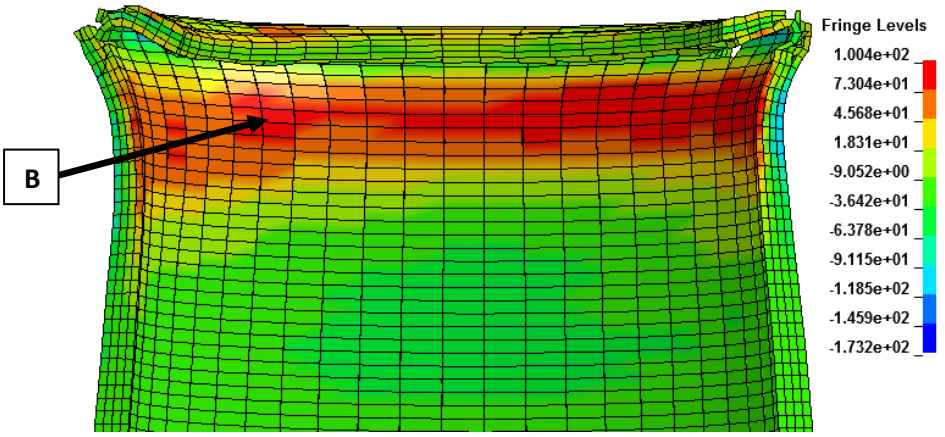

Figure 109: Axial stress plot [MPa] PA/GF/SiO_2 – 4mm displacement

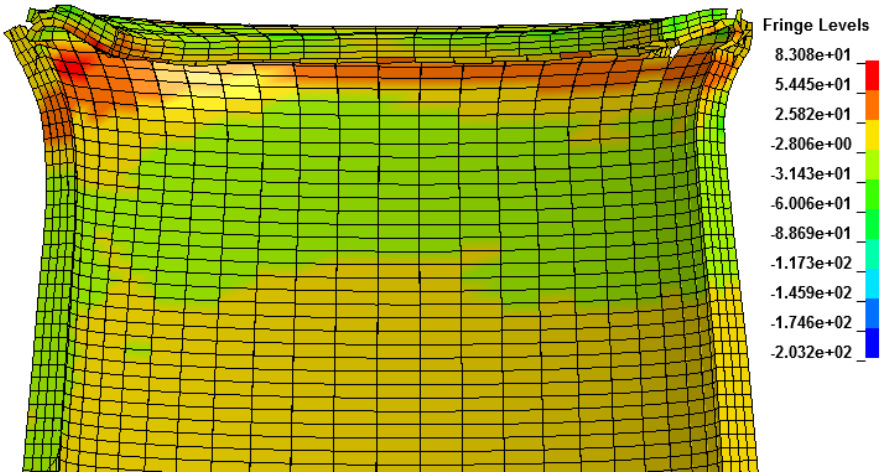

Figure 110: Circumferential stress plot [MPa] PA/GF/SiO_2 – 4mm displacement

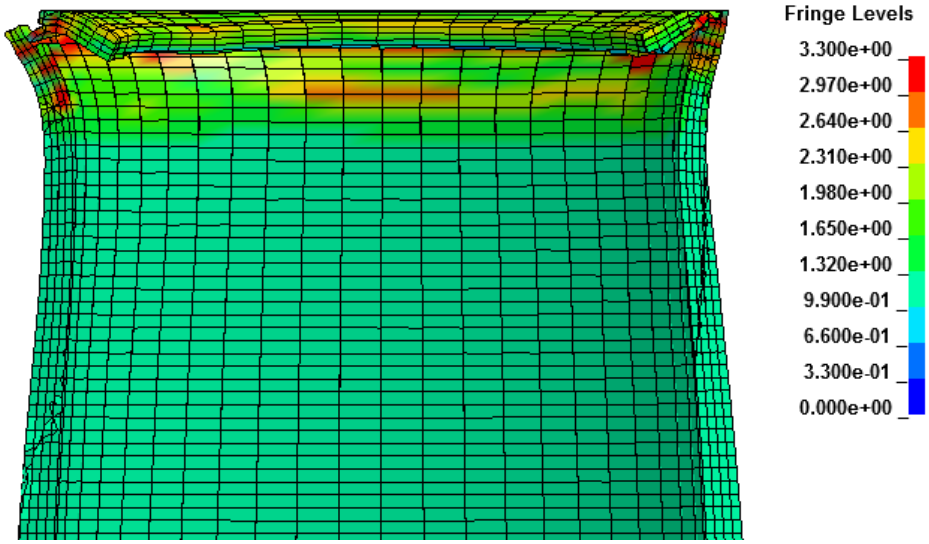

Figure 111: Strain energy density plot [mJ/mm^3 PA/GF/SiO_2 – 4mm displacement

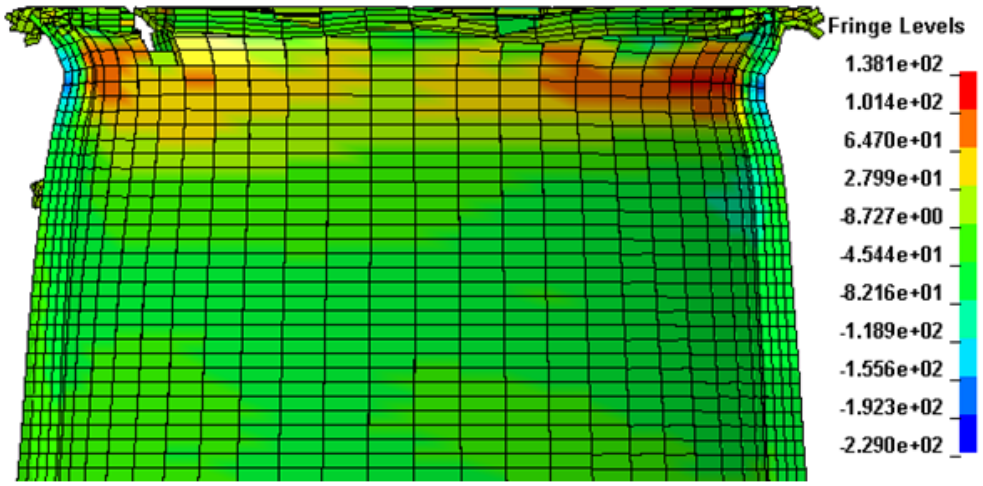

Figure 112: Axial stress plot [MPa] PA/GF – 4mm displacement

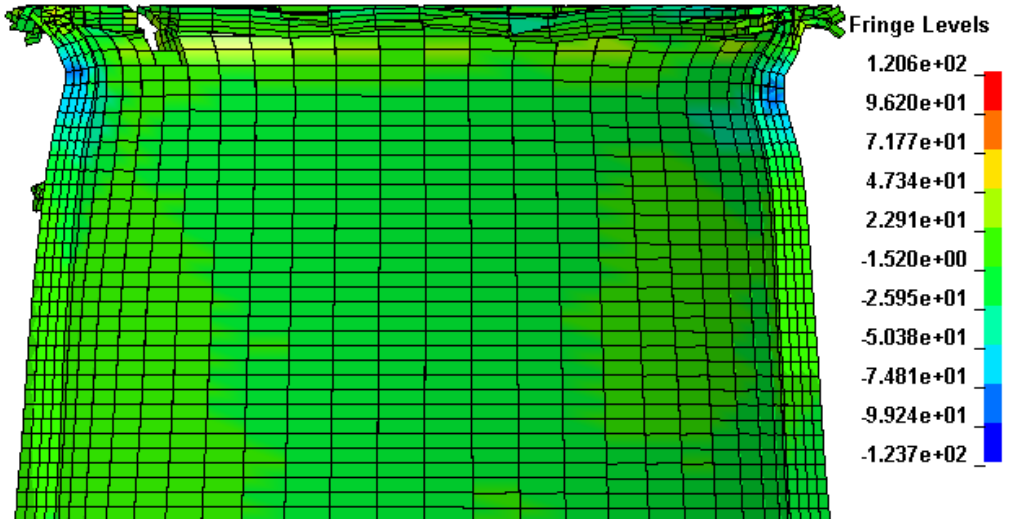

Figure 113: Circumferential stress plot [MPa] PA/GF – 4mm displacement

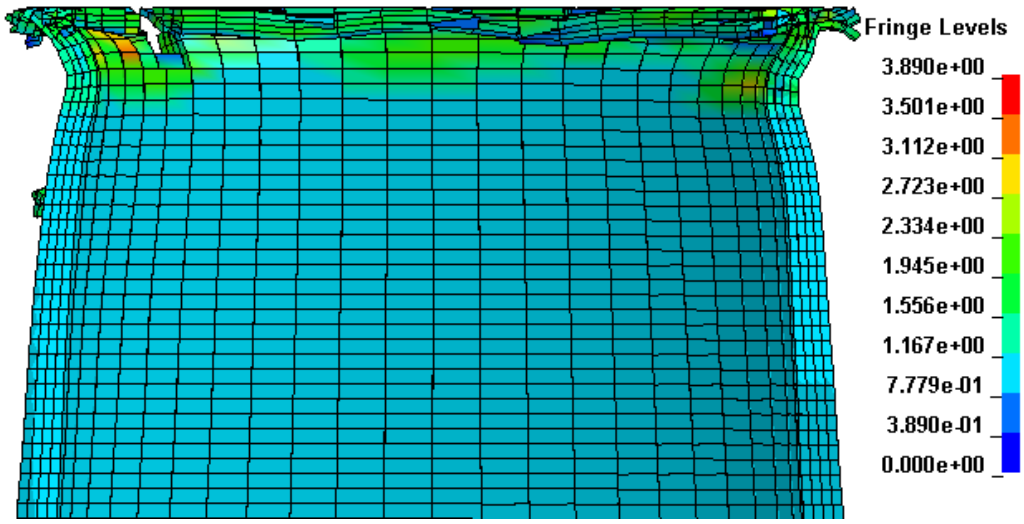

Figure 114: Strain energy density plot [mJ/mm^3] PA/GF – 4mm displacement

The bending induces biaxial tension on the inner surface and biaxial compression on the outer surface of the wall. This is why the failure initiates on the inner surface due to the biaxial tensile stress state (see Figure 115). The whole two stage process repeats during the test four times in PA/GF/SiO_2 and three times in PA/GF which are visible on the load-displacement curves as sudden changes in the measured load.

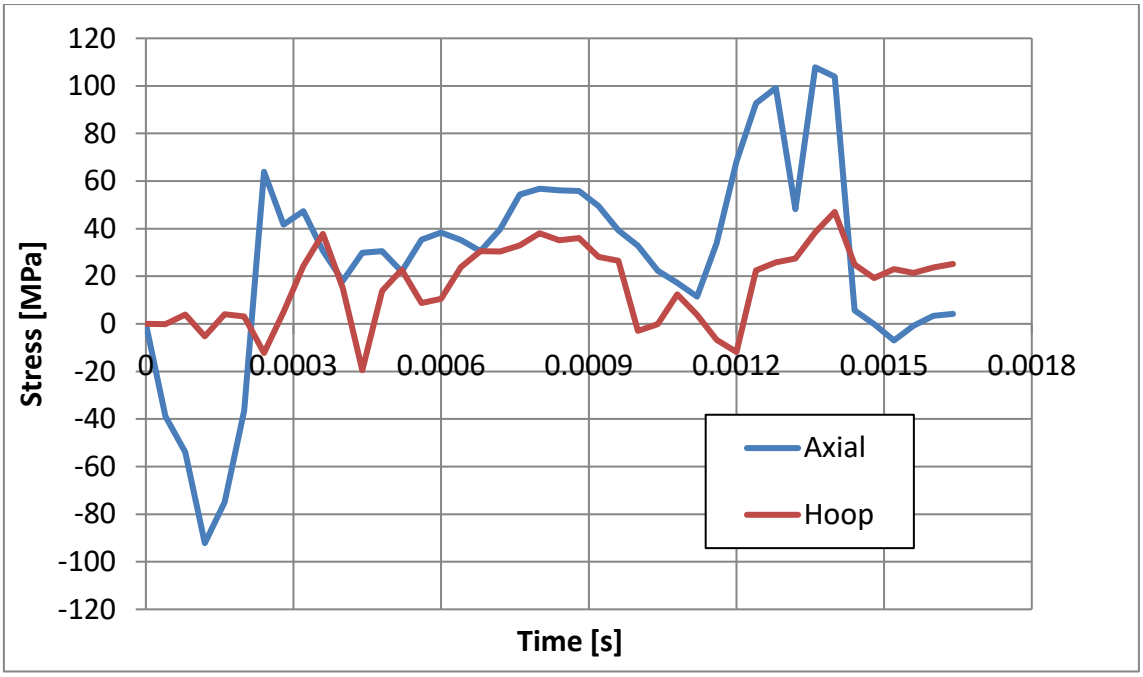

Figure 115: Axial and circumferential stress plots at the inner surface (point B in Figure 109)

6.3.4 Dynamic crash test

The main results concerning the energy absorption capabilities of the composite structures are listed in Table 29. A visual comparison of the modelled and actual drop weight impact tests are presented in Figure 116 to Figure 124. Dynamic load-displacement curves, extracted from the numerical models and the experiments, are presented in Figure 125 and Figure 126.

Analysing the obtained data it can be seen, that the models represented the dynamic crashing behaviour of the conical structures with good accuracy. Table 29 shows the main crashing parameters extracted from the load-displacement

curves. It can be seen that the error in the predicted energy absorption of PA/GF/SiO_2 composite is below 4%. This is a consequence of well predicted mean crashing loads and the crashing length. However a large difference is observed in the values of the initial load peak (25%). This discrepancy is a result of difficulties in fully replicating the triggering mechanism of the initial fracture in the FE model.

Regarding the PA/GF composite the difference between the measured and predicted energy absorption is around 6%. In this case the mean crashing loads are slightly underestimated. The main reason for that is the unstable failure mode undergone by the structure. This failure mode is difficult to represent due to the unpredictable behaviour of the structure. The size of the cracks and broken fragments can vary from test to test due to the imperfections present in the material and configuration of the test. If the fracture mode is stable the influence of these parameters on the structural response is diminished. Due the same reasons as for PA/GF/SiO_2 composite the value of the initial peak load is also overestimated by 25%.

Table 29: Dynamic crashing characteristics

Material	Crash length [mm]	Collapse mode	Initial peak [kN]	Mean crashing load [kN]	Energy absorbed [kJ]
PA/GF_FE	71.2	II	154	47.1	2.56
PA/GF_Ex	69.4	II	207	51.6	2.41
PA/GF/SiO2_FE	58.5	III	169	54.9	2.86
PA/GF/SiO2_Ex	56.8	III	123	56	2.75

Figure 116 to Figure 124 show that the model predicted the failure mode of the structures, made of PA/GF (mode II) and PA/GF/SiO_2 composites (mode III).

Regarding the PA/GF composite, it can be seen that the model captures the brittle behaviour of the material. The axial cracks, initiated at an early stage of

the crash, propagate through the structure affecting its integrity. As a result of the extensive cracking, large fragments are sheared off from the structure. This results in a low energy absorption capability of the material. The final shape of the crashed specimens (Figure 119 and Figure 124) made of PA/GF material, is similar in both the experiment and the FE simulation. It consists of remaining unbroken fragment of the structure, with irregular shape and number of cracks. There is no significant plastic deformation visible on the fracture surface or the broken fragments.

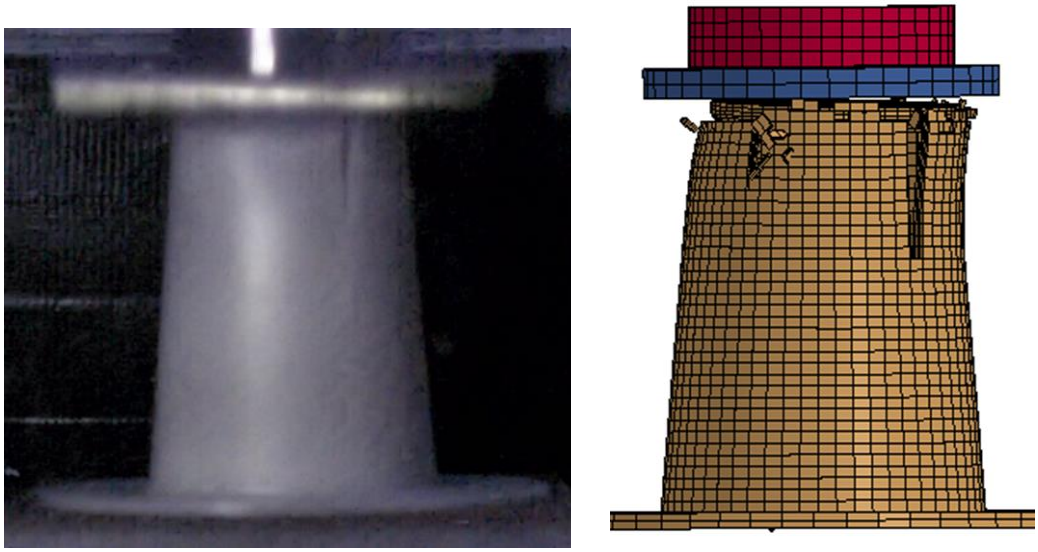

Figure 116: Modelled and experimental dynamic crash test PA/GF – 15 mm displacement

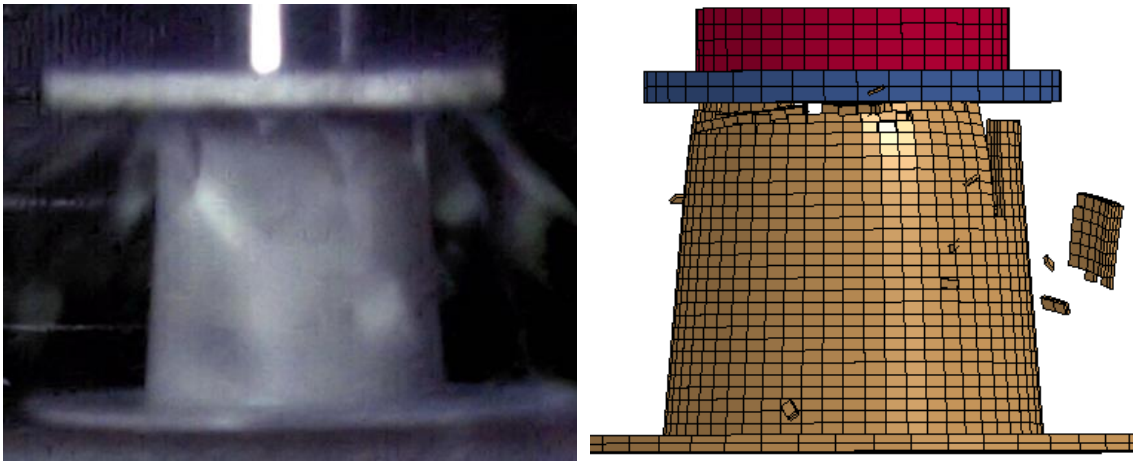

Figure 117: Modelled and experimental dynamic crash test PA/GF – 45 mm displacement

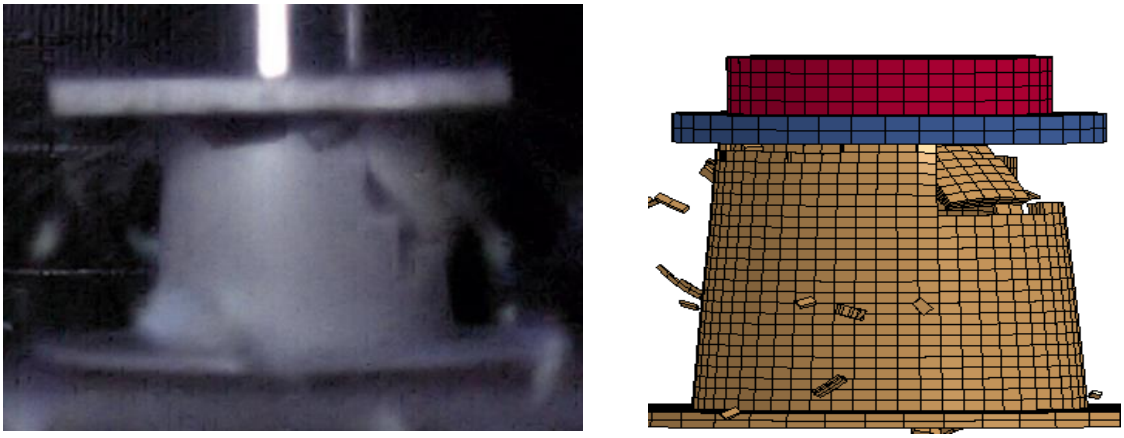

Figure 118: Modelled and experimental dynamic crash test PA/GF – 55 mm displacement

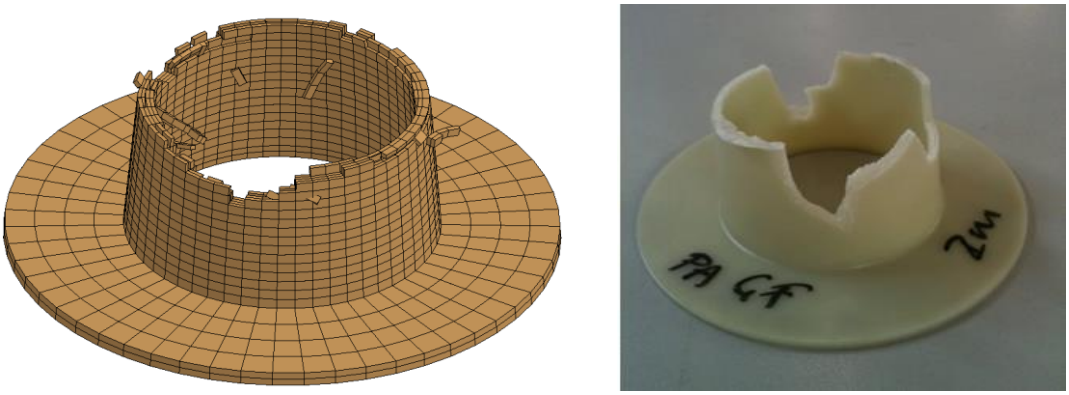

Figure 119: Modelled and experimental dynamic crash test PA/GF – final shape

In the case of the PA/GF/SiO_2 composite the FE model was also effective in predicting the fracture behaviour of the structure. The transition from unstable to stable failure of the structure was accurately captured by the FE model. There is no significant axial cracking initiated in the remaining structure, therefore its integrity is unaffected. The failure is stable and progressive, and is observed as a combination of plastic deformation and local fragmentation. The final shape of the modelled specimen corresponds to the one seen in the experiments (see Figure 124). The remaining fragment does not contain any axial cracks and its failure surface is relatively flat. Furthermore, the height of the crashed specimen is similar to that measured on the actual sample (FE – 64mm and Experiment - 63mm).

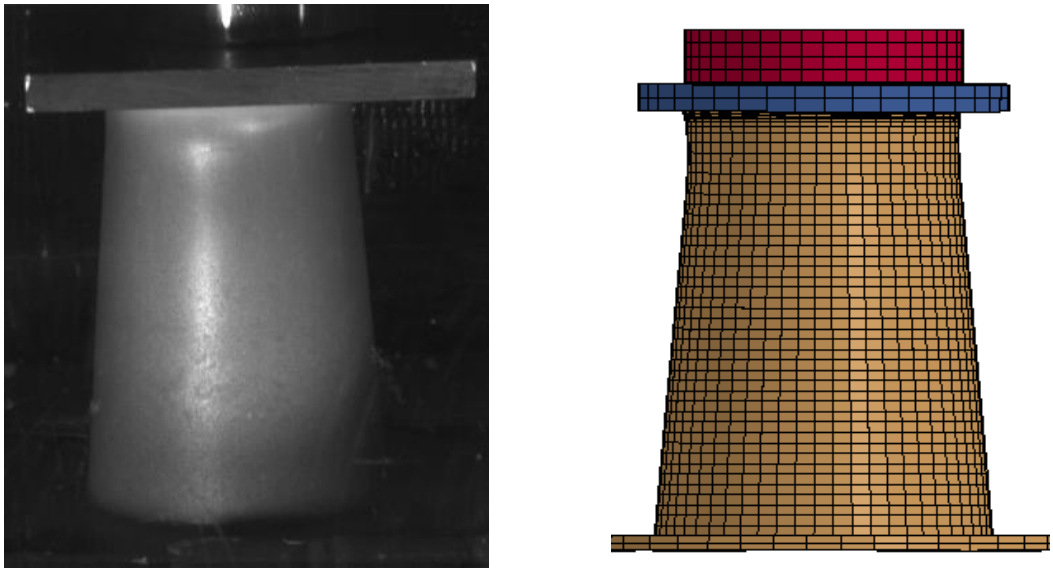

Figure 120: Modelled and experimental dynamic crash test PA/GF/SiO_2 – 4 mm displacement

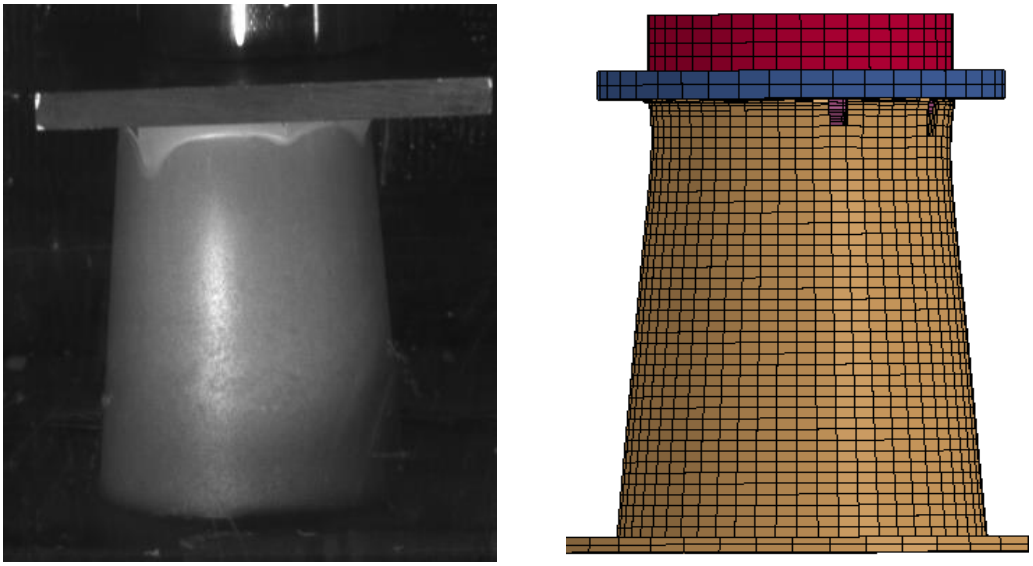

Figure 121: Modelled and experimental dynamic crash test PA/GF/SiO_2 – 8 mm displacement

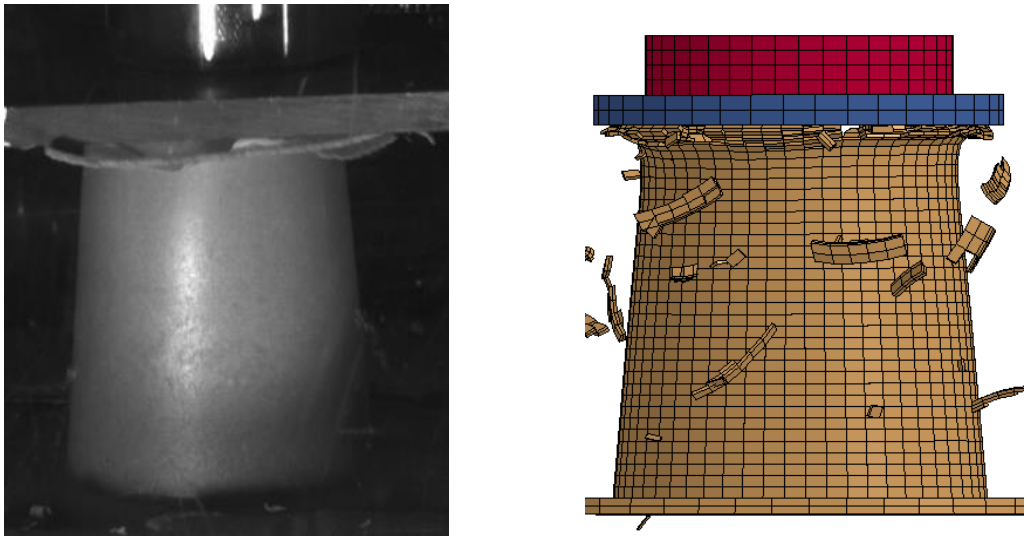

Figure 122: Modelled and experimental quasi-static crash test PA/GF/SiO_2 – 35 mm displacement

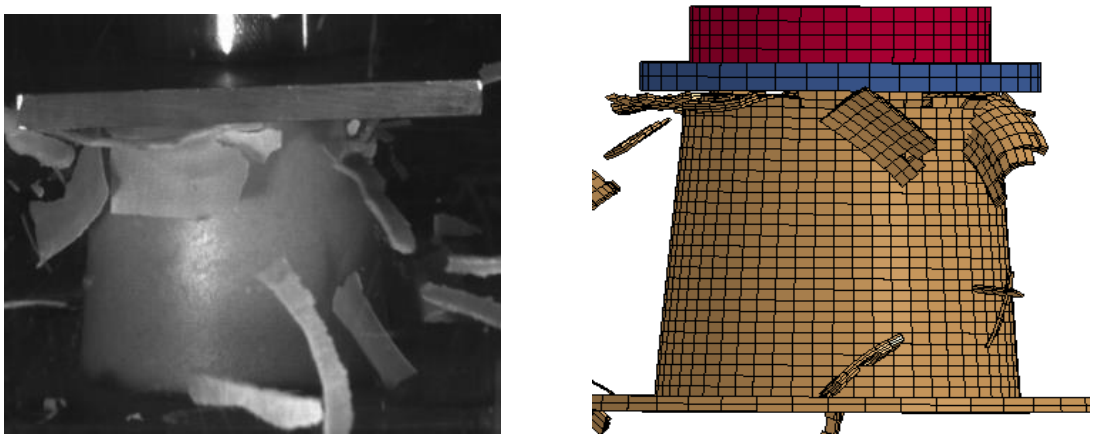

Figure 123: Modelled and experimental quasi-static crash test PA/GF/SiO_2 – 45 mm displacement

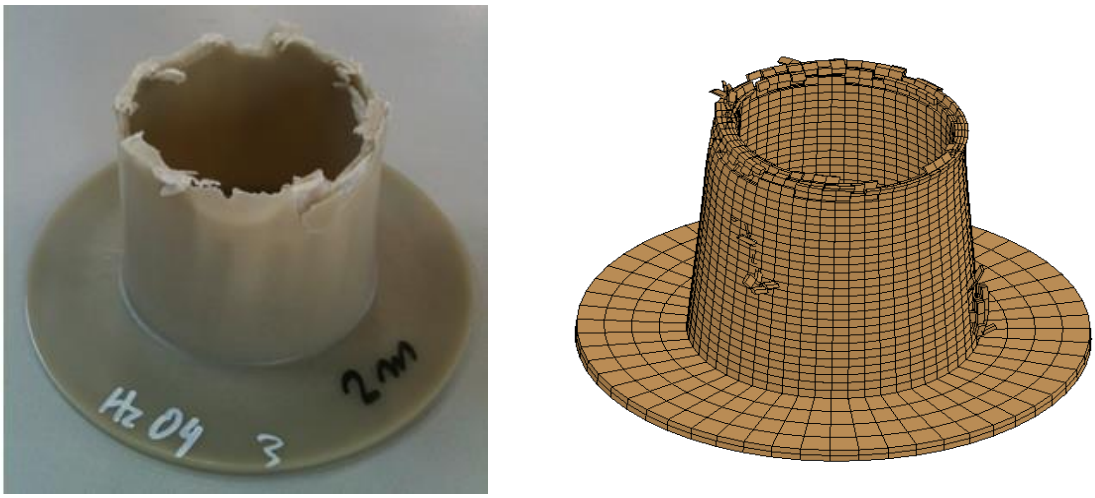

Figure 124: Modelled and experimental quasi-static crash test PA/GF/SiO_2 – final shape

Analysing the load displacement curves of both composites it is clearly visible that the models predicted the shape measured during the experiments. After the initial load peak, limited by the triggering of initial failure, a secondary load peak is observed. This is followed by a period of nearly zero load, associated with a limited ability of the structure to resist the loads. This limitation is caused by the axial cracks, which were triggered at an early stage of the crash (see Figure 116). In the case of PA/GF composite the axial cracks propagate quickly into the structure, causing a further reduction in its ability to resist the applied loads. This effect is observed as lower mean crashing loads. After all the material affected by the initial cracking is detached from the structure, the impactor comes into contact with the remaining part of the structure. This is visible on the plot as a second load peak, with a similar magnitude as the initial one. As the fracture surface is irregular, the applied loads are concentrated on a small area, causing localized failure, which damages the overall integrity of the structure. Beyond this point, the structure is no longer able to resist the loads, and therefore does not absorb the energy. The load measurement drops to zero beyond the displacement of 48mm. However, the actual crashing length is significantly larger (FE - 71.2mm, experiment 69.4mm).

As the PA/GF/SiO_2 composite is more ductile, the cracks initiated at an early stage do not propagate deep into the structure. This is why, to cause further crashing of the structure, a higher crashing load needs to be applied. This is visible on the plot as a gradual increase in load with progressing displacement (see Figure 126). Further crashing is realized in stages of alternating plastic deformation and material failure. This is represented on the curve as several load peaks. It is important to note that after the initial stage, the structure made of PA/GF/SiO_2 composite fail in a stable and progressive manner. Hence, after the initial stage of the crash, the crashing loads do not drop to any values near to zero.

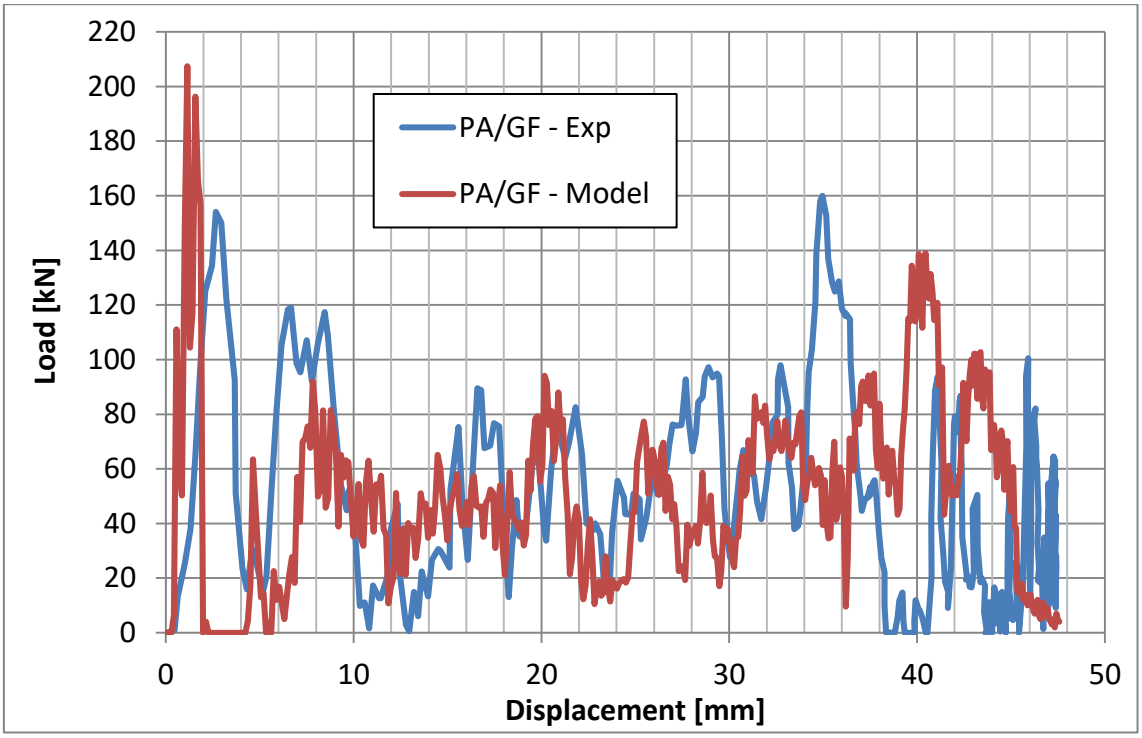

Figure 125: Dynamic load-displacement curves PA/GF

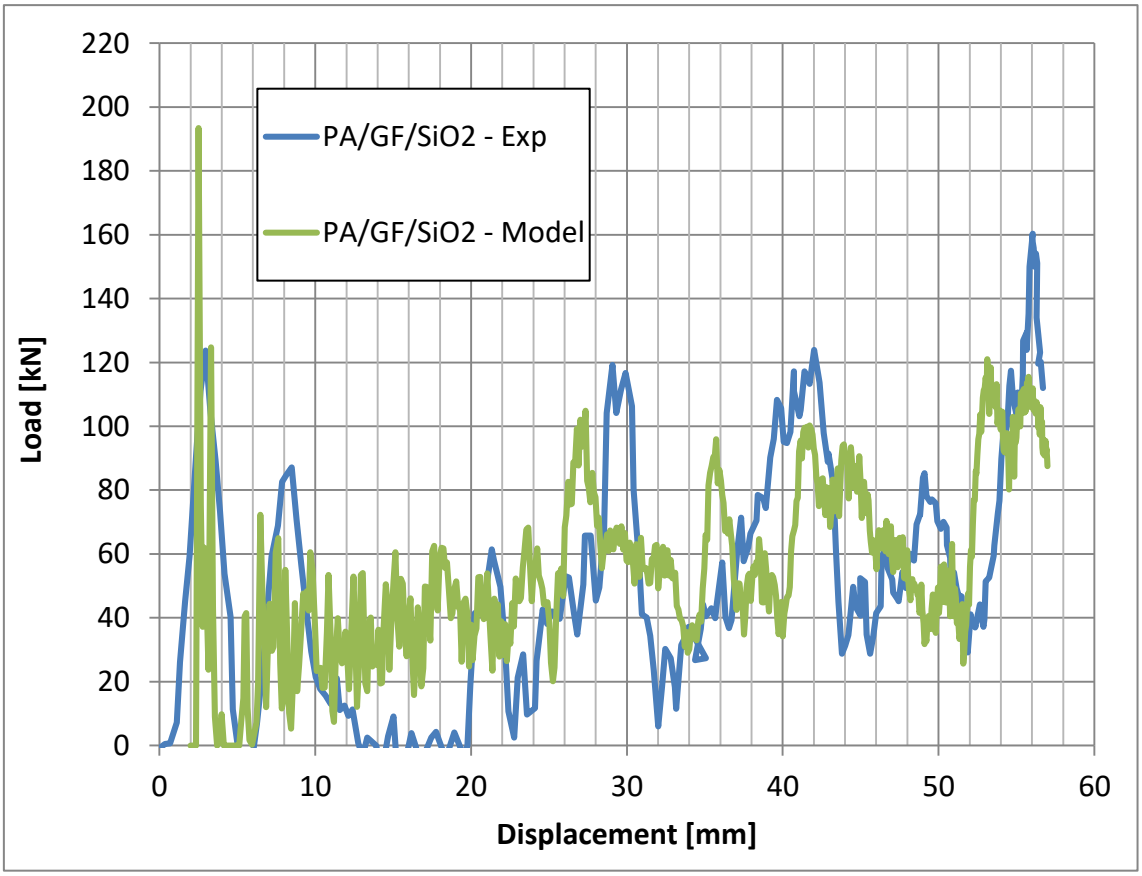

Figure 126: Dynamic load-displacement curves PA/GF/SiO_2

The stress plots shown in Figure 127 to Figure 139 explain in more details the difference in fracture mode observed between the two composites. At an early stage of the crash, the elasto-plastic deformation is initiated by the axial compressive loads in both composites (see Figure 127 and Figure 131). This causes an initiation of the axial cracks (see Figure 128 and Figure 132). However, only in the PA/GF composite the cracks propagate deeply into the structure, despite that high circumferential stress is present around the crack tip in both structures (see Figure 130 and Figure 132) . As a result, in the PA/GF composite large fragments of the material are detached from the structure at an early stage of the crashing event. On the contrary, in PA/GF/SiO_2 composite its high ductility does not allow for propagation of the cracks. That is why high axial stress, initiated by the bending of the cone wall, dominates the failure and leads to detachment of the small fragments (see Figure 134-Figure 136).

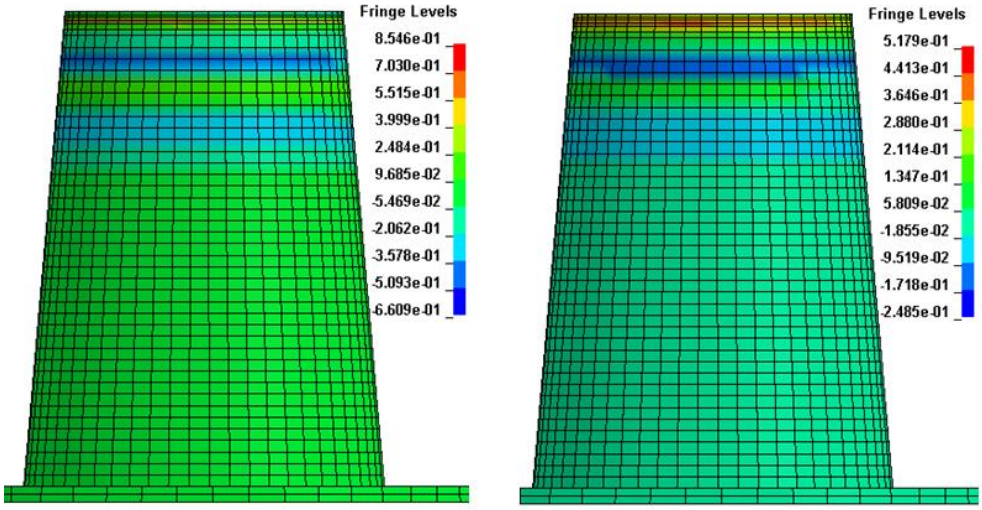

Figure 127: Axial (left) and circumferential (right) stress plots [MPa] PA/GF – 1mm displacement

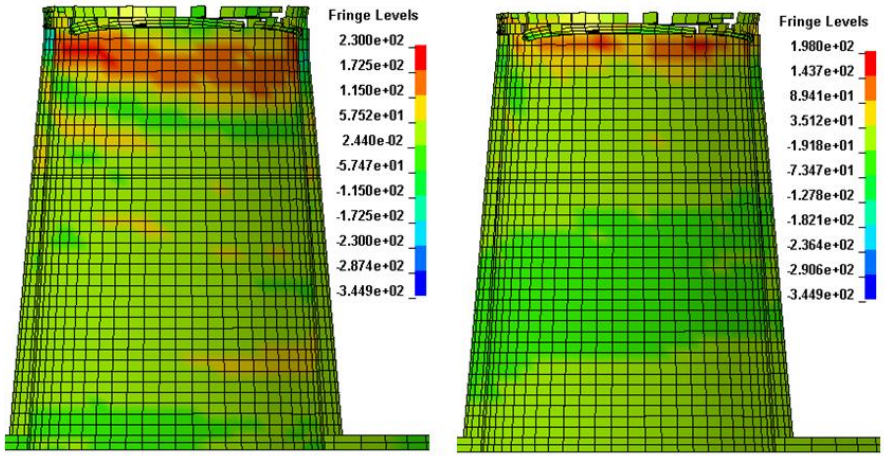

Figure 128: Axial (left) and circumferential (right) stress plots [MPa] PA/GF – 4mm displacement

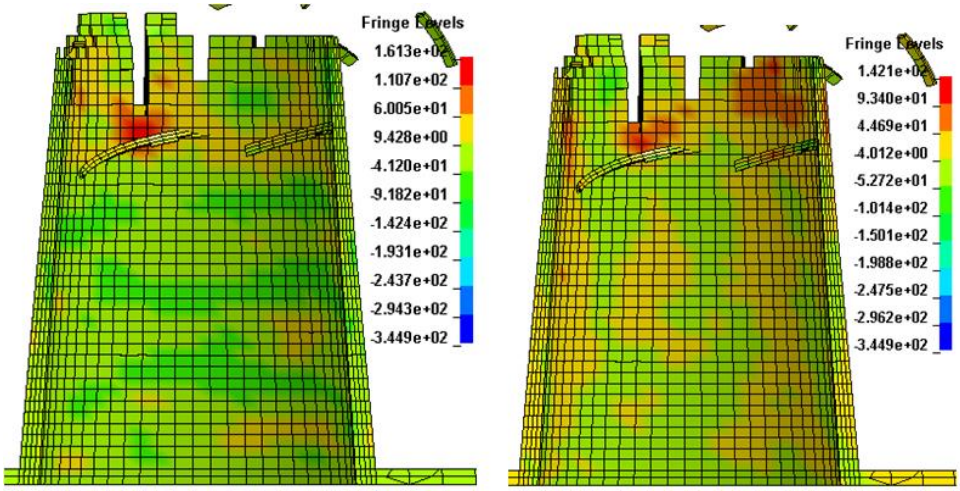

Figure 129: Axial (left) and circumferential (right) stress plots [MPa] PA/GF – 10mm displacement

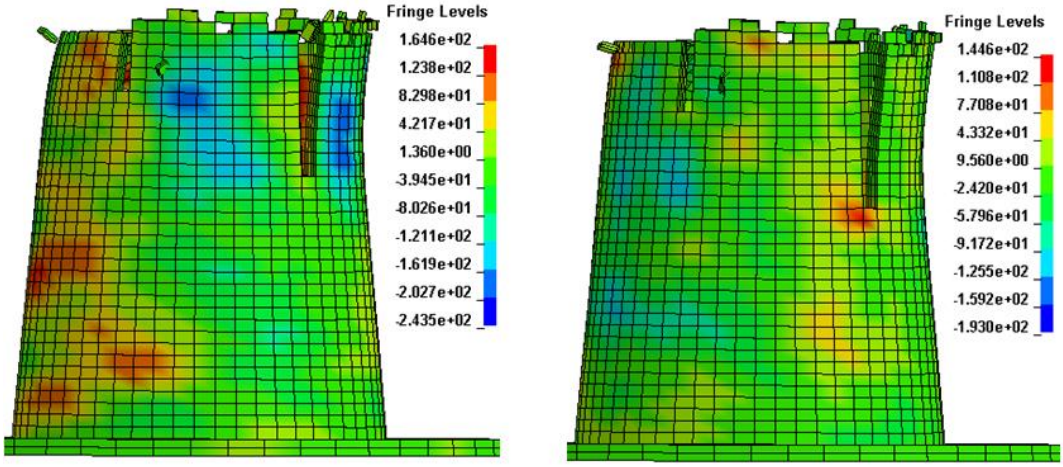

Figure 130: Axial (left) and circumferential (right) stress plots [MPa] PA/GF – 20mm displacement

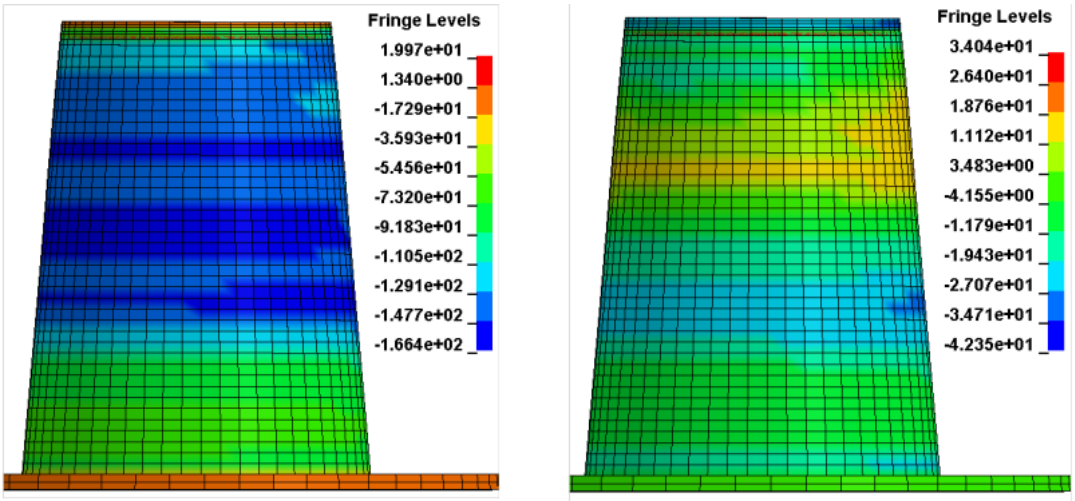

Figure 131: Axial (left) and circumferential (right) stress plots [MPa] PA/GF/SiO_2 – 1mm displacement

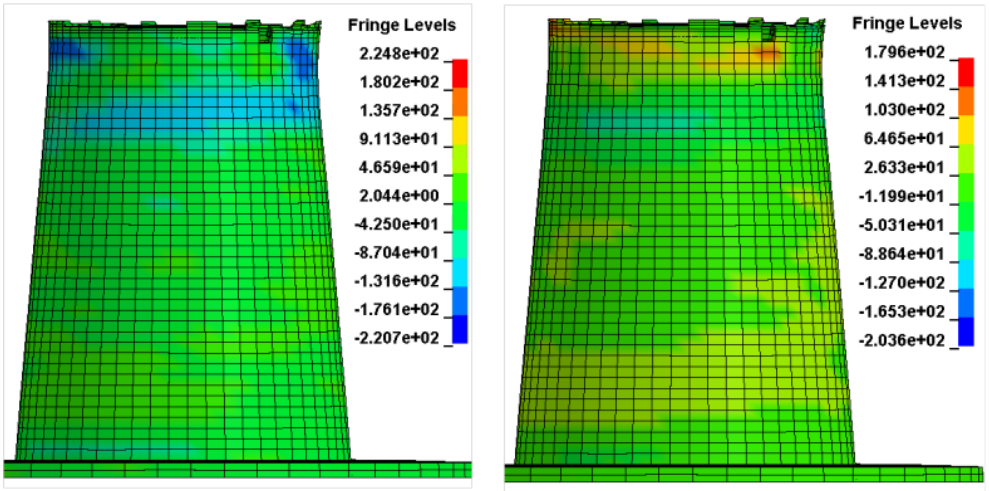

Figure 132: Axial (left) and circumferential (right) stress plots [MPa] PA/GF/SiO_2 – 4mm displacement

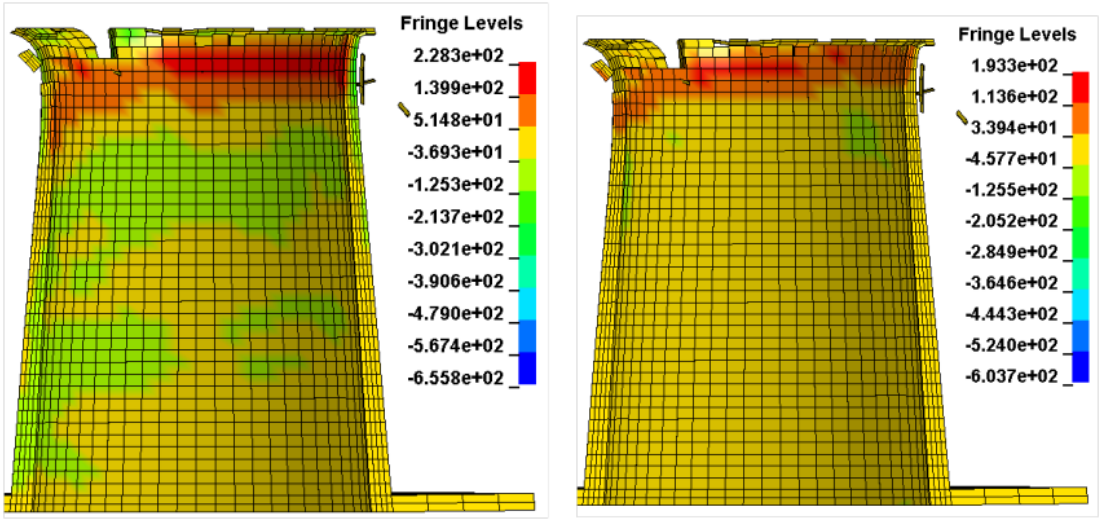

Figure 133: Axial (left) and circumferential (right) stress plots [MPa] PA/GF/SiO_2 – 10mm displacement

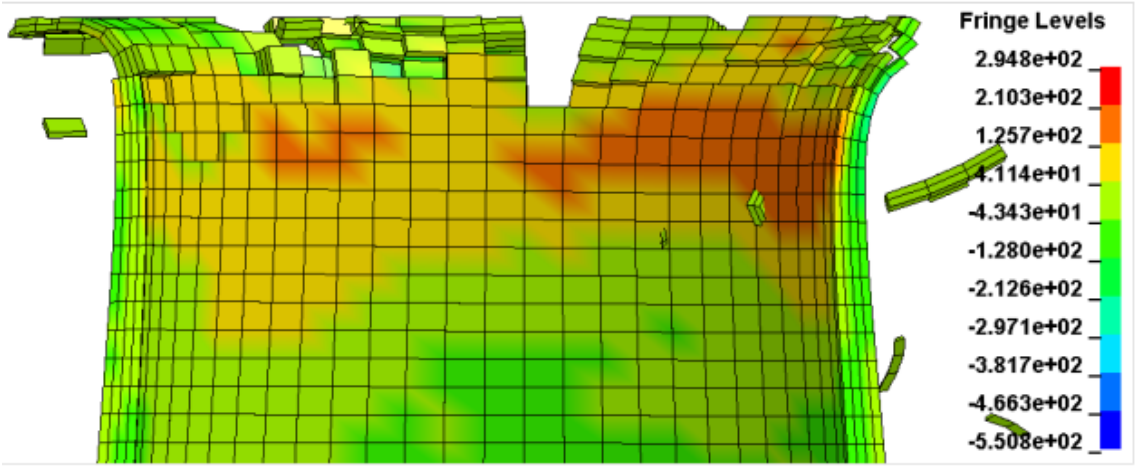

Figure 134: Axial stress plot [MPa] PA/GF/SiO_2 – 10mm displacement

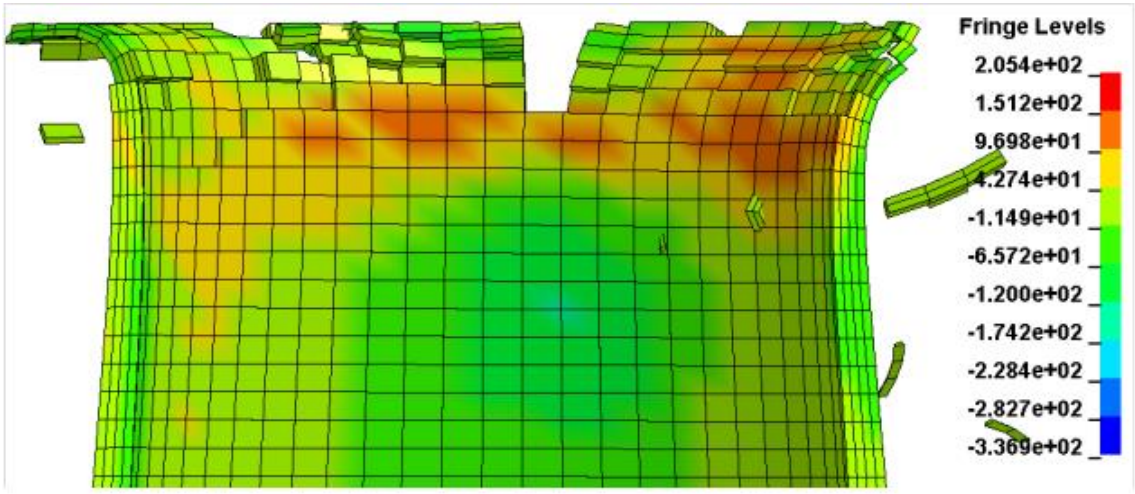

Figure 135: Circumferential stress plot [MPa] PA/GF/SiO_2 – 10mm displacement

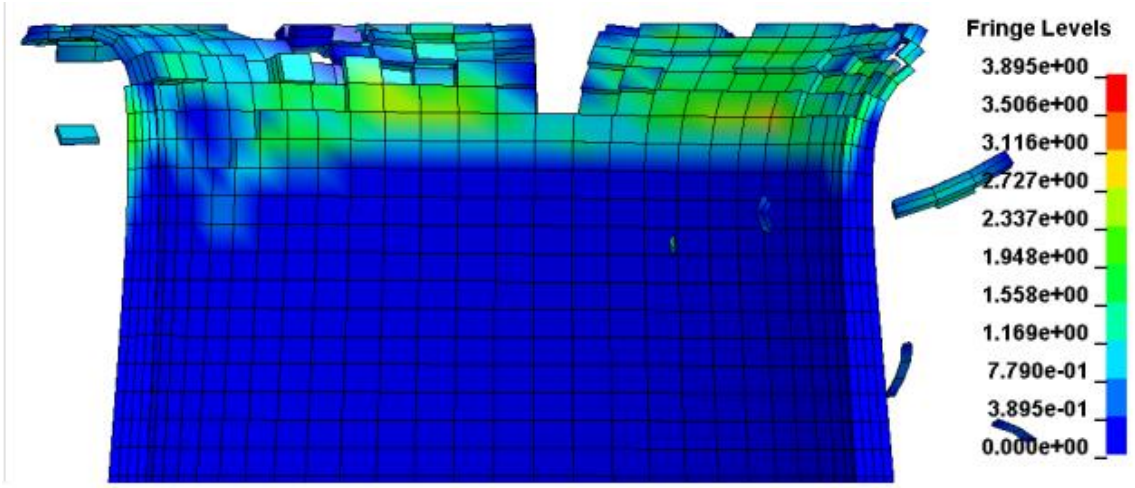

Figure 136: Strain energy density [mJ/mm^3] PA/GF/SiO_2 – 10mm displacement

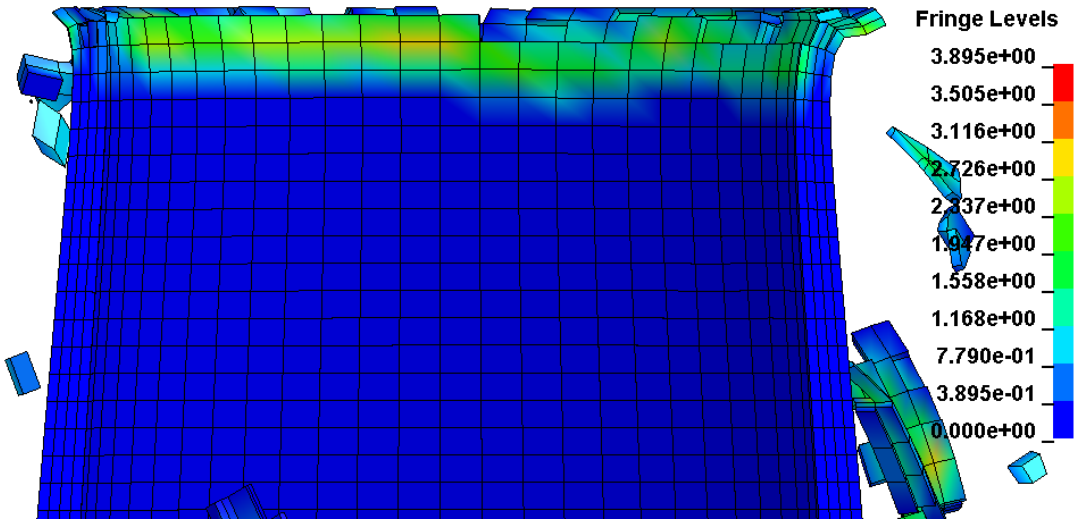

Figure 137: Strain energy density [mJ/mm^3] PA/GF/SiO_2 – 20mm displacement

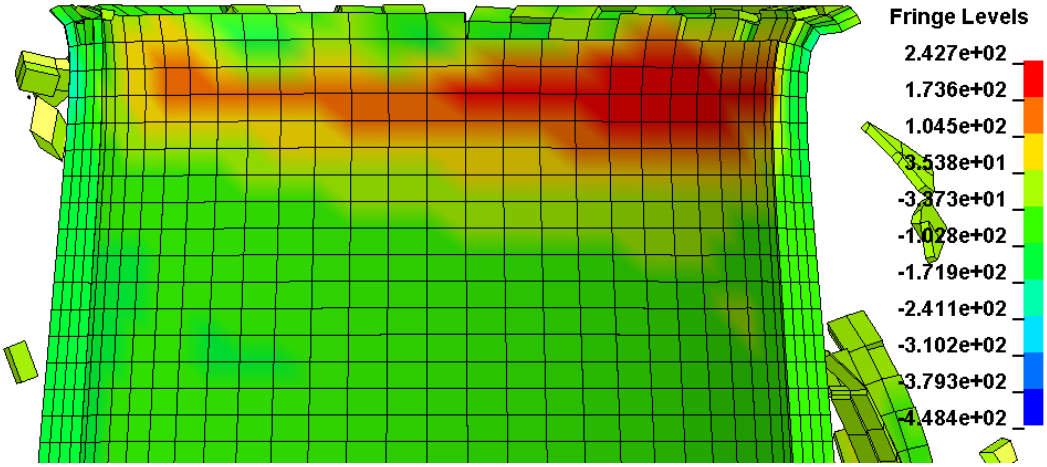

Figure 138: Axial stress plot [MPa] PA/GF/SiO_2 – 20mm displacement

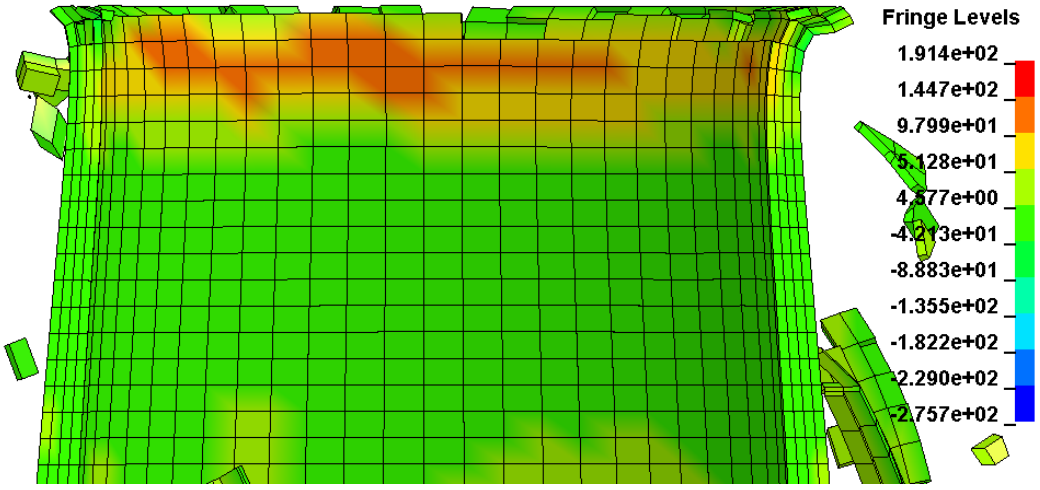

Figure 139: Circumferential stress plot [MPa] PA/GF/SiO_2 – 20mm displacement

6.4 Discussions

6.4.1 Mesh sensitivity

In order to demonstrate that the generated FE models provide accurate representation of the crash tests, a mesh sensitivity studies have been carried out. Figure 143 shows a variation in the impact energy absorption prediction error due to the number of elements in the model. Four different mesh refinements have been used for the purpose of this study. It can be seen that above 19,000 elements for the static test and 15,000 elements for the dynamic test, the error curves start to flatten. This shows that any further increase in the number of elements would result only in an insignificant reduction in the prediction error. This is why it can be concluded the prediction errors observed in the models are not associated with the mesh density.

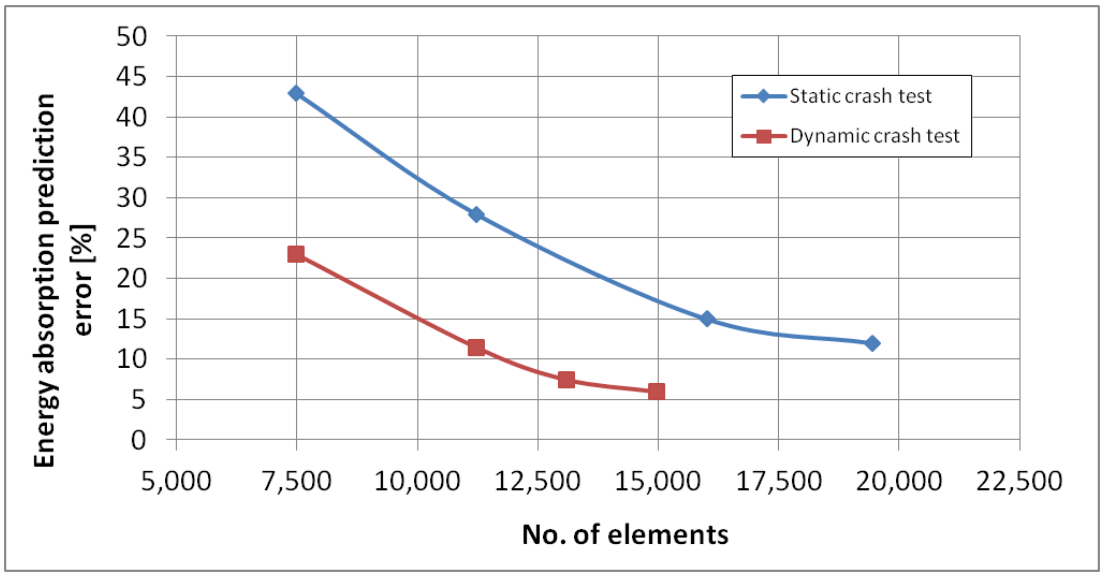

Figure 140: Mesh sensitivity

6.4.2 Accuracy of the model

The main features of the UMAT, presented in Chapter 5, were developed based on the requirements defined in a series of uniaxial specimen testing as well as structural testing, carried out at static and dynamic conditions. Namely, these are orthotropic elasto-plasticity, pressure dependent yield, strain rate sensitive elasto-plasticity and failure as well as strain energy density based failure criterion.

The main benefit of failure criterion, defined by maximum allowable strain energy density, is that it takes into account the entire nonlinear stress-strain response. In practise this means that the element will fail once both its stress and strain reach the critical values. This is crucial when the material is characterized by the hardening modulus near zero. In such a case the failure, defined only by maximum allowable stress, may be premature if the maximum stress is reached before the maximum strain. This is visualized on the example shown in Figure 141. The stress reaches maximum value at the strain equal to 6%. However, the sample can sustain further deformation up to a value of 6.8%. If the failure was defined by maximum stress this would induce significant error in the material failure prediction.

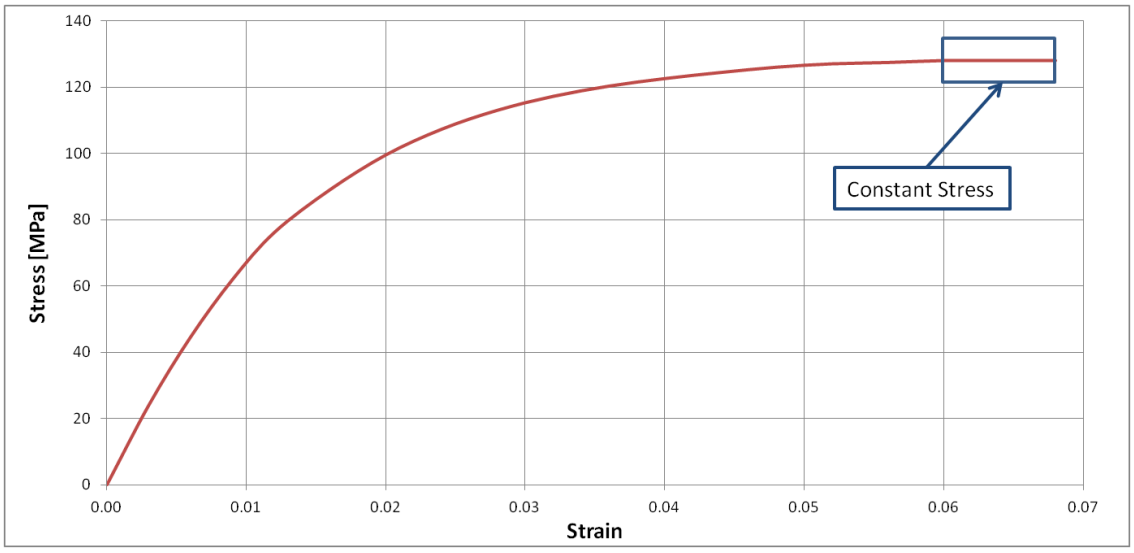

Figure 141: Low hardening material response

Furthermore, if the ultimate value of the strain energy density is being scaled, rather than stress or strain, for strain rate sensitivity or multi-axial yielding purposes, it warranties more accurate predictions. This is due to the fact that the differences between the strain energy densities measured at different strain rates, or loading conditions are insignificant in relation to differences in ultimate strengths or strains (see Table 9, Table 10 and Table 21). Another important improvement, in relation to standard Ls-Dyna models, is the use of

pressure sensitive yield criteria. In practice this means that the model is able to represent different yield and strength in tension and compression. As the structures studied in this thesis are subject to both tensile and compressive loads applied at the same time, this feature is crucial to provide accurate results.

The numerical modelling was also carried out on the conical structures subjected to static and dynamic crashing loads. A good correlation between the numerical predictions and the experiments was visible on the load displacement plots. However, some discrepancies were observed in the values of the crashing loads. The most evident difference was observed in the values of the initial load peak, which were over-predicted in the model. This error was introduced by the inadequate representation of failure triggering mechanism. The magnitude of the initial peak depends on the strength of the material. However, it has been observed that there is a weak point on the connection between the top surface of the structure and the conical surface of the wall. The sharp edge connecting the two surfaces causes a fibre breakage during the injection moulding process. This results in diminished material properties present in that region. As the difference in the material properties was not possible to measure it was not taken into account in the FE model. This causes the over prediction of the initial load peak, observed in the simulations, which uses global material properties derived in the uniaxial specimen test.

Furthermore, it was observed that the models tend to underestimate the crashing loads in the quasi-static test. The most likely reason for that error is limited data available at shear conditions, as well as lack of biaxial test results. As discussed in chapter 6.2, the shear data was taken from the literature, therefore it does not fully represent the actual properties of the materials tested. The shear loads play a more important role in failure of the structure at static conditions; they are around 15% of the tensile loads (see Figure 142. In the case

of the dynamic test the shear loads are less than 5% of the tensile loads, therefore their influence on the material failure is insignificant (see Figure 143).

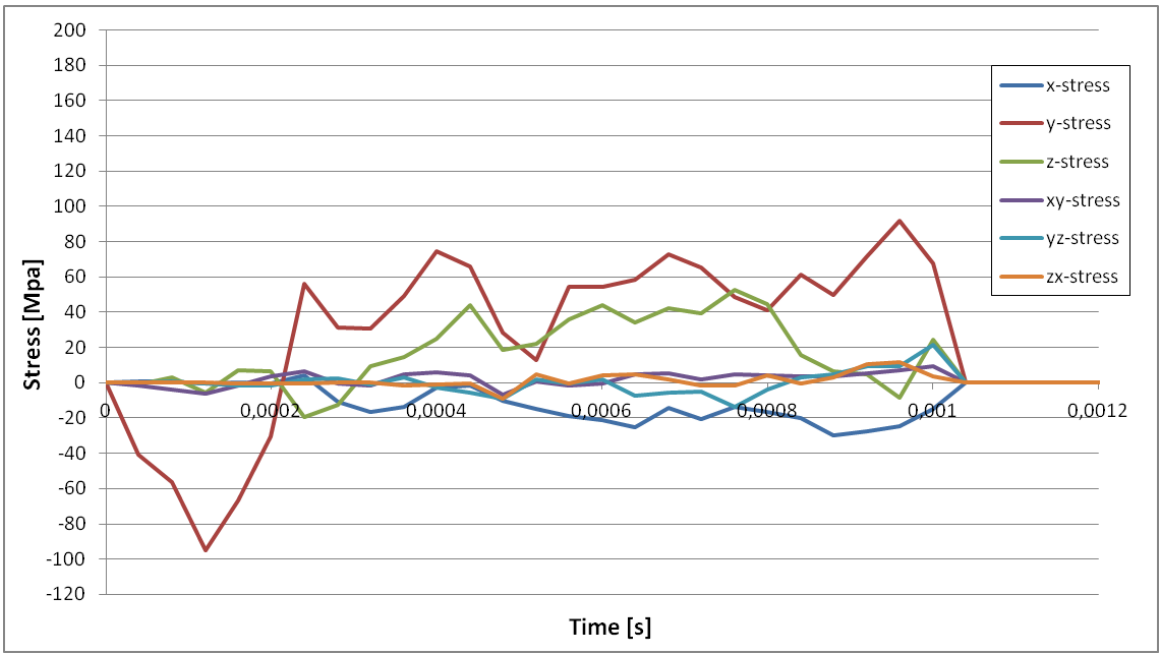

Figure 142: Stress components at the crack tip - static test

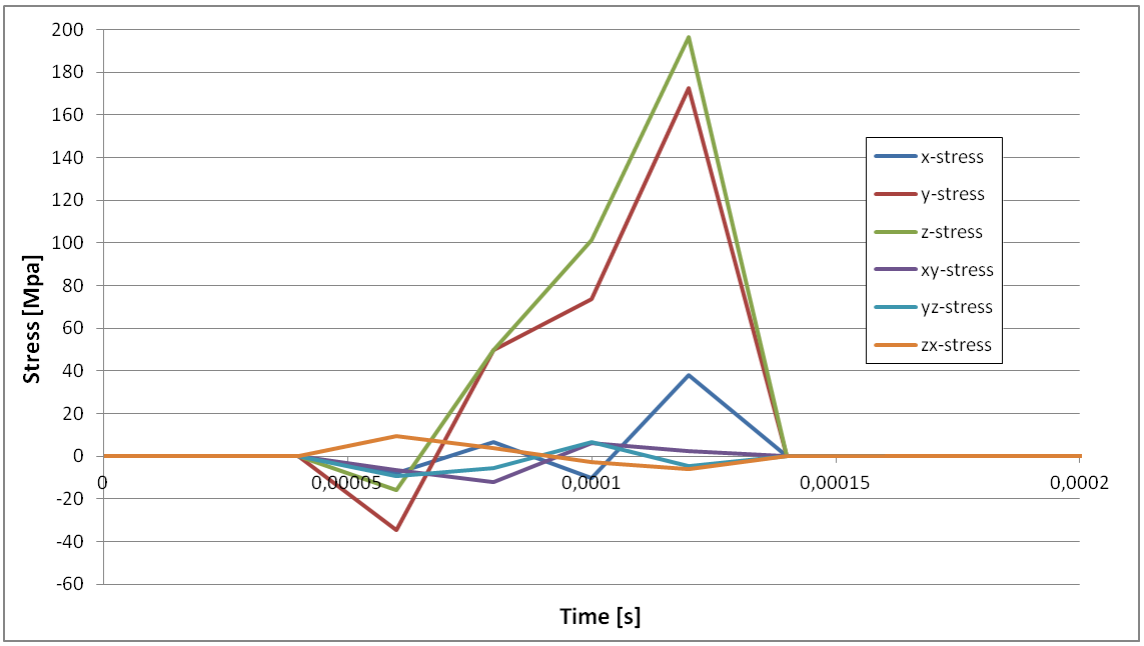

Figure 143: Stress components at the crack tip - dynamic test

6.4.3 Fracture mechanism

The analysis and discussion in the previous chapter show that the FE models built using the UMAT can provide an accurate representation of the static and dynamic crash tests. This is why these models can be used with confidence to predict the fracture mechanism process observed in the conical composite structures and, understand how it affects their energy absorption capability.

The amount of plastic deformation, as well as material failure present in the structure, is governed by the applied stress field. The stress field consist of three uniaxial and three shear components. In case of axial crashing the biggest contribution to plastic deformation and failure comes from the axial and circumferential stress components. In the quasi-static crash test, a secondary role is played by the two shear components, whereas their effect can be completely neglected in the case of the dynamic test. As is shown in Figure 108 and Figure 115, the failure of the structure is a result of biaxial tensile stress state, regardless of the material or loading condition. However, the fracture mechanism, which is a result of that biaxial stress state, is highly dependent on the material properties and the loading condition. In the neat PA/GF composite the ductility of the material in the transverse direction is insufficient to resist the applied deformations. This is why axial cracks are initiated (see Figure 112). In the case of the composite tested at the dynamic condition the ductility is even lower, therefore the cracks easily propagate deeply into the structure (see Figure 130). This causes significant damage to the structural integrity of the sample, indicating low energy absorption capability of that material. In the composite filled with SiO_2 particles, the ductility is significantly improved. This is why the axial cracks do not initiate during the static test (see Figure 109), or initiate but do not propagate as observed in the dynamic test (see Figure 133). As a result the failure is initiated in the circumferential rather than axial

direction. This effect changes the overall collapse mechanism of the structure and improves the energy absorption capability of the structure.

6.5 Conclusions

The FE modelling of the nanocomposite materials and structures has been carried out using the UMAT implemented into Ls-Dyna software. The mechanical properties derived from a series of experiments were used to determine and calibrate various parameters of the model. The initial validation of the numerical results was carried out, based on the uniaxial tensile and compressive tests. Subsequently, the FE models of the static and dynamic crash tests were generated, using the calibrated properties. The results obtained using the UMAT were compared against the structural experiments. Furthermore, the models were used to extract valuable information regarding the failure mechanism observed in the structures, subjected to static and dynamic loads. They also helped to gain a better understanding of how the silica particles change the fracture mechanism of glass-fibre reinforced polyamide composite.

A comparison of the numerical and experimental results of the uniaxial specimen tests proved high reliability of the model at simple stress conditions. The numerical stress-strain curves matched the experimental ones with very good accuracy, at both tensile and compressive loads, as well as longitudinal and transverse directions. The idea of scaling the parameters of hardening function, rather than just the yield strength, proved to be highly effective in predicting dynamic behaviour of polymer based composites. Furthermore, the strain energy density based failure criterion proved to be accurate in predicting the failure at various strain rates and loading conditions.

The numerical modelling of the conical structures, subjected to static and dynamic crashing loads, provided information about the performance of the UMAT, when used in a complex multi-axial stress state. The UMAT was fully

capable of predicting the failure modes observed in all studied structures. It captured the differences between the specimens tested at static and dynamic loads, such as change in ductility and the effect of that change on the fracture mechanism. Moreover, it correctly captured the effect of the SiO_2 filler on the fracture mechanism of the structure. This was visible as an increased ability of the material to resist propagation of the cracks, which affected the overall structural collapse mechanism. Furthermore, it was observed in the FE models that the failure in the conical structure is a result of a biaxial tensile stress state (axial and circumferential). A change in the fracture mechanism, observed after addition of secondary filler, was mainly due to the change in the axial and circumferential strength and ductility. This is why, based on the stress analysis, it can be concluded that the proper balance between the axial and circumferential strength and ductility provides an adequate mechanism, which is highly efficient in the impact energy absorption.

7. General Conclusions

Short-fibre reinforced polymer composites are low cost materials with good mechanical and processing properties. This makes them an attractive alternative to metals for application in structural components. However, their main drawbacks are low ductility and toughness, introduced by the addition of glass-fibres into polymer matrix. As these properties drive the ability of a structure to resist impact loads, structures made of short-fibre reinforced polymers are often susceptible to impact damages and are ineffective in impact energy absorption. These limit their application in structural components which can be subjected to impact loads.

Recent advances in the field of nano-technology provided new opportunities for the composite materials. Numerous studies in this field proved that the addition of nano-sized filers can yield significant enhancement in the mechanical properties of polymeric materials. Properties such as stiffness, strength and ductility can be improved in the presence of nano-fillers within the polymer. However, the effect of nano-fillers on the mechanical properties of glass-fibre reinforced polymers has not yet been fully understood; particularly, whether the increased ductility observed in the nano-reinforced polymer can still be maintained in the three-phase composite. This is why the main aim of this project was to study the effect of various nano and micro fillers on the mechanical properties of hybrid three-phase composite materials. Furthermore, it aimed to study the effect of this change in the mechanical properties of the composites, on the failure mechanism observed in crashworthiness structures made of these composites. For this purpose several different composites were manufactured based on glass-fibre (GF) reinforced polyamide 6 (PA6) and polypropylene (PP). As a nano-reinforcement two different types of silica-particles (SiO_2) and montmorillonite (MMT) were used, whereas as a micro filer, glass-spheres (GS) were utilised. As a result the following eight different

composites were produced: PA/GF, PA/GF/SiO_2, PA/GF/MMT, PA/GF/GS, PP/GF, PP/GF/SiO_2, PP/GF/MMT, PP/GF/GS. In order to study the effect of secondary filler on the mechanical properties of the composites tensile and compressive uniaxial tests were carried out. Furthermore, energy absorbing structures, in the form of crash cones, were manufactured using the composite materials. A series of drop weight impact tests were undertaken to study the effect of secondary filler on the failure mechanism and energy absorption capabilities of three-phase composites. Moreover, a number of FE models was developed using the Ls-Dyna software with User Defined Material Model (UMAT). This was required to obtain a better understanding of the failure mechanism observed in various composite materials. Furthermore, an accurate material model designed and validated specifically for the studied materials was required, to provide reliable tool that can ease the design process of the structure made of the three-phase composite material.

Based on the experiments undertaken and the numerical simulations the following conclusions were drawn:

- The effect of secondary fillers on the mechanical properties of PA based composites was positive. MMT and GS caused an increase in stiffness and strength of the composite. The SiO_2 filler increased the ductility of the composite, with little effect on its stiffness and strength.
- All mechanical properties of PP composites were decreased after the addition of secondary filler, possibly due to a combination of weak filler-matrix interphase region and dispersion issues.
- Addition of SiO_2 particles led to an increase in the ductility of the PA material in all the directions (longitudinal and transverse), as well as at both static and dynamic conditions. This proves that the common issue with brittleness of short-fibre reinforced composites can be diminished by incorporation of SiO_2 particles.

- Addition of the secondary reinforcement into glass-fibre reinforced polymer composites has a significant influence on the crashing response of the composite material.
- By changing the matrix and the reinforcement material it is possible to change the micro-mechanism of failure, and therefore, control the energy absorption characteristics of the composite.
- Secondary reinforcement in PA composites leads to an increase in energy absorption capabilities of the structure.
- Energy absorption capabilities of PP composites have been decreased after the addition of secondary reinforcement. The possible reason for this phenomenon was dispersion issues with the nano-particles and week filler-matrix interphase.
- The main reason for improved energy absorption capability is the reduced axial cracking of the structure induced by circumferential loads. The extensive cracking observed in the neat PA/GF composite was diminished by the two different mechanisms. First, improved ductility of the composite after the addition of SiO_2 particles. Second, improved stiffness and strength of the composite after the addition of GS particles.
- Yielding and failure of the conical structures subjected to axial crashing load is a result of a biaxial tensile stress state (axial and circumferential).
- Optimized balance between the axial and circumferential strength and ductility provides an adequate failure mechanism, which is highly efficient in the impact energy absorption.
- The results show that the materials are anisotropic and pressure sensitive, with highly nonlinear plasticity, as well as rate sensitive modulus, yield and strength. None of the currently available material models in Ls-Dyna can accurately represent all these requirements.

- Anisotropic pressure sensitive Hoffman yield criterion can accurately predict yielding of three-phase polymer composite subjected to uniaxial and multi-axial stress state.
- Second order exponential hardening function provides very accurate fit to a highly nonlinear plastic stress-strain curve.
- Strain energy density based failure criterion takes into account the entire nonlinear stress-stress response providing more accurate results than stress or strain based criteria.
- Strain rate sensitive modulus and hardening function coefficients provide more accurate representation of the dynamic response, in relation to standard method based on strain rate sensitive yield strength.

8. Further work

This project was focused on the understanding of the effect of secondary filler on the mechanical properties of hybrid three-phase composites. The amount of nano-filler in the composites was constant in all the tested specimens (2%). Future studies should focus on the effect of nano-filler content on the mechanical properties of the three-phase composites. It would be beneficial to understand what content of SiO_2 particles is the most optimal for the composite ductility. Furthermore, similar studies should be carried out on MMT filed composite, to understand the effect of its content on the strength, stiffness and ductility of the composite. Additional studies should also be undertaken on the improvement of the nano-filler dispersion. In this work there were some agglomerates present in the composites. It would be important to understand whether the small decrease in the strength and stiffness, measured in the SiO_2 filled composite, could be diminished if a fully dispersed state is achieved. Similar investigation should be conducted on MMT filed composites to understand whether the measured increase in brittleness is caused only by the presence of MMT filler, or is significantly influenced by the dispersion state.

Regarding the modelling side of the project, a few discrepancies have been observed between the experimental and numerical results. In order to gain a better understanding of where the discrepancies are coming from, further testing is required. The shear data was taken from the literature. As a result some inaccuracies are expected. Furthermore, biaxial testing should be carried out to more accurately derive the biaxial failure coefficient, and validate the accuracy of multi-axial failure and yield criterions.

Appendix A: Ls-Dyna input file – Tensile test

```
$# LS-DYNA Keyword file created by LS-PrePost 3.2 -30Sep2012(12:31)
$# Created on Apr-21-2013 (16:31:55)
*KEYWORD
*TITLE
$# title
specimen in traction
*CONTROL_TERMINATION
$$  ENDTIM    ENDCYC     DTMIN    ENDENG    ENDMAS
$#  endtim    endcyc     dtmin    endeng    endmas
     0.015         0     0.000     0.000     0.000
*CONTROL_TIMESTEP
$#  dtinit    tssfac      isdo    tslimt     dt2ms      lctm     erode     ms1st
     0.000  0.900000         0     0.000         0         0         0         0
$#  dt2msf   dt2mslc     imscl
     0.000         0         0
*DATABASE_BINARY_D3PLOT
$$ DT/CYCL      LCDT      BEAM     NPLTC
$#      dt      lcdt      beam     npltc    psetid
    0.0001         0         0         0         0
$#   ioopt
         0
*DATABASE_EXTENT_BINARY
$#   neiph     neips    maxint    strflg    sigflg    epsflg    rltflg    engflg
        40        10         3         0         1         1         1         1
$#  cmpflg    ieverp    beamip     dcomp      shge     stssz    n3thdt   ialemat
         0         0         0         1         1         1         2         1
$# nintsld   pkp_sen      sclp    unused     msscl     therm    intout    nodout
         0         0  1.000000         0         0         0  0STRESS    STRESS
$#    dtdt    resplt
         0         0
*BOUNDARY_PRESCRIBED_MOTION_SET_ID
$#      id                                                              heading
         1traction
$#    nsid       dof       vad      lcid        sf       vid     death     birth
         1         1         2         1  1.000000         0     0.000     0.000
*BOUNDARY_SPC_SET_ID
$#      id                                                              heading
         1fixture
$#    nsid       cid      dofx      dofy      dofz     dofrx     dofry     dofrz
         2         0         1         1         1         0         0         0
*PART
$# title
SPECIMEN
$#     pid     secid       mid     eosid      hgid      grav    adpopt      tmid
         1         1         1         0         0         0         0         0
*SECTION_SOLID_TITLE
solid specimen
$#   secid    elform       aet
         1         1         0
*MAT_USER_DEFINED_MATERIAL_MODELS_TITLE
UMAT
$#     mid        ro        mt       lmc       nhv    iortho     ibulk        ig
         1 1.3600E-9        43        40        44         1         1         7
$#   ivect     ifail    itherm    ihyper      ieos      lmca    unused    unused
         0         1         0         0         0         0         0         0
$#    aopt      mafc        xp        yp        zp        a1        a2        a3
  2.000000  1.000000     0.000     0.000     0.000  1.000000     0.000     0.000
$#      v1        v2        v3        d1        d2        d3      beta
     0.000     0.000     0.000  1.000000  1.000000     0.000     0.000
$# p1     p2        p3        p4        p5        p6        p7        p8
6800      4223      4223      0.35      0.35      0.35      2519      2519
$# p9     p10       p11       p12       p13       p14       p15       p16
2519      1         1         1.0e-05   50        0.01      4.99      4.22
$# p17    p18       p19       p20       p21       p22       p23       p24
4.22      30        30        30        0.785     0.785     0.785     5
$# p25    p26       p27       p28       p29       p30       p31       p32
-1.15     1         40.8      25.3      25.3      46.1      46.1      46.1
$# p33    p34       p35       p36       p37       p38       p39       p40
19.4      19.4      19.4      4.99      105       0.006     -91       0.6
```

```
*DEFINE_CURVE_TITLE
displacement curve
$#    lcid      sidr       sfa       sfo      offa      offo    dattyp
         1         0     0.000     0.000     0.000     0.000         0
$#                a1                  o1
              0.00               0.000
            0.0100               10.00
            0.0150               15.00
*SET_NODE_LIST_TITLE
fixture
$#     sid       da1       da2       da3       da4    solver
         2     0.000     0.000     0.000     0.000MECH
$#    nid1      nid2      nid3      nid4      nid5      nid6      nid7      nid8
*SET_NODE_LIST_TITLE
traction
$#     sid       da1       da2       da3       da4    solver
         1     0.000     0.000     0.000     0.000
$#    nid1      nid2      nid3      nid4      nid5      nid6      nid7      nid8
*ELEMENT_SOLID
$#   eid     pid      n1      n2      n3      n4      n5      n6      n7      n8
*NODE
$#   nid               x               y               z      tc      rc
*END
```

Appendix B: Ls-Dyna input file – Static crash test

```
$# LS-DYNA Keyword file created by LS-PrePost 3.2 -30Sep2012(12:31)
$# Created on Aug-16-2014 (18:32:56)
*KEYWORD
*TITLE
$# title
cone_static
*CONTROL_CONTACT
$$  SLSFAC    RWPNAL    ISLCHK    SHLTHK    PENOPT    THKCHG     ORIEN    ENMASS
$#  slsfac    rwpnal    islchk    shlthk    penopt    thkchg     orien    enmass
     0.000     0.000         1         0         0         0         1         2
$$  USRSTR    USRFRC     NSBCS    INTERM     XPENE     SSTHK      ECDT   TIEDPRJ
$#  usrstr    usrfrc     nsbcs    interm     xpene     ssthk      ecdt   tiedprj
         0         0         0         0  4.000000         0         0         0
$#   sfric     dfric      edc       vfc        th     th_sf    pen_sf
     0.300     0.300     0.000     0.000     0.000     0.000     0.000
$#  ignore    frceng   skiprwg    outseg   spotstp   spotdel   spothin
         0         0         0         0         0         0     0.000
$$ DT/CYCL      LCDT      BEAM     NPLTC
$#    isym    nserod    rwgaps    rwgdth     rwksf      icov    swradf    ithoff
         0         0         0     0.000  1.000000         0     0.000         0
$#  shledg    pstiff    ithcnt    tdcnof     ftall    unused    shltrw
         0         0         0         0         0         0     0.000
$$  DTINIT    TSSFAC      ISDO    TSLIMT     DT2MS      LCTM     ERODE     MSIST
*CONTROL_HOURGLASS
$$     IHQ        QH
$#     ihq        qh
         5  0.030000
*CONTROL_TERMINATION
$$  ENDTIM    ENDCYC     DTMIN    ENDENG    ENDMAS
$#  endtim    endcyc     dtmin    endeng    endmas
  0.010000         0     0.000     0.000     0.000
*CONTROL_TIMESTEP
$#  dtinit    tssfac      isdo    tslimt     dt2ms      lctm     erode     ms1st
     0.000     0.000         0     0.000     0.000         0         0         0
$$     IHQ        QH
$#  dt2msf   dt2mslc     imscl
     0.000         0         0
$$   SFRIC     DFRIC       EDC    INTVFC        TH     TH_SF    PEN_SF
$$  IGNORE    FRCENG   SKIPRWG    OUTSEG   SPOTSTP   SPOTDEL   SPOTHIN
$$DATABASE_OPTION -- Control Cards for ASCII output
*DATABASE_RWFORC
$#      dt    binary      lcur     ioopt
 4.0000E-5         0         0         1
*DATABASE_BINARY_D3PLOT
$$ DT/CYCL      LCDT      BEAM     NPLTC
$#      dt      lcdt      beam     npltc    psetid
 4.0000E-5         0         0         0         0
$#   ioopt
         0
*DATABASE_EXTENT_BINARY
$#   neiph     neips    maxint    strflg    sigflg    epsflg    rltflg    engflg
         4         0         3         0         1         1         1         1
$#  cmpflg    ieverp    beamip     dcomp      shge     stssz    n3thdt   ialemat
         0         0         0         1         1         1         2         1
$# nintsld   pkp_sen      sclp    unused     msscl     therm    intout    nodout
         0         0  1.000000         0         0         0STRESS    STRESS
$#    dtdt    resplt
         0         0
*BOUNDARY_SPC_NODE
$HMNAME LOADCOLS       1support
$HWCOLOR LOADCOLS       1      37
$#     nid       cid      dofx      dofy      dofz     dofrx     dofry     dofrz
```

```
*CONTACT_ERODING_SINGLE_SURFACE_ID
$HMNAME GROUPS      16contact_single
$HWCOLOR GROUPS      16       3
$#     cid                                                                title
        16
$#    ssid      msid     sstyp     mstyp    sboxid    mboxid       spr       mpr
         1         0         3         0         0         0         0         0
$#      fs        fd        dc        vc       vdc    penchk        bt        dt
  0.300000  0.300000     0.000     0.000     0.000         0     0.000     0.000
$#     sfs       sfm       sst       mst      sfst      sfmt       fsf       vsf
     0.000     0.000     0.000     0.000     0.000     0.000     0.000     0.000
$#    isym    erosop      iadj
         0         1         1
*CONTACT_AUTOMATIC_SINGLE_SURFACE_ID
$HMNAME GROUPS      20automatic
$HWCOLOR GROUPS      20       4
$#     cid                                                                title
        20
$#    ssid      msid     sstyp     mstyp    sboxid    mboxid       spr       mpr
         1         0         3         0         0         0         0         0
$#      fs        fd        dc        vc       vdc    penchk        bt        dt
   0.30000   0.30000     0.000     0.000     0.000         0     0.000     0.000
$#     sfs       sfm       sst       mst      sfst      sfmt       fsf       vsf
     0.000     0.000     0.000     0.000     0.000     0.000     0.000     0.000
*CONTACT_ERODING_NODES_TO_SURFACE
$#     cid                                                                title
$#    ssid      msid     sstyp     mstyp    sboxid    mboxid       spr       mpr
         1         2         3         3         0         0         0         0
$#      fs        fd        dc        vc       vdc    penchk        bt        dt
     0.300     0.300     0.000     0.000     0.000         0     0.0001.0000E+20
$#     sfs       sfm       sst       mst      sfst      sfmt       fsf       vsf
  1.000000  1.000000     0.000     0.000  1.000000  1.000000  1.000000  1.000000
$#    isym    erosop      iadj
         0         1         1
*PART
$# title
wall
$#     pid     secid       mid     eosid      hgid      grav    adpopt      tmid
         1         1         3         0         0         0         0         0
*SECTION_SOLID
$HMNAME PROPS       1composite
$#   secid    elform       aet
         1         1         4
*MAT_USER_DEFINED_MATERIAL_MODELS_TITLE
UMAT
$#     mid        ro        mt       lmc       nhv    iortho     ibulk        ig
         3 1.3600E-9        43        40        44         1         1         7
$#   ivect     ifail    itherm    ihyper      ieos      lmca    unused    unused
         0         1         0         0         0         0         0         0
$#    aopt      mafc        xp        yp        zp        a1        a2        a3
  4.000000  2.000000     0.000     0.000     0.000     0.000     0.000     0.000
$#      v1        v2        v3        d1        d2        d3      beta
     0.000     0.000  1.000000     0.000     0.000     0.000     0.000
$# p1     p2        p3        p4        p5        p6        p7        p8
6800      4223      4223      0.35      0.35      0.35      2519      2519
$# p9     p10       p11       p12       p13       p14       p15       p16
2519      1         1         1.0e-05   50        0.01      4.99      4.22
$# p17    p18       p19       p20       p21       p22       p23       p24
4.22      30        30        30        0.785     0.785     0.785     5
$# p25    p26       p27       p28       p29       p30       p31       p32
-1.15     1         40.8      25.3      25.3      46.1      46.1      46.1
$# p33    p34       p35       p36       p37       p38       p39       p40
19.4      19.4      19.4      4.99      105       0.006     -91       0.6
```

```
*RIGIDWALL_GEOMETRIC_FLAT_MOTION_ID
$HMNAME GROUPS      19Moving_Rigidwall
$HWCOLOR GROUPS      19       3
$#      id                                                                |
        19
$#    nsid    nsidex     boxid     birth     death
         0         0         0     0.000     0.000
$#      xt        yt        zt        xh        yh        zh      fric
     0.000-7.816E-14 125.00000     0.000-7.816E-14 124.00000  0.300000
$#    xhev      yhev      zhev      lenl      lenm
     0.000     0.000     0.000     0.000     0.000
$#    lcid       opt        vx        vy        vz
         8         1     0.000     0.000 -1.000000
*DEFINE_CURVE
$HMNAME CURVES       8motion
$HWCOLOR CURVES       8       3
$HMCURVE     1    3 motion
$#    lcid      sidr       sfa       sfo      offa      offo    dattyp
         8         0  1.000000  1.000000     0.000     0.000         0
$#                a1                  o1
              0.000               0.000
           0.010000          100.000000
*SET_PART_LIST
$HMSET
$HMNAME SETS       1set
$#     sid       da1       da2       da3       da4    solver
         1  1.000000  0.100000 2000.0000  2.000000
$#    pid1      pid2      pid3      pid4      pid5      pid6      pid7      pid8
         1         0         0         0         0         0         0         0
*ELEMENT_SOLID
$#   eid     pid      n1      n2      n3      n4      n5      n6      n7      n8
*NODE
*END
```

Appendix C: Ls-Dyna input file – Dynamic crash test

```
$# LS-DYNA Keyword file created by LS-PrePost 3.2 -30Sep2012(12:31)
$# Created on Sep-26-2014 (09:13:14)
*KEYWORD
*TITLE
$# title
cone_impact
*CONTROL_CONTACT
$$  SLSFAC    RWPNAL    ISLCHK    SHLTHK    PENOPT    THKCHG     ORIEN    ENMASS
$#  slsfac    rwpnal    islchk    shlthk    penopt    thkchg     orien    enmass
     0.000  2.000000         1         0         0         0         1         2
$#  usrstr    usrfrc     nsbcs    interm     xpene     ssthk      ecdt   tiedprj
         0         0         0         0  0.100000         0         0         0
$#   sfric     dfric       edc       vfc        th     th_sf    pen_sf
  0.300000  0.300000     0.000     0.000     0.000     0.000     0.000
$#  ignore    frceng   skiprwg    outseg   spotstp   spotdel   spothin
         0         0         0         0         0         0     0.000
$#    isym    nserod    rwgaps    rwgdth     rwksf      icov    swradf    ithoff
         0         0         0     0.000  1.000000         0     0.000         0
$#  shledg    pstiff    ithcnt    tdcnof     ftall    unused    shltrw
         0         0         0         0         0         0     0.000
*CONTROL_HOURGLASS
$$     IHQ        QH
$#     ihq        qh
         4  0.030000
*CONTROL_TERMINATION
$$  ENDTIM    ENDCYC     DTMIN    ENDENG    ENDMAS
$#  endtim    endcyc     dtmin    endeng    endmas
  0.015000         0     0.000     0.000     0.000
*CONTROL_TIMESTEP
$$  DTINIT    TSSFAC      ISDO    TSLIMT     DT2MS      LCTM     ERODE     MSIST
$#  dtinit    tssfac      isdo    tslimt     dt2ms      lctm     erode     ms1st
     0.000  0.900000         0     0.000     0.000         0         1         0
$#  dt2msf   dt2mslc     imscl
     0.000         0         0
*DATABASE_BNDOUT
$#      dt    binary      lcur     ioopt
 1.0000E-5         3         0         1
*DATABASE_RCFORC
$#      dt    binary      lcur     ioopt
 1.0000E-5         1         0         1
*DATABASE_SPCFORC
$#      dt    binary      lcur     ioopt
 1.0000E-5         1         0         1
*DATABASE_BINARY_D3PLOT
$$ DT/CYCL      LCDT      BEAM     NPLTC
$#      dt      lcdt      beam     npltc    psetid
 2.0000E-5         0         0         0         0
$#   ioopt
         0
*DATABASE_EXTENT_BINARY
$#   neiph     neips    maxint    strflg    sigflg    epsflg    rltflg    engflg
        40         0         3         0         1         1         1         1
$#  cmpflg    ieverp    beamip     dcomp      shge     stssz    n3thdt   ialemat
         0         0         0         1         1         1         2         1
$# nintsld   pkp_sen      sclp    unused     msscl     therm    intout    nodout
         0         0  1.000000         0         0         0STRESS    STRESS
$#    dtdt    resplt
         0         0
```

```
*CONTACT_ERODING_SURFACE_TO_SURFACE_ID
$HMNAME GROUPS       14cont
$HWCOLOR GROUPS       14      11
$#     cid                                                                title
        14
$#    ssid       msid     sstyp     mstyp    sboxid    mboxid       spr       mpr
        15          7         3         3         0         0         0         0
$#      fs         fd        dc        vc       vdc    penchk        bt        dt
  0.300000  0.300000     0.000     0.000     0.000         0     0.000     0.000
$#     sfs        sfm       sst       mst      sfst      sfmt      fsf       vsf
     0.000     0.000     0.000     0.000     0.000     0.000     0.000     0.000
$#    isym    erosop      iadj
         0         1         1
*CONTACT_SURFACE_TO_SURFACE
$#     cid                                                                title
$#    ssid       msid     sstyp     mstyp    sboxid    mboxid       spr       mpr
        16          7         3         3         0         0         0         0
$#      fs         fd        dc        vc       vdc    penchk        bt        dt
  0.300000  0.300000     0.000     0.000     0.000         0     0.0001.0000E+20
$#     sfs        sfm       sst       mst      sfst      sfmt      fsf       vsf
  1.000000  1.000000     0.000     0.000  1.000000  1.000000  1.000000  1.000000
*CONTACT_SURFACE_TO_SURFACE_ID
$#     cid                                                                title
         5
$#    ssid       msid     sstyp     mstyp    sboxid    mboxid       spr       mpr
        17          7         3         3         0         0         0         0
$#      fs         fd        dc        vc       vdc    penchk        bt        dt
  0.300000  0.300000     0.000     0.000     0.000         0     0.0001.0000E+20
$#     sfs        sfm       sst       mst      sfst      sfmt      fsf       vsf
  1.000000  1.000000     0.000     0.000  1.000000  1.000000  1.000000  1.000000
*CONTACT_ERODING_SURFACE_TO_SURFACE_ID
$#     cid                                                                title
         6
$#    ssid       msid     sstyp     mstyp    sboxid    mboxid       spr       mpr
        15         16         3         3         0         0         0         0
$#      fs         fd        dc        vc       vdc    penchk        bt        dt
  0.300000  0.300000     0.000     0.000     0.000         1     0.000  0.002900
$#     sfs        sfm       sst       mst      sfst      sfmt      fsf       vsf
     0.000     0.000     0.000     0.000     0.000     0.000     0.000     0.000
$#    isym    erosop      iadj
         0         1         1
*CONTACT_SURFACE_TO_SURFACE_ID
$#     cid                                                                title
         6
$#    ssid       msid     sstyp     mstyp    sboxid    mboxid       spr       mpr
         6          7         3         3         0         0         0         0
$#      fs         fd        dc        vc       vdc    penchk        bt        dt
  0.300000  0.300000     0.000     0.000     0.000         0     0.0001.0000E+20
$#     sfs        sfm       sst       mst      sfst      sfmt      fsf       vsf
  1.000000  1.000000     0.000     0.000  1.000000  1.000000  1.000000  1.000000
*PART
$# title
impactor
$#     pid     secid       mid     eosid      hgid      grav    adpopt      tmid
         6         1        12         0         0         0         0         0
*SECTION_SOLID
$HMNAME PROPS       1composite
$#   secid    elform       aet
         1         1         0
```

```
*MAT_RIGID
$HMNAME MATS       2Impactor
$#     mid        ro         e        pr         n    couple         m     alias
        12 2.2770E-6 2.1000E+5  0.330000     0.000     0.000     0.000
$#     cmo      con1      con2
     0.000         0         0
$# lco or a1      a2        a3        v1        v2        v3
     0.000     0.000     0.000     0.000     0.000     0.000
*PART
$# title
plate
$#     pid     secid       mid     eosid      hgid      grav    adpopt      tmid
         7         1         4         0         0         0         0         0
*MAT_RIGID
$HMNAME MATS       plate
$#     mid        ro         e        pr         n    couple         m     alias
         4 7.5000E-9 2.1000E+5  0.330000     0.000     0.000     0.000
$#     cmo      con1      con2
     0.000         0         0
$# lco or a1      a2        a3        v1        v2        v3
     0.000     0.000     0.000     0.000     0.000     0.000
*PART
$# title
wall
$#     pid     secid       mid     eosid      hgid      grav    adpopt      tmid
        15         1         3         0         0         0         0         0
*MAT_USER_DEFINED_MATERIAL_MODELS_TITLE
UMAT
$#     mid        ro        mt       lmc       nhv    iortho     ibulk        ig
         3 1.3600E-9        43        40        44         1         1         7
$#   ivect     ifail    itherm    ihyper      ieos      lmca    unused    unused
         0         1         0         0         0         0         0         0
$#    aopt      mafc        xp        yp        zp        a1        a2        a3
  4.000000  2.000000     0.000     0.000     0.000     0.000     0.000     0.000
$#      v1        v2        v3        d1        d2        d3      beta
     0.000     0.000  1.000000     0.000     0.000     0.000     0.000
$# p1     p2        p3        p4        p5        p6        p7        p8
6800      4223      4223      0.35      0.35      0.35      2519      2519
$# p9     p10       p11       p12       p13       p14       p15       p16
2519      1         1         1.0e-05   50        0.01      4.99      4.22
$# p17    p18       p19       p20       p21       p22       p23       p24
4.22      30        30        30        0.785     0.785     0.785     5
$# p25    p26       p27       p28       p29       p30       p31       p32
-1.15     1         40.8      25.3      25.3      46.1      46.1      46.1
$# p33    p34       p35       p36       p37       p38       p39       p40
19.4      19.4      19.4      4.99      105       0.006     -91       0.6
*INITIAL_VELOCITY_RIGID_BODY
$HMNAME LOADCOLS       3initial velocity
$HWCOLOR LOADCOLS       3      11
$#     pid        vx        vy        vz       vxr       vyr       vzr      icid
         6     0.000     0.000-6500.0000     0.000     0.000     0.000         0
*ELEMENT_SOLID
$#   eid     pid      n1      n2      n3      n4      n5      n6      n7      n8
*NODE
$#   nid               x               y               z      tc      rc
*END
```

Appendix D: Impactor design

- **Technical drawing**

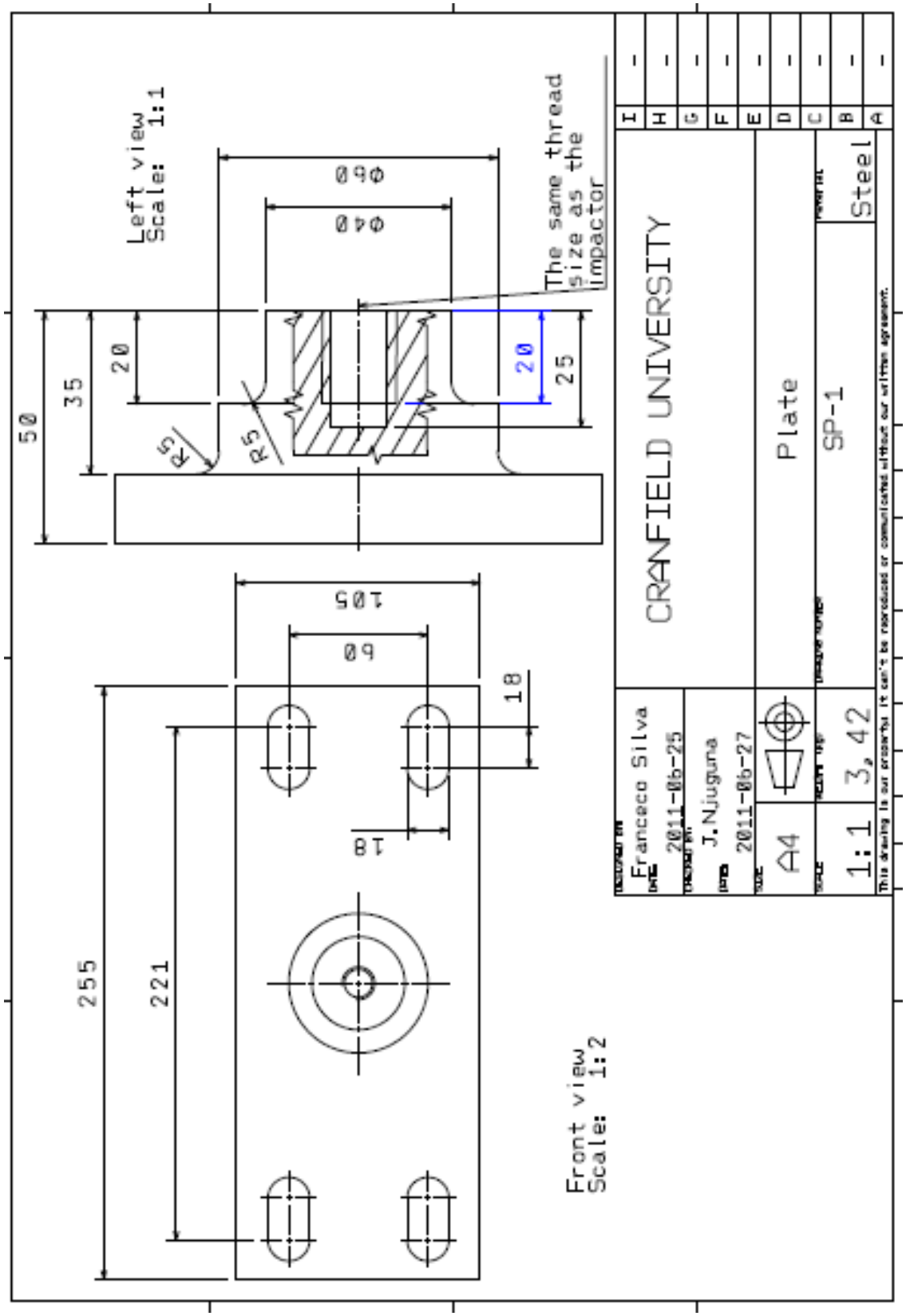

- **FE analysis**

The impactor has been designed to withstand off-axis impact load with the maximum value of 200kN, which corresponds to the maximum allowable load supported by the load cell. The worst impact scenario was studied using Ansys software. The results presented in the figure below show that maximum stress induced in the structure is below the yield stress (350MPa) of the selected material (steel).

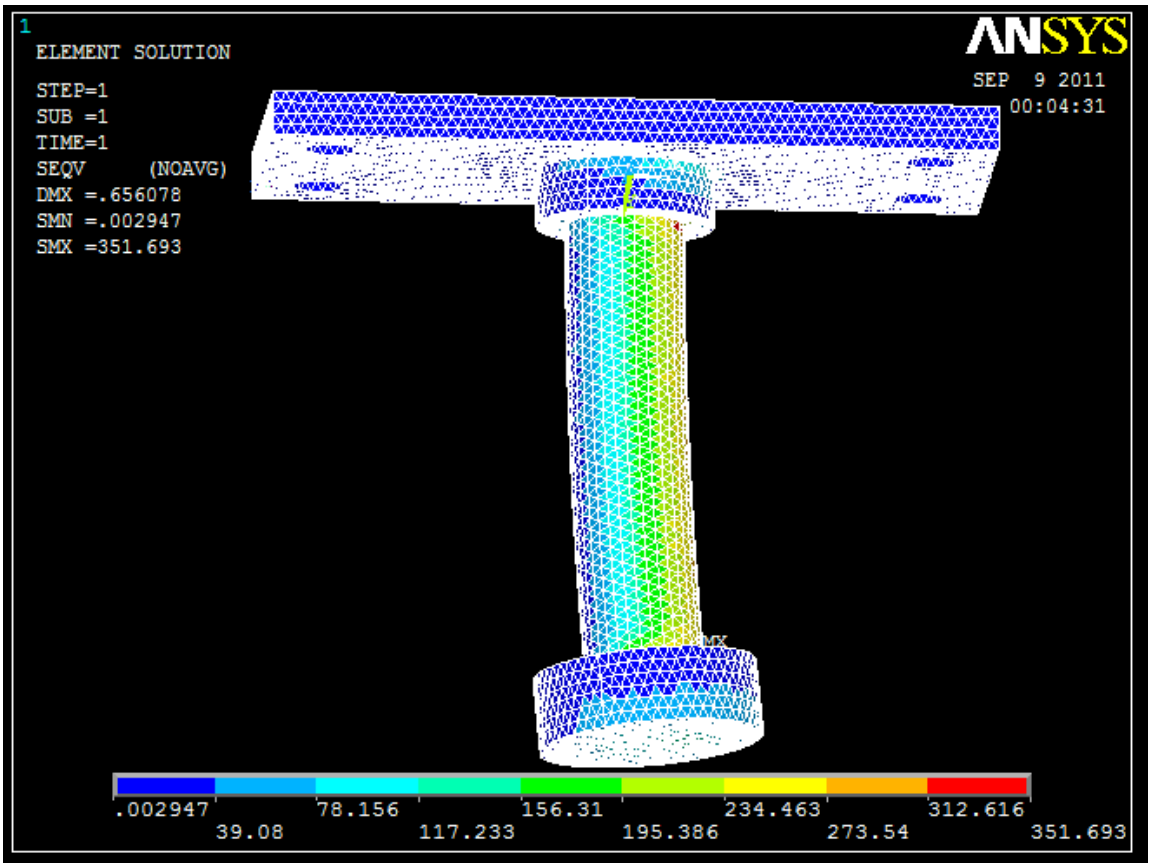

Appendix E: UMAT development procedure

This appendix demonstrates how to generate a User Defined Material Model (UMAT) for Ls-Dyna. The main information about the format and structure of the UMAT can be found in Appendix A of LS-Dyna manual [5]. Additional information can be found in the following publications [182-184].

The following steps show a common procedure used when developing and implementing a UMAT:

- Theoretical development: In the first step it is required to represent the material model as a set of mathematical equations. This includes stiffness matrix, yield criterion, hardening function and failure criterion. Additionally, all this parameters can be described as a function of deformation conditions such as temperature or strain rate. Details about mathematical representation of the UMAT are presented in Section 5.1.
- Numerical implementation: In the second step it is required to implement the model within a framework of stress integration algorithm based on incremental theory of plasticity. To find the unknown stress using an FE code, when nonlinear problem is considered, it is required to integrate the nonlinear constitutive equations knowing the incremental strains. The most efficient method to achieve that is to use the cutting-plane algorithm as developed by Simo and Ortiz [178; 179]. Details of the material model implementation are presented in Section 5.2.
- Fortran Implementation: Once the theoretical development and implementation are completed the model needs to be incorporated into Ls-Dyna. This is carried out by developing a Fortran subroutine, which must be compatible with Fortran version used to develop Ls-Dyna source code. This is either Fortran 77 or 90 depending on Ls-Dyna version.

- Implementation into Ls-Dyna: Once the Fortran subroutine is written it needs to be implemented into LS-Dyna source code. Furthermore, a new Ls-Dyna executable file needs to be generated. This can be carried out in the following steps:

1. Download all the required files, contained in a zip file, from the following LSTC web page: ftp.lstc.com. This includes the Ls-Dyna source code (dyna21.f), as well as 'Makefile' used to compile the executable.
2. Open the dyn21.file in a text editor and search for 'subroutine umat41'. This is the location where the example UMAT subroutines are stored.
3. Implement the developed subroutine into dyn21.file, replacing one of the example subroutines, following the format shown in the Ls-Dyna manual.
4. Using Intel Fortan Compiler generate a new Ls-Dyna executable file by typing the command 'nmake'.
5. To invoke the UMAT in the Ls-Dyna input file, define the following card:

   *MAT_USER_DEFINED_MATERIAL_MODELS

6. Define the material properties in the card, as specified in the developed material model.

The definition of the material properties in the developed UMAT has the following form:

p_1	p_2	p_3	p_4	p_5	p_6
Young's modulus E_1	Young's modulus E_2	Young's modulus E_3	Poisson's ratio v_{12}	Poisson's ratio v_{23}	Poisson's ratio v_{13}
p_7	p_8	p_9	p_{10}	p_{11}	p_{12}
Shear Modulus G_{12}	Shear Modulus G_{23}	Shear Modulus G_{13}	Strain rate sensitivity if >0	-	Iteration tolerance
p_{13}	p_{14}	p_{15}	p_{16}	p_{17}	p_{18}
Number of iterations	Strain rate of elastic modulus	Failure function β_1	Failure function β_2	Failure function β_3	Failure function β_4
p_{19}	p_{20}	p_{21}	p_{22}	p_{23}	p_{24}
Failure function β_5	Failure function β_6	Failure function β_{12}	Failure function β_{13}	Failure function β_{23}	Number of strain rates
p_{25}	p_{26}	p_{27}	p_{28}	p_{29}	p_{30}
Hardening exponent d	Orthotropic (=0) or transversely isotropic (=1)	Yield function a_{12}	Yield function a_{23}	Yield function a_{31}	Yield function a_{11}
p_{31}	p_{32}	p_{33}	p_{34}	p_{35}	p_{36}
Yield function a_{22}	Yield function a_{33}	Yield function a_{44}	Yield function a_{55}	Yield function a_{66}	Static failure energy
p_{37}	p_{38}	p_{39}	p_{40}		
Hardening parameter a	Hardening exponent b	Hardening parameter c	Yield strain	-	-

Appendix F: List of publications

Research papers

- Silva, F., Njuguna, J., Sachse, S., Pielichowski, K. and Leszczynska, A. The Influence of Multiscale Fillers Reinforcement into Impact Resistance and Energy Absorption Properties of Polyamide 6 and Polypropylene Nanocomposite Structures. *Materials & Design 50,* (2013): 244-252.

- Silva, F., Sachse, S., Zhu, H., Pielichowski, K., Leszczyńska, A. and Njuguna, J. The Effect of Matrix and Reinforcement Material Selection on the Tensile Properties of Hybrid Composites. *The Journal of Sustainable Mobility* 1.1 (2014), 37-52.

Book chapters

- Njuguna, J., Silva, F. and Sachse, S. Nanocomposites for vehicle structural applications. *Nanofibers, Production, Properties and Functional Applications,* (2011), 402-434.

Conference talks

- Silva, F., Sachse, S. and Njuguna, J. Mechanical properties and impact-energy absorption of injection moulded nanocomposites structures. *ECCM15-15th European Conference on Composite Materials,* Venice, Italy, (2012).

- Silva, F., Sachse, S. and Njuguna, J. Energy absorption characteristics of nano-composite conical structures. *NanoStruc - International Conference on Structural Nano Composites,* Cranfield University, Bedfordshire, United Kingdom, (2012).

Co-authored publications

- Sachse, S., Poruri, M., Silva, F., Michalowski, S., Pielichowski, K. and Njuguna, J. Effect of nanofillers on low energy impact performance of sandwich structures with nanoreinforced polyurethane foam cores. *Journal of Sandwich Structures and Materials* 16.2 (2014): 173-194.

- Sachse, S., Silva, F., Pielichowski, K., Leszczynska, A. and Njuguna, J. Compression strength and low-velocity impact performance of nanocored sandwich composites. *Mechanics of nano, micro and macro composite structures* (2012): 18-20.

- Sachse, S., Silva, F., Zhu, H., Irfan, A., Leszczyńska, A., Pielichowski, K. and Ermini, V. The effect of nanoclay on dust generation during drilling of PA6 nanocomposites. *Journal of Nanomaterials* (2012): 26.

REFERENCES

[1] Gibson, R. F. (2011), ***Principles of composite material mechanics,*** **CRC Press.**

[2] Mouti, Z., Westwood, K., Kayvantash, K. and Njuguna, J. (2010), "Low Velocity Impact Behavior of Glass Filled Fiber-Reinforced Thermoplastic Engine Components", ***Materials,*** **vol. 3, no. 4, pp. 2463-2473.**

[3] Njuguna, J., Pielichowski, K. and Alcock, J. R. (2007), "Epoxy-Based Fibre Reinforced Nanocomposites", ***Advanced Engineering Materials,*** **vol. 9, no. 10, pp. 835-847.**

[4] McWilliams, A. (2006), "Nanocomposites, nanoparticles, nanoclays, and nanotubes", ***NANO21C, BCC Research, Norwalk, CT,*** **.**

[5] K. Weimar (September 2001), "Ls-DYNA User's Guide", .

[6] Shalin, R. E. (1995), ***Polymer matrix composites,*** **Springer.**

[7] Gay, D., Hoa, S. V. and Tsai, S. W. (2002), ***Composite materials: design and applications,*** **CRC press.**

[8] De, S. and White, J. (1996), ***Short fibre-polymer composites,*** **Elsevier.**

[9] Fu, S. Y., Feng, X. Q., Lauke, B. and Mai, Y. W. (2008), "Effects of particle size, particle/matrix interface adhesion and particle loading on mechanical properties of particulate–polymer composites", ***Composites Part B: Engineering,*** **vol. 39, no. 6, pp. 933-961.**

[10] Gibson, R. F. (1994), ***Principles of composite material mechanics,*** **McGraw-Hill New York.**

[11] Saheb, D. N. and Jog, J. (1999), "Natural fiber polymer composites: a review", ***Advances in Polymer Technology,*** **vol. 18, no. 4, pp. 351-363.**

[12] Thomason, J. (1995), "The interface region in glass fibre-reinforced epoxy resin composites: 1. Sample preparation, void content and interfacial strength", ***Composites,*** **vol. 26, no. 7, pp. 467-475.**

[13] Simeoli, G., Acierno, D., Meola, C., Sorrentino, L., Iannace, S. and Russo, P. (2014), "The role of interface strength on the low velocity impact behaviour of PP/glass fibre laminates", ***Composites Part B: Engineering,*** **vol. 62, pp. 88-96.**

[14] Njuguna, J., Pena, I., Zhu, H., Rocks, S., Blázquez, M. and Desai, S. (2009), "Opportunities and environmental health challenges facing integration of

polymer nanocomposites: technologies for automotive applications", *International Journal of Applied Polymers and Technologies,* vol. 1, pp. 2-3.

[15] Rodiles, R. F. and Rosenau, B. (2008), "Tailor-made Solutions: Polyamides (PA)", *Kunststoffe international,* , no. 10, pp. 82.

[16] Wust, A., Glaser, S., Wollny, A. and Hess, H. (2011), "More Crash Safety from High-Performance Polyamides and Optimized Simulation Methods", *ATZ worldwide eMagazine,* vol. 113, no. 2, pp. 34-39.

[17] Drake, N. (1998), *Thermoplastics and Thermoplastic Composities in the Automotive Industry 1997-2000,* iSmithers Rapra Publishing.

[18] Ghosh, S., Khastgir, D., Bhowmick, A. K. and Mukunda, P. (2000), "Thermal degradation and ageing of segmented polyamides", *Polymer Degradation and Stability,* vol. 67, no. 3, pp. 427-436.

[19] Karian, H. (2003), *Handbook of polypropylene and polypropylene composites, revised and expanded,* CRC press.

[20] Bernasconi, A. and Cosmi, F. (2011), "Analysis of the dependence of the tensile behaviour of a short fibre reinforced polyamide upon fibre volume fraction, length and orientation", *Procedia Engineering,* vol. 10, pp. 2129-2134.

[21] Hassan, A., Yahya, R., Yahaya, A., Tahir, A. and Hornsby, P. (2004), "Tensile, impact and fiber length properties of injection-molded short and long glass fiber-reinforced polyamide 6, 6 composites", *Journal of Reinforced Plastics and Composites,* vol. 23, no. 9, pp. 969-986.

[22] Sato, N., Kurauchi, T., Sato, S. and Kamigaito, O. (1988), "Reinforcing mechanism by small diameter fiber in short fiber composite", *Journal of Composite Materials,* vol. 22, no. 9, pp. 850-873.

[23] Thomason, J. (2007), "Structure–property relationships in glass reinforced polyamide, part 2: The effects of average fiber diameter and diameter distribution", *Polymer composites,* vol. 28, no. 3, pp. 331-343.

[24] Ramsteiner, F. and Theysohn, R. (1985), "The influence of fibre diameter on the tensile behaviour of short-glass-fibre reinforced polymers", *Composites Science and Technology,* vol. 24, no. 3, pp. 231-240.

[25] Thomason, J. (2006), "Structure–property relationships in glass-reinforced polyamide, part 1: The effects of fiber content", *Polymer composites,* vol. 27, no. 5, pp. 552-562.

[26] Thomason, J. (2008), "The influence of fibre length, diameter and concentration on the modulus of glass fibre reinforced polyamide 6, 6",

Composites Part A: Applied Science and Manufacturing, **vol. 39, no. 11, pp. 1732-1738.**

[27] Thomason, J. (2009), "The influence of fibre length, diameter and concentration on the impact performance of long glass-fibre reinforced polyamide 6, 6", *Composites Part A: Applied Science and Manufacturing,* **vol. 40, no. 2, pp. 114-124.**

[28] Güllü, A., Özdemir, A. and Özdemir, E. (2006), "Experimental investigation of the effect of glass fibres on the mechanical properties of polypropylene (PP) and polyamide 6 (PA6) plastics", *Materials & Design,* **vol. 27, no. 4, pp. 316-323.**

[29] Zhao, G. and Cho, C. (2007), "Damage initiation and propagation in composite shells subjected to impact", *Composite structures,* **vol. 78, no. 1, pp. 91-100.**

[30] Bartus, S. and Vaidya, U. (2005), "Performance of long fiber reinforced thermoplastics subjected to transverse intermediate velocity blunt object impact", *Composite structures,* **vol. 67, no. 3, pp. 263-277.**

[31] Santulli, C., Brooks, R., Long, A., Warrior, N. and Rudd, C. (2002), "Impact properties of compression moulded commingled E-glass–polypropylene composites", *Plastics, rubber and composites,* **vol. 31, no. 6, pp. 270-277.**

[32] Bigg, D. (1994), "The impact behavior of thermoplastic sheet composites", *Journal of Reinforced Plastics and Composites,* **vol. 13, no. 4, pp. 339-354.**

[33] Cantwell, W. and Morton, J. (1991), "The impact resistance of composite materials--a review", *Composites,* **vol. 22, no. 5, pp. 347-362.**

[34] Naik, N. and Meduri, S. (2001), "Polymer-matrix composites subjected to low-velocity impact: effect of laminate configuration", *Composites Science and Technology,* **vol. 61, no. 10, pp. 1429-1436.**

[35] Alcock, B., Cabrera, N., Barkoula, N., Wang, Z. and Peijs, T. (2008), "The effect of temperature and strain rate on the impact performance of recyclable all-polypropylene composites", *Composites Part B: Engineering,* **vol. 39, no. 3, pp. 537-547.**

[36] Garcia-Gonzalez, D., Rodriguez-Millan, M., Rusinek, A. and Arias, A. (2015), "Low temperature effect on impact energy absorption capability of PEEK composites", *Composite Structures,* **vol. 134, pp. 440-449.**

[37] Russo, P., Acierno, D., Simeoli, G., Iannace, S. and Sorrentino, L. (2013), "Flexural and impact response of woven glass fiber fabric/polypropylene composites", *Composites Part B: Engineering,* **vol. 54, pp. 415-421.**

[38] Blumentritt, B., Vu, B. and Cooper, S. (1975), "Fracture in oriented short fibre-reinforced thermoplastics", *Composites,* vol. 6, no. 3, pp. 105-114.

[39] Ramsteiner, F. and Theysohn, R. (1985), "The influence of fibre diameter on the tensile behaviour of short-glass-fibre reinforced polymers", *Composites Science and Technology,* vol. 24, no. 3, pp. 231-240.

[40] Laura, D., Keskkula, H., Barlow, J. and Paul, D. (2003), "Effect of rubber particle size and rubber type on the mechanical properties of glass fiber reinforced, rubber-toughened nylon 6", *Polymer,* vol. 44, no. 11, pp. 3347-3361.

[41] Liang, J. and Li, R. (2000), "Rubber toughening in polypropylene: a review", *Journal of Applied Polymer Science,* vol. 77, no. 2, pp. 409-417.

[42] Bucknall, C. (1990), "Fracture resistance in rubber-toughened polymers", *Makromolekulare Chemie. Macromolecular Symposia,* Vol. 38, Wiley Online Library, pp. 1.

[43] Sui, G., Wong, S. and Yue, C. (2001), "Effect of extrusion compounding on the mechanical properties of rubber-toughened polymers containing short glass fibers", *Journal of Materials Processing Technology,* vol. 113, no. 1, pp. 167-171.

[44] Mamalis, A. G. (1998), *Crashworthiness of composite thin-walled structural components,* Technomic Pub. Co., Lancaster, Pa.

[45] Brown, J. (2010), "Crashworthiness", *Cranfield University, Shool of Engineering, lecture notes, .*

[46] Farley, G. L. (1986), "Effect of fiber and matrix maximum strain on the energy absorption of composite materials", *Journal of Composite Materials,* vol. 20, no. 4, pp. 322.

[47] Farley, G. L. (1983), "Energy absorption of composite materials", *Journal of Composite Materials,* vol. 17, no. 3, pp. 267.

[48] Hamada, H., Coppola, J., Hull, D., Maekawa, Z. and Sato, H. (1992), "Comparison of energy absorption of carbon/epoxy and carbon/PEEK composite tubes", *Composites,* vol. 23, no. 4, pp. 245-252.

[49] Farley, G. L. (1991), "The effects of crushing speed on the energy-absorption capability of composite tubes", *Journal of Composite Materials,* vol. 25, no. 10, pp. 1314.

[50] Thornton, P. (1990), "The crush behavior of pultruded tubes at high strain rates", *Journal of Composite Materials,* vol. 24, no. 6, pp. 594.

[51] Wang, Y., Feng, J., Wu, J. and Hu, D. (2016), "Effects of fiber orientation and wall thickness on energy absorption characteristics of carbon-reinforced composite tubes under different loading conditions", *Composite Structures,* vol. 153, pp. 356-368.

[52] Thornton, P. (1979), "Energy absorption in composite structures", *Journal of Composite Materials,* vol. 13, no. 3, pp. 247.

[53] Luo, J. J. and Daniel, I. M. (2003), "Characterization and modeling of mechanical behavior of polymer/clay nanocomposites", *Composites Science and Technology,* vol. 63, no. 11, pp. 1607-1616.

[54] Thostenson, E. T., Li, C. and Chou, T. W. (2005), "Nanocomposites in context", *Composites Science and Technology,* vol. 65, no. 3-4, pp. 491-516.

[55] Ma, J., Mo, M. S., Du, X. S., Rosso, P., Friedrich, K. and Kuan, H. C. (2008), "Effect of inorganic nanoparticles on mechanical property, fracture toughness and toughening mechanism of two epoxy systems", *Polymer,* vol. 49, no. 16, pp. 3510-3523.

[56] Rong, M. Z., Zhang, M. Q., Zheng, Y. X., Zeng, H. M., Walter, R. and Friedrich, K. (2001), "Structure-property relationships of irradiation grafted nano-inorganic particle filled polypropylene composites", *Polymer,* vol. 42, no. 1, pp. 167-183.

[57] Johnsen, B., Kinloch, A., Mohammed, R., Taylor, A. and Sprenger, S. (2007), "Toughening mechanisms of nanoparticle-modified epoxy polymers", *Polymer,* vol. 48, no. 2, pp. 530-541.

[58] Ou, Y., Yang, F. and Yu, Z. Z. (1998), "A new conception on the toughness of nylon 6/silica nanocomposite prepared via in situ polymerization", *Journal of Polymer Science Part B: Polymer Physics,* vol. 36, no. 5, pp. 789-795.

[59] Gu, H., Guo, Y., Wong, S. Y., He, C., Li, X. and Shim, V. (2013), "Effect of interphase and strain-rate on the tensile properties of polyamide 6 reinforced with functionalized silica nanoparticles", *Composites Science and Technology,* vol. 75, pp. 62-69.

[60] Friedrich, K., Fakirov, S. and Zhang, Z. (2005), *Polymer composites: from nano-to-macro-scale,* Springer Verlag.

[61] Ajayan, P. M., Schadler, L. S., Braun, P. V., Picu, C. and Keblinski, P. (2003), *Nanocomposite science and technology,* Wiley Online Library.

[62] Sprenger, S., Kothmann, M. H. and Altstaedt, V. (2014), "Carbon fiber-reinforced composites using an epoxy resin matrix modified with reactive liquid rubber and silica nanoparticles", *Composites Science and Technology,* vol. 105, pp. 86-95.

[63] Zheng, Y., Zheng, Y. and Ning, R. (2003), "Effects of nanoparticles SiO2 on the performance of nanocomposites", *Materials Letters,* vol. 57, no. 19, pp. 2940-2944.

[64] Cho, J. and Paul, D. (2001), "Nylon 6 nanocomposites by melt compounding", *Polymer,* vol. 42, no. 3, pp. 1083-1094.

[65] Ruiz-Hitzky, E. (1993), "Conducting polymers intercalated in layered solids", *Advanced Materials,* vol. 5, no. 5, pp. 334-340.

[66] Chin, I. J., Thurn-Albrecht, T., Kim, H. C., Russell, T. P. and Wang, J. (2001), "On exfoliation of montmorillonite in epoxy", *Polymer,* vol. 42, no. 13, pp. 5947-5952.

[67] Wu, C. L., Zhang, M. Q., Rong, M. Z. and Friedrich, K. (2002), "Tensile performance improvement of low nanoparticles filled-polypropylene composites", *Composites Science and Technology,* vol. 62, no. 10-11, pp. 1327-1340.

[68] Daniel, I., Miyagawa, H., Gdoutos, E. and Luo, J. (2003), "Processing and characterization of epoxy/clay nanocomposites", *Experimental Mechanics,* vol. 43, no. 3, pp. 348-354.

[69] Sinha Ray, S. and Okamoto, M. (2003), "Polymer/layered silicate nanocomposites: a review from preparation to processing", *Progress in Polymer Science,* vol. 28, no. 11, pp. 1539-1641.

[70] Hussain, F., Hojjati, M., Okamoto, M. and Gorga, R. E. (2006), "Review article: polymer-matrix nanocomposites, processing, manufacturing, and application: an overview", *Journal of Composite Materials,* vol. 40, no. 17, pp. 1511.

[71] Pavlidou, S. and Papaspyrides, C. (2008), "A review on polymer-layered silicate nanocomposites", *Progress in Polymer Science,* vol. 33, no. 12, pp. 1119-1198.

[72] Wilson Jr, O., Olorunyolemi, T., Jaworski, A., Borum, L., Young, D., Siriwat, A., Dickens, E., Oriakhi, C. and Lerner, M. (1999), "Surface and interfacial properties of polymer-intercalated layered double hydroxide nanocomposites", *Applied Clay Science,* vol. 15, no. 1-2, pp. 265-279.

[73] Oriakhi, C. O., Farr, I. V. and Lerner, M. M. (1997), "Thermal characterization of poly (styrene sulfonate)/layered double hydroxide nanocomposites", *Clays and Clay Minerals,* vol. 45, no. 2, pp. 194-202.

[74] Alexandre, M. and Dubois, P. (2000), "Polymer-layered silicate nanocomposites: preparation, properties and uses of a new class of materials", *Materials Science and Engineering: R: Reports,* vol. 28, no. 1-2, pp. 1-63.

[75] Pavlidou, S. and Papaspyrides, C. (2008), "A review on polymer-layered silicate nanocomposites", *Progress in Polymer Science,* vol. 33, no. 12, pp. 1119-1198.

[76] Lee, D. C. and Jang, L. W. (1998), "Characterization of epoxy-clay hybrid composite prepared by emulsion polymerization", *Journal of Applied Polymer Science,* vol. 68, no. 12, pp. 1997-2005.

[77] Lan, T., Kaviratna, P. D. and Pinnavaia, T. J. (1995), "Mechanism of clay tactoid exfoliation in epoxy-clay nanocomposites", *Chemistry of Materials,* vol. 7, no. 11, pp. 2144-2150.

[78] Kornmann, X., Lindberg, H. and Berglund, L. A. (2001), "Synthesis of epoxy-clay nanocomposites: influence of the nature of the clay on structure", *Polymer,* vol. 42, no. 4, pp. 1303-1310.

[79] ZHANG, M., ZENG, H., ZHANG, L. and LIN, G. (1993), "Fracture characteristics of discontinuous carbon fibre-reinforced PPS and PES-C composites", *Polymers & Polymer Composites,* vol. 1, no. 5, pp. 357-365.

[80] Ng, C., Schadler, L. and Siegel, R. (1999), "Synthesis and mechanical properties of TiO2-epoxy nanocomposites", *Nanostructured Materials,* vol. 12, no. 1-4, pp. 507-510.

[81] Wetzel, B., Haupert, F. and Qiu Zhang, M. (2003), "Epoxy nanocomposites with high mechanical and tribological performance", *Composites Science and Technology,* vol. 63, no. 14, pp. 2055-2067.

[82] Zhang, H., Zhang, Z., Friedrich, K. and Eger, C. (2006), "Property improvements of in situ epoxy nanocomposites with reduced interparticle distance at high nanosilica content", *Acta Materialia,* vol. 54, no. 7, pp. 1833-1842.

[83] Bharadwaj, R., Mehrabi, A., Hamilton, C., Trujillo, C., Murga, M., Fan, R., Chavira, A. and Thompson, A. (2002), "Structure-property relationships in cross-linked polyester-clay nanocomposites", *Polymer,* vol. 43, no. 13, pp. 3699-3705.

[84] Kojima, Y., Usuki, A., Kawasumi, M., Okada, A., Kurauchi, T. and Kamigaito, O. (1993), "Sorption of water in nylon 6-clay hybrid", *Journal of Applied Polymer Science,* vol. 49, no. 7, pp. 1259-1264.

[85] Shadler LS, Jiang K, Andrews R Eitan A. (2003), "Nanotube Reinforced Polymer Composites: Tailoring the Interface for Improved Mechanical Properties", Vol. 422(b), San Diego, .

[86] Crosby, A. J. and Lee, J. Y. (2007), "Polymer nanocomposites: the "nano" effect on mechanical properties", *Polymer reviews,* vol. 47, no. 2, pp. 217-229.

[87] Yuan, Q. and Misra, R. (2006), "Impact fracture behavior of clay-reinforced polypropylene nanocomposites", *Polymer,* vol. 47, no. 12, pp. 4421-4433.

[88] Sun, L., Gibson, R. F., Gordaninejad, F. and Suhr, J. (2009), "Energy absorption capability of nanocomposites: A review", *Composites Science and Technology,* vol. 69, no. 14, pp. 2392-2409.

[89] Viana, J. (2013), "Polymeric materials for impact and energy dissipation", *Plastics, rubber and composites, .*

[90] Bartczak, Z., Argon, A. S., Cohen, R. E. and Weinberg, M. (1999), "Toughness mechanism in semi-crystalline polymer blends: I. High-density polyethylene toughened with rubbers", *Polymer,* vol. 40, no. 9, pp. 2331-2346.

[91] Bartczak, Z., Argon, A. S., Cohen, R. E. and Weinberg, M. (1999), "Toughness mechanism in semi-crystalline polymer blends: II. High-density polyethylene toughened with calcium carbonate filler particles", *Polymer,* vol. 40, no. 9, pp. 2347-2365.

[92] Subramaniyan, A. K. and Sun, C. (2007), "Toughening polymeric composites using nanoclay: Crack tip scale effects on fracture toughness", *Composites Part A: Applied Science and Manufacturing,* vol. 38, no. 1, pp. 34-43.

[93] Viana, J. (2006), "Polymeric materials for impact and energy dissipation", *Plastics, Rubber and Composites, 35,* vol. 6, no. 7, pp. 260-267.

[94] Wang, J., Fang, Z., Gu, A., Xu, L. and Liu, F. (2006), "Effect of amino-functionalization of multi-walled carbon nanotubes on the dispersion with epoxy resin matrix", *Journal of Applied Polymer Science,* vol. 100, no. 1, pp. 97-104.

[95] Cooper, C. A., Ravich, D., Lips, D., Mayer, J. and Wagner, H. D. (2002), "Distribution and alignment of carbon nanotubes and nanofibrils in a polymer matrix", *Composites Science and Technology,* vol. 62, no. 7-8, pp. 1105-1112.

[96] Kireitseu, M., Hui, D. and Tomlinson, G. (2008), "Advanced shock-resistant and vibration damping of nanoparticle-reinforced composite material", *Composites Part B: Engineering,* vol. 39, no. 1, pp. 128-138.

[97] Wetzel, B., Rosso, P., Haupert, F. and Friedrich, K. (2006), "Epoxy nanocomposites-fracture and toughening mechanisms", *Engineering Fracture Mechanics,* vol. 73, no. 16, pp. 2375-2398.

[98] Evans, A. (1972), "The strength of brittle materials containing second phase dispersions", *Philosophical Magazine,* vol. 26, no. 6, pp. 1327-1344.

[99] Javni, I., Zhang, W., Karajkov, V., Petrovic, Z. and Divjakovic, V. (2002), "Effect of nano-and micro-silica fillers on polyurethane foam properties", *Journal of Cellular Plastics,* vol. 38, no. 3, pp. 229.

[100] Chen, J., Huang, Z. and Zhu, J. (2007), "Size effect of particles on the damage dissipation in nanocomposites", *Composites Science and Technology,* vol. 67, no. 14, pp. 2990-2996.

[101] Cho, J., Joshi, M. and Sun, C. (2006), "Effect of inclusion size on mechanical properties of polymeric composites with micro and nano particles", *Composites Science and Technology,* vol. 66, no. 13, pp. 1941-1952.

[102] Yoo, Y., Spencer, M. and Paul, D. (2011), "Morphology and mechanical properties of glass fiber reinforced Nylon 6 nanocomposites", *Polymer,* vol. 52, no. 1, pp. 180-190.

[103] Akkapeddi, M. (2000), "Glass fiber reinforced polyamide-6 nanocomposites", *Polymer Composites,* vol. 21, no. 4, pp. 576-585.

[104] Clifford, M. J. and Wan, T. (2010), "Fibre reinforced nanocomposites: mechanical properties of PA6/clay and glass fibre/PA6/clay nanocomposites", *Polymer,* vol. 51, no. 2, pp. 535-539.

[105] Daud, W., Bersee, H. E., Picken, S. J. and Beukers, A. (2009), "Layered silicates nanocomposite matrix for improved fiber reinforced composites properties", *Composites Science and Technology,* vol. 69, no. 14, pp. 2285-2292.

[106] Wu, S., Wang, F., Ma, C. M., Chang, W., Kuo, C., Kuan, H. and Chen, W. (2001), "Mechanical, thermal and morphological properties of glass fiber and carbon fiber reinforced polyamide-6 and polyamide-6/clay nanocomposites", *Materials Letters,* vol. 49, no. 6, pp. 327-333.

[107] Rapaport, D. C. (2004), *The art of molecular dynamics simulation,* Cambridge Univ Pr.

[108] Belytschko, T., Xiao, S., Schatz, G. and Ruoff, R. (2002), "Atomistic simulations of nanotube fracture", *Physical Review B,* vol. 65, no. 23, pp. 235430.

[109] Namilae, S. (2005), "Multiscale model to study the effect of interfaces in carbon nanotube-based composites", *Journal of Engineering materials and technology,* vol. 127, pp. 222.

[110] Lu, Y., Yang, Q., He, X. and Liew, K. (2016), "Modeling the interfacial behavior of carbon nanotube fiber/polyethylene composites by molecular dynamics approach", *Computational Materials Science,* vol. 114, pp. 189-198.

[111] Cornwell, C. and Wille, L. (1997), "Elastic properties of single-walled carbon nanotubes in compression", *Solid State Communications,* vol. 101, no. 8, pp. 555-558.

[112] Ansari, R., Ajori, S. and Rouhi, S. (2015), "Elastic properties and buckling behavior of single-walled carbon nanotubes functionalized with diethyltoluenediamines using molecular dynamics simulations", *Superlattices and Microstructures,* vol. 77, pp. 54-63.

[113] Fisher FT, B. L. (2006), "Nanomechanics of nanoreinforced polymers.", *Handbook of theoretical and computational nanoscience. American Scientific Publishers,* , pp. 253-360.

[114] Aboudi, J. (1990), "The nonlinear behavior of unidirectional and laminated composites-A micromechanical approach", *Journal of Reinforced Plastics and Composites,* vol. 9, no. 1, pp. 13.

[115] Rabinowitz, S., Ward, I. and Parry, J. S. C. (1970), "The effect of hydrostatic pressure on the shear yield behaviour of polymers", *Journal of Materials Science,* vol. 5, no. 1, pp. 29-39.

[116] Pae, K. and Mears, D. (1968), "The effects of high pressure on mechanical behavior and properties of polytetrafluoroethylene and polyethylene", *Journal of Polymer Science Part B: Polymer Letters,* vol. 6, no. 4, pp. 269-273.

[117] Pugh, H. L. D., Chandler, E., Holliday, L. and Mann, J. (1971), "The effect of hydrostatic pressure on the tensile properties of plastics", *Polymer Engineering & Science,* vol. 11, no. 6, pp. 463-473.

[118] Bardia, P. and Narasimhan, R. (2006), "Characterisation of Pressure-sensitive Yielding in Polymers", *Strain,* vol. 42, no. 3, pp. 187-196.

[119] Bowden, P. and Jukes, J. (1972), "The plastic flow of isotropic polymers", *Journal of Materials Science,* vol. 7, no. 1, pp. 52-63.

[120] Mears, D., Pae, K. and Sauer, J. (1969), "Effects of hydrostatic pressure on the mechanical behavior of polyethylene and polypropylene", *Journal of Applied Physics,* vol. 40, no. 11, pp. 4229-4237.

[121] Sauer, J., Mears, D. and Pae, K. (1970), "Effects of hydrostatic pressure on the mechanical behaviour of polytetrafluoroethylene and polycarbonate", *European Polymer Journal,* vol. 6, no. 7, pp. 1015-1032.

[122] Ol'khovik, O. (1983), "Apparatus for testing the strength of polymers in a three-dimensional stressed state", *Mechanics of Composite Materials,* vol. 19, no. 2, pp. 270-275.

[123] Quinson, R., Perez, J., Rink, M. and Pavan, A. (1997), "Yield criteria for amorphous glassy polymers", *Journal of Materials Science,* vol. 32, no. 5, pp. 1371-1379.

[124] Sternstein, S. and Ongchin, L. (1969), "Yield criteria for plastic deformation of glassy high polymers in general stress fields", *Polymer preprints,* vol. 10, no. 2, pp. 1117–1124.

[125] Caddell, R. M., Raghava, R. S. and Atkins, A. G. (1974), "Pressure dependent yield criteria for polymers", *Materials Science and Engineering,* vol. 13, no. 2, pp. 113-120.

[126] Franklin, H. G. (1968), "Classic theories of failure of anisotropic materials", *Fibre Science and Technology,* vol. 1, no. 2, pp. 137-150.

[127] Sandhu, R. (1972), *A survey of failure theories of isotropic and anisotropic materials,* .

[128] Sendeckyj, G. (1972), "A brief survey of empirical multiaxial strength criteria for composites", *Astm Stp,* vol. 497, pp. 41-51.

[129] Hinton, M. J., Kaddour, A. S. and Soden, P. D. (2004), *Failure criteria in fibre reinforced polymer composites: the world-wide failure exercise,* Elsevier.

[130] Hinton, M., Kaddour, A. and Soden, P. (2002), "A comparison of the predictive capabilities of current failure theories for composite laminates, judged against experimental evidence", *Composites Science and Technology,* vol. 62, no. 12, pp. 1725-1797.

[131] Hill, R. (1948), "A theory of the yielding and plastic flow of anisotropic metals", *Proceedings of the Royal Society of London.Series A.Mathematical and Physical Sciences,* vol. 193, no. 1033, pp. 281-297.

[132] Azzi, V. and Tsai, S. (1965), "Anisotropic strength of composites", *Experimental Mechanics,* vol. 5, no. 9, pp. 283-288.

[133] Hoffman, O. (1967), "The brittle strength of orthotropic materials", *Journal of Composite Materials,* vol. 1, no. 2, pp. 200-206.

[134] Tsai, S. W. and Wu, E. M. (1971), "A general theory of strength for anisotropic materials", *Journal of Composite Materials,* vol. 5, no. 1, pp. 58-80.

[135] Gol'denblat, I. and Kopnov, V. (1965), "Strength of glass-reinforced plastics in the complex stress state", *Polymer Mechanics,* vol. 1, no. 2, pp. 54-59.

[136] Shenoi, R. and Hawkins, G. (1996), "Micromechanics approaches to predict damage in FRP composite laminates", .

[137] Jones, R. M. (1998), ***Mechanics of composite materials,*** **CRC Press.**

[138] Narayanaswami, R. and Adelman, H. M. (1977), "Evaluation of the tensor polynomial and Hoffman strength theories for composite materials", ***Journal of Composite Materials,*** **vol. 11, no. 4, pp. 366-377.**

[139] Zhang, W. and Evans, K. (1988), "A strain-based tensor polynomial failure criterion for anisotropic materials", ***The Journal of Strain Analysis for Engineering Design,*** **vol. 23, no. 4, pp. 179-186.**

[140] Sandhu, R. (1974), "Ultimate Strength Analysis of Symmetric Laminates.", ***AIR FORCE FLIGHT DYNAMICS LAB,WRIGHT-PATTERSON AFB OHIO,*** **vol. No. AFFDL-TR-73-137, no. AD 779927.**

[141] Sandhu, R. (1976), "Nonlinear behavior of unidirectional and angle ply laminates", ***Journal of Aircraft,*** **vol. 13, no. 2, pp. 104-111.**

[142] Zand, B., Butalia, T. S., Wolfe, W. E. and Schoeppner, G. A. (2012), "A strain energy based failure criterion for nonlinear analysis of composite laminates subjected to triaxial loading", ***Journal of Composite Materials,*** **vol. 46, no. 19-20, pp. 2515-2537.**

[143] Wolfe, W. E. and Butalia, T. S. (1998), "A strain-energy based failure criterion for non-linear analysis of composite laminates subjected to biaxial loading", ***Composites Science and Technology,*** **vol. 58, no. 7, pp. 1107-1124.**

[144] Doudican, B. M., Zand, B., Amaya, P., Butalia, T. S., Wolfe, W. E. and Schoeppner, G. A. (2013), "Strain energy based failure criterion: Comparison of numerical predictions and experimental observations for symmetric composite laminates subjected to triaxial loading", ***Journal of Composite Materials,*** **vol. 47, no. 6-7, pp. 847-866.**

[145] Drysdale, W. (1985), "MODELLING OF RATE-DEPENDENT ANISOTROPIC MATERIAL BEHAVIOR BY PLASTICITY THEORY", ***Le Journal de Physique Colloques,*** **vol. 46, no. C5, pp. C5-73-C5-80.**

[146] Perzyna, P. (1966), "Flmdamental Problems in Viseoplasticity", ***Advances in Applied Mechanics,*** **vol. 9, pp. 243.**

[147] Wang, W., Sluys, L. and De Borst, R. (1997), "Viscoplasticity for instabilities due to strain softening and strain-rate softening", ***International Journal for Numerical Methods in Engineering,*** **vol. 40, no. 20, pp. 3839-3864.**

[148] Winnicki, A., Pearce, C. and Bićanić, N. (2001), "Viscoplastic Hoffman consistency model for concrete", ***Computers & Structures,*** **vol. 79, no. 1, pp. 7-19.**

[149] *, Data to Decision Platform for Engineers and Scientists*, **available at: www.d3view.com (accessed 01/2015).**

[150] **Lobo, H. (2007), "Methodology for Selection of Material Models for Plastics Impact Simulation",** *6th European LS-DYNA Users' Conference,* **.**

[151] **Aboudi, J. (1988), "Micromechanical analysis of the strength of unidirectional fiber composites",** *Composites Science and Technology,* **vol. 33, no. 2, pp. 79-96.**

[152] **Kanit, T., Forest, S., Galliet, I., Mounoury, V. and Jeulin, D. (2003), "Determination of the size of the representative volume element for random composites: statistical and numerical approach",** *International Journal of Solids and Structures,* **vol. 40, no. 13-14, pp. 3647-3679.**

[153] **Mori, T. and Tanaka, K. (1973), "Average stress in matrix and average elastic energy of materials with misfitting inclusions",** *Acta Metallurgica,* **vol. 21, no. 5, pp. 571-574.**

[154] **Ashton, J., Halpin, J. C. and Petit, P. H. (1969),** *Primer on composite materials: analysis,* **Technomic Pub. Co. Stamford, Conn.**

[155] **Halpin, J. (1969), "Stiffness and Expansion Estimates for Oriented Short Fiber Composites",** *Journal of Composite Materials,* **vol. 3, no. 4, pp. 732.**

[156] **Eshelby, J. (1957), "The Determination of the Elastic Field of an Ellipsoidal Inclusion, and Related Problems",** *Proceedings of the Royal Society of London.Series A.Mathematical and Physical Sciences,* **vol. 241, no. 1226, pp. 376.**

[157] **Eshelby, J. (1961), "Elastic inclusions and inhomogeneities",** *Progress in solid mechanics,* **vol. 2, no. 1, pp. 89-140.**

[158] **Tucker, C. and Liang, E. (1999), "Stiffness predictions for unidirectional short-fiber composites: review and evaluation",** *Composites Science and Technology(UK),* **vol. 59, no. 5, pp. 655-671.**

[159] **Fornes, T. and Paul, D. (2003), "Modeling properties of nylon 6/clay nanocomposites using composite theories",** *Polymer,* **vol. 44, no. 17, pp. 4993-5013.**

[160] **Wu, Y. P., Jia, Q. X., Yu, D. S. and Zhang, L. Q. (2004), "Modeling Young's modulus of rubber-clay nanocomposites using composite theories",** *Polymer Testing,* **vol. 23, no. 8, pp. 903-909.**

[161] **Wilkinson, A., Man, Z., Stanford, J., Matikainen, P., Clemens, M., Lees, G. and Liauw, C. (2007), "Tensile properties of melt intercalated polyamide 6-Montmorillonite nanocomposites",** *Composites Science and Technology,* **vol. 67, no. 15-16, pp. 3360-3368.**

[162] Chavarria, F. and Paul, D. (2004), "Comparison of nanocomposites based on nylon 6 and nylon 66", *Polymer,* vol. 45, no. 25, pp. 8501-8515.

[163] Talò, M., Krause, B., Pionteck, J., Lanzara, G. and Lacarbonara, W. (2016), "An updated micromechanical model based on morphological characterization of carbon nanotube nanocomposites", *Composites Part B: Engineering,* .

[164] Chen, J., Huang, Z. and Mai, Y. W. (2003), "Constitutive relation of particulate-reinforced viscoelastic composite materials with debonded microvoids", *Acta Materialia,* vol. 51, no. 12, pp. 3375-3384.

[165] Boutaleb, S., Zaïri, F., Mesbah, A., Naït-Abdelaziz, M., Gloaguen, J., Boukharouba, T. and Lefebvre, J. (2009), "Micromechanics-based modelling of stiffness and yield stress for silica/polymer nanocomposites", *International Journal of Solids and Structures,* vol. 46, no. 7-8, pp. 1716-1726.

[166] Mesbah, A., Zaïri, F., Nait-Abdelaziz, M., Gloaguen, J., Anoukou, K., Zaoui, A., Qu, Z., Boukharouba, T. and Lefebvre, J. (2014), "Micromechanics-based constitutive modeling of plastic yielding and damage mechanisms in polymer–clay nanocomposites: Application to polyamide-6 and polypropylene-based nanocomposites", *Composites Science and Technology,* vol. 101, pp. 71-78.

[167] Ju, J. and Sun, L. (2001), "Effective elastoplastic behavior of metal matrix composites containing randomly located aligned spheroidal inhomogeneities. Part I: Micromechanics-based formulation", *International Journal of Solids and Structures,* vol. 38, no. 2, pp. 183-201.

[168] Smit, R., Brekelmans, W. and Meijer, H. (1998), "Prediction of the mechanical behavior of nonlinear heterogeneous systems by multi-level finite element modeling", *Computer Methods in Applied Mechanics and Engineering,* vol. 155, no. 1-2, pp. 181-192.

[169] Sheng, N., Boyce, M., Parks, D., Rutledge, G., Abes, J. and Cohen, R. (2004), "Multiscale micromechanical modeling of polymer/clay nanocomposites and the effective clay particle", *Polymer,* vol. 45, no. 2, pp. 487-506.

[170] Julian Y.H. Chia, Kais Hbaieb, Brian Cotterell (2006), "MODELLING CLAY GALLERY FAILURE IN CLAY NANOCOMPOSITES", *16 TH INTERNATIONAL CONFERENCE ON COMPOSITE MATERIALS,* .

[171] Lee, W., Son, J., Kang, N., Park, I. and Park, Y. (2009), "Finite-element analysis of deformation behaviors in random-whisker-reinforced composite", *Scripta Materialia,* vol. 61, no. 6, pp. 580-583.

[172] **Chawla, N., Sidhu, R. and Ganesh, V. (2006), "Three-dimensional visualization and microstructure-based modeling of deformation in particle-reinforced composites", *Acta Materialia,* vol. 54, no. 6, pp. 1541-1548.**

[173] **Fereidoon, A., Rajabpour, M. and Hemmatian, H. (2013), "Fracture analysis of epoxy/SWCNT nanocomposite based on global–local finite element model", *Composites Part B: Engineering,* vol. 54, pp. 400-408.**

[174] **Chia, J. Y. H. (2009), "Finite Element Modelling Clay Nanocomposites and Interface Effects on Mechanical Properties", *IUTAM Symposium on Modelling Nanomaterials and Nanosystems, IUTAM Bookseries, Volume 13. ISBN 978-1-4020-9556-6. Springer Netherlands, 2009, p. 241,* Vol. 1, pp. 241.**

[175] **Adam, L., Delaere, K., Gérard, J., Assaker, R., Doghri, I. and Kaszacs, M. (2009), "Multi-Scale Modeling of Polymer Nanocomposites", *eXstream engineering S.A.,* .**

[176] **Maier, C. and Calafut, T. (1998), *Polypropylene: the definitive user's guide and databook,* William Andrew.**

[177] **Zoukrami, F., Haddaoui, N., Vanzeveren, C., Sclavons, M. and Devaux, J. (2008), "Effect of compatibilizer on the dispersion of untreated silica in a polypropylene matrix", *Polymer International,* vol. 57, no. 5, pp. 756-763.**

[178] **Simo, J. and Ortiz, M. (1985), "A unified approach to finite deformation elastoplastic analysis based on the use of hyperelastic constitutive equations", *Computer Methods in Applied Mechanics and Engineering,* vol. 49, no. 2, pp. 221-245.**

[179] **Ortiz, M. and Simo, J. (1986), "An analysis of a new class of integration algorithms for elastoplastic constitutive relations", *International Journal for Numerical Methods in Engineering,* vol. 23, no. 3, pp. 353-366.**

[180] **, *MatWeb - The Online Material Property Data*, available at: www.matweb.com (accessed 10.01.2015).**

[181] **Lobo, H. and Hurtado, J. (2006), "Characterization and modeling of nonlinear behavior of plastics", *ABAQUS User Conference,* .**

[182] **Erhart, T. (2010), "An Overview of User Defined Interfaces in LS-DYNA", *ed.Stuttgart, Germany: Dynamore GmbH,* .**

[183] **Unosson, M. and Buzaud, E. (2000), "Scalar and Vectorized User Defined Material Routines in LS-DYNA", *2000.,* .**

[184] Abedrabbo, N., Pourboghrat, F. and Carsley, J. (2006), "Forming of aluminum alloys at elevated temperatures–Part 2: Numerical modeling and experimental verification", *International Journal of Plasticity,* vol. 22, no. 2, pp. 342-373.